Université catholique de Louvain
Institut de la Matière Condensée
et des Nanosciences (IMCN)
Molécules, Solides
et Réactivité (MOST)

UCL
Université
catholique
de Louvain

Photo-reactivity of Iridium(III) bis-terdentate complexes and applications

JACQUES Alexandre

Promoteur : Professeur Benjamin ELIAS

Thèse de doctorat présentée en vue de l'obtention du diplôme de Docteur en Sciences

---

Louvain-la-Neuve

2015

Members of the jury

Prof. Daniel Peeters

Université catholique de Louvain, president of the jury

Prof. Frédérique Loiseau

Université Joseph Fourier, France

Prof. Andrée Kirsch-De Mesmaeker

Université libre de Bruxelles

Prof. Sophie Hermans

Université catholique de Louvain

Prof. Charles-André Fustin

Université catholique de Louvain

Prof. Benjamin Elias (Supervisor)

Université catholique de Louvain

Remerciements

Tout d'abord, je tiens à remercier le Professeur Benjamin Elias pour la confiance qu'il m'a accordée et l'incroyable liberté dont j'ai pu bénéficier durant ces quatre années. Je le remercie chaleureusement pour ses conseils judicieux, son soutien, son optimisme permanent mais également pour ses porte-mines. Je sais qu'il aurait aimé que je synthétise de l'ADN de manière tout à fait autonome. Malheureusement, cela n'a pas été possible malgré ma passion pour le plus célèbre des doubles brins. En tout cas, j'espère qu'il retiendra autre chose de notre collaboration que ces traces suspectes sur mes chaussures un beau jour de l'été 2012.

Le Professeur Elias m'a, par ailleurs, permis de rencontrer des chimistes de grande qualité. Parmi eux, je dois reconnaitre que Fanny restera l'une des plus importantes. Je voudrais la remercier pour ses conseils précieux et sa rigueur scientifique (même si celle-ci m'a par moment parue excessive). Nos rencontres régulières auront eu le mérite d'aiguiser mon sens de l'auto-critique. Je suis en tout cas en admiration devant la passion qui vous anime toujours après toutes ces années de recherche. Par ailleurs, je tiens également à remercier Ludo et Lio de l'ULB pour leur aide dans les mesures de durées de vie de mes complexes.

Mes remerciements s'adressent également aux personnes avec qui, à un moment ou à un autre, j'ai eu la chance de travailler. Tout

d'abord le Prof. Charles-André Fustin ainsi qu'Olivier Bertrand (Goody) qui m'ont initié à la science des polymères. Je tiens également à remercier le Prof. Sophie Hermans ainsi que Florence pour leur aide au greffage de complexes sur graphène (mais pas seulement). Mais aussi Koen pour les structures DRX de complexes d'Ir(III).

En outre, je tiens à remercier chaleureusement le Prof. Garry Hanan (Université de Montréal) de m'avoir acueilli dans son labo pour un mois. J'ai pu ainsi retrouver l'ambiance si particulière d'une ville comme Montréal et sa mentalité américaine mais pas trop. Je remercie tous les membres du groupe pour leur accueil sympathique et plus particulièrment Olivier Schott qui m'a permis de conduire mes expériences de photo-production d'hydrogène dans de bonnes conditions ainsi que Mihaela Cibian et Thomas Auvray pour les calculs théoriques.

Je souhaite également remercier les membres du labo avec qui j'ai partagé de chouettes moments. Quentin et son air d'ange, Mika et son emblématique air nonchalant, Cédric et sa grande gueule, Christophe et sa zen attitude (et aussi notre collaboration en photocatalyse), Johan et son amour pour les bières belges (que je partage évidemment), mais aussi Simon et son raffinement légendaire, Robin, l'agro qui murmurait à l'oreille des chimistes et Justin, l'autre luxembourgeois pur jus. Mais j'adresse un remerciement particulier à mon PG (Guillaume je crois), pour ces années passées dans notre

petit bureau. J'ai beaucoup apprécié ton calme légendaire et ta faculté à résoudre les problèmes informatiques avec brio et légèreté.

De plus, je remercie les personnes qui sont passées plus brièvement par le labo (les réthos, Maud, Diamante, Nathalie, Sergio, Larry et mon IPL, Jonathan). Ca aura été un plaisir de vous transmettre mon petit savoir. Toute cette petite troupe aura pu vaquer à leur occupation dans de bonnes conditions grâce à l'intransigeance de Stephe qui n'a toléré aucun débordement aussi insignifiant soit-il et de Sabrina (boys, boys, boys, ...). Enfin, un clin d'œil particulier à Agnès qui a partagé un certain nombre de nos repas de midi.

Il me tient à cœur de souligner le travail fourni par ceux qui travaillent dans l'ombre : Jessica (magasin), Raoul (Masse), Cécile et Alain (RMN), Laurent (HPLC), Brigitte (sa grosse machine qui nettoie) et Chantal ma pétale qui nous a remué et beaucoup aidé dans cette aventure.

Mis à part la science, j'aurai partagé beaucoup de bons moments avec les chercheurs du groupe du Prof. Olivier Riant qui m'ont si souvent donné l'occasion d'aller me désaltérer à l'Only… Comment ne pas remercier mes amis, Greggy, Bil, Jon, Beber et Moineau (indissociables) ? Eux pour qui la chimie reste un gros point d'interrogation mais avec qui j'ai partagé tant de merveilleux moments. Je n'oublie pas mes deux petits filleuls Mathis et Germain, eux qui me procurent tant de joie lors de leur découverte de la vie.

Merci surtout à Florence non seulement pour son expertise en nanotube et autre graphène mais aussi et surtout pour son amour et sa capacité à me supporter. Mes remerciements vont également à celle qui me réjouit chaque matin, Tika.

Je remercie aussi ma sœur et mes parents pour leur soutien et leurs encouragements tout au long de mes études. Je garderai de cette aventure un excellent souvenir à bien des égards.

Abbreviations

A	Adenine
Å	Angström
Ac	Acetyl
acac	acetylacetonate
APCI	Atmospheric Pressure Chemical Ionization
Ar	Argon
a.u.	arbitrary unit
B3LYP	Becke, 3-paramater, Lee-Yang-Parr Functional
bpy	2,2'-bipyridine
C	Cytosine
Cat	Catalyst
CB	Cucurbituril
dAMP	deoxyAdenosine-5'-MonoPhosphate
DCC	N,N'-dicyclohexylcarbodiimide
dCMP	deoxyCytosine-5'-MonoPhosphate
DFT	Density functional theory
dGMP	deoxyGuanosine-5'-MonoPhosphate
DLS	Dynamic Light Scattering
DMF	N,N-dimethylformamide
dmgH	dimethylglyoximate
$dmgH_2$	dimethylglyoxime
DMAP	4-Dimethylaminopyridine
DMI	1,3-Dimethyl-2-imidazolidinone

DMSO	Dimethyl Sulfoxide
DNA	DesoxyriboNucleic Acid
$(DOH)_2pn$	N_2, N_2'-propanediylbis-2,3-butanedione-2-imine-3-oxime
DSSC	Dye-Sensitized Solar Cell
dTMP	deoxyThymidine-5'-MonoPhosphate
ε	Molar Extinction Coefficient
EDTA	Ethylenediaminetetraacetic Acid
ESI	Electrospray ionization
Φ	Quantum yield
G	Guanine
GC	Gas Chromatography
GO	Graphene Oxide
h	hour
HER	Hydrogen Evolution Reaction
HMPA	Hexamethylphosphoramide
HOMO	Highest Occupied Molecular Orbital
HRMS	High Resolution Mass Spectrometry
Hz	Hertz
IC	Internal Conversion
IR	Infra-red
ISC	Inter-system crossing
k_r	Radiative rate constant
k_{nr}	Non-Radiative rate constant
l	Orbital quantum number
LC	Ligand Centered

LCST	Lower Critical Solution Temperature
LED	Light-Emitting Diode
LFSE	Ligand Field Splitting Energy
LLCT	Ligand-to-Ligand Charge Transfer
LMCT	Ligand-to-Metal Charge Transfer
LUMO	Lowest Unoccupied Molecular Orbital
MC	Metal Centered
Me	Methyl
MeO-Phtpy	4'-(4-MethoxyPhenyl)-2,2':6',2"-terpyridine
MLCT	Metal-to-Ligand Charge Transfer
MMLCT	Metal/Ligand-to-Ligand Charge Transfer
mmol	millimole
MO	Molecular Orbital
η	Solar energy conversion efficiency
NMR	Nuclear Magnetic Resonance
NOESY	Nuclear Overhauser Effect SpectroscopY
OLED	Organic Light-Emitting Diode
PEG	Polyethylene glycol
Phtpy	4'-phenyl-2,2':6',2"- terpyridine
PLED	Polymer Light-Emitting Diode
ppm	part per million
ppy	2-phenylpyridine
PS	PhotoSensitizer
PTSA	Para-Toluene Sulfonic Acid
Py	Pyridine

Q	Quencher
rGO	reduced Graphene Oxide
RT	Room temperature
SCE	Saturated Calomel Electrode
T	Thymine
τ	Lifetime of the excited state
TCEP	Tris(2-carboxyethyl)-phosphine
TD-DFT	Time Dependent- Density Functional Theory
TEA	Triethylamine
TEOA	Triethanolamine
TFA	Trifluoroacetic Acid
TGA	ThermoGravimetric Analysis
THF	Tetrahydrofuran
TOF	TurnOver Frequency
TON	TurnOver Number
tpy	2,2':6',2"-terpyridine
TW	TeraWatt
UV	Ultra-violet
Vis	Visible
VR	Vibrational Relaxation
Wt	Weight
XPS	X-ray Photoelectron Spectroscopy

Structure of ligands

bpy

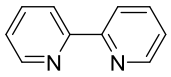

2,2'-bipyridine

ppy

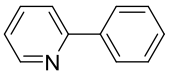

2-phenylpyridine

tpy

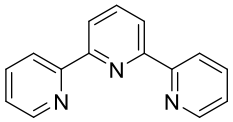

2,2':6',2''-terpyridine

4'-Phtpy

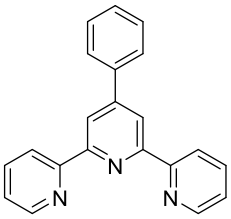

4'-phenyl-
2,2':6',2''-terpyridine

4'-MeO-Phtpy

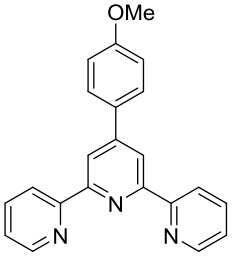

4'-(4-Methoxyphenyl)-
2,2':6',2''-terpyridine

4'-MeO-tppy

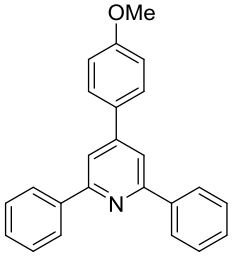

2,6-diphenyl-4-
(4'-methoxyphenyl) pyridine

4'-COOH-Phtpy

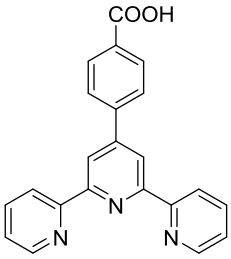

4'-(4-Carboxyphenyl)-
2,2':6',2''-terpyridine

4'-COOMe-Phtpy

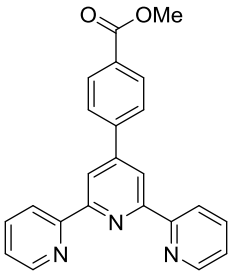

4'-(4-Carboxymethylphenyl)-
2,2':6',2''-terpyridine

4'-(3,5-diMeO-Ph)tpy

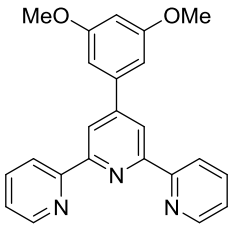

4'-(3,5-dimethoxyphenyl)-
2,2':6',2''-terpyridine

4'-(3,4,5-triMeO-Ph)tpy

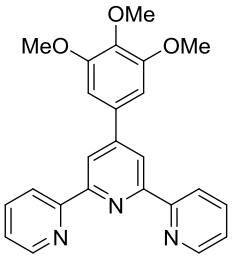

4'-(3,4,5-trimethoxyphenyl)-
2,2':6',2''-terpyridine

4'-(2,4,6-triMeO-Ph)tpy

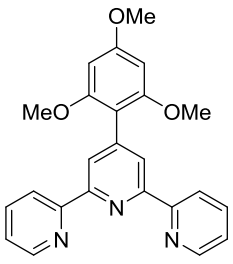

4'-(2,4,6-trimethoxyphenyl)-
2,2':6',2''-terpyridine

4'-HO-CH_2-Phtpy

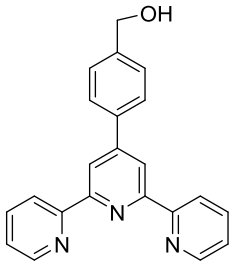

(4-([2,2':6',2''-terpyridin]-4'-yl)
phenyl)methanol

4'-Py-tpy

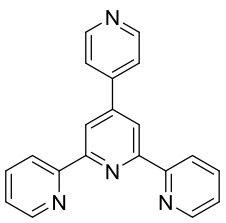

4'-(Pyridyl)-
2,2':6',2''-terpyridine

4'-Me-Py-tpy

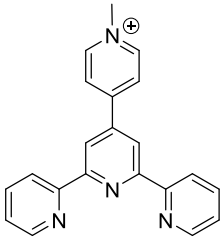

4'-(4-methyl-pyridinio)
2,2':6',2''-terpyridine

4'-Ac-Py-tpy

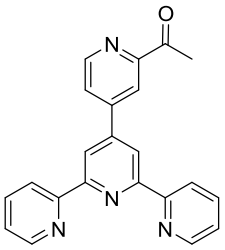

1-(6'-(pyridin-2-yl)-[2,2':4',4''-
terpyridin]-2''-yl)ethan-1-one

Tri-tpy

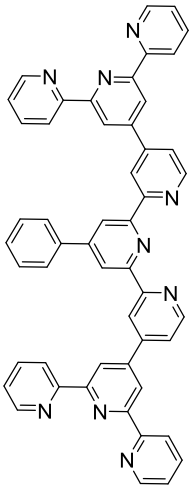

4''''-phenyl-6',6'''''-di(pyridin-2-yl)-
2,2':4',4'':2'',2''':6''',2'''':4'''',4''''':2''''',2''''''-
sepipyridine

Tetra-tpy

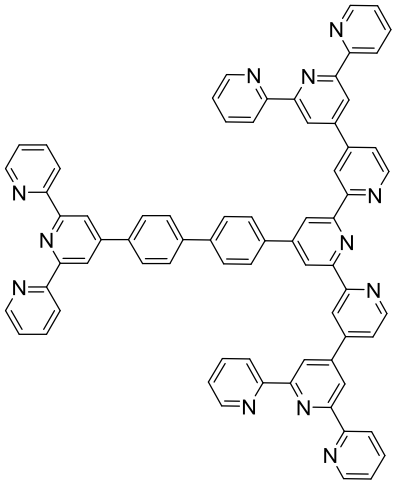

4''''-(4'-([2,2':6',2''-terpyridin]-4'-yl)-
[1,1'-biphenyl]-4-yl)-6',6'''''-di(pyridin-2-yl)-
2,2':4',4'':2'',2''':6''',2'''':4'''',4''''':2''''',2''''''-sepipyridine

dmgH$_2$

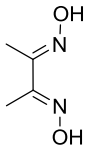

dimethylglyoxime

Hexa-tpy

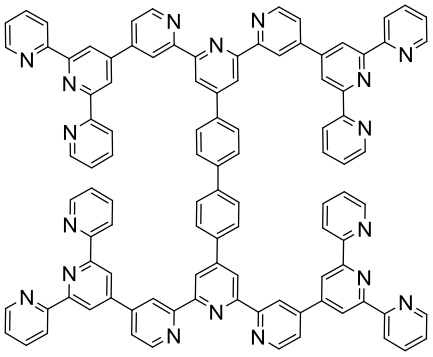

4,4'-bis(6',6'''''-di(pyridin-2-yl)-[2,2':4',4'':2'',2''':6''',2'''':4'''',4''''':2''''',2''''''
-sepipyridin]-4''''-yl)-1,1'-biphenyl

Table of Content

Abstract

Luminescence phenomena have fascinated mankind for centuries. The ability of a system to emit light is largely widespread in nature especially in deep-ocean. The scientific understanding of light emission has led to impressive improvements these last years. As a result, Light-Emitting Materials have recently emerged virtually everywhere. The material composition is variable. However, iridium-based complexes have been frequently used since a couple of years in order to benefit from their easy color tunability. The usual complexes bear three bidentate ligands. However, the development of two tridentate ligands-based complexes display some advantages which have been too scarcely used to develop some innovating applications.

During this Ph.D. thesis, we have studied the spectroelectrochemical properties of some novel luminescent Ir(III) complexes chelated by two tridentate ligands. By modifying the coordination sphere, the properties of the resulting assemblies can be modulated and compared one to another. Based on this study, the synthesized Ir(III) derivatives have been used as photocatalysts for both organic reactions and reduction of protons into molecular hydrogen. In addition, the studied Ir(III) complexes can successfully act as DNA photo-probes. Finally, a new methodology to reach functionalized multi-terdentate ligands has been developed.

Résumé

Les phénomènes de luminescence fascinent l'humanité depuis la nuit des temps. La capacité d'un système à émettre de la lumière est largement répandue dans la nature, particulièrement dans les océans. La compréhension des mécanismes d'émission de lumière par le monde scientifique a mené à des avancées impressionnantes lors de ces dernières années. Par exemple, les matériaux émettant de la lumière se retrouvent depuis peu dans pratiquement tous les domaines. La composition de ces matériaux est variable. Cependant, des complexes à base d'iridium sont fréquemment utilisés depuis quelques années afin de tirer profit de leur versatilité au niveau des couleurs émises. Les complexes généralement utilisés possèdent trois ligands bidentates. Cependant, le développement de complexes avec deux ligands tridentates présente plusieurs avantages mais n'a que trop rarement découlé sur des applications.

Lors de cette thèse de doctorat, nous avons étudié les propriétés spectroelectrochimiques de nouveaux complexes luminescents d'iridium(III) chélatés par des ligands tridentates. En modifiant la sphère de coordination autour du centre métallique, il est possible de moduler les propriétés photochimiques et électrochimiques des composés. Sur base de cette étude, les dérivés d'iridium(III) synthétisés ont été utilisés comme photocatalyseur soit pour transformer des substrats organiques, soit pour réduire des protons en dihydrogène. Par ailleurs, les complexes d'Ir(III) étudiés ont démontré leur capacité à jouer le rôle de photo-sondes à ADN. Finalement, une nouvelle méthodologie permettant de construire des ligands portant plusieurs sites chélatants terpyridiniques a été développée.

Chapter 1 - Introduction

1.1. General introduction

The supply of renewable and sustainable energy will definitely be one of the major issues for the 21st century. Nowadays, the global annual energy consumption is about 4.6 x 10^{20} J, which corresponds to an average energy consumption rate of 16 TW (TeraWatt).[1] This rate should reach 20 TW by 2030. To give an idea, this annual consumed energy requires approximately one million years for the earth to generate in the form of fossil fuels.[2] Therefore, the need for renewable energies becomes obvious and increasingly urgent. Wind and hydroelectric energies have been developed during last years in order to deal with energy requirements. However, the amount of globally exploitable wind and hydroelectric power remains not sufficient to cope with increasing energy demand.[3] Another energy source which has been suggested is the sun which provides an average global intensity of about 4.93 MJ/m^2. This represents 3 x 10^{24} J per year. The sun furnishes therefore more energy to the earth in an hour than the world consumes in a year.[2] Accordingly, there is a tremendous potential in converting the sun's energy into either electricity or chemical fuels. Whereas the former has been widely employed to generate photovoltaic cells and related devices,[4] the latter still remains sparsely developed. The efficient production of clean solar fuels would represent one of the most important breakthrough of modern science.[5]

Conversion of solar energy into chemical energy, especially light-driven water splitting into molecular hydrogen (H_2) and oxygen (O_2), represents an interesting approach since hydrogen combustion results in benign product (water) with a very high energy density (119kJ/g).[6] Subsequently, hydrogen stored energy is recovered by systems such as fuel cells which could act an essential role in cars of the future. Although the overall water splitting process can be described by a very simple global equation (Scheme 1.1), it involves a not trivial multi-electronic pathway.

$$H_2O \longrightarrow H_2 + \frac{1}{2} O_2 \qquad E^o = -1{,}23\ V/NHE$$

Scheme 1.1 – Water splitting equation.

The process may be divided into two half reactions (Scheme 1.2): the reduction of protons into H_2 and the oxidation of water into O_2 with an electron flow connecting both processes.

$$2\,H^+ + 2\,e^- \longrightarrow H_2$$

$$H_2O \longrightarrow \frac{1}{2} O_2 + 2\,H^+ + 2\,e^-$$

Scheme 1.2 – Two half reactions of water splitting: hydrogen evolution (upper equation) and water oxidation into dioxygen (bottom equation).

Since the discovery of the first water splitting system based on TiO_2 and Pt electrodes in 1972 by Fujishima and Honda,[7] numerous inorganic semiconductor based devices have been reported.[8-13] Over the past 40 years, many new photocatalysts exhibited high photocatalytic activities for water splitting into molecular oxygen and hydrogen in the ultraviolet (UV) region.[14-17] Best of all, photocatalytic water splitting using visible-light irradiation has also emerged during the last 20 years[12,18,19] although the photocatalytic efficiency of these systems remains much lower as compared with UV-absorbing materials.[20] However, in these heterogeneous photocatalysts, the electron-transfer processes depend on many interfacial parameters that are somewhat difficult to control.[21]

The development of homogenous molecular devices may provide a solution to deal with these interfacial issues. Nevertheless, in contrast to the great advancement made in the studies of purely inorganic substances, the molecular approach still requires substantial improvements in order to meet the necessary criteria for practical applications.[22-25] Up to now, each reaction (*i.e.* reduction of proton into hydrogen and oxidation of water into oxygen)

has usually been developed and studied separately because the whole process is too challenging to be carried out in a single step. In our laboratory, we specifically focus on the reduction of protons to H_2. One of the key features for these systems is the charge separation: each photon leads to the transfer of one electron. As a result, several building blocks are required to reach this goal. There are three essential items (Figure 1.1): a light-absorbing unit (A) (also named charge injector) connected to a catalytic center (C) by a bridging electronic relay (B). Under light irradiation, photo-excited electrons should be able to flow from the absorption unit (A) to the catalytic center (C) through the bridging electronic relay (B). In addition, sacrificial electron donor (such as EDTA, Et_3N, sodium ascorbate, …) has to be used to regenerate the oxidized charge injector. Pioneer researches[26,27] entailed multi-components systems where each item is separated. In other words, the components of the system are not covalently linked. However, hydrogen evolution efficiency was found lower compared with single-component devices where building blocks are connected to each other.[28]

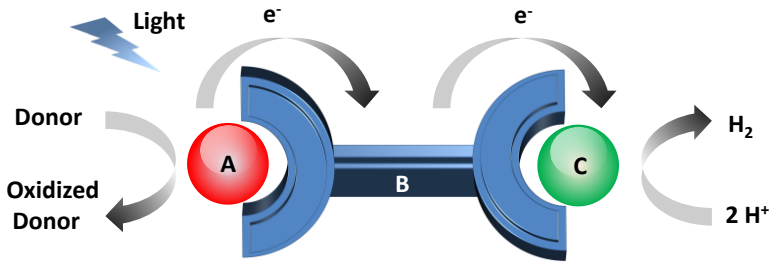

Figure 1.1 – Simplified scheme of a single-component dihydrogen photochemical molecular device. A – light-absorbing unit; C – catalytic center for proton reduction; B – Bridging electronic relay.[1]

In the literature, several single-component systems for dihydrogen photo-production based on transition metals have been synthesized and studied.[21,29-31] They usually involve ruthenium,[32-34] osmium,[35] rhenium,[36,37] or zinc[38,39] as charge injectors (A) and precious metals such as platinum

derivatives[40-42] as catalytic center (C) bridged by organic ligands (B). For all of these photocatalysts, charge injectors (A) are made of bidentate ligands chelating the metal center. However, (photo-)redox properties of these devices remain difficult to tune efficiently upon ligand modifications[43] which is an important drawback to develop such systems. Elements of photochemistry are essential to understand this issue since the key process relies on light-triggered reactions. As a consequence, general information about photochemistry is now depicted.

1.2. Elements of photochemistry

1.2.1. Electronic transitions

According to the molecular orbitals theory, the s, p, d, f,… atomic orbitals (AO) of each element of a given compound are combined together to generate a new set of molecular orbital (MO). Depending on which AO are involved, different MO may be obtained: the σ MO localized along interatomic axis arising from a combination of s or p orbitals; the π MO, formed from two p atomic orbitals overlapping laterally (termed π bonds) and found in double and triple bonds; the n MO corresponding to lone pairs. The σ and π orbitals may have a bonding or anti-bonding character (termed "*"). In addition to these MO used in organic molecules, organometallic complexes involve metallic d orbitals combinations (dσ, dπ). In photochemical processes, two orbitals are especially important: the Highest Occupied Molecular Orbital (HOMO) and the Lowest Unoccupied Molecular Orbital (LUMO).

1.2.2. Absorption of light

UV-visible light absoption of a compound leads to electronic transitions directly reflecting the relative energy of these molecular orbitals. An electronic transition is the promotion of an electron from a fully occupied

orbital to an unoccupied orbital by absorption of a photon. In other words, these electronic transitions imply going from the ground state to the excited state, both states being featured by a different occupation of molecular orbitals. The energy difference between these two electronic states corresponds to UV-visible range. In addition, the spin of electrons is also important. In the ground state, the HOMO orbital is usually occupied by two electrons with opposite spins. The spin multiplicity equals to 1 and the state is termed *singlet* (S_0). When one of the two electrons of opposite spins (belonging to a molecular orbital of a molecule in the ground state) is promoted to a molecular orbital of higher energy, its spin is in principle unchanged so that the multiplicity remains equal to 1. As a result, both the ground and excited states are called singlet state (S_0 for the ground state, and S_1, S_2, ... for the excited states) (Figure 1.2). The corresponding transition is called a singlet–singlet transition. It will be shown later that a molecule in a singlet excited state may undergo conversion into a state where the promoted electron has changed its spin; there are then two electrons with parallel spins and the multiplicity is 3. Such a state is called a *triplet* state because it corresponds to three states of equal energy. According to Hund's Rule, the triplet state has a lower energy than that of the corresponding singlet state.

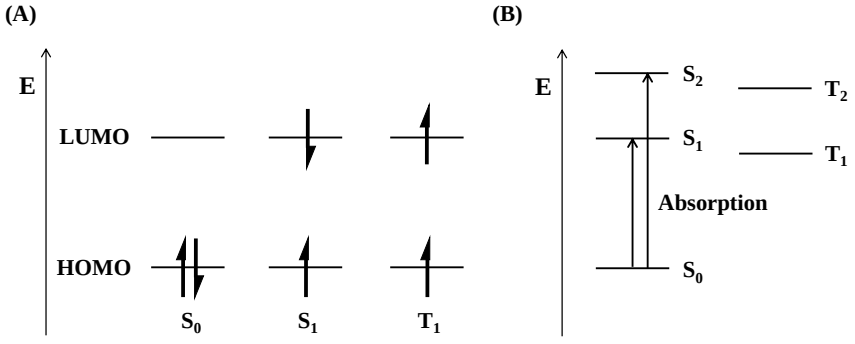

Figure 1.2 – (A) Distinction between singlet and triplet states and (B) energy levels for singlet and triplet states.

1.2.3. The Beer-Lambert Law

The efficiency of light absorption at a given wavelength λ is characterized by the absorbance A(λ) defined as:

$$A(\lambda) = \log \frac{I_\lambda^0}{I_\lambda} \quad \text{(equation 1)}$$

where I_λ^0 and I_λ are respectively the light intensities of the beams entering and leaving the absorbing medium. Most often, the absorbance can be correlated to the concentration of a given species *i* using the Beer-Lambert law:

$$A_i(\lambda) = \varepsilon_i(\lambda) l C_i \quad \text{(equation 2)}$$

where $\varepsilon_i(\lambda)$ is the molar extinction coefficient ($L.mol^{-1}.cm^{-1}$) of the species *i*, l is the absorption path length (cm) and C_i is the concentration of *i* in the sample ($mol.L^{-1}$).

1.2.4. Selection rules

All the electronic transitions between two different electronic states are not allowed. Two major "selection rules" govern electronic absorption transitions:

- Spin selection rule

Only electronic transitions between states of same multiplicities are allowed, *i.e.* singlet-singlet and triplet-triplet transitions are allowed whereas singlet-triplet and triplet-singlet are forbidden.[44]

- Symmetry selection rule (Laporte rule)

Transitions could be forbidden for symmetry reasons. In a molecule possessing a center of symmetry, electronic transitions are not allowed between orbitals of different parity. In other words, a change in polarity is

required ($\Delta l = \pm 1$ where l is the orbital quantum number). As a result, d-d transitions are theoretically forbidden. Nevertheless, detailed considerations rely on group theory and its consequences on transition probabilities are beyond the scope of this introduction. Interestingly, symmetry-forbidden transitions may be observed because the molecular vibrations cause departure of perfect symmetry (vibronic coupling). The molar absorption coefficients of these transitions may be very small and the corresponding absorption bands exhibit well-defined vibronic bands.[44]

1.2.5. Radiative and non-radiative transitions between electronic states

As disclosed before, the absorption of a photon leads to the formation of an electronic excited state. This latter can undergo different processes to return to the ground state which is either radiative or non-radiative (respectively characterized by a radiative rate constant (k_r) and a non-radiative rate constant (k_{nr})). Perrin-Jablonski diagram is convenient for visualizing in a simple way the possible processes (Figure 1.3).

1.2.5.1. Vibrational relaxation (VR)

The vibrational relaxation is the de-excitation (within a same electronic state) corresponding to the return from vibrational excited states to the vibrational ground state. This process usually occurs in two steps with different time-scales. Firstly, the energy is fastly (0.1 to 10 ps) dissipated in the different vibrators of the molecule by intramolecular vibrational relaxation. Then, the energy is slowly dispersed (10 to 100 ps) in the environment and therefore transferred to the solvent.

1.2.5.2. Internal conversion (IC)

Internal conversion (IC) is a non-radiative transition between two electronic states of the same spin multiplicity. In solution, this process is

followed by a vibrational relaxation towards the lowest vibrational level of the lowest electronic excited state. The succession of these two processes becomes the main phenomenon for the excited states S_2, S_3,… to S_1. As a result, the emission of a molecule exclusively arises from these lowest excited states (S_1 or T_1) to their ground states. This process is known as the "Kasha rule".[45]

1.2.5.3. Fluorescence

The lowest energy singlet excited state (S_1) may return to the ground state (S_0) with emission of a photon by a process called *fluorescence*. The fluorescence usually does not depend on excitation wavelength since more energetic excited states (S_2, S_3, …) return in the most stable S_1 state according to the Kasha rule.

1.2.5.4. Intersystem crossing (ISC)

Intersystem crossing (ISC) is a non-radiative transition between two isoenergetic vibrational levels belonging to electronic states of different multiplicities. According to selection rules, transitions between states of different multiplicities are forbidden. Nevertheless, ISC is possible due to spin-orbit coupling which can be understood in a primitive way by considering the motion of an electron in a Bohr-like orbit. The rotation of this electron around the nucleus generates a magnetic moment; moreover, the electron spins on its own axis, which generates another magnetic moment. Spin-orbit coupling results from the interaction between these two magnets.[44] The efficiency of this coupling varies with the fourth power of the atomic number explaining why ISC is favored by the presence of a heavy metal.

1.2.5.5. Phosphorescence and non-radiative de-excitation

In solution at room temperature, non-radiative de-excitation from the triplet state T_1 is predominant over radiative de-excitation called *phosphorescence*. In fact, the transition from T_1 to S_0 is forbidden (but it can be observed because of spin–orbit coupling) so that the radiative rate constant is very low as compared with the fluorescence.

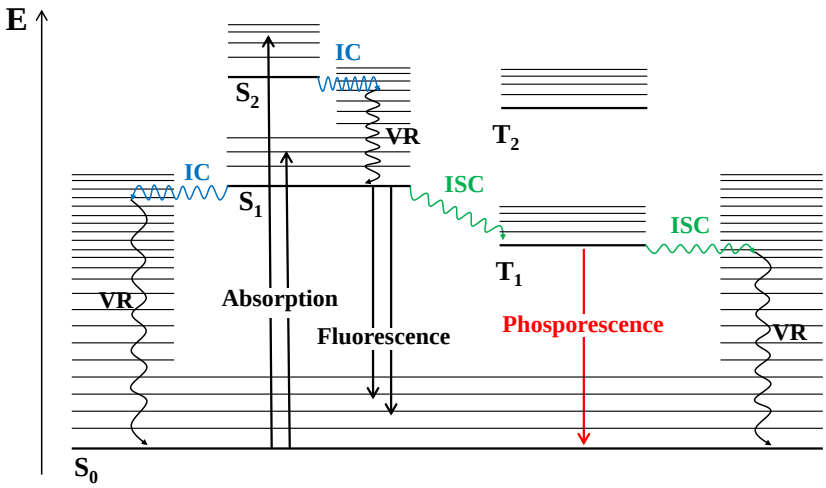

Figure 1.3 – Perrin–Jablonski diagram and illustration of the absorption, fluorescence and phosphorescence processes.

1.2.6. Lifetimes and quantum yields

1.2.6.1. Excited-state lifetimes

Unlike the more energetic excited states, S_1 and T_1 excited states are not directely involved in internal conversion or vibrational relaxation processes so that they may be implied in other deactivation processes. A crucial parameter related to excited states is their lifetime τ. This latter is determined by the different rate constants associated to processes leading to disappearance of excited molecules. Upon a light pulse, the disappearence rate of an excited state A* can be written as:

$$-\frac{d[A^*]}{dt} = (k_r + k_{nr})[A^*] \quad \text{(equation 3)}$$

where k_r is the rate constant of luminescence (fluorescence and phosphorescence) and k_{nr} is the sum of all the non-radiative rate constants. Integration of this equation in function of the time evolution yields the following expression:

$$[A^*]_{(t)} = [A^*]_0 \exp[-(k_r + k_{nr})t] = [A^*]_0 \exp\left(-\frac{t}{\tau}\right) \quad \text{(equation 4)}$$

with $\tau = \frac{1}{k_r + k_{nr}}$ and defined as the "excited state lifetime".

It is worthwhile mentioning that the lifetime can be experimentally measured. Indeed, the time-dependent luminescence intensity $I_{(t)}$ is directly connected to the population of the luminescent excited state:

$$I_{(t)} = k_r [A^*]_{(t)} = k_r [A^*]_0 \exp\left(-\frac{t}{\tau}\right) \quad \text{(equation 5)}$$

where the luminescence intensity $I_{(t)}$ is measured with an arbitrary unit (see Chapter 9). The luminescence decay time τ is one of the most important characteristics of a luminescent molecule because it defines the time window of observation for dynamic phenomena. No accurate information on the rate of processes occurring at time-scales shorter than about $\tau/100$ or longer than about $10\ \tau$ can be obtained, whereas at intermediate times, the time evolution of phenomena can be followed. For organic molecules, singlet and triplet excited state lifetimes, *i.e.* fluorescence and phosphorescence, are respectively from 10 ps to 100 ns and from 1 μs to 1 s.

1.2.6.2. Quantum yields

The luminescence quantum yield (Φ) is the fraction of excited molecules that returns to the ground state S_0 with emission of photons:

$$\Phi = \frac{k_r}{k_r + k_{nr}} = k_r \tau \quad \text{(equation 6)}$$

In other words, the luminescence quantum yield is the ratio of the number of emitted photons to the number of absorbed photons. The experimental determination of Φ is described in Chapter 9.

1.2.7. Luminescence quenching

As mentioned before, an electronic excited state could be deactivated in radiative or not radiative way. In addition, this excited state can react by different pathways. These reactions are classified as *photo-induced*. When the excited state is luminescent, the photo-induced process competes with the luminescence which can be partially or totally *quenched.* The different possible intermolecular processes responsible for luminescence quenching are gathered in the Table 1.1. Intramolecular reactions in the excited state can also affect the luminescence: intramolecular electron or proton transfers, rotations, isomerizations, … Hereafter, we give an overview of the intermolecular de-excitation processes of excited molecules responsible for luminescence quenching.

Phenomenological approach

Several cases can be identified in which an intermolecular process involving a luminescent molecule M* and a quencher Q is in competition with intrinsic de-excitation of M*. In addition, one should differenciate the experimental conditions in which luminescent quenching occurs.

First case: Q is in large excess compared to M* so that there is a high probability that M* and Q, at the time of excitation, are at a distance where the interaction is significant. Therefore, no mutual approach during the excited state lifetime is required. The luminescence quenching is called *static* and is characterized by a pseudo-first order rate constant. In this case, the excited-state reaction happens under non-diffusive conditions. This situation is also relevant for intramolecular luminescence quenching.

Second case: Q is not in large excess compared to M*. However, mutual approach of M* and Q is not possible during the excited-state lifetime because the lifetime is too short or the medium is too viscous. Therefore, only a long-range (up to 8 nm)[44] quenching may occur.

Third case: Q is not in large excess compared to M* and the mutual approach of both species is possible during the excited state lifetime of M*. A diffusion step (determining or not) is involved in the luminescence kinetic process which is termed a *dynamic quenching*. At higher concentration of Q, static quenching can occur in addition to dynamic quenching.

Table 1.1 – Main photophysical processes responsible for luminescence quenching.

Photophysical process	Reaction
Electron transfer	$M^* + A \rightarrow M^+ + A^-$ or $M^* + D \rightarrow M^- + D^+$
Proton transfer	$MH^* + B \rightarrow M^{-*} + BH^+$ or $M^* + AH \rightarrow MH^{+*} + A^-$
Energy transfer	$M^* + Q \rightarrow M + Q^*$
Excimer formation	$M^* + M \rightarrow (MM)^*$
Exciplex formation	$M^* + Q \rightarrow (MQ)^*$

Classical models for dynamic (third case) and static (first case) quenching are now presented. Here, we focus on Stern-Volmer kinetics that ignore the

transient effects although more complex models exist to take for these effects into account.[46-48]

Dynamic quenching

Stern and Volmer[49] were the first to theoretically describe the dynamic quenching. The kinetic processes are depicted in Figure 1.4.

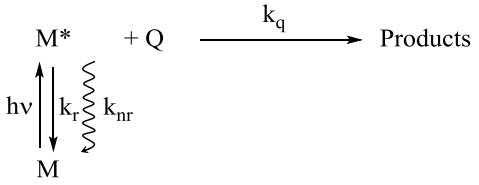

Figure 1.4 – Processes involved in dynamic quenching as well as rate constants: k_r and k_{nr} are respectively the radiative and non-radiative rate constants for M* and k_q is the rate constant of the bimolecular quenching.

According to this simplified scheme, the concentration of M* depending on time following a pulse excitation obeys the following differential equation:

$$-\frac{d[M^*]}{dt} = -(k_r + k_{nr} + k_q[Q])[M^*] = -\left(\frac{1}{\tau_0} + k_q[Q]\right)[M^*] \quad \text{(equation 7)}$$

with $\tau_0 = \frac{1}{k_r + k_{nr}}$, the luminescent excited state lifetime without quencher Q. The integration of this equation yields the expression of the concentration of the excited state in function of time, which can be connected to the luminescence intensity:

$$[M^*] = [M^*]_0 \exp\left\{-\left(\frac{1}{\tau_0} + k_q[Q]\right)t\right\} \quad \text{(equation 8)}$$

$$I_{(t)} = k_r[M^*] = k_r[M^*]_0 \exp\left\{-\left(\frac{1}{\tau_0} + k_q[Q]\right)t\right\}$$

$$= I_0 \exp\left\{-\left(\frac{1}{\tau_0} + k_q[Q]\right)t\right\} \quad \text{(equation 9)}$$

The fluorescence decay is thus a single exponential whose time constant is:

$$\tau = \frac{1}{\frac{1}{\tau_0} + k_q[Q]} = \frac{\tau_0}{1 + k_q\tau_0[Q]} \qquad \text{(equation 10)}$$

The Stern-Volmer relation in lifetime is then defined to express the luminescence lifetime without and with quencher ratio in function of the concentration of the quencher:

$$\frac{\tau_0}{\tau} = 1 + k_q\tau_0[Q] \qquad \text{(equation 11)}$$

The Stern-Volmer model enables to characterize the dynamics of the quenching by luminescence stationary measurements. Indeed, the ratio of luminescence quantum yields with and without quencher (Φ and Φ_0) provides the Stern-Volmer relation in intensity:

$$\frac{\Phi_0}{\Phi} = \frac{I_0}{I} = \frac{\tau_0}{\tau} = 1 + k_q\tau_0[Q] = 1 + K_{SV}[Q] \qquad \text{(equation 12)}$$

where I, τ, I_0 and τ_0 are respectively the luminescence intensity and lifetime with and without quencher. $K_{SV} = k_q\tau_0$ is the Stern-Volmer constant. Usually, the ratio I_0/I is plotted against the quencher concentration (Stern–Volmer plot). If the variation is found to be linear, the slope gives the Stern–Volmer constant (Figure 1.5). Then, k_q can be easily calculated if the excited-state lifetime in the absence of quencher is known.

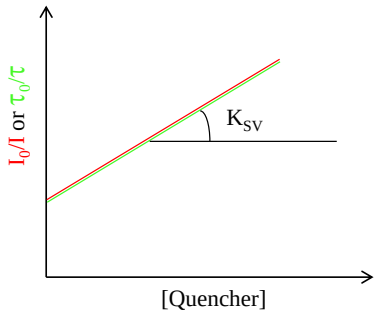

Figure 1.5 – Stern-Volmer plot obtained for a pure dynamic quenching.

Basically, two distinct dynamic quenching processes should be considered because the quenching rate constant k_q includes two processes (Figure 1.6): (i) the equilibrium formation of the association complex between the excited luminescent molecule and the quencher $(M\cdots Q)^*$ (characterized by k_d and k_{-d} rate constants) (ii) as well as the rate of the reaction (k_R) between these two species in the association complex. In a dynamic quenching, two cases may be identified:

- the bimolecular dynamic quenching process is diffusion-limited ($k_R >> k_d$) so that the constant quenching k_q equals to k_d.
- the bimolecular process is not diffusion-limited ($k_R \approx k_d$) and the quenching constant equals to $k_q = pk_d$ where p is the efficiency of the " reaction ".

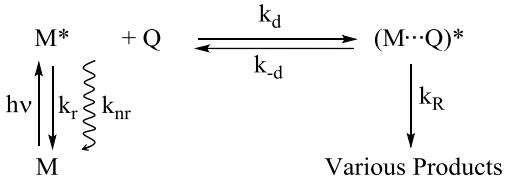

Figure 1.6 – Representation of dynamic quenching and associated rate constants: k_r and k_{nr} are respectively the radiative and non-radiative rate constants of the luminescent molecule M*, k_d is the diffusion rate constant for the approach between M and Q, k_R is the reaction rate constant for various reactions.

In non-viscous solvent, a rate constant (k_q value) close to 10^9-10^{10} M^{-1} s^{-1} indicates that an efficient process limited by diffusion of investigated species occurs.

Static quenching

The luminescence quenching may be not diffusion dependent (first case of the phenomenological approach). This static quenching involves either the

formation of a non-luminescent complex in the ground state or occurs when the quencher and the luminescent species cannot change their position in space during the excited state lifetime of M*. These cases may be observed in viscous media or in rigid matrices. Two models can be considered to describe the static quenching (Figure 1.7).

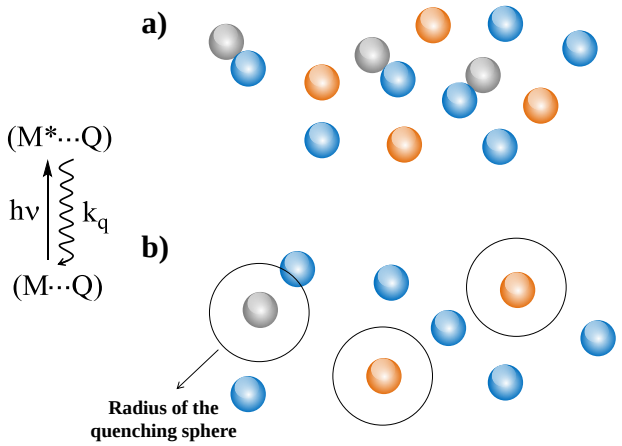

Figure 1.7 – Illustration of the static quenching either (a) upon the formation of a non-luminescent complex in the ground state or (b) by the sphere of effective quenching model (Perrin's model) (the orange spheres correspond to luminescent excited states; the grey ones, the non-luminescent quenched excited states; the blue ones, the quenchers.

✓ **Formation of a non-luminescent ground state complex**

Let us consider the formation of a non-luminescent complex (M···Q) with a 1:1 stoechiometry according to the equilibrium:

$$M + Q \rightleftharpoons (M\cdots Q)$$

The observed luminescence will be due to luminescent molecules which are not associated to a quencher in the ground state. As a result, the excited state lifetime of uncomplexed luminescent molecules M* are not affected in contrast to dynamic quenching. However, the overall emission will decrease

because the part of luminescent molecules linked to quencher does not contribute to luminescence anymore. The emission intensity decrease against the quencher concentration can be obtained using the complex equilibrium constant:

$$K_S = \frac{[(M\cdots Q)]}{[M][Q]} \quad \text{or} \quad [M]_0 = [M] + [(M\cdots Q)] \qquad \text{(equation 13)}$$

where $[M]_0$ is the total concentration of M and K_S is the static quenching constant. Therefore,

$$\frac{[M]}{[M]_0} = \frac{1}{1 + Ks[Q]} \qquad \text{(equation 14)}$$

Considering that the luminescence intensities are proportional to the concentrations (which is valid in dilute solutions), the equation 14 can be rewritten under a Stern-Volmer like form:

$$\frac{I_0}{I} = 1 + K_S[Q] \qquad \text{(equation 15)}$$

Once again, the static quenching constant (Ks) value can be obtained by plotting the ratio I_0/I as a function of the quencher concentration (Figure 1.8 a).

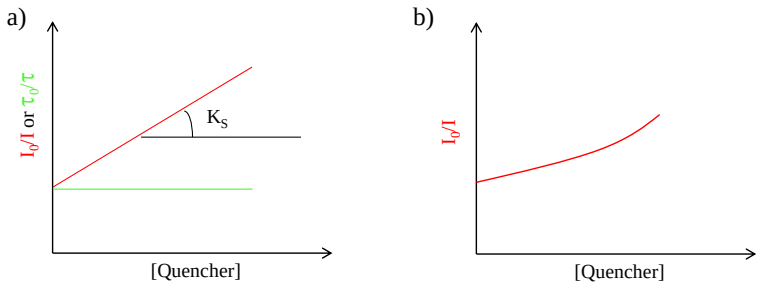

Figure 1.8 – Stern-Volmer like plot obtained for (a) a pure static quenching or (b) with linearity loss at high quencher concentration in the Perrin's model.

✓ **Sphere of effective quenching (Perrin model)**

The model described above assumes the formation of "complexes" between the luminophore M and the quencher in the ground state. If so, this association usually involves a modification of the absorption spectra of the luminophore. However, for less specific or weaker interactions, or having a different stoichiometry ratio than 1:1, the Perrin model provides a better description of the reality.

According to Perrin, the quenching of the luminophore is supposed to be complete if a quencher molecule Q is located inside a *quenching sphere* of volume V_q surrounding the luminophore M (Figure 1.7b). If a quencher is outside to the quenching sphere, it does not affect the luminescence of M at all. As a result, the emission intensity decreases upon addition of quencher whereas the lifetime of the excited state of M is unaltered.

The probability that *n* quenchers reside within the volume V_q is expected to obey a Poisson distribution:

$$P_n = \frac{\langle n \rangle^n}{n!} \exp(-\langle n \rangle) \qquad \text{(equation 16)}$$

$$\text{with } \langle n \rangle = V_q N_a [Q] \qquad \text{(equation 17)}$$

where $\langle n \rangle$ is the mean number of quenchers Q in the volume V_q (expressed in L), N_a is the Avogadro's number and [Q] is the concentration in quencher ($mol.L^{-1}$). The probability that there is no quencher in this volume is:

$$P_0 = \exp(-\langle n \rangle) = \exp(-V_q N_a [Q]) \qquad \text{(equation 18)}$$

Therefore, because of the luminescence intensity is proportional to P_0, Perrin's model gives:

$$\frac{I_0}{I} = \exp(-V_q N_a [Q]) \qquad \text{(equation 19)}$$

At low concentration of quencher, the exponential dependence can be restricted to the two first terms of the Taylor-MacLaurin series:

$$\frac{I_0}{I} = 1 + V_q N_a [Q] \qquad \text{(equation 20)}$$

so that the concentration dependence is almost linear as in the case of the Stern-Volmer plot. At higher concentration, the I_0/I ratio is not linear anymore and shows an upward curvature (Figure 1.8b).

1.2.8. Photo-induced electron transfer

It is important to mention that Stern-Volmer equation is not specific to a defined phenomenon. In other words, luminescence quenching could be caused by processes such as energy transfer, proton transfer, electron transfer or excimer formation. In this work, we will focus on photo-induced electron transfer. Therefore, few words about this process are required. Photo-induced electron transfer is often responsible for luminescence quenching. In addition, photo-induced charge transfer is crucial in a wide range of applications, especially for the conversion of light in chemical energy (*e.g.* natural and artificial photosynthesis). This process involves an electron transfer from a molecule to another taking place solely upon irradiation. Moreover, oxidation and reduction properties of a luminescent molecule are enhanced upon irradiation (Figure 1.9). Oxidation (E_{ox}*) and reduction (E_{red}*) potentials in the excited state can be estimated from oxidation/reduction potentials in the ground state (E_{ox}/E_{red}) and the energy of transition E_{00} as depicted in equations 21 and 22. The E_{00} energy transition may be assimilated to the energy associated to emission wavelength maximum of the luminescent compound ($\lambda_{max\ em}$).

$$E_{ox}^* = E_{ox} - \Delta E_{00} \approx E_{ox} - E_{\lambda max\ em} \qquad \text{(equation 21)}$$

$$E_{red}^* = E_{red} + \Delta E_{00} \approx E_{red} + E_{\lambda max\ em} \qquad \text{(equation 22)}$$

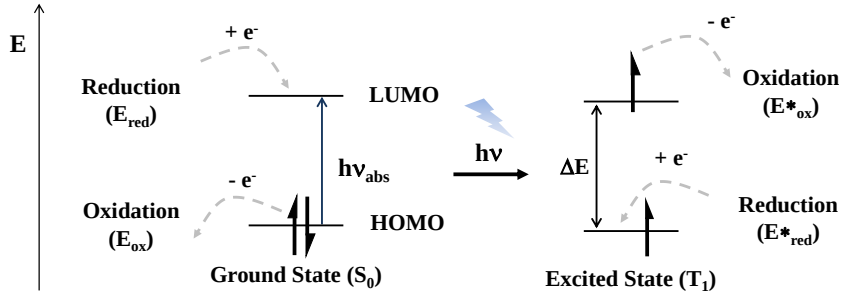

Figure 1.9 – Schematic representation of oxidizing and reducing power enhancement upon irradiation for a given molecule.

A photo-induced electron transfer may be reductive or oxidative depending on species involved as depicted in the Figure 1.10. Briefly, the electron transfer occurs either from donor (D*) in its excited state to acceptor (A) (oxidative) or from donor (D) to acceptor in its excited state (A*) (reductive). Interestingly, the driving force (ΔG_{ET}) for the electron transfer can be estimated by the Rehm-Weller[50] equation (equation 23) according to electrochemical and spectroscopic parameters of studied species in a given solvent:

$$\Delta G_{ET} = (E_D{}^{\bullet+}{}_{/D} - E_{A/A}{}^{\bullet-}) - \Delta E_{00} - e^2/\varepsilon d \quad \text{(equation 23)}$$

where $E_D{}^{\bullet+}{}_{/D}$ and $E_{A/A}{}^{\bullet-}$ are the reduction potentials, ΔE_{00} is the energy transition depicted in equations 21-22 and $e^2/\varepsilon d$ term corresponds to coulombic correction due to attraction between radical species obtained upon electron transfer. This last term is negligible for polar solvent due to high dielectric constant ε values.

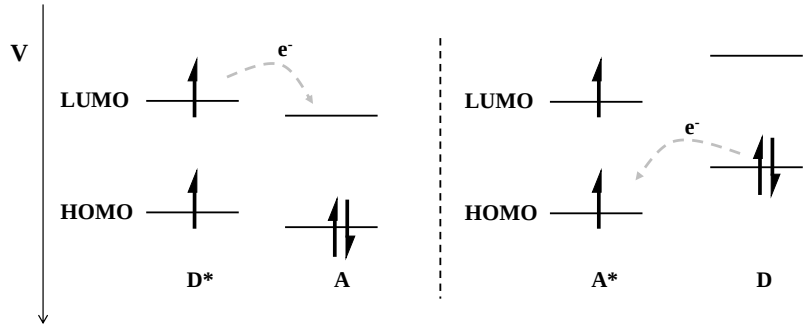

Figure 1.10 – Schematic oxidative (left) and reductive (right) photo-induced electron transfer.

Some transition metal complexes are particularly interesting to trigger such photo-induced electron transfer due to their photo-stability, relatively long lifetime of the excited state and redox tunability. This is the reason why they are involved in lots of supramolecular systems.

1.3. Iridium (III) complexes: photophysics, photochemistry and applications

Among all transition metal complexes, iridium based systems have become more and more popular over the past decade as highlighted on Figure 1.11.[51] This emerging interest in developing Ir(III) complexes is due to their useful optoelectronic properties which have been exploited in diverse applications from emitting materials[52-54] to biological probes.[55-57] The increasing interest for such complexes deeply originates from their inherent properties in terms of structure and underpinning spectro-electrochemical behaviour. We will discuss below the main features of Ir(III) complexes and why they differ from other transition metals.

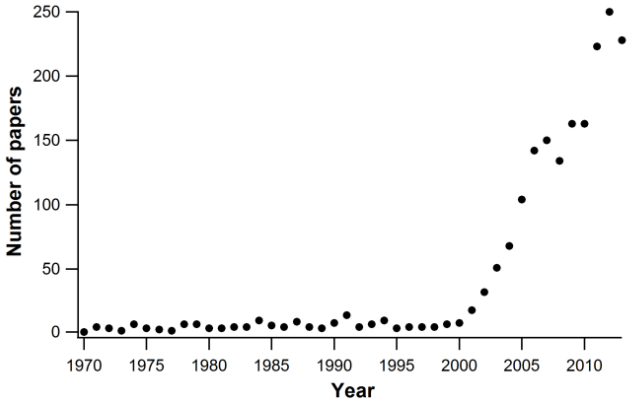

Figure 1.11 – Scifinder search (September 4, 2015) for the number of papers (2071) published with keywords "luminescence" and "iridium".

1.3.1. Complexes geometry

Ir(III) is a $5d^6$ metal center and the electronic properties of its octahedral complexes share several features with those of other well-known complexes of Fe(II), Ru(II) and Os(II) whose metal centers are respectively $3d^6$, $4d^6$ and $5d^6$. The metal center is surrounded by several ligands mono or poly-dentates. In this Ph.D. thesis, we focus on formally neutral N-coordinating (polypyridyl) and negatively charged C-coordinating (cyclometalated) ligands. Remarkably, Ir(III) allows to chelate up to 3 negative carbons. To the best of our knowledge, this is the only transition metal enabling tris-cyclometalated coordination. This structural property of Ir(III) complexes makes them highly interesting as we will discussed subsequently. Depending on ligand charge, the resulting assembly could be neutral, mono or poly-charged. For charged complexes, the counter-ions play an essential role in terms of solubility. Usually, chloride or nitrate anions allows to solubilize Ir(III) complexes in water while hexafluorophosphate is preferably used for organic solvent. Up to now, numerous research groups have synthesized Ir(III) tris-bidentate complexes (Figure 1.12).[58-61]

Although they own some advantageous properties in some applications such as OLED's[62] or oxygen sensors[63,64] due to their high luminescence quantum yield,[65] bidentate ligand arrangement does not provide a convenient environment for the construction of linear supramolecular assembly due to optical (Δ and Λ) and geometrical (*fac* and *mer*) isomers upon ligand substitution.

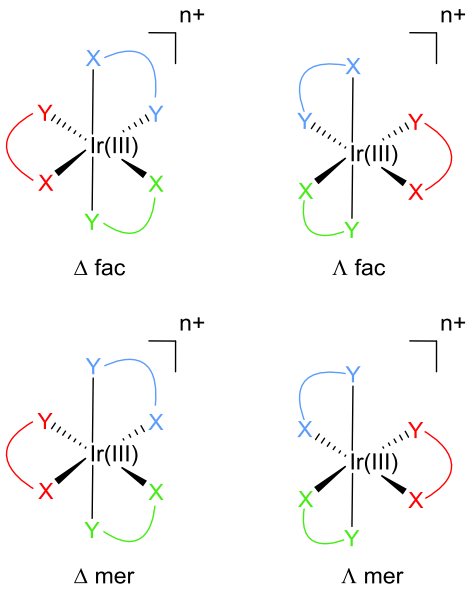

Figure 1.12 – Four possible optical and geometrical isomers for tris-bidentate Ir(III) complexes with unsymmetrical chelate ligands.

In contrast, the geometry of tridentate ligands such as 2,2′:6′,2″-terpyridine (tpy) is ideal for the design of rigid arrays with unambiguously determined structure presenting no geometrical and optical isomers.[66] Other tridentate ligands bearing cyclometalating carbon(s) instead of nitrogen able to coordinate Ir(III) also deserve a particular attention. This is why we focus on bis-terdentate Ir(III) complexes with general structure such as represented in Figure 1.13. For sake of clarity, Ir(III) complexes are gathered on the basis of their Carbon/Nitrogen ratio (C/N) ranging from C/N = 0/6 to C/N =

3/3. Moreover, left and right ligands are respectively termed l (red) and l' (blue).

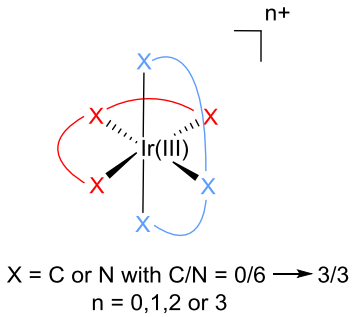

Figure 1.13 – Structure of Ir(III) bis-terdentate complexes.

1.3.2. Photophysical properties of Ir(III) complexes

With respect to the molecular orbital theory (*vide infra*), the MO's of Ir(III) bis-terdentate complexes can be conveniently described according to their predominant atomic (or molecular) orbital contribution as followed (Figure 1.14):

(1) predominantly ligand centered σ_l and σ_l' orbitals (strongly bonding)

(2) predominantly ligand centered π_l and π_l' orbitals (bonding)

(3) metal centered $d\pi_{Ir}$ orbitals (essentially non-bonding)

(4) predominantly ligand centered π^*_l and π^*_l' orbitals (anti-bonding)

(5) predominantly metal centered $d\sigma^*_{Ir}$ orbitals (strongly anti-bonding).

In the ground electronic configuration of an octahedral Ir(III) complex, orbitals of types (1), (2) and (3) are completely filled.

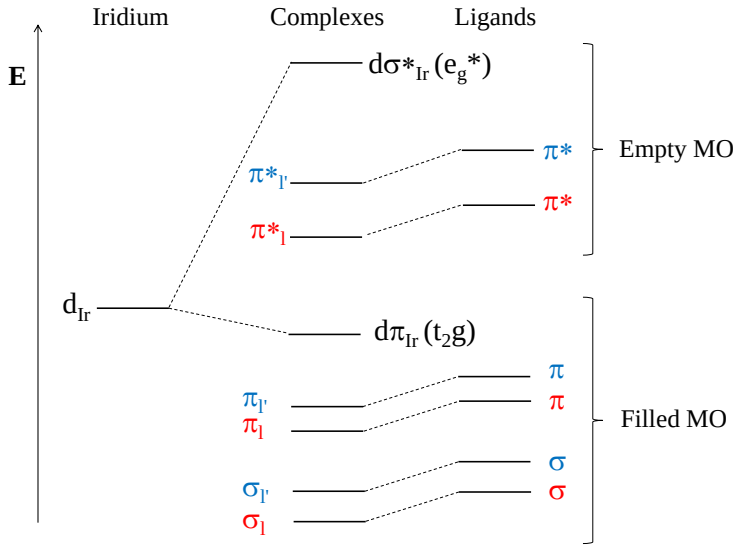

Figure 1.14 – Simplified diagram of molecular orbital energy levels for an octahedral Ir(III) complex.

Based on molecular orbitals, several electronic transitions upon absorption of a photon could theoretically be observed (Figure 1.15):

- Metal Centered transitions (MC)

These electronic transitions occur between $d\pi_{Ir}$ and $d\sigma^*_{Ir}$ metal centered orbitals. For Ir(III) complexes, these transitions are usually very high in energy and therefore not accessible in the UV-vis spectral range. This large energy gap results from the high oxidation state of iridium (Ir(III)), the large size of its 5d orbitals, and the high ligand-field splitting energy (LFSE) due to cyclometalated C-Ir bond(s).

- Ligand Centered transitions (LC)

These electronic transitions happen from a bonding π_l to an anti-bonding π^*_l orbitals, both ligand centered. The energy for these transitions is in the UV

part of the spectral range. Their molar extinction coefficients are usually high (close to 10^5 M^{-1} cm^{-1}).

- Metal-to-Ligand Charge Transfer (MLCT)

The MLCT transitions correspond to a one electron transition from the metal centered $d\pi_{Ir}$ orbital to an anti-bonding ligand centered π^*_l molecular orbital. These HOMO-LUMO transitions could be seen as an intramolecular oxydo-reduction process (equation 24). Therefore, MLCT transitions involve a strong molecular polarity shift at the excited state.

$$[Ir(III)(l)_2]^{n+} + h\nu \rightarrow [Ir(IV)(l)(l^{\bullet -})]^{n+} * \text{ (equation 24)}$$

These transitions are usually observed in the visible spectral part and their molar extinction coefficients are about 10^4 M^{-1} cm^{-1}.

- Ligand-to-Ligand Charge transfer (LLCT)

For this kind of electronic transitions, one electron goes from a bonding π_l ligand centered orbital to an anti-bonding $\pi^*_{l'}$ orbital of another ligand l'. Similarly to MLCT, LLCT transitions lead to a dipole in the excited state (equation 25).

$$[Ir(III)(l)_2]^{n+} + h\nu \rightarrow [Ir(III)(l^{\bullet +})(l^{\bullet -})]^{n+} * \text{ (equation 25)}$$

LLCT transitions are also observed in the visible spectral part and their molar extinction coefficients are about 10^4 M^{-1} cm^{-1}.

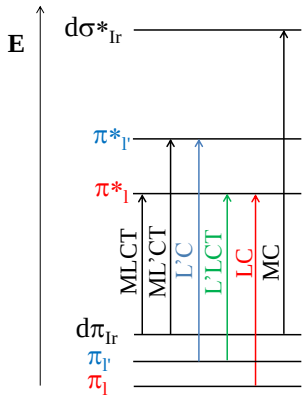

Figure 1.15 – Main electronic transitions for Ir(III) complexes.

Unlike widely studied polyazaaromatic Ru(II) complexes where the nature of the electronic transition is often unambiguously identified[67,68], a mixture of LC/MLCT/LLCT transitions is usually found for Ir(III) complexes.[69] Moreover, depending on the ligands nature, the resulting complex can display different spectroscopic features. As a result, the whole visible range can be covered by selecting suitable bidentate ligands around the Ir(III) core.[65] This easy color tunability of Ir(III) complexes differentiates them from other organometallic compounds. Therefore, a single photophysical model cannot be drawn in this case.

1.3.3. Oxidation and reduction properties

The reduction of polypyridyl and cyclometalated Ir(III) complexes corresponds to the addition of one electron on ligand centered π^*_l molecular orbital following the equation:

$$[Ir(III)(l)_2]^{n+} + 1\ e^- \rightarrow [Ir(III)(l^{\bullet -})(l)]^{(n-1)+} * \quad \text{(equation 26)}$$

Therefore, reduction process never induces the formation of an “Ir(II)” metal center although the global charge is n-1.

The oxidation of polypyridyl Ir(III) complexes involves the removal of one electron of metal centered $d\pi_{Ir}$ molecular orbital.[34] Nevertheless, when cyclometalated ligands coordinate the Ir(III) metal center, the strong covalency of Ir-C bonds makes this simple assignment unsatisfactory. In this case, the highest occupied molecular orbital (HOMO) should preferably be delocalized over the Ir-ligand fragment.[70]

A key point is that number of cyclometalated carbons around Ir(III) center greatly influences the reduction and oxidation potentials and the nature of the orbitals involved in the oxidation processes. For instance, cyclometalated complexes in which there is only one coordinating carbon have a very high oxidation potential (typically > 2V/SCE)[70] and is Metal-Centered whereas those with three cyclometalated carbons have an oxidation potential close to 0.7 V/SCE[71]. Electrochemical properties of Ir(III) complexes are dramatically enhanced in their excited states similarly to other transition metals such as Ru(II). Indeed, Ir(III) complexes are better oxidant and reductant upon light absorption. As discussed before, despite their interesting properties, Ir(III) bis-terdentate complexes have not sufficiently been exploited yet to benefit from this reduction and oxidation properties enhancement.

1.4. Bis-Terdentate Ir(III) complexes : selected examples

Photo-induced electron transfer processes rely on a deep understanding of spectro-electrochemical properties for considered compounds. Since this work essentially deals with photo-induced electron transfer between Ir(III) bis-terdentate complexes and other partners, their main properties should preferably be highlighted. Accordingly, the synthesis, electrochemical and spectroscopic properties of Ir(III) bis-terdentate complexes are successively addressed. Each complex group (from C/N = 0/6 to C/N = 3/3) is discussed separately due to their important properties

heterogeneity. Selected applications arising from Ir(III) bis-terpyridine complexes are described. A rational photophysical scheme summarizing spectroscopic and reduction/oxidation properties closes these introductory notes.

1.4.1. Ir(III) bis-terpyridine complexes and applications (C/N = 0/6)

1.4.1.1. Synthesis, electrochemical and spectroscopic properties

Luminescent $[Ir(tpy)_2]^{3+}$ complex was reported for the first time in 1990.[72] However, the synthesis and purification turned out to be tremendously difficult leading to relative lack of interest for such compounds during several years. Almost ten years later, some milder conditions were developed by Lucia Flamigni *et al.*[73]. The reaction was carried out in two steps following the Scheme 1.3. In the first step, $[Ir(tpy)Cl_3]$ was obtained as an intermediate upon heating $IrCl_3.3H_2O$ and tpy at 160 °C in ethylene glycol for 15 minutes. Subsequently, reaction with a second tpy ligand in almost same conditions afforded $[Ir(tpy)_2]^{3+}$ as a yellow solid. Despite development of "milder" conditions, the synthesis always requires high temperature to overcome the great inertness of the d_6 Ir(III) metallic center.

Electrochemical studies reveal two "one-electron" reduction waves respectively at -0.77 and -0.93 V *vs.* SCE[73] ascribed to ligands reduction. These values are analogous to those obtained for $[Ir(bpy)_3]^{3+}$.[74] No oxidation wave of Ir(III) into Ir(IV) is observed in the explored potential range.

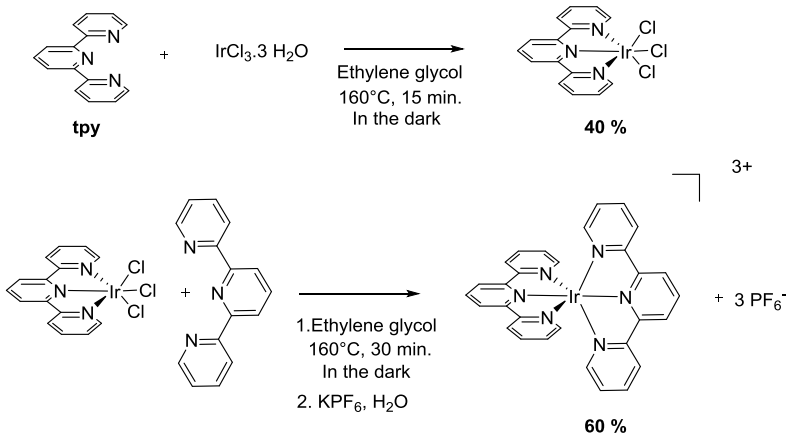

Scheme 1.3 – Synthetic scheme of $[Ir(tpy)_2]^{3+}$.

The absorption and emission spectra are displayed in Figure 1.16. Well-resolved absorption profile with extinction coefficient order of 10^4-10^5 M^{-1} cm^{-1} suggests a predominantly LC (Ligand Centered) $\pi_l \rightarrow \pi^*_l$ transition. This attribution is confirmed by narrow and well-resolved emission profile typically observed for such transitions. Quantum yield is low ($\Phi \approx 0.025$) whereas lifetime of the excited state is relatively long (τ = 1.0 µs under air).[73]

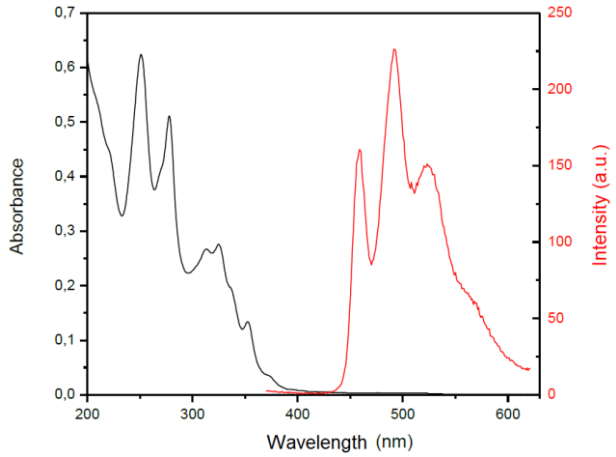

Figure 1.16 – Absorption (left) and emission (right) spectra of $[Ir(tpy)_2]^{3+}$ (2.10^{-5} M) in CH_3CN at room temperature under air.[75]

Substitution of tpy-based ligand is straightforwardly achieved leading to a wide variety of derivatives.[76,77] The resulting Ir(III) complexes spectroscopic properties are substantially altered upon these modifications. For instance, along the two complexes depicted in Figure 1.17, the emission wavelength is shifted to lower energy (λ_{max} = 458 and 506 nm respectively for $[Ir(tpy)_2]^{3+}$ and $[Ir(ttpy]_2]^{3+}$ where ttpy = 4′-(4-Tolyl)-2:2′,6′:2′′-terpyridine) as a result of a larger ligand size.

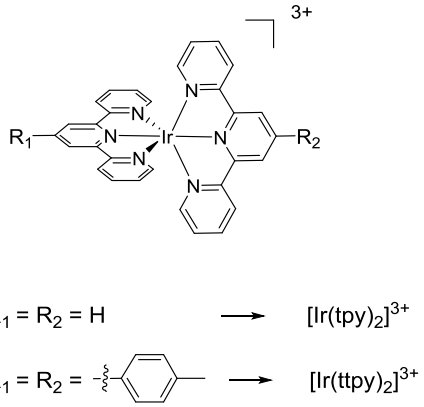

Figure 1.17 – Structure of Ir(III) bis-terpyridine derivatives $[Ir(tpy)_2]^{3+}$ and $[Ir(ttpy]_2]^{3+}$.

Notably, the emission shifts from a predominant ^{3}LC character for $[Ir(tpy)_2]^{3+}$ to a mixed ^{3}LC/^{3}MLCT for $[Ir(ttpy]_2]^{3+}$. These changes in nature of the emission are highlighted by usual features (Figure 1.18):

- Emission profile: ^{3}MLCT emission usually yields broad emission band while ^{3}LC luminescence leads to narrower and well-resolved bands.
- Hypsochromic shift of the λ_{max} as well as appearance of vibrational bands from room temperature to 77 K (rigid matrix).
- Radiative rate constant (k_r value) is higher (~ 10^5 s^{-1}) for ^{3}MLCT than for ^{3}LC cases.

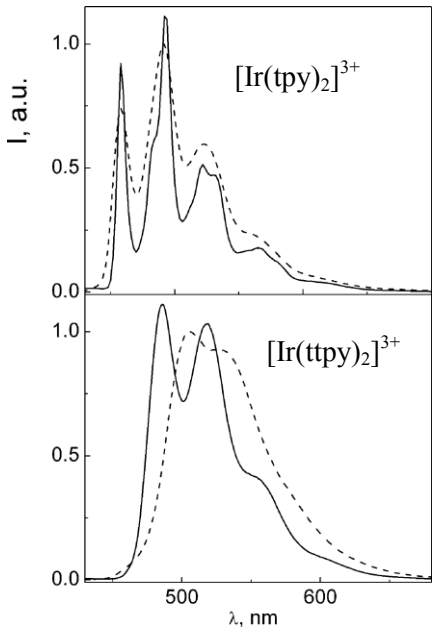

Figure 1.18 – Luminescence profiles at room temperature (dashed line) and at 77 K (full line) for a ^{3}LC emitter, $[Ir(tpy)_2]^{3+}$ (upper panel), and a mixed ^{3}LC/^{3}MLCT emitter, $[Ir(ttpy)_2]^{3+}$ (bottom panel).[69]

1.4.1.2. Applications of Ir(III) bis-terpyridine complexes

The properties of Ir(III) bis-terpyridine complexes described above enable chemists to design novel systems. Besides, we introduce some selected examples based on their:

- Chemical inertess for supramocular assemblies

- Photo-redox behaviour (for photo-induced electron transfer)

✓ **Supramolecular assemblies**

Due to their high chemical stability and multi-charged structures, Ir(III) bis-terpyridine complexes have recently gained interest as key components for the development of supramolecular interactions.

Firstly, the building of linear chain structures using a back to back twin bowl tris(spiroborate) cyclophane as host and $[Ir(tpy)_2]^{3+}$ as guest was achieved. Tris(spiroborate) cyclophanes were readily prepared from equimolar amounts of 2,2′,3,3′-tetrahydroxy-1,1′-binaphthyls and boric acid at 150°C in DMF according to Wuest's procedure (Scheme 1.4).[78] The spiroborate linkage was chosen for the spontaneous cyclophane formation, because its accessibility and unique thermodynamic behaviour allowed to obtain highly symmetric cyclic structures from simple bis(dihydroxyarene) unit in a self-organization manner.[79-81]

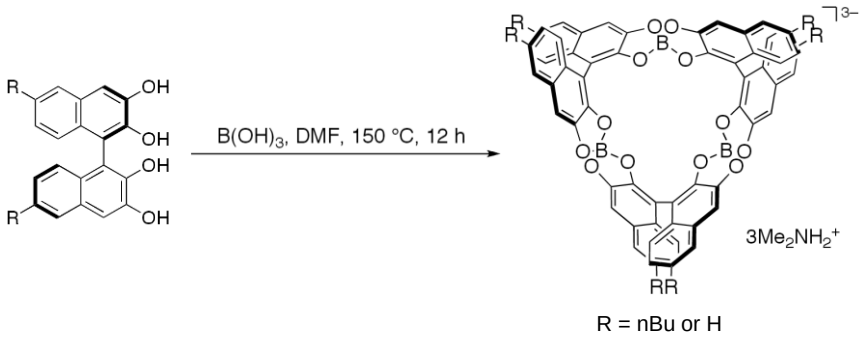

Scheme 1.4 – Preparation of the tris(spiroborate) cyclophanes.

The molecular recognition behaviour of the negatively charged (three times) cyclophanes for $[Ir(tpy)_2]^{3+}$ is induced by π- and electrostatic interactions at both side of a symmetry plane (Scheme 1.4). The molecular coupling behaviour mimicks vertebrate spine making possible to glue various cationic guest molecules to each other via dual-host guest interactions (Figure 1.19).[82]

Temperature-responsive gelation behaviour was obtained in this supramolecular chain system (Figure 1.20). The heating of an equimolar cyclophane (10 mM) and $[Ir(tpy)_2]^{3+}$ (10 mM) solution in HMPA above the lower critical solution temperature (LCST, *i.e.* critical temperature below

which the components of a mixture are miscible for all composition)[83] quickly leads to a phase transition from solution to organogel. After cooling at room temperature, the gel reverted to the solution phase within 15 minutes. Interestingly, this process is fully reversible and LCST was estimated to be 78.5 °C at this concentration.

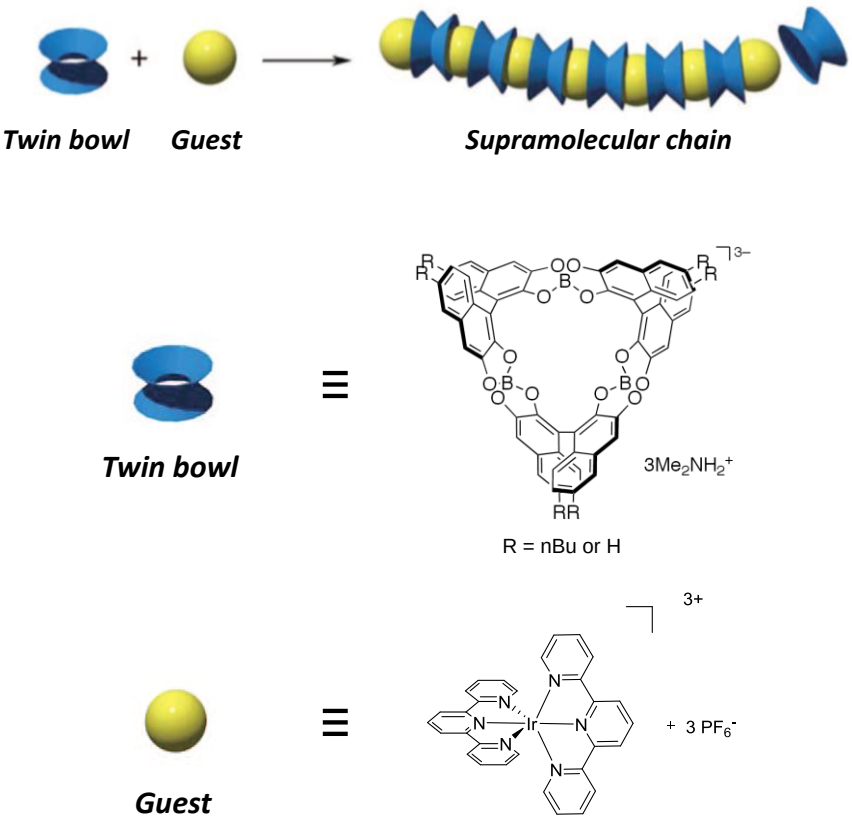

Figure 1.19 – Schematic representation of the formation of supramolecular chain structure by iterative clathration of twin-bowl-shaped cyclophane (host) with $[Ir(tpy)_2]^{3+}$ (guest) (adapted from [82]).

The linear structure was confirmed by ^1H NMR and X-ray crystallographic analysis (Figure 1.21).

This example highlights the ability of $[Ir(tpy)_2]^{3+}$ to properly behave and resist in supramolecular assembly.

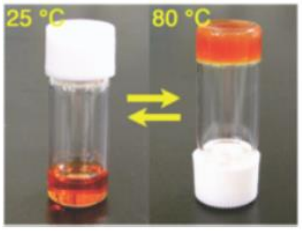

Figure 1.20 – Temperature-responsive gel appeared from a solution of cyclophane (10 mM) and $[Ir(tpy)_2](3PF_6)$ (10 mM) in HMPA. Before (left) and after (right) heated to 80 °C. (adapted from[82]).

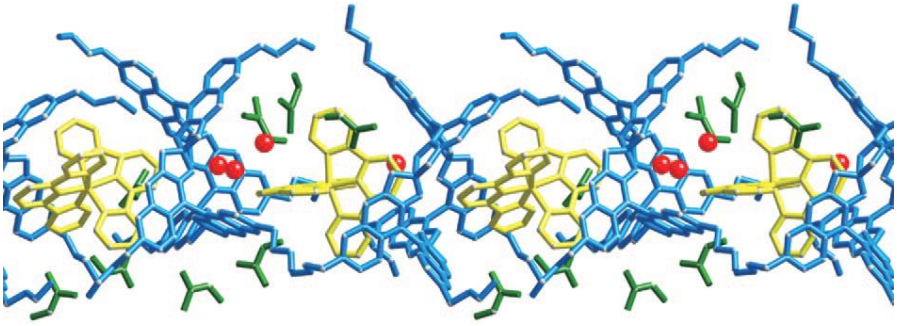

Figure 1.21 – Crystal structure of tris(spiroborane) cyclophane (blue), $[Ir(tpy)_2]^{3+}$ (yellow), water (red), and DMF (green). Hydrogen atoms are omitted for clarity (adapted from[82]).

Secondly, supramolecular interactions between both cationic Ir(III) and Fe(II) bis-terpyridine complexes and cucurbituril were evidenced.[84] Cucurbiturils are made of glycoluril monomers linked by methylene bridges (Scheme 1.5). Cucurbiturils are synthesized from urea and dialdehyde to give intermediate glycoluril. Subsequently, this intermediate is condensed with formaldehyde to give the targeted cucurbituril which is commonly written as cucurbit[n]uril, where n is the number of glycoluril units.

Common abbreviation for such structure is CB[n]. Three decades ago, it was evidenced that CB[6] formed some tight complexes with amphiphilic guests.[85] The complex formation was attributed to beneficial interactions between (i) the carbonyl moieties of CB[6] and the positive charges of the guest (ii) the hydrophobic cavity of the macrocycle and the hydrophobic subunits of the guest. Although this assessment remains valid, it seems that more subtle interactions based on both enthalpic and entropic considerations participate to the recognition process.[86-89]

In this example, the supramolecular interactions between $[Ir(ttpy)_2]^{3+}$ (Figure 1.17) and CB[7] were studied. ^{1}H NMR analysis revealed that the tolyl moiety was encapsulated inside the cucurbituril and the saturation was reached upon addition of two equivalents of CB[7].

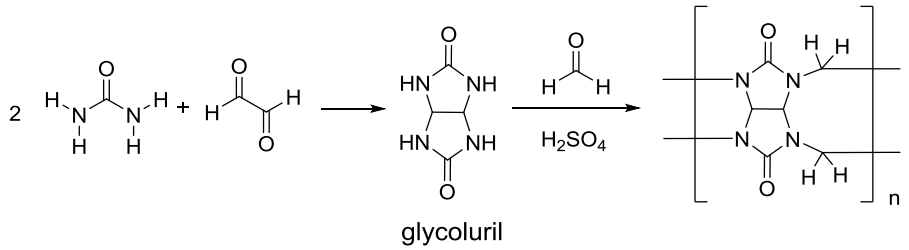

Scheme 1.5 – General procedure for the synthesis of cucurbiturils.

According to these ^{1}H NMR analyses, in addition to classical recognition processes (*vide infra*), CH···O hydrogen bonds between some hydrogen atoms of tolyl and the oxygens of the carbonylated function of CB[7] would also be responsible for the interactions. However, the use of the neutral $[(ttpy)IrCl_3]$ complex instead of $[Ir(ttpy)_2]^{3+}$ led to a complete loss of affinity toward CB[7]. These results suggest that CH···O hydrogen bonding between the metal-ligand complex and the carbonylated rims of CB[7] is solely allowed in the presence of a neighboring positive charge.

Although no assembly afforded crystals suitable for quality X-Ray diffraction, NOESY (Nuclear Overhauser Effect SpectroscopY) experiments as well as some theoretical considerations lead to convenient model to explain the supramolecular structure (Figure 1.22).

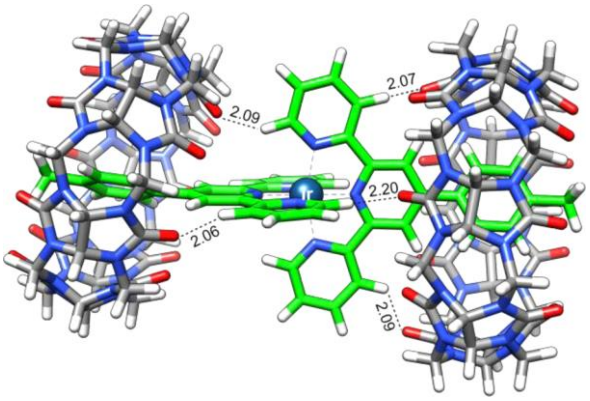

Figure 1.22 – Optimized structure of complex $[Ir(ttpy)_2]^{3+}.(CB[7])_2$ obtained by theoretical calculations. Distances between host and guest atoms are given in Angstroms (Å).[84]

The recognition properties of the metal−ligand complexes were subsequently applied to build supramolecular oligomers. The larger CB[8] acted as a non-covalent linker between metal/terpyridine complexes and interconnected two 4′-substituents inside its cavity. Self-sorting between CB[8] and metal/terpyridine complexes bearing 4′-(2-naphthyl) and 4′-(2,3,5,6-tetrafluorophenyl) substituents was observed and may afford well-organized oligomers with alternating Fe(II) and Ir(III) cations (Figure 1.23).

In this work, the authors showed that Ir(III) bis-terpyridine complexes were excellent candidates to build supramolecular systems thanks to their ionic forms, the easy derivatization of the chelating terpyridines and their non-labile behaviour. This high stability is also checked under irradiation as illustrated by the more “biological” following example.

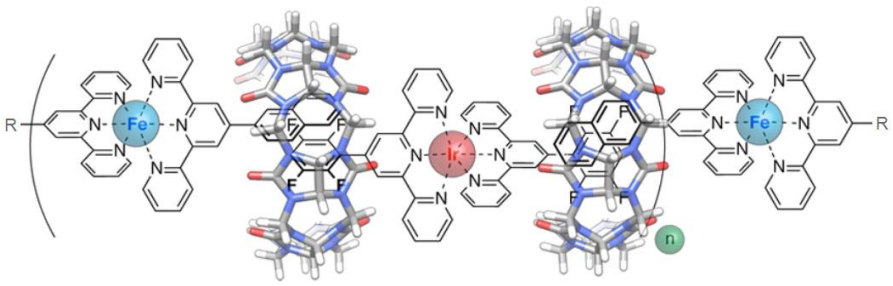

Figure 1.23 – Structure of alternating Fe(II)-Ir(III) oligomers (R = 2-Naphtyl).[84]

✓ **Biological application**

The bioconjugate chemistry is defined as the chemical modification or conjugation of biomolecules.[90] This research area makes possible the synthesis of biologically active complexes with unique properties.[91] The activation of such systems can be triggered by the use of light energy to drive biological processes with potential applications as bio-solar cells.[92] As mentioned before, one of the major advantages of some transition metal complexes arises from the possibility to transfer electrons to a partner upon irradiation.

As a result, light responsive bioconjugates based on a redox enzyme (iso-1 cytochrome c) and Ru(II) complexes were developed to convert light energy to biologically relevant processes under normal physiological conditions.[92] Few years later, the photo-reduction of an Ir(III) bis-terpyridine cytochrome c bioconjugate was also investigated (Figure 1.24).[93] During the synthesis, the maleimide function of Ir(III) complex reacts with the single available cysteine residue of CYS102 which generates the desired Ir(III)-cyt c bioconjugate. In these experiments, EDTA was used as a sacrificial electron donor in order to reduce the photo-excited Ir(III) complex. Subsequently, a photo-induced electron transfer between the mono-reduced iridium chromophore donor and the cyt c acceptor takes place.

The photo-reduction of cytochrome c was monitored by UV absorbance at 550 nm. After light irradiation, a band characteristic of the reduced cyt c moiety appears at this wavelength indicating that the reduction properly occurred.[94] The bioconjugate allows photo-switchability between on/off states controlling the reduction of cyt c. Compared to the equivalent Ru(II)-cyt c bioconjugate, the Ir(III) one showed a ~640-fold increase in quantum efficiency. The significant improvement can be due to the longer luminescence lifetime of Ir(III) bis-terpyridine complexes at room temperature.[95] This result highlights the superiority of Ir(III) complexes over Ru(II) ones for similar assemblies in terms of photo-induced electron transfer performance.

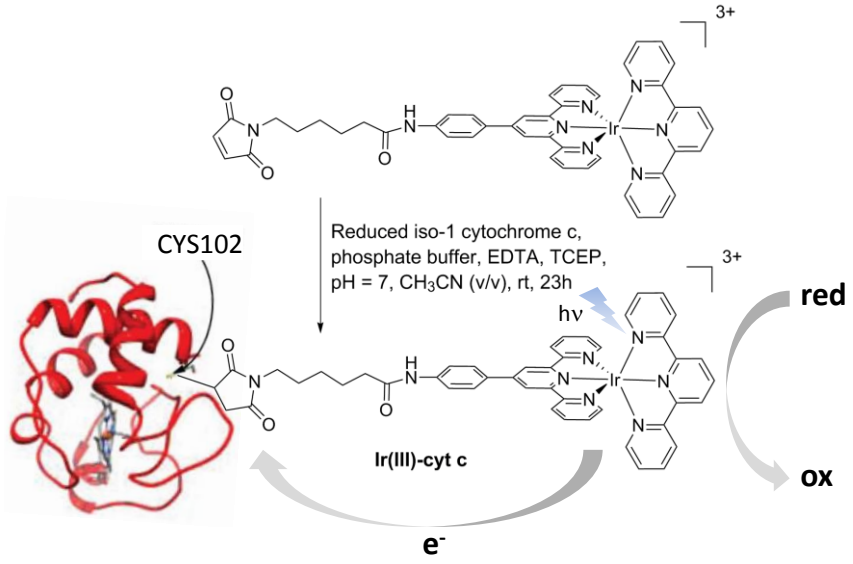

Figure 1.24 – Structure of the bioconjugate Ir(III)-cyt c.[93]

- ✓ **Ir(III) bis-tpy complexes in multicomponent arrays for long-lived charge separation**

Intramolecular photo-induced charge transfers are responsible for charge separated states required for artificial photosynthesis. Systems with long-lived charge separated states are subject to ongoing researches since

they might lead to controlled photo-chemical reactions. Therefore, luminescence sensitivity of Ir(III) bis-terpyridine complexes enables to easily probe photo-induced electron or hole transfer. Remarkable Ir(III) bis-terpyridine-based systems able to reach such states have been reported.[96,97] The most efficient charge separated state is provided by a triad termed DAPA-Ir-NDI (where DAPA is an aromatic amine and NDI is a naphthalene diimide) (Figure 1.25). The excitation of both Ir and DAPA units in the triad leads to the charge separated state $DAPA^{+}$-Ir^{-}-NDI which quickly (60 ps) evolves to $DAPA^{+}$-Ir-DNI^{-}. This state slowly decays on 120 μs under Ar[66] and is almost insensitive to oxygen (τ = 100 μs under air). To the best of our knowledge, this represents one of the most successful examples of charge separation based on transition metal complexes under air.

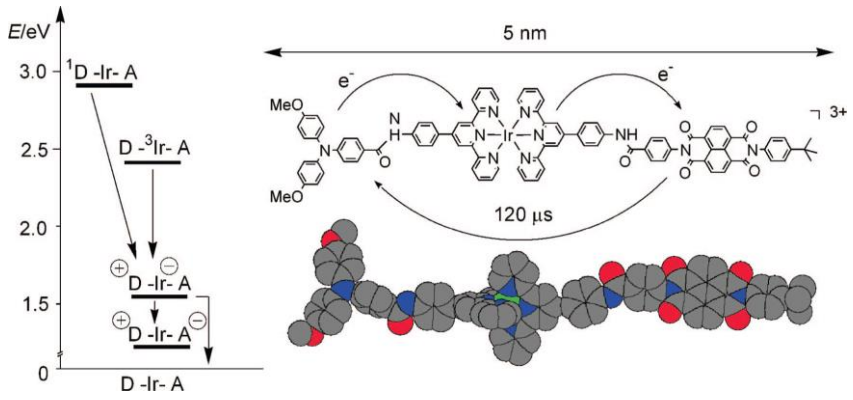

Figure 1.25 – Energy levels and photo-induced processes for Ir(III) bis-tpy-based triad in CH_3CN.[66]

Although Ir(III) bis-terpyridine complexes allow to photo-induce electron transfer, reduction and oxidation potentials as described before usually remain not much affected by ligand substitution on the terpyridine ligand. This issue can be overcome by modifying the first coordination sphere as it has been done for Ir(III) tris-bidentate complexes. For the latter, variation of C/N ratio from 0/6 to 3/3 enables to efficiently tune the (photo-)

reduction and (photo-)oxidation properties.[43] However, this strategy has been sparsely applied to terdentate ligand despite obvious potential of such structures. This is probably reflecting the difficult synthesis and purification for these complexes.[73] As a consequence, almost no application has arisen from these molecules yet.[98] This is why we essentially should limit the discussion to the synthesis and photophysical properties of Ir(III) cyclometalated bis-terdentate complexes.

1.4.2. Ir(III) cyclometalated bis-terdentate complexes

1.4.2.1. Synthesis and spectroscopic data of Ir(III) mono-cyclometalated complexes (C/N = 1/5)

The synthesis of dichlorobridged dimer as an intermediate is achieved by heating 1,3-di(2-pyridyl)4,6-dimethylbenzene (dpyxH) and $IrCl_3.3H_2O$ in 2-ethoxyethanol at 130 °C (Scheme 1.6). In a second step, this intermediate reacts with the desired tpy ligand. It is worthwhile to mention that two methyls on the dpyxH ligand are required to avoid undesired cyclometalated by-products. Although no electrochemical data are provided, spectroscopic studies reveal that these complexes essentially absorb below 400 nm (pale yellow). The lower-energy bands are ascribed to an almost purely Ligand to Ligand Charge Transfer (LLCT) from dpyb to tpy ligand on the basis of DFT calculations. Unfortunately, these complexes are almost not emissive ($\Phi < 10^{-3}$ in deaerated CH_3CN)[99] even at 77 K. Their use as charge photo-injector is therefore deeply compromised due to more difficult direct light excitation.

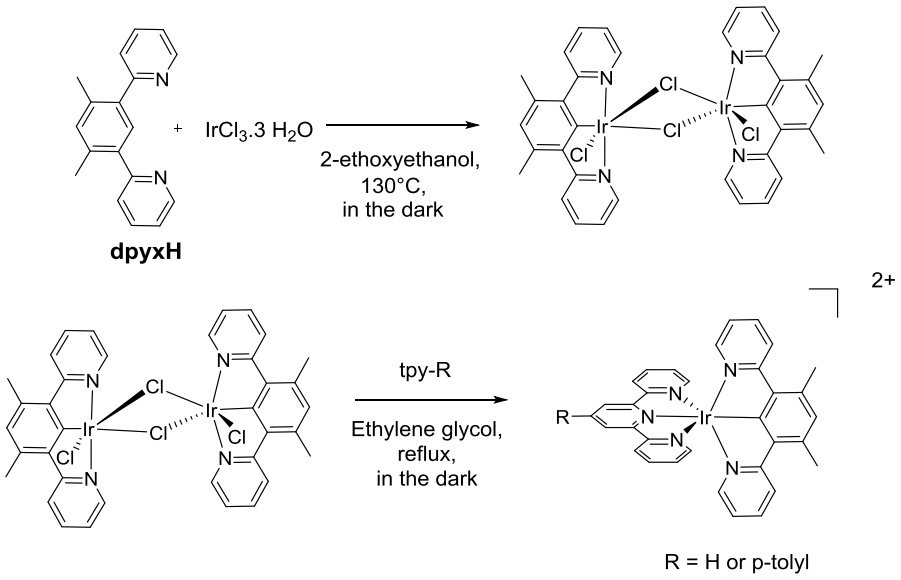

Scheme 1.6 – Synthesic scheme of Ir(III) bis-terdentate (C/N = 1/5) complexes.[99]

1.4.2.2. Synthesis, spectroelectrochemical data and application of Ir(III) bis-cyclometalated complexes (C/N = 2/4)

Their synthesis relies on the same Ir(III) trichloride intermediate used for Ir(III) bis-terpyridine complexes. It reacts with cyclometalated ligand in refluxing ethylene glycol for 1h in the presence of silver nitrate to help removing chlorides from intermediate (Scheme 1.7). Electrochemical studies revealed two reversible one-electron processes. On the one hand, there is a reduction wave at - 1.27 V/SCE assigned to the reduction of tpy ligand. On the other hand, an oxidation process observed at + 1.08 V/SCE is carefully attributed to Ir-dppy fragment (dppy = 2,6-diphenyl-pyridine).

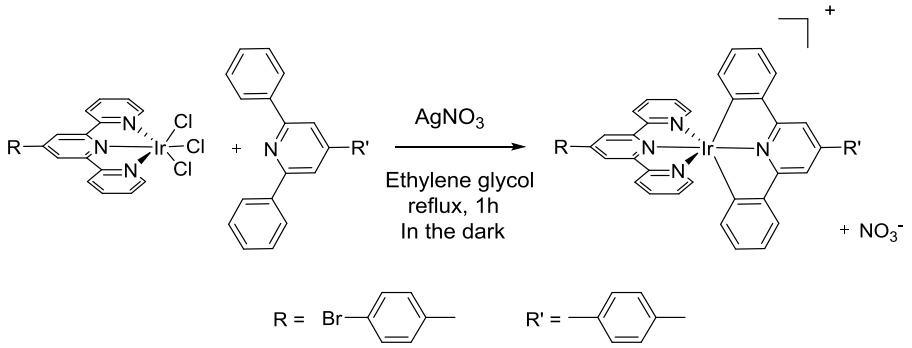

Scheme 1.7 – Synthetic strategy to form Ir(III) bis-terdentate (C/N = 2/4) complexes.

The electronic absorption spectrum is shown in Figure 1.26. There are two strong absorption bands at 284 and 320 nm which are ascribed to Ligand Centered $\pi_l \rightarrow \pi^*_l$ transitions. In the visible region, lower energy transitions are observed at 438 and 520 nm. These transitions have been attributed to a mixture of ^{1}MLCT/^{1}LLCT transitions as suggested by DFT theoretical calculations.[100]

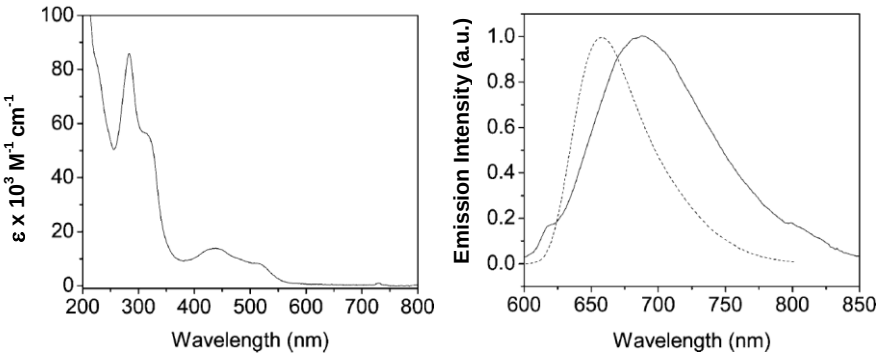

Figure 1.26 – Absorption (left) and emission (right) spectra at RT (solid line) and 77 K (dashed line) of [[(4′-(4-bromophenyl)-2:2′,6′:2″-terpyridine)Ir(2,6-diphenyl-4-(4-tolyl)pyridine)](NO$_3$)] (Scheme 1.7) in acetonitrile under Argon.[101]

This complex emits in acetonitrile at room temperature (Figure 1.26, right spectrum). The emission energy (λ_{max} = 690 nm) is lower than the corresponding bis-terpyridine complexe (λ_{max} = 506 nm for $[Ir(ttpy)]^{3+}$).[102] This is due to destabilizing effect of the two cyclometalated carbons on the HOMO. The emission is also red-shifted compared to the tris-bidentate $[Ir(ppy)_2(bpy)]^+$ complex (λ_{max} = 606 nm).[103] This is the result of the lower energy of terpyridine acceptor compared to the bipyridine ligand. Emission originates in this case from a mixture of ^{3}LLCT/^{3}MLCT excited states. The quantum yield (Φ = 0.032) is relatively low in degassed acetonitrile compared with other common bis-cyclometalated complexes (*e.g.* Φ = 0.34 for $[Ir(ppy)_2(acac)]$).[104] However, the luminescence lifetime (τ = 1.7 μs under Ar) is not particularly short (τ = 1.7 μs for $[Ir(ppy)_2(acac)]$ under Ar) which implies that the emitting state has a low radiative rate constant (k_r = 1.9 x 10^4 s^{-1} *vs.* k_r = 2.1 x 10^5 s^{-1} for $[Ir(ppy)_2(acac)]$).[104] Moreover, the emission of the complex is strongly quenched by oxygen (τ = 200 ns under air). The emission spectrum at 77 K (Figure 1.26) is blue shifted, broad and structureless. That rules out an LC nature of the emission for which vibrational structures would appear but is consistent with a charge-transfer nature of the emitting exciting state.

To the best of knowledge, only one application arises from Ir(III) bis-cyclometalated complexes where they are used as photosensitizers for nanocrystalline TiO_2-based Dye-Sensitized Solar Cells (DSSCs).[98] DSSCs are electrochemical devices capable of performing the direct conversion of light into electricity. Among these latter systems, the most famous one consists in a "N_3 dye" (where N_3 dye = cis-bis-(4,4′-dicarboxy-2,2′-bipyridine)dithiocyanato ruthenium(II) ($Ru(dcbpy)_2(NCS)_2$), Figure 1.27) adsorded on nanocrystalline TiO_2 films, also known as the Grätzel Cell.[105] The overall solar energy conversion efficiency (η) for this cell is close to 10 %.

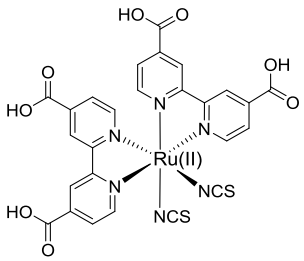

Figure 1.27 – Structure of the Ru(II) photosensitizer used in the Grätzel Cell.[105]

The principle of DSSCs is illustrated in Figure 1.28.[106] Upon photo-excitation of the sensitizer dye, electrons are injected from the excited dye to the conduction band (CB) of the semiconductor film (injection, Figure 1.28). At this stage, the injected electrons can recombine with the oxidized sensitizer dye (recombination, Figure 1.28). The recombination process competes with the regeneration of the oxidized sensitizer dyes by the redox mediator (Rereduction, Figure 1.28) which is I_3^-/I^- redox couple in the case of the Grätzel cell. The electrons may also be transported in the semiconductor film as the conducting electrons (Transport, Figure 1.28). The conducting electrons can react with the redox mediator molecules or with molecules in the solution during transport, before reaching the back contact electrode (Leak reaction, Figure 1.28). Finally, the remaining electrons flow into the external circuit.[106]

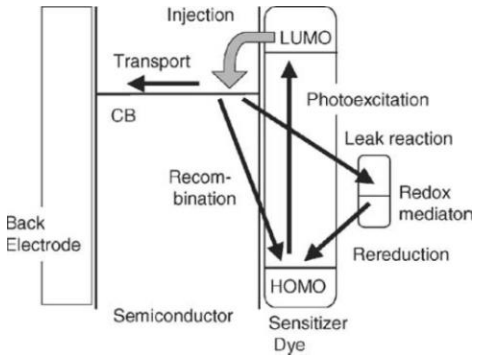

Figure 1.28 – Primary reaction steps in DSSCs.[106]

To date, the most efficient DSSCs incorporate Ru(II) polypyridine complexes[107,108] bearing carboxyl groups as dye for anchoring on nanocrystalline TiO_2 surface. As mentioned before, cyclometalated Ir(III) complexes display some more interesting features such as a longer excited state lifetime or higher quantum yield in organic solvent as compared to Ru(II) complexes. As a result, cyclometalated Ir(III) tris-bidentate ligands have been recently tested to act as dyes in DSSCs.[109,110] Nevertheless, unlike the large absorption in the visible range found for Ru(II) polypyridine complexes[111], the synthesized Ir(III) tris-bidentate complexes only slightly absorb in the visible range with low molar extinction coefficient (between 700 and 2550 M^{-1} cm^{-1} at about 420 nm).[109,110] That is obviously an important drawback to build some sustainable DSSCs expected to efficiently absorb sunlight.

To tackle this issue, Nakabayshi *et al.*[98] synthesized a bis-cyclometalated Ir(III) complex with terdentate ligands (Figure 1.29) to take advantages of its high molar extinction coefficient at longer wavelength (*ca.* 520 nm, 10000 M^{-1} cm^{-1}) as well as its high photo-stability. The solar energy conversion efficiency of their Ir(III) complex reached $\eta = 2.16$ % as compared to $\eta = 3.32$ % when N_3 is used as dye in the same conditions of the preparation of the cell. According to the authors, this disappointing result was due to the preparation of the cell which is optimized for N_3 but not necessarily for their Ir(III) complex.[98] Better cell preparation should increase the solar energy conversion efficiency of the system because of the higher stability and longer excited-state lifetime of their bis-cyclometalated complex.[98]

This example shows that terdentate bis-cyclometalated Ir(III) complexes deserve a particular interest for their inherent properties. This is

why we will focus on this scaffold in the Chapters 3, 4 and 5 of this manuscript.

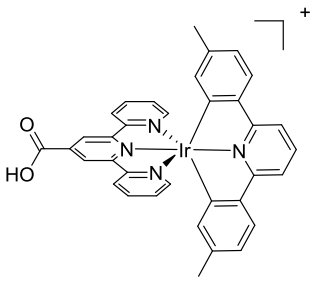

Figure 1.29 – Structure of bis-cyclometalated Ir(III) complex used in DSSCs.

1.4.2.3. Synthesis and spectroscopic data of Ir(III) tris-cyclometalated complexes (C/N = 3/3)

These complexes are obtained by the reaction between dichlorobriged dimer (Scheme 1.8) and molten 2,6-diphenylpyridine ($dppyH_2$) itself as the reaction solvent (m.p. = 74-76°C).[112] Silver trifluoromethanesulfonate is an additive making easier complexation by removing chloride anions.

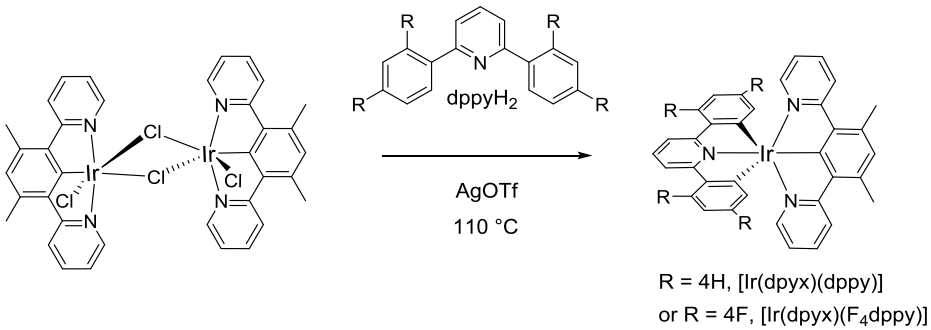

Scheme 1.8 – Synthetic scheme of Ir(III) bis-terdentate (C/N = 3/3) complexes.

The resulting neutral complexes [Ir(dpyx)(dppy)] and [Ir(dpyx)(F_4dppy)] display some intense absorption bands in the UV region ascribed to LC transitions (Figure 1.30). Lower energy absorption bands tail into the visible region and are presumably due to Metal-to-Ligand Charge Transfer transitions (MLCT). The lower energy of the MLCT transition for bis-terdentate Ir(III) complexes compared with *fac*-[Ir(ppy)$_3$] is attributed to the stabilization of acceptor ligand π* orbitals (LUMO) due to increased electronic delocalization. The blue-shifted absorption band for fluorinated complex could be explained by stabilization of the HOMO as a result of the electron withdrawing effect of these fluorine atoms.

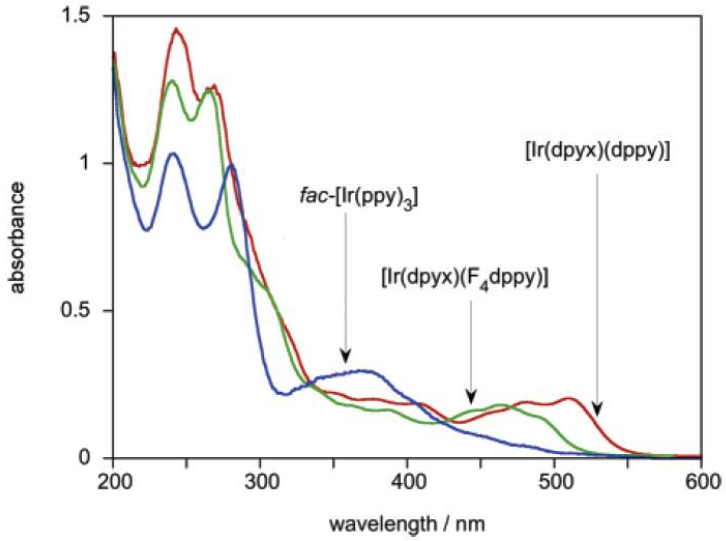

Figure 1.30 – Absorption spectra of [Ir(dpyx)(dppy] (red) and [Ir(dpyx)(F_4dppy)] (green) in acetonitrile at 295 K, together with the spectrum of *fac*-[Ir(ppy]$_3$] (blue) for comparison (adapted from [99]).

Unlike previously discussed Ir(III) bis-terdentate complexes, C/N = 3/3 complexes are strongly luminescent in deaerated acetonitrile displaying a broad structureless emission band, typically observed for Charge Transfer states (Figure 1.31).[69] In agreement with absorption observations,

luminescence of Ir(III) bis-terdentate complexes is red-shifted compared to *fac*-[Ir(ppy)$_3$] essentially due to the same reasons. The quantum yields are much higher than for previous Ir(III) terdentate complexes (Φ = 0.21 and 0.41 respectively for [Ir(dpyx)(dppy] and [Ir(dpyx)(F$_4$dppy)] under Ar). Sadly, photo-dissociation quickly occurs in solution under light irradiation. The photo-decomposition product is presumably [Ir(dpyx)(dppyH)L] (L = Solvent), the result of cleavage of a Ir-C bond. Such a process is also observed for the structurally similar *mer*-[Ir(ppy)$_3$], where dissociation of one of the *trans*-related Ir-C bonds in the excited state is followed by isomerization to the *fac* isomer.[71]

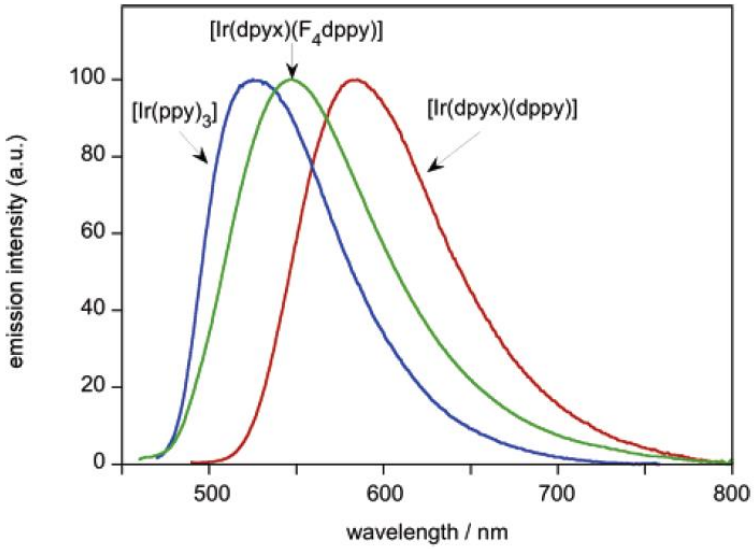

Figure 1.31 – Emission spectra of [Ir(dpyx)(dppy] (red) and [Ir(dpyx)(F$_4$dppy)] (green) in acetonitrile at 295 K, together with the spectrum of *fac*-[Ir(ppy]$_3$] (blue) for comparison (adapted from [99]).

1.4.3. Summary of luminescent properties

As depicted, Ir(III) bis-terdentate complexes differ greatly from one another in terms of their luminescent properties especially with regard to

their quantum yield. However, this effect could be rationalized by considering the influence of the number of cyclometallated carbon atoms on the energies of ligand and metal orbitals (Figure 1.32). For sake of clarity, 2,2′:6′,2″-terpyridine, 1,3-di(pyridine-2-yl)benzene and 2,6-diphenylpyridine are respectively termed N^N^N, N^C^N and C^N^C.

$[Ir(N^N^N)_2]^{3+}$ complexes moderately luminesce in solution at room temperature ($\Phi \approx 0.01$) with an emission implying LC transitions (at least for the parent $[Ir(tpy)_2]^{3+}$ complex).

The addition of a first cyclometalated carbon leads to a complete luminescence quenching for $[Ir(N^N^N)(N^C^N)]^{2+}$ complex. The HOMO becomes predominantly localized on the N^C^N ligand due to the destabilizing cyclometalated carbon. Since the LUMO remains N^N^N ligand-based, the electronic transition involves an almost pure N^C^N $\rightarrow$ N^N^N Ligand-to-Ligand Charge Transfer (LLCT) with few contribution of $d\pi_{Ir}$ metal centered orbital. Therefore, there is a low orbital overlapping and probably inefficient spin-orbit coupling entailing to a low radiative rate constant.

The introduction of a second cyclometallating carbon atom on the same ligand raises the energy of metal centered orbital so that the LLCT is now presumably mixed with some Metal-to-Ligand Charge Transfer (MLCT) transitions. As a result, there is an increase in the radiative rate constant for $[Ir(N^N^N)(C^N^C)]^{+}$ complexes.

When a third cyclometallating carbon atom is introduced, the $d\pi_{Ir}$ metal centered orbital energy as well as the ligand centered orbital π^*_l are both raised leading to unequivocal MLCT nature of the excited state. Consequently, [Ir(N^C^N)(C^N^C)] complexes are bright emitters.

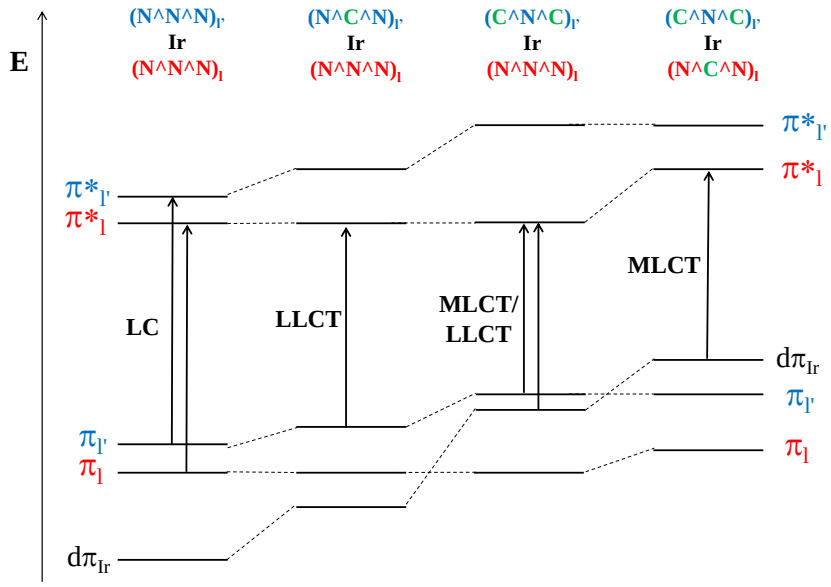

Figure 1.32 – Simplified schematic energy level diagram exhibiting the influence of cyclometallation on the frontier orbitals in bis-terdentate Ir(III) complexes leading to excited states of different character. l and l' represent two different ligands (adapted from [113]).

Chapter 2 - Objectives and strategy

2.1 Objectives

This Ph.D. thesis is related to the field of alternative energies. Artificial photosynthesis relies on systems able to efficiently photo-induce charge separation. To reach this goal, the efficiency of each unit of the supramolecular device (Figure 1.1) has to be optimized. Whereas a wide variety of charge injectors (Part A, Figure 1.1) and catalysts for hydrogen evolution (Part C, Figure 1.1) has been evaluated, the bridging unit (Part B in Figure 1.1) usually consists of bidentate-based ligands without any clear other option.[1,28] Bis-terdentate complexes feature inherently linear symmetry which is an attractive motif toward directional control of electron transfer.[114] To the best of our knowledge, no supramolecular assembly with a bridging terdentate moiety exhibiting hydrogen photo-evolution has been reported yet. This is why we first focus on such structures during this Ph.D. thesis. To go a step further, the goal of our research group is to design an innovative supramolecular assembly by replacing the organic bridging ligand by an oligonucleotide (Figure 2.1) for several reasons that will be set out below.

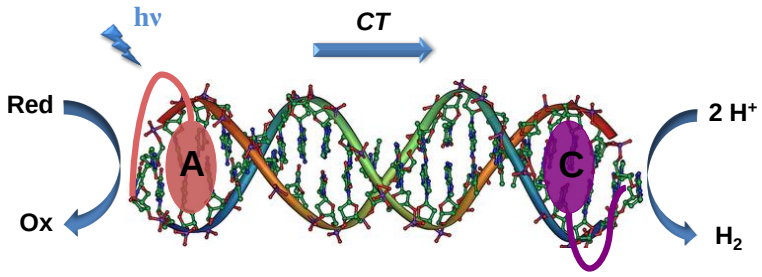

Figure 2.1 – Structure of the target supramolecular system for hydrogen photo-evolution (A – Chage photo-injector; C – Catalyst for H_2 production; CT – Charge Transfer).

Overall, spectroscopic, reduction and oxidation properties of the charge photo-injectors remain unsatisfactory despite obvious recent progress.[2] Iridium(III) complexes provide an interesting solution to tackle

this problem. As disclosed in the introduction, bis-terdentate Ir(III) complexes can be advantageous due to their spectro-electrochemically tuning upon change of Carbon/Nitrogen (C/N) ratio. However, mono (C/N = 1/5) and tris-cyclometalated (C/N = 3/3) Ir(III) complexes should be ruled out due to their respective non-luminescent and photo-labile behaviour in solution. Therefore, only bis-terpyridine (C/N = 0/6) and bis-cyclometalated (C/N = 2/4) complexes have been considered (Figure 2.2). For sake of clarity, they will respectively be termed in this manuscript $\mathbf{[IrN_6]^{3+}}$ and $\mathbf{[IrN_4C_2]^{+}}$ to take into account for their "cyclometalated" character or not.

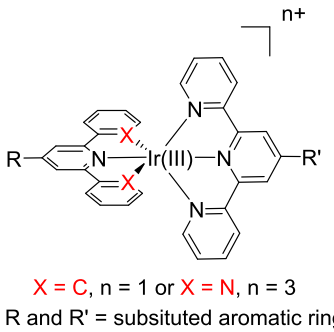

Figure 2.2 – Structure of Ir(III) complexes studied in this Ph.D. thesis.

Unlike Ir(III) bis-terpyridine complexes where spectroscopic, reduction and oxidation properties have been satisfactory studied, luminescent excited-state nature of cyclometalated $\mathbf{[IrN_4C_2]^{+}}$ complexes deeply relies on theoretical considerations.[100] Therefore, we propose to find some experimental evidences supporting these expectations. Accordingly, complexes bearing substituents sensitive to their environment (Figure 2.3) have to alter frontier orbital energy level so that expected MLCT/LLCT spectroscopic properties are modified in a predictive manner.

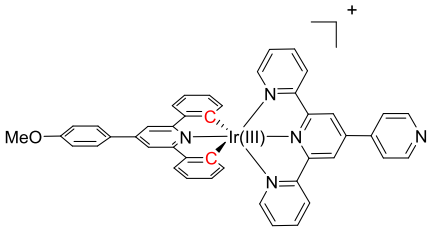

Figure 2.3 – Structure of an $[IrN_4C_2]^+$ complex bearing basic sites.

Based on spectro-electrochemical properties of the structure shown in the Figure 2.3, we postulate that coordination of the pendent pyridyl group should enable synthesis of dyades for hydrogen photo-production. Since cobalt derivatives are straightforwardly built and efficient for such catalyst (see Chapter 4 for more details),[28] they were ultimately chosen (Figure 2.4). Compared with systems already known where the bridging ligand is a bidendate one, we hope for a more efficient electron transfer due to proximity and linear arrangement of charge photo-injector and catalyst moieties. In addition, $[IrN_4C_2]^+$ complexes allow to widely harvest visible light and have already been assessed to convert light into electricity as mentioned in the introduction (see 1.4.2.2). The experiments of hydrogen photo-production were carried out in collaboration with Prof. Garry Hanan (Université de Montréal, Canada) who has developed an experimental set up for molecular hydrogen quantification.

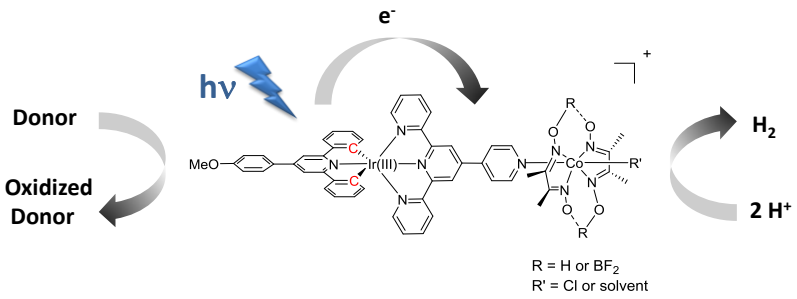

Figure 2.4 – Structure of iridium-cobalt dyades for hydrogen photo-production.

Dihydrogen photo-evolution unambiguously involves photo-induced electron transfers. However, such processes have gone far beyond this scope. Photo-induced electron transfer also plays an essential role in nature. Charge migration in DNA double strand activated by light represents an entire research field widely studied in the last three decades (see Chapter 5 for more details).[115-117] Holes or electrons charge transfer can be specifically triggered depending on photo-chemical properties of charge injectors. The comparison between $[IrN_6]^+$ and $[IrN_4C_2]^+$ in this role should therefore lead to different behaviours according to their distinct features (Figure 2.5).

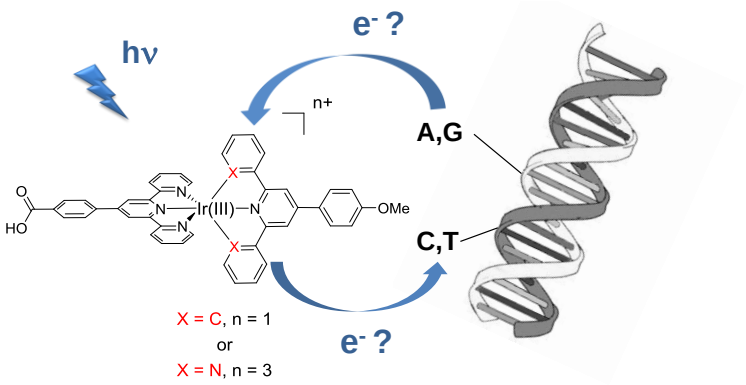

Figure 2.5 – Representation of possible photo-induced electron transfers between Ir(III) complexes ($[IrN_4C_2]^+$ and $[IrN_6]^{3+}$) and DNA oligonucleotides.

Although our laboratory is interested in hydrogen photo-evolution, other catalysts relying on Ir(III) bis-terdentate complexes are not without any relevance. Indeed, the thermal, chemical and photo-stability of Ir(III) derivatives represent all the structural requirements of good photocatalyst candidates. These features are especially true for $[IrN_6]^{3+}$ complexes for which examples have been recently reported (see 1.4.1.2). As a result, their efficiency has been assessed in a photo-induced five-membered ring cyclization (Scheme 2.1).

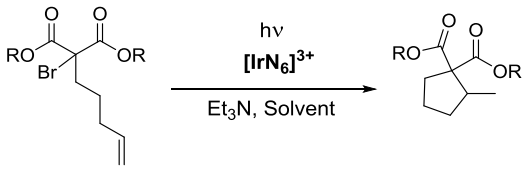

Scheme 2.1 – Photocatalyzed five-membered ring cyclization.

The grafting of Ir(III) bis-terpyridine on solid support would enable the development of supported homogeneous catalysis. In collaboration with Prof. Sophie HERMANS (UCL) who has developed expertise in this field, the synthesis of functionalized Ir(III) bis-terpyridine complexes (easier to synthesize in large amount compared with $\mathbf{[IrN_4C_2]^+}$ complexes) has been investigated. Their covalent and non-covalent grafting onto graphene derivatives as well as their photocatalytic activities has been tested respectively by Florence PENNETREAU (Prof. Sophie HERMANS) and Christophe RUBAY (Prof. Benjamin ELIAS).

The last part of the manuscript takes us away from photo-reactivity of Ir(III) bis-terdentate complexes although the starting point of this project was clearly in connection with this (see Chapter 7 for more details). As a result, this chapter deals with a synthetic approach based on the Kröhnke synthesis leading to multi-tpy ligands (Figure 2.6). Compared with other strategies, our synthetic method enables to easily substitute the terminal aromatic ring from benzaldehyde modifications which be used for the synthesis of larger Ir(III) entities.

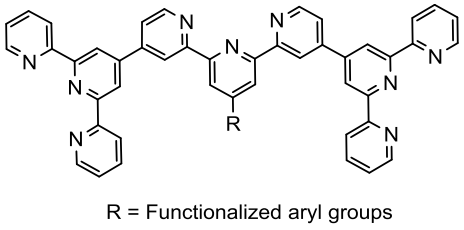

Figure 2.6 – Structure of multi-terpyridines.

2.2 Content of the Ph.D. manuscript

The result and discussion sections have been divided into five chapters presented as publications in peer reviewed journals (published or submitted) except for chapter 6 where my contribution has been limited to the synthesis and characterization of Ir(III) complexes.

The chapter 3 focuses on the effect of protonation or methylation on spectroscopic properties of an $\mathbf{[IrN_4C_2]^+}$ complex. In combination with theorical calculations, this study has confirmed the MLLCT (Metal/Ligand to Ligand Charge Transfer) character of the excited state for these complexes.

The chapter 4 exploits the insight gained in chapter 3 to build $\mathbf{[IrN_4C_2]^+}$ based dyads in order to photo-produce molecular hydrogen.

The chapter 5 unveils a comparative study of $\mathbf{[IrN_4C_2]^+}$ and $\mathbf{[IrN_6]^{3+}}$ photo-reactivity towards DNA building blocks and oligonucleotides.

The chapter 6 describes the synthesis and photophysical properties of $\mathbf{[IrN_6]^{3+}}$ complexes and their use in organic homogeneous and supported homogeneous photocatalysis.

The chapter 7 brings to light a synthetic method enabling to access to functionalized multi-terpyridines ligands.

The chapter 8 gathers the conclusions and outlooks of this manuscript. In addition, the chapter 9 and 10 respectively detail the instrumental techniques as well as some supporting data.

Important data stored in Supporting Information for publication have been integrated in the chapters in order to facilitate the reading of this research work. For sake of clarity, the experimental section is presented at

the end of each chapter and not at the end of this manuscript where only the synthesis of terdentate ligands and some additional computational data are given.

Chapter 3 - Protonation of Bis-terdentate cyclometalated Ir(III) complexes : evidence for a metal-ligand to ligand based charge-transfer excited state

3.1 Foreword

The results presented hereafter reflect our wish to shed light on the nature of the electronic transitions observed for $[IrN_4C_2]^+$ complexes. This project was motivated by the fact that these structures display some peculiar properties in term of spectroscopic properties.[101] Whereas the LUMO is unambiguously centered on the terpyridine part, the HOMO nature presents a much more puzzling behaviour. Time-Dependent Density Functional Theory (TD-DFT) investigations reveal that this latter orbital implies both metal and cyclometalated ligand leading to a LLCT/MLCT (also written MLLCT) mixture of electronic transitions.[100]

Our objective was to provide some experimental evidence that the cyclometalated ligand really participates in electronic transitions. If so, we predict that protonation of the ligands should alter frontier orbitals. In addition, we wished to control both HOMO and LUMO energy. This is why we built a $[IrN_4C_2]^+$ complex with one basic site on each ligand with large basicity difference so that we can selectively protonate only one site without affecting the other. We choose a basic pyridine function on the terpyridine part and a much less basic methoxy group on the cyclometalated ligand. The control of acid strength and concentration enabled to significantly modify the absorption and emission properties of the synthesized complexes.

The study evidenced that cyclometalated ligand effectively participates to electronic transitions as predicted. Moreover, these observations have been supported by further theoretical calculations performed by two Ph. D. students of the Prof. Garry HANAN (Université de Montréal, Canada), Mihaela CIBIAN and Thomas AUVRAY.

Journal

Inorganic Chemistry **2015**, *submitted*.

Title

Protonation of Bis-terdentate cyclometalated Ir(III) complexes : experimental evidence for a CT excited state from ML to L

Authors

Alexandre JACQUES [a], Thomas AUVRAY [b], Mihaela CIBIAN [b], Garry S. HANAN [b], Andrée KIRSCH – De MESMAEKER [c] and Benjamin ELIAS [a*]

Affiliations

[a] Université catholique de Louvain, Institut de la Matière Condensée et des Nanosciences, Place Louis Pasteur 1, L4.01.02, B-1348, Louvain-la-Neuve, Belgium.

[b] Département de Chimie, Pavillon J.-A. Bombardier, 5155 Chemin de la Rampe, Université de Montréal, Montréal, Québec, Canada, H3T 2B1.

[c] Université libre de Bruxelles, Service de Chimie Organique et Photochimie, CP160/08, 50 Av F. D. Roosevelt, B-1050, Brussels, Belgium.

Abstract

*Two bis-terdentate cyclometalated Ir(III) complexes with polypyridyl (N^N^N) and cyclometalated (C^N^C) ligands (**[Ir-Py]**$^{+}$ and **[Ir-Py-Me]**$^{2+}$, respectively (Figure 3.1), have been synthesized and characterized. Their absorption and emission properties have been examined, more particularly in MeCN as a function of the addition of different acids. Depending on the acid strength and concentration, two distinct effects have been observed. For acetic acid at high concentration or trifluoroacetic acid (TFA) at low concentration, the pyridine moiety of **[Ir-Py]**$^{+}$ is protonated; its spectroscopic behaviour is then similar to that of **[Ir-Py-Me]**$^{2+}$. Moreover at higher concentration in TFA, the methoxy group of both complexes is protonated. The spectroscopic and electrochemical data as well as the attribution of the lowest energy transitions in absorption and emission to charge-transfer from a metal-ligand to ligand-based energy levels (MLLCT) are also supported by DFT and TD-DFT calculations.*

3.2 Introduction

Transition metal complexes have attracted the interest of increasing number of researchers these past decades due to their exceptional properties.[111] Among the available transition metal ions, Ir(III) is becoming one of the most interesting elements to design new complexes because of its strong spin-orbit coupling, its high quantum yield of luminescence with organic ligands as well as the ability to fine-tune its properties by ligand modifications.[43] Due to these remarkable properties, iridium(III) complexes are useful for the development of supramolecular devices, with photo-induced energy[118,119] and/or electron transfer.[97,120,121] More recently, the incorporation of strong donor ligands has been exploited to red-shift the absorption and emission bands in transition metal complexes, such as in Ru(II),[122-127] Re(I)[128] and Ir(III)[129] complexes. The strong donor ligands increase the energy of the HOMO and leave the LUMO level relatively unaffected which gives rise to the red-shift. An even greater effect comes from the use of anionic cyclometalating ligands, such as those derived from 2-phenylpyridine, which gives rise to Ir(III) complexes like $[Ir(C^N)_2(N^N)]^+$ (C^N = cyclometalated ligand, N^N = polypyridine). Indeed, Ir(III) complexes of cyclometalating ligands have attracted much attention for their potential applications in various fields such as photo-catalysis,[130-132] dye-sensitized solar cells,[133] electroluminescence and electrochemiluminescence,[51,134] DNA sensors[135] and in cell imaging.[57,136] Compared to cyclometalated Ir(III) tris-bidentate complexes, their bis-terdentate equivalents have been less investigated mainly due to difficulties of their synthesis and purification.[137] However, they present several important advantages. Indeed, Ir(III) terpyridyl complexes derivatized on the 4′-position by suitable substituents circumvent the occurrence of geometrical isomers as with tris-bidentate arrangements. This problem has been well documented in Ru(II) chemistry of bidentate and tridendate ligands.[138] The

Ir(III) complexes of tridentate ligands also allow the design of systems for linear charge separation for photo-induced intramolecular electron transfer. In the literature, cyclometalated iridium(III) complexes involving two tridentate ligands, one N^N^N tpy derivative (tpy = 2:2′,6′:2″-terpyridine) and one C^N^C dppy derivative (dppy = 2,6-diphenylpyridine), have been first reported by Scandola *et al.*[101] Using computational techniques, the predominant emitting excited state has been attributed to a Ligand-to-Ligand charge-transfer state (LLCT) from the cyclometalated iridium fragment to the tpy.[100] However, clear-cut experimental proofs in favor of LLCT transitions were not easily attained. As potential applications based on these scaffolds require a deeper understanding of their photo-redox properties, we sought to design and study novel and tunable $[Ir(N^N^N)(C^N^C)]^+$ complexes.

In this work, we report the synthesis and characterization of two new Ir(III) complexes obtained from the coordination of a terpyridyl ligand and a triphenylpyridyl ligand *i.e.* $[Ir(4′\text{-Py-tpy})(4′\text{-MeO-tppy})]^+$ (4′-Py-tpy = 4′-(4-pyridinyl)-2,2′;6′,2″ terpyridine and 4′-MeO-tppy = 2,6-diphenyl-4-(4′-methoxyphenyl)pyridine) and its *N*-methylated equivalent *i.e.* $[Ir(4′\text{-Me-Py-tpy})(4′\text{-MeO-tppy})]^{2+}$ (4′-Me-Py-tpy = 4′-(4-methyl-pyridinio**)**-2,2′;6′,2″-terpyridine) termed **$[Ir\text{-}Py]^+$** and **$[Ir\text{-}Py\text{-}Me]^{2+}$**, respectively (Figure 3.1). The impact of acidity on the spectroscopic properties of both complexes in MeCN is analyzed from an experimental and theoretical approach and will provide experimental evidence for excited states with charge-transfer from a metal-ligand based HOMO to a ligand-based LUMO (MLLCT).

3.3 Results

3.3.1 Synthesis and characterization

The synthesis of the 2 Ir(III) complexes (Figure 3.1) was achieved in two steps from the Ir(III) chloride salt according to methodologies previously described;[100,101] they were purified by column chromatography (see experimental). Both complexes were unambiguously characterized by ^{1}H NMR spectroscopy and high-resolution mass spectrometry (HRMS) (see Experimental Section, Figures 3.13 and 3.14).

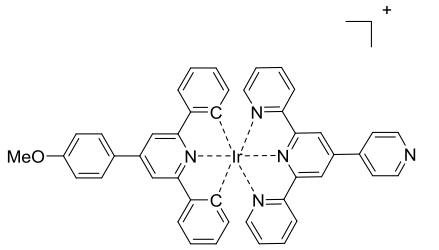

[Ir-Py]$^{+}$

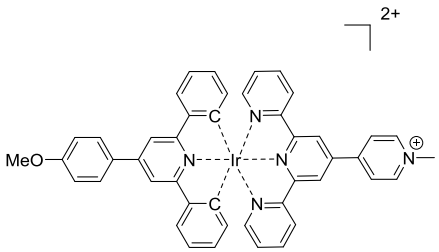

[Ir-Py-Me]$^{2+}$

Figure 3.1 – Structure of [Ir(4′-Py-tpy)(4′-MeO-tppy)]$^{+}$ (**[Ir-Py]$^{+}$**) and [Ir(4′-Me-Py-tpy)(4′-MeO-tppy)]$^{2+}$ (**[Ir-Py-Me]$^{2+}$**).

Firstly, the redox potentials of the two complexes have been determined from cyclic voltammetry measurements. From these experimental data, we gained more information on the relative energy levels of the two species. The data are gathered in Table 3.1. Both complexes

display one reversible oxidation wave at 1.16/1.19 V *vs.* Ag/AgCl (Figures 3.16 and 3.17 in the Experimental Section). These similar oxidation potentials are in agreement with a similar oxidation process, which indicates that the HOMOs have a similar energy level in the two compounds. The potential values are also in a range similar to those of other cyclometalated complexes[100,101] and the waves are reversible. We propose that the oxidation process involves the whole cyclometalated iridium fragment (Ir-tppy-MeO) which is supported by DFT calculations (see Computational Studies).

At negative potentials, there are two reduction waves for [**Ir-Py-Me**]$^{2+}$, the first one at -0.71 V *vs.* Ag/AgCl (Figure 3.2) is ascribed to the reduction of the *N*-methyl-pyridinium substituent. In the literature, a value in the same potential range has been found for the first reduction wave of [Pt(4′-Me-Py-tpy)(Cl)]$(ClO_4)_2.H_2O$ (-0.45 *vs.* Ag/AgCl).[139] As the potential of this first reduction can be related to the LUMO level of the complex, it indicates that the LUMO of [**Ir-Py-Me**]$^{2+}$ is much more stabilized than that of **[Ir-Py]**$^{+}$ (Figure 3.12). The second reduction wave of [**Ir-Py-Me**]$^{2+}$ at -1.14 V *vs.* Ag/AgCl is ascribed to the reduction of its tpy motif, as found for **[Ir-Py]**$^{+}$, with only a weak effect caused by the substituent (Table 3.1 and Figures 3.2 and 3.15 in the Experimental Section).

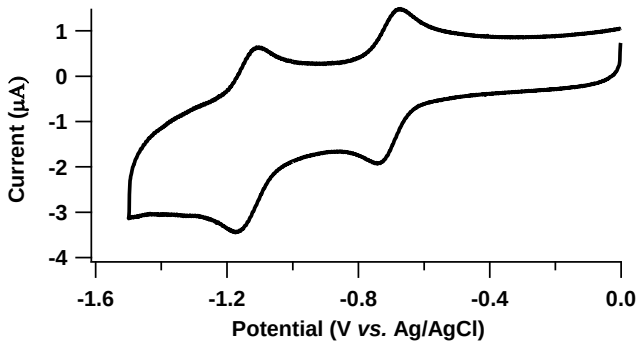

Figure 3.2 – Reduction voltammogram of **[Ir-Py-Me]**$^{2+}$ (10^{-5} M) in MeCN (0.1 V/s) with Bu_4NClO_4 0.1 M as supporting electrolyte.

Spectroscopic methods were then used to determine the optical gap as well as the excited state's nature. The absorption and emission spectra in MeCN are shown in Figure 3.3 and the corresponding data are gathered in Table 3.1. Intense absorption bands between 281-327 nm are ascribed to Ligand Centered transitions (LC), based on previous studies of cyclometalated Ir(III) complexes;[101] as shown in Table 3.1, they are not affected upon methylation of the pyridine substituent.

Table 3.1 – Spectroscopic and electrochemical data for the complexes **[Ir-Py]$^+$** and **[Ir-Py-Me]$^{2+}$**.

Complexes	**[Ir-Py]$^+$**	**[Ir-Py-Me]$^{2+}$**
$\lambda_{max\ abs}$, nm[b] (ε, x 10^{-3} $M^{-1}cm^{-1}$)	514 (5.5), 445 (9.1), 324 (41.6), 283 (53.6)	540 (6.7), 476 (9.3), 327 (31.8), 281 (42.2)
$\lambda_{max\ Em}$ under air at 298 K	705	-[a]
$\lambda_{max\ Em}$ at 77 K	673	720
τ (μs) under air at 298 K	0.22	-[a]
τ (μs) under argon at 298 K	1.05	-[a]
Φ[c] (Air)	0.0014	-[a]
Φ[c] (Ar)	0.0064	-[a]
k_r (x 10^3 s^{-1})[d]	6.1	-[a]
E_{ox}[e] (V *vs.*Ag/AgCl)	1.16 (r, ΔE_p = 70 mV)	1.19 (r, ΔE_p = 62 mV)
E_{red}[e] (V *vs.*Ag/AgCl)	-1.16 (r, ΔE_p = 72 mV)	-0.71 (r, ΔE_p = 73 mV); -1.14 (r, ΔE_p = 71 mV)

[a]Non emissive. [b]Measured in MeCN. [c]Quantum yield was measured under air using $[Ru(bpy)_3]^{2+}$ as reference Φ_{ref} = 0.028 in H_2O,[140] λ_{Exc} = 450 nm, 293 K. [d]Radiative rate constant under argon at 298 K ($k_r = \Phi/\tau$). [e]Electrochemical data were recorded at room temperature in MeCN ([Complex] = 10^{-5} M) with Bu_4NClO_4 0.1 M as supporting electrolyte; (r) = reversible, (ΔE_p) (peak-to-peak difference).

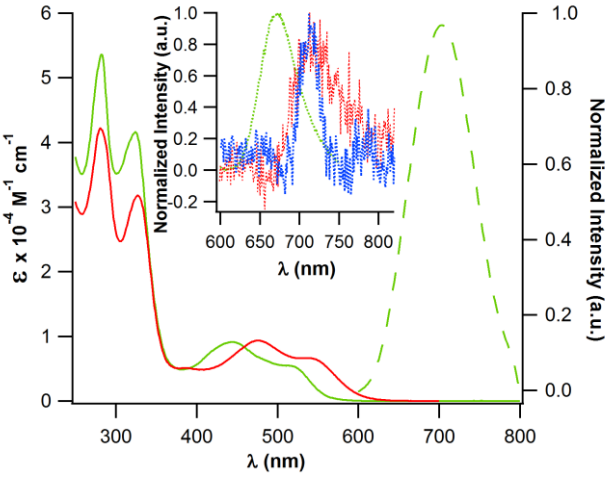

Figure 3.3 – Absorption spectra of **[Ir-Py]**$^{+}$ and **[Ir-Py-Me]**$^{2+}$ (red) in MeCN; emission of **[Ir-Py]**$^{+}$ (dotted green line) under air at room temperature and excitation at 520 nm. Inset: emission spectra at 77 K of **[Ir-Py]**$^{+}$ (green), **[Ir-Py-Me]**$^{2+}$ (red) and **[Ir-Py-H]**$^{2+}$ (blue) in a mixture EtOH/MeOH (4/1) (λ_{exc} = 520 nm).

Absorption bands also appear in the visible. In contrast to the LC transitions, these bands are affected by methylation of the pyridine substituent. Thus, a red shift of *ca.* 30 nm is observed upon methylation of **[Ir-Py]**$^{+}$ giving [**Ir-Py-Me]**$^{2+}$ (Figure 3.3). Regarding the luminescence properties at 298 K, only the **[Ir-Py]**$^{+}$ is emissive (Figure 3.3). At 77 K, the luminescence of **[Ir-Py]**$^{+}$ in MeOH/EtOH is shifted to the blue (Figure 3.3, inset). For [**Ir-Py-Me]**$^{2+}$ a weak emission with a maximum around 725 nm can be detected at 77 K (Figure 3.3, inset) with no discernable emission at room temperature. These observations lead to different conclusions. (i) For **[Ir-Py]**$^{+}$, the unstructured room temperature emission is blue-shifted at 77 K, which is characteristic of a CT emission. (ii) The fact that a very weak emission for [**Ir-Py-Me]**$^{2+}$ can be detected at 77 K around 725 nm (Figure 3.3, inset) indicates the participation of a luminescent excited state. This

latter is affected by important radiationless deactivation at 298 K, probably caused by the methyl group, which could introduce supplementary vibrational modes of deactivation. (iii) A single emission lifetime of the order of 1 μs for **[Ir-Py]**$^{+}$ is also compatible with usual CT excited state lifetimes.[141] In spite of the fact that the spectroscopy in absorption and emission is compatible with the attribution of the lowest energy transitions to CT transitions for both Ir complexes, it is not clear at this stage whether they can be described as LLCT, MLCT, or a mixture of both (MLLCT). In order to answer this question, DFT and TD-DFT calculations were performed with **[Ir-Py]**$^{+}$ and [**Ir-Py-Me]**$^{2+}$ and for comparison purposes, with the protonated form of **[Ir-Py]**$^{+}$, referred to as **[Ir-Py-H]**$^{2+}$.

3.3.2 Computational studies

The ground and vertical excited state electronic structures were investigated by the means of DFT/TD-DFT calculations using the B3LYP method,[142-144] the 6-31G* basis set[145] for C, H, and N and the VDZ (valence double ζ) with the SBKJC effective core potential basis set[146-148] for Ir. Solvent (MeCN) was included by a polarizable continuum model.

The computed HOMO, HOMO-1, LUMO and LUMO+1 for **[Ir-Py]**$^{+}$, [**Ir-Py-Me]**$^{2+}$ and **[Ir-Py-H]**$^{2+}$ are depicted in Table 3.2 while further details on electronic and geometrical structure can be found in the Tables 3.3 – 3.8 (see Experimental Section for Tables 3.3 – 3.5 and Annexes for Tables 3.6 – 3.8). Figure 3.4 compares the energy levels of selected occupied and unoccupied molecular orbitals (MOs) of the S_0 state. The contributions of the Ir(III) as well as those of the two ligands (4′-MeO-tppy) and (4′-Py-tpy) are represented with different colors and the precise percentages of these contributions can be found in Tables 3.3 – 3.5 of the Experimental Section. The calculated HOMO–LUMO gaps follow the trend observed in the electrochemical measurements as well as in the absorption spectra, with **[Ir-**

Py]$^{+}$ exhibiting a larger HOMO–LUMO gap as the LUMO of **[Ir-Py-Me]**$^{2+}$ and **[Ir-Py-H]**$^{2+}$ are stabilized after protonation/methylation while the HOMO levels are almost not affected. However, the order of HOMO and HOMO-1 is inverted for the protonated and methylated form of the complexes so the 4′-Py-tpy ligand contribution becomes negligible in the HOMO level of **[Ir-Py-Me]**$^{2+}$ and **[Ir-Py-H]**$^{2+}$ while it is significant in the case of **[Ir-Py]**$^{+}$. The LUMO and LUMO+1 are centered on the 4′-Py-tpy ligand in all three complexes.

The TD-DFT results (summarized in Figures 3.18, 3.19 and Tables 3.3, 3.4 and 3.5 of the Experimental Section) show that in all of the complexes, the lowest energy transitions correspond to a metal-ligand to ligand charge transfer (MLLCT) as it corresponds to a transition from an orbital centered on the Ir-tppy-OMe fragment to an orbital centered on the 4′-Py-tpy ligand (Figure 3.4). In the case of **[Ir-Py-Me]**$^{2+}$ and **[Ir-Py-H]**$^{2+}$, the main contribution (above 90%) corresponds to the HOMO → LUMO transition whereas it corresponds to the HOMO-1 → LUMO for **[Ir-Py]**$^{+}$ which is in agreement with the inversion between HOMO and HOMO-1 discussed above.

To summarize, theoretical investigation shows us that upon protonation or methylation, the electronic structure of **[Ir-Py]**$^{+}$ is equally affected by the stabilization of the LUMO level leading to a red-shift of the absorption band. In all of the cases, the lowest energy transition corresponds to a MLLCT transition from the Ir-tppy-OMe fragment towards the 4′-Py-tpy ligand.

Table 3.2 – Representation of the molecular orbitals from HOMO-1 through LUMO+1 for **[Ir-Py]**$^{+}$, **[Ir-Py-H]**$^{2+}$ and **[Ir-Py-Me]**$^{2+}$.

[Ir-Py]$^{+}$	**[Ir-Py-H]**$^{2+}$	**[Ir-Py-Me]**$^{2+}$
LUMO+1 (-2.5eV)	LUMO+1 (-2.7eV)	LUMO+1 (-2.68eV)
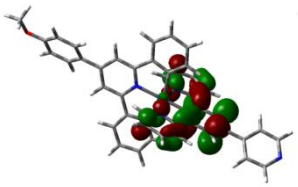	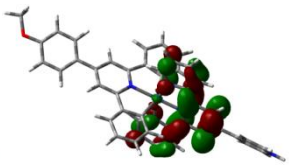	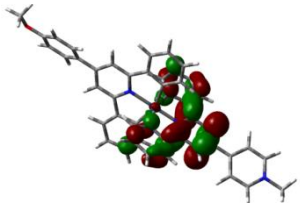
LUMO (-2.63eV)	LUMO (-3.33eV)	LUMO (-3.27 eV)
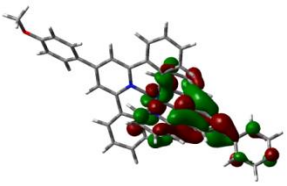	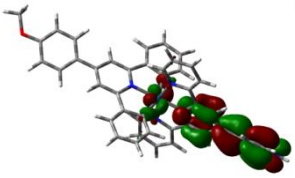	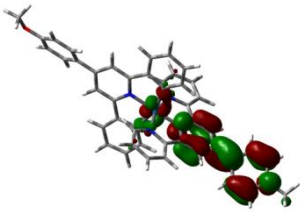
HOMO (-5.78eV)	HOMO (-5.9eV)	HOMO (-5.89eV)
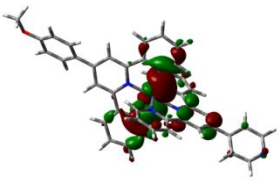	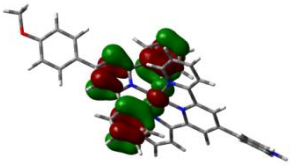	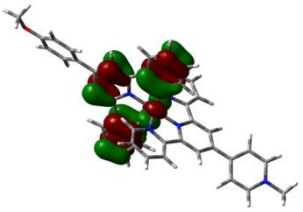
HOMO-1 (-5.79eV)	HOMO-1 (-5.94eV)	HOMO-1 (-5.93eV)
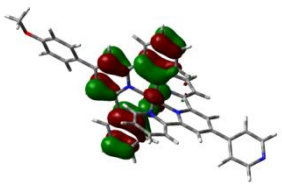	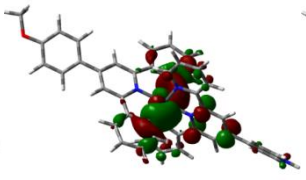	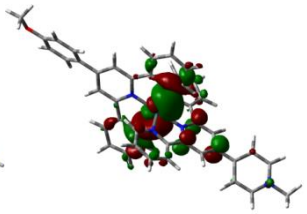

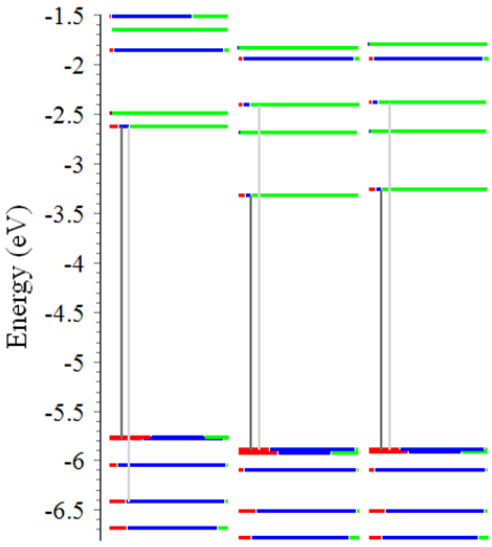

Figure 3.4 – Energy diagram for **[Ir-Py]**$^{+}$ (left), **[Ir-Py-H]**$^{2+}$ (middle) and **[Ir-Py-Me]**$^{2+}$ (right). The contribution of **Ir** (red), **MeO-tppy** (blue) and **4′-Py-tpy** (green) are presented for each orbital. The dark and light grey bands represent the transition involved in the lowest energy absorption (see Experimental Section for numerical values).

3.3.3 Acid-base titration studies

In order to examine experimentally in this case the effect on the spectroscopic charge-transfer transitions, acid-base titration experiments were performed. Indeed, if MLLCT transitions are predominant, the corresponding absorption and emission energy should be greatly affected by protonation. In the present case, a MLLCT process should correspond to a charge transfer from the electron rich ligand (4′-MeO-tppy)/Ir fragment to the electron poor ligand (4′-Py-tpy or 4′-Me-Py-tpy). Therefore, depending on the acid strength and concentration (with MeCN as solvent), either the electron poor ligand (4′-Py-tpy) or both the electron rich and electron poor ligands can be

protonated. This should dramatically alter the energy of the CT transition. Titration experiments were thus carried out in MeCN with two acids that have different pKa values, acetic acid (pKa = 23.51)[149] and trifluoroacetic acid (TFA) (pKa = 12.65).[150]

3.3.4 Spectroscopic behaviour upon addition of acetic acid

Modifications of absorption and emission bands are shown in Figure 3.5 for **[Ir-Py]**$^+$ upon addition of acetic acid in MeCN. For **[Ir-Py-Me]**$^{2+}$ (Figure 3.6) in the same conditions, no change is observed, due to the fact that acetic acid is not a strong enough acid to protonate the methoxy group. For [**Ir-Py]**$^+$ there is a clear bathochromic shift of the visible band upon addition of acetic acid. The presence of isosbestic points (387 nm, 455 nm) indicates at least the existence of two species in equilibrium. No shift is noticed for the higher energy absorption bands (283 nm and 324 nm) but the absorbance slightly decreases. The emission of **[Ir-Py]**$^+$ dramatically decreases with the addition of acetic acid. These absorption and emission modifications are due to the gradual protonation of the pyridine substituent of **[Ir-Py]**$^+$, which once protonated, becomes a better acceptor in the CT transition with a concomittant decrease in the LUMO energy.

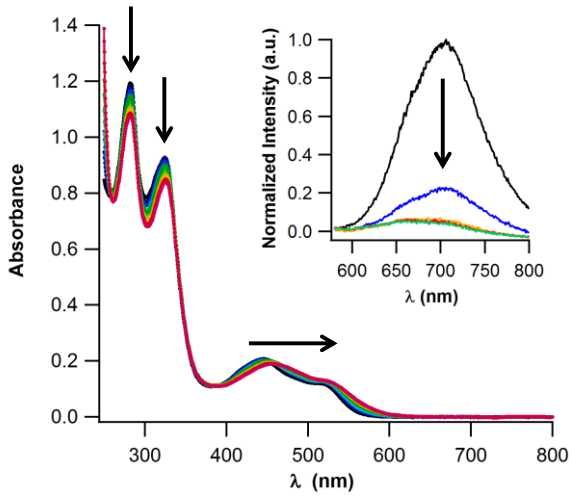

Figure 3.5 – Absorption and emission (inset) spectral changes for a 2.2 x 10^{-5} M solution of **[Ir-Py]**$^{+}$ in MeCN for increasing concentrations of acetic acid (0.5 M, 0.9 M, 1.4 M, 1.8 M , 2.2 M, 2.6 M, 2.9 M, 3.3 M, 3.6 M).

This is of course compatible with a MLLCT transition. No further change by supplementary addition of acetic acid can be observed with the exception of a slight solvatochromic effects caused by a too large amount of acid in MeCN. The effect of a stronger acid, the TFA, was then checked.

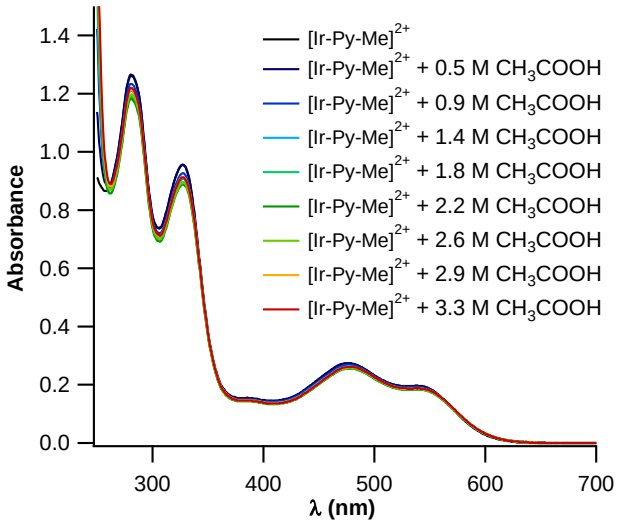

Figure 3.6 – Absorption spectral changes observed for a 3.0 x 10^{-5} M solution of **[Ir-Py-Me]$^{2+}$** in acetonitrile for increasing concentrations of acetic acid (0.5 M, 0.9 M, 1.4 M, 1.8 M , 2.2 M, 2.6 M, 2.9 M, 3.3 M, 3.6 M).

3.3.5 Spectroscopic behaviour upon addition of TFA at low concentrations

In the presence of TFA from the 100 mM range to higher concentrations *i.e.* when the pyridine moiety is completely protonated, the absorption spectra of both **[Ir-Py]$^{+}$** and **[Ir-Py-Me]$^{2+}$** are affected, however, the changes depend on the acid concentration (Figures 3.7 and 3.10). The addition of low concentrations of TFA (mM range) induces similar changes as those observed with acetic acid in absorption (with the same isosbestic points) and emission of **[Ir-Py]$^{+}$** (Figures 3.5 and 3.7). Moreover, as in the case of acetic acid, these low TFA concentrations have no effect on the absorption of **[Ir-Py-Me]$^{2+}$** (Figure 3.8). The effect of a stronger acid in mM concentration is thus the same as with the acetic acid; the absorption spectrum of the protonated **[Ir-Py]$^{+}$** is quite similar to that of **[Ir-Py-Me]$^{2+}$**

in MeCN (Figure 3.9) in agreement with the computational results (Figure 3.4). As mentioned above for **[Ir-Py-Me]$^{2+}$**, the absence of emission of protonated **[Ir-Py]$^{+}$** could also be attributed to important radiationless deactivations.[151,152] In this case, it could be due to stronger interactions with the solvent molecules when the complex is protonated as compared to not protonated. Moreover, the protonated **[Ir-Py]$^{+}$** presents an emission at 77 K similar to that of **[Ir-Py-Me]$^{2+}$** (inset of Figure 3.3). From the absorption and emission changes of **[Ir-Py]$^{+}$** with the TFA addition in low concentrations, an association constant K_{a1} between TFA (Figure 3.7, insets) and the complex (reaction 1) could be determined by the Benesi-Hildebrand method[153] (equation 1):

$$\textbf{[Ir-Py]}^{+} + CF_3COOH \underset{}{\overset{K_{a1}}{\rightleftharpoons}} \textbf{[Ir-Py-H]}^{2+} + CF_3COO^{-} \quad \text{(reaction 1)}$$

$$\frac{1}{A\text{-}A_0} = \frac{1}{K_{a1}[CF_3COOH]\Delta\varepsilon\textbf{[Ir-Py]}^{+}} + \frac{1}{\Delta\varepsilon\textbf{[Ir-Py]}^{+}} \quad \text{(equation 1)}$$

where A_0 is the absorbance of the **[Ir-Py]$^{+}$** without acid, A is the absorbance at different TFA concentrations at 525 nm, K_{a1} is the association constant, and $\Delta\varepsilon$**[Ir-Py]$^{+}$** is the difference between the molar extinction coefficient of **[Ir-Py]$^{+}$** and its associated form with TFA. The adjustment to a linear plot obtained by the Benesi-Hildebrand relation (Figure 3.7, insets) is in agreement with a 1:1 binding stoichiometry (reaction 1). The corresponding values of K_{a1} calculated from the absorption and emission data are 1400 ± 200 M^{-1} and 1530 ± 75 M^{-1}, respectively. These similar values indicate that the red-shift of the absorption and loss of emission correspond to the appearance of the red-absorbing and non-luminescent protonated **[Ir-Py]$^{+}$** form, *i.e.* **[Ir-Py-H]$^{2+}$**.

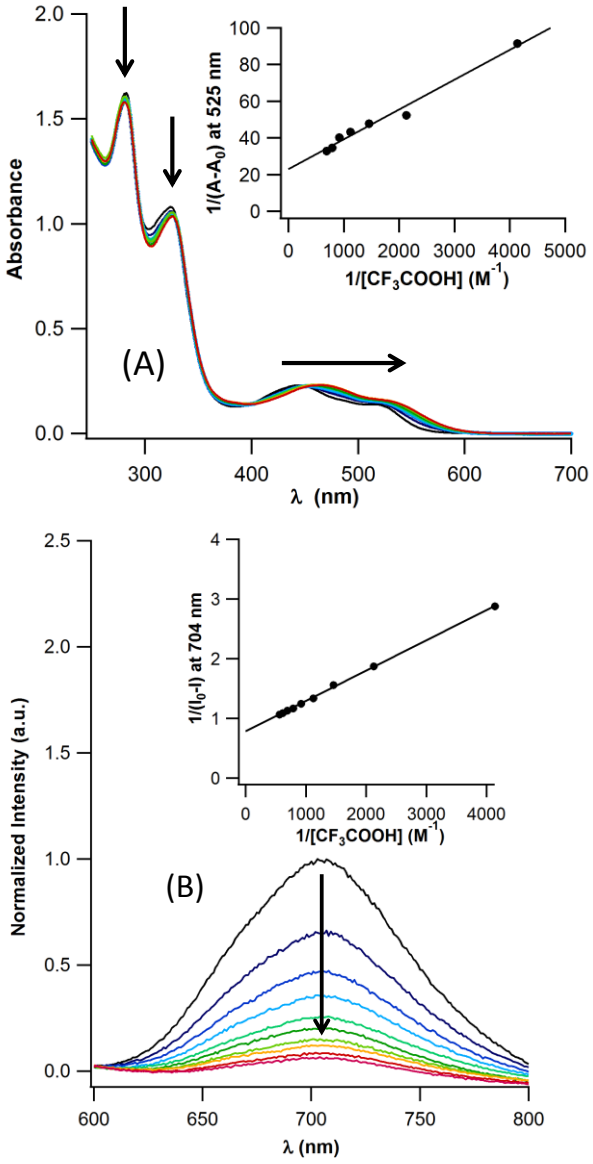

Figure 3.7 – Absorption (A) and emission (B) changes for a 2.6 x 10^{-5} M solution of **[Ir-Py]**$^{+}$ in MeCN for low increasing concentrations of trifluoroacetic acid (0.24 mM, 0.47 mM, 0.69 mM, 0.89 mM , 1.09 mM, 1.27 mM, 1.45 mM, 1.62 mM). Inset: Corresponding Benesi-Hildebrand plot with CF_3COOH when monitoring absorbance changes at 525 nm (A) and emission changes at 704 nm (B).

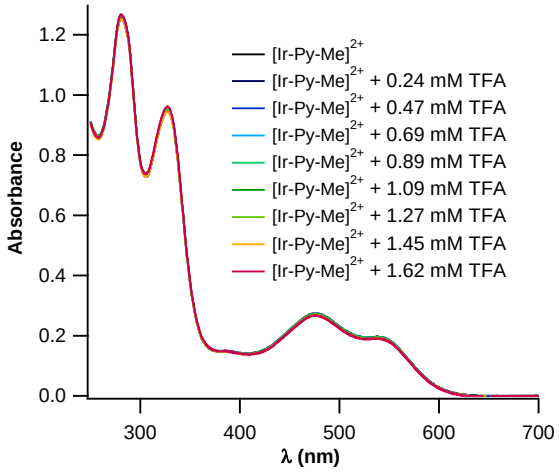

Figure 3.8 – Absorption spectral changes observed for a 3.0 x 10^{-5} M solution of **[Ir-Py-Me]$^{2+}$** in acetonitrile for low increasing concentrations of trifluoroacetic acid (0.24 mM, 0.47 mM, 0.69 mM, 0.89 mM , 1.09 mM, 1.27 mM, 1.45 mM, 1.62 mM).

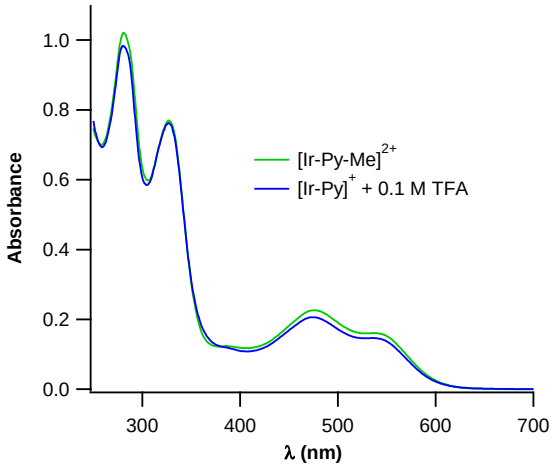

Figure 3.9 – Absorption spectra of **[Ir-Py-Me]$^{2+}$** (green) and **[Ir-Py]$^{+}$** in the presence of 0.1 M in TFA (blue) in acetonitrile.

3.3.6 Spectroscopic behaviour upon addition of TFA at higher concentrations

When higher concentrations of TFA (in the 0.1 M range) are used, both absorption spectra, *i.e.* that of **[Ir-Py]**$^{+}$ and **[Ir-Py-Me]**$^{2+}$ (Figure 3.10), are modified with the addition of TFA.

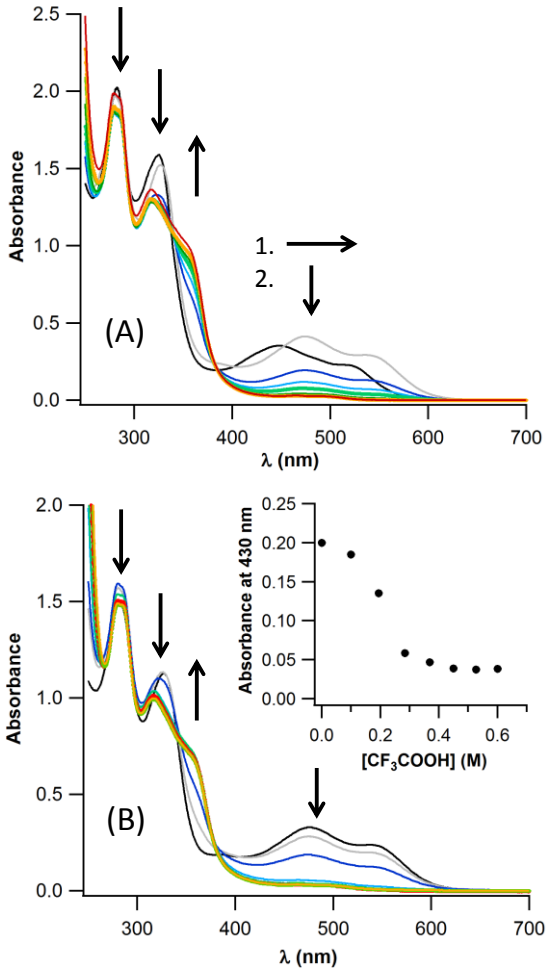

Figure 3.10 – Absorption changes for a 2.6 x 10^{-5} M solution of **[Ir-Py]**$^{+}$ (A) and a 3.6 x 10^{-5} M solution of **[Ir-Py-Me]**$^{2+}$ (B) in MeCN with high increasing concentrations of TFA (0.10 M, 0.19 M, 0.28 M, 0.37 M, 0.45 M, 0.53 M, 0.60 M) . Inset for 3.10 B: titration curve by monitoring the absorbance at 430 nm.

Thus, there is not only the 30 nm red-shift of the visible band of **[Ir-Py]**$^{+}$, but also an important hypochromic effect on the lowest energy band for both complexes, even a total disappearance of this band for higher TFA concentrations with a new band appearing at 360 nm (Figure 3.10 A and 3.10 B). The similar spectral modification of both complexes can be attributed to protonation of the common fragment in their structures, *i.e.* the 4′-MeO-tppy. At such high proton concentrations, the MeO group of the ligand 4′-MeO-tppy can indeed be protonated. We have checked by ^{1}H NMR analysis that for these high TFA concentrations, the complex does not decompose. By plotting the absorbance change of **[Ir-Py-Me]**$^{2+}$ at 430 nm as a function of increasing TFA concentrations (Figure 3.10 B, inset), it is estimated that approximately 0.3 M in TFA is required to transform **[Ir-Py-Me]**$^{2+}$ in its almost fully protonated form **[Ir-Py-H-Me]**$^{3+}$.

Replacing MeCN by water does not lead to the complete disappearance of the visible band as found for MeCN (Figure 3.11). This is probably due to the fact that H_3O^+ is not strong enough to protonate the **[Ir-Py-Me]**$^{2+}$.

In the case of **[Ir-Py]**$^{+}$ in MeCN, in the high TFA concentration range when the methoxy group is protonated, the presence of a mixture of the two different protonated forms of the complex in equilibrium (causing a mixture of bathochromic shift and hypochromic effect) prevents the determination of a consistent second association constant K_{a2} according to reaction 2.

$$\textbf{[Ir-Py-H]}^{+} + CF_3COOH \overset{K_{a2}}{\rightleftharpoons} \textbf{[Ir-Py-H}_\textbf{2}\textbf{]}^{2+} + CF_3COO^{-} \quad \text{(reaction 2)}$$

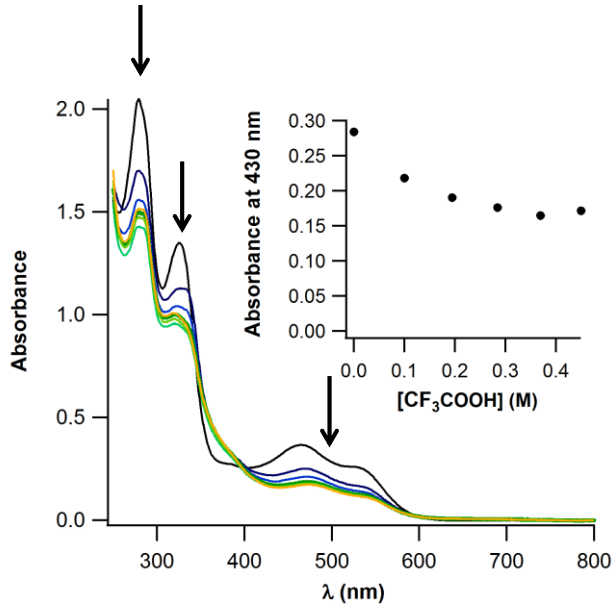

Figure 3.11 – Absorption spectral changes observed for a 3.0 x 10^{-5} M solution of **[Ir-Py-Me]**$^{2+}$ in H_2O for increasing concentrations of TFA (0.10 M, 0.19 M, 0.28 M, 0.37 M , 0.46 M).

In conclusion, these titration results clearly show that protonation of the methoxy group of both complexes, **[Ir-Py]**$^{+}$ (already in its first protonated form) and **[Ir-Py-Me]**$^{2+}$, can be correlated with a disappearance of their absorption band in the visible. These results are also compatible with MLLCT transitions.

3.4 Discussion and conclusions

The electrochemical data for **[Ir-Py]**$^{+}$ and **[Ir-Py-Me]**$^{2+}$ are in full agreement with the computational results which indicate that the lowest transitions correspond to MLLCT. Moreover the effect of protonation observed on the absorption and emission behaviour of the two complexes corroborates also the theoratical data. The LUMO of **[Ir-Py]**$^{+}$ is centered on its 4′-Py-tpy ligand, whereas the closely spaced HOMO and HOMO-1 are

centered on its Ir-tppy-MeO fragment, the HOMO-to-LUMO or HOMO-1-to-LUMO transition corresponds thus to a CT from the iridium-ligand fragment (Ir-tppy-MeO) to the tpy motif (MLLCT). Based on this scheme, the first protonation of **[Ir-Py]$^+$** on the pyridine substituent stabilizes the LUMO level and this stabilization is similar to the one due to the 4′-Py-tpy methylation in **[Ir-Py-Me]$^{2+}$** (Figure 3.12). Therefore, the absorption band of mono-protonated **[Ir-Py]$^+$**, shifted to the red of the absorption band of the non-protonated **[Ir-Py]$^+$**, becomes quite similar to that of **[Ir-Py-Me]$^{2+}$** (Figure 3.9). After the second protonation of **[Ir-Py]$^+$**, or first protonation of **[Ir-Py-Me]$^{2+}$**, on the methoxy group of both complexes, the corresponding HOMO levels are stabilized (Figure 3.12), resulting in a hypsochromic shift of the lowest energy absorption of both complexes and the disappearance of the MLLCT band close to the energy of the LL absorption bands (Figures 3.10 and 3.12). The results of this work show also that the HOMO of the two Ir complexes are not purely Ir centred as is the case, for example, for MLCT transitions in Ru(II) complexes, but it is characteristic of the whole fragment (Ir-tppy-MeO) and could thus be termed MLLCT (Metal-Ligand fragment to Ligand Charge Transfer) as referenced by Williams *et al.* for other cyclometalated bis-terdentate Ir(III) complexes.[154,155] The energy level of this HOMO is very much sensitive to the substituent since as shown in this case when the methoxyphenyl group is protonated, the MLLCT transition becomes much more energetic and overlaps LL transitions. The attribution of MLLCT to the lowest energy absorption and emission (at 298 K and 77 K) for **[Ir-Py]$^+$**, protonated **[Ir-Py]$^+$**, and **[Ir-Py-Me]$^{2+}$** in MeCN is also in perfect agreement with the conclusions from theoretical calculations reported by Scandola *et al.* for other cyclometalated Ir(III) complexes.[101]

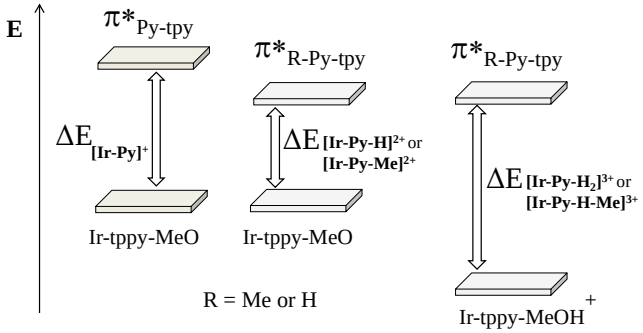

Figure 3.12 – Schematic diagram: energy levels for **[Ir-Py]$^{+}$**), its protonated (or methylated) form **[Ir-Py-H]$^{2+}$** (or **[Ir-Py-Me]$^{2+}$**) and the protonated **[Ir-Py-Me]$^{2+}$**; representation of the associated transition energies ($\Delta E_{\mathbf{[Ir\text{-}Py]}^{+}}$, $\Delta E_{\mathbf{[Ir\text{-}Py\text{-}H]}^{2+}}$($\sim\Delta E_{\mathbf{[Ir\text{-}Py\text{-}Me]}^{2+}}$) and $\Delta E_{\mathbf{[Ir\text{-}Py\text{-}H2]}^{3+}}$ ($\sim\Delta E_{\mathbf{[Ir\text{-}Py\text{-}H\text{-}Me]}^{3+}}$)).

3.5 Experimental Section

3.5.1 Synthetic procedures

4′-((4-pyridinyl)-2,2′;6′,2″ terpyridine) (4′-Py-tpy) was prepared following the previously described methods from 2-acetyl-pyridine and 4-pyridinecarboxaldehyde.[76,156] (4′-(4-methyl-pyridinio)-2,2′;6′,2″-terpyridine)([4′-Me-Py-tpy]$^{+}$) was synthetized by a selective methylation of 4′-Py-tpy as previously described.[139] 2,6-diphenyl-4-(4′-Methoxyphenyl)pyridine) (4′-MeO-tppy) was prepared by grinding two equivalents of acetophenone and NaOH in the presence of p-anisaldehyde followed by cyclization with ammonium acetate.[157] Synthetic details are given in the Chapter 10.

[Ir(4′-Py-tpy)(4′-MeO-tppy)]$^{+}$.NO_3^{-} ([Ir-Py]$^{+}$)

$(NH_4)_3IrCl_6$ (100 mg, 0.21 mmol) was added to a solution of 4′-Py-tpy (65 mg, 0.21 mmol) in DMF (3 mL). The mixture was heated at 120°C for 6h. The dark red precipitate was isolated and washed with water (2x), EtOH and $CHCl_3$.The crude [(4′-Py-tpy)-$IrCl_3$] (100 mg, 0.16 mmol), 4′-MeO-tppy (55 mg, 0.16 mmol) and $AgNO_3$ (136 mg, 0.80 mmol) was refluxed in degassed ethylene glycol (4 mL) in the dark and under Ar for 16h. On cooling, the mixture was filtered through Celite to remove AgCl. The Celite plug was washed with MeOH, which was subsequently evaporated. Water was added and the aqueous layer was extracted with $CHCl_3$ (3 times). The organic solutions were combined and evaporated to dryness. The crude product was purified by column chromatography on SiO_2 (MeCN/saturated aqueous KNO_3 (10/1)). The first eluted orange band was recovered and the solvent evaporated. The red powder was washed with water and dried under vacuum to afford **[Ir-Py]$^{+}$** (55 mg, 29 %). ^{1}H NMR (CD_3CN, 300 MHz) (Figure 3.13) : δ (ppm), 8.99 (s, 2H, $H_{3'}$ and $H_{5'}$ of tpy-C_6H_5N), 8.93 (d, 2H, H_a of tpy-C_6H_5N, J_{Ha-Hb} = 6.1 Hz), 8.66 (d, 2H, H_3 of tpy-C_6H_5N, J_{H3-H4} = 7.6 Hz), 8.27 (s, 2H, $H_{3'}$ and $H_{5'}$ of tppy-OMe), 8.11-8.07 (m, 4H, H_b of tpy-C_6H_5N and H_3 of tppy-OMe), 8.01-7.95 (m, 4H, H_b of tppy-OMe and H_4 tpy-C_6H_5N), 7.88 (d, 2H, H_6 of tpy-C_6H_5N, J_{H6-H5} = 5.8 Hz), 7.30-7.25 (m, 2H, H_5 of tpy-C_6H_5N), 7.24 (d, 2H, H_a of tppy-OMe, J_{Ha-Hb} = 8.8 Hz), 6.99 (td, 2H, H_4 of tppy-OMe, $J_{H4-H5\ (H3)}$ = 7.3 Hz, J_{H4-H6} = 1.2 Hz), 6.75 (td, 2H, H_5 of tppy-OMe, $J_{H5-H4\ (H6)}$ = 7.3 Hz, J_{H5-H3} = 1.2 Hz), 6.23 (dd, 2H, H_6 of tppy-OMe, J_{H6-H5} = 7.3 Hz, J_{H6-H4} = 0.8 Hz), 3.95 (s, 3H, OMe). HRMS (ESI): m/z calculated for $[C_{44}H_{31}N_5O_1{}^{193}Ir - NO_3]^+$, 838.2152; found: 838.2146.

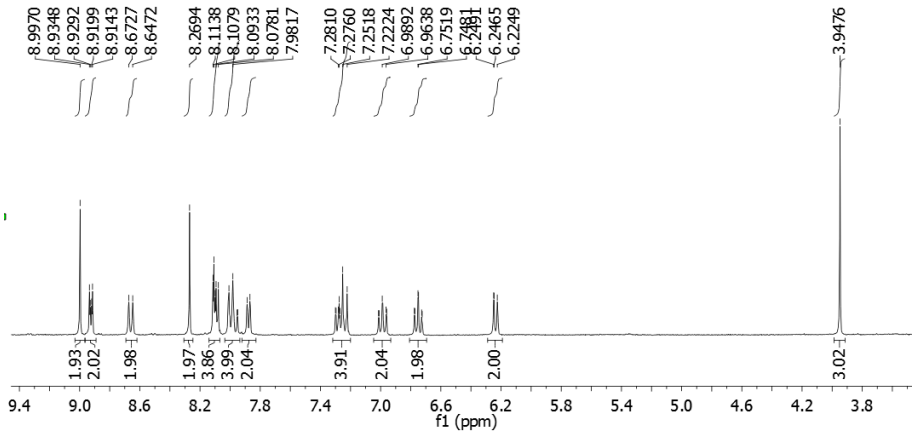

Figure 3.13 – ^{1}H NMR of **[Ir-Py]**$^+$ (300 MHz, CD_3CN).

[Ir(4′-Me-Py-tpy)IrCl$_3$](I)

[Me-Py-tpy](I) (50 mg, 0.11 mmol) and $(NH_4)_3IrCl_6$ (53 mg, 0.11 mmol) were heated at 120°C for 6h in DMF (3 mL). The dark red precipitate was isolated and washed with water (twice), MeCN and Et_2O. Yield: 34 mg (42%). ^{1}H NMR (DMSO-d_6, 300 MHz) : δ (ppm), 9.51 (s, 2H, $H_{3'}$ and $H_{5'}$), 9.34 (d, 2H, H_a, J_{Ha-Hb} = 6.7 Hz), 9.23 (dd, 2H, H6, J_{H6-H5} = 5.6 Hz, J_{H6-H4} = 1.1 Hz), 9.01 (d, 2H, H_b, J_{Hb-Ha} = 6.5 Hz), 8.98 (d, 2H, H_3, J_{H3-H4} = 7.9 Hz), 8.38 (td, 2H, H_4, $J_{H4-H3(H5)}$) = 8.0 Hz, J_{H4-H6} = 1.3 Hz), 8.03 (m, 2H, H_5), 4.45 (s, 3H, Me). MS (ESI): m/z calculated for $[C_{21}H_{17}N_4Cl_3{}^{193}Ir - I]^+$, 623.01; found: 622.92.

[Ir(4′-Me-Py-tpy)(4′-MeO-tppy]$^{2+}$.2NO$_3^-$ ([Ir-Py-Me]$^{2+}$)

This complex was prepared using the same procedure as that used for complex **([Ir-Py]$^+$)** except that [Ir(4′-Me-Py-tpy)$IrCl_3$](I) was used instead of [(Py-tpy)-$IrCl_3$]. Yield: 10 mg (25%). ^{1}H NMR (CD_3CN, 500 MHz) (Figure 3.14) : δ (ppm), 9.16 (s, 2H, $H_{3'}$ and $H_{5'}$ of tpy-C_6H_5N-Me), 8.96 (d, 2H, H_a of tpy-C_6H_5N-Me, J_{Ha-Hb} = 6.7 Hz), 8.78 (d, 2H, H_b of tpy-C_6H_5N-Me, J_{Hb-Ha} = 6.8 Hz), 8.75 (d, 2H, H_3 of tppy-OMe, J_{H3-H4} = 8.0 Hz), 8.29 (s, 2H, $H_{3'}$ and $H_{5'}$ of tppy-OMe), 8.10 (d,

2H, H_b of tppy-OMe, J_{Hb-Ha} = 8.8 Hz), 8.04-8.00 (m, 4H, H_4 and H_3 tpy-C_6H_5N-Me), 7.91 (dd, 2H, H_6 of tpy-C_6H_5N-Me, J_{H6-H5} = 5.8 Hz, J_{H6-H4} = 1.1 Hz), 7.31 (ddd, 2H, H_5 of tpy-C_6H_5N-Me, J_{H5-H4} = 7.3 Hz, J_{H5-H6} = 5.8 Hz, J_{H5-H3} = 1.3 Hz), 7.24 (d, 2H, H_a of tppy-OMe, J_{Ha-Hb} = 8.8 Hz), 6.99 (td, 2H, H_4 of tppy-OMe, $J_{H4-H5\ (H3)}$ = 7.3 Hz, J_{H4-H6} = 1.1 Hz), 6.75 (td, 2H, H_5 of tppy-OMe, $J_{H5-H4\ (H6)}$ = 7.3 Hz, J_{H5-H3} = 1.1 Hz), 6.21 (dd, 2H, H_6 of tppy-OMe, J_{H6-H5} = 7.3 Hz, J_{H6-H4} = 0.8 Hz), 4.44 (s, 3H, Me) 3.95 (s, 3H, OMe). HRMS (ESI): m/z calculated for $[C_{45}H_{34}N_5O_4{}^{193}Ir - NO_3]^+$, 915.2265; found: 915.2273, m/z calculated for $[C_{45}H_{34}N_5O^{193}Ir - 2\ NO_3]^{2+}$, 426.6191; found: 426.6192 .

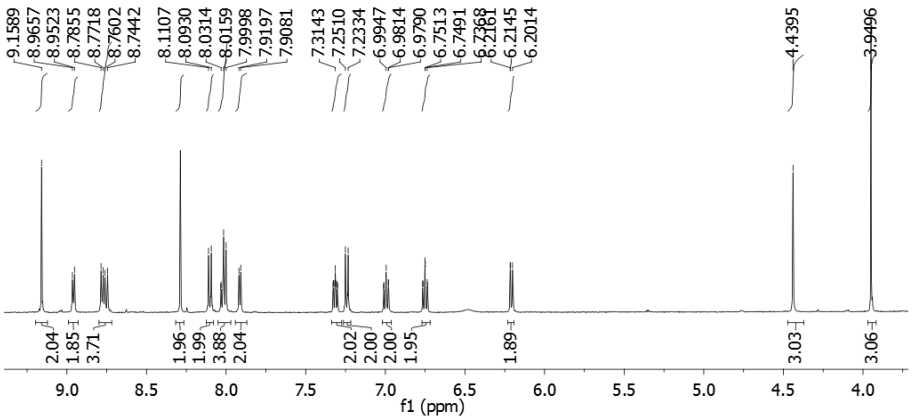

Figure 3.14 – ^{1}H NMR of **[Ir-Py-Me]$^{2+}$** (500 MHz, CD_3CN).

3.5.2 Materials and methods

^{1}H NMR (300 and 500 MHz) experiments were performed in CD_3CN on a Bruker AC-300 Avance II (300 MHz) or on a Bruker AM-500 (500 MHz). The chemical shifts (given in ppm) were measured versus the residual peak of solvent as internal standard. HRMS were recorded on a Q-Extractive orbitrap from ThermoFisher. The samples were ionized by ESI (capillary temperature: 250 °C, vaporizer temperature: 250 °C, sheath gas flow rate: 20). UV-vis absorption spectra were

recorded on a Shimadzu UV-1700. Room temperature fluorescence spectra were recorded on Varian Cary Eclipse. Complexes were excited at 520 nm. Luminescence lifetimes were measured with a modified Applied Photophysics laser kinetic spectrometer by exciting the samples at 355 nm with a Nd-YAG pulsed laser (Continuum NY 61-10). Emitted light as a function of time was detected with a R-928 Hamamatsu photomultiplier tube the ouput of which was applied to a digital oscilloscope (Hewlett-Packard HP 54200A) interfaced with a Dell Dimension DE051 computer. The signals were averaged over at least 16 shots and corrected for baseline. Igor 6.1 software was used for the decay analysis. Cyclic voltammetry was carried out in a one-compartment cell, using a glassy carbon disk working electrode (approximate area = 0.03 cm^2), a platinum wire as counter electrode and an Ag/AgCl electrode as reference. The potential of the working electrode was controlled by an Autolab PGSTAT 100 potentiostat through a PC interface. The cyclic voltammograms were recorded with a sweep rate of 100 or 400 mV s^{-1} in dried acetonitrile (Acros, HPLC grade). Tetrabutylammonium perchlorate (0.1 M) was used as supporting electrolyte and the samples were purged by argon before each measurement. DFT calculations were performed using Gaussian 09.[158] The B3LYP method[142-144] was used to carry the DFT[159,160,161] and TD-DFT[162-164] calculations. The 6-31G* basis set[145] was used for C, H, and N, and the VDZ (valence double ζ) with the SBKJC effective core potential basis set[146-148] was used for Ir. Geometry optimizations were conducted without symmetry constraints. Frequency calculations on each optimized structure confirmed that energy minima had been reached in all cases The energy, oscillator strength, and related MO contributions for the 100 lowest singlet–singlet and 10 lowest singlet–triplet excitations were obtained from the TD-DFT/singlets and the TD-DFT/triplets output files, respectively, for the S_0-optimized

geometry. GaussView3.0.9,[165] GaussSum 3.0[166] and Chemissian 4.33[167] software were used for data analysis, visualization and surface plots. All calculations were performed with MeCN as solvent solution by use of the polarized continuum (PCM) solvation model as implemented in Gaussian 09.[168,169]

3.5.3 Electrochemistry

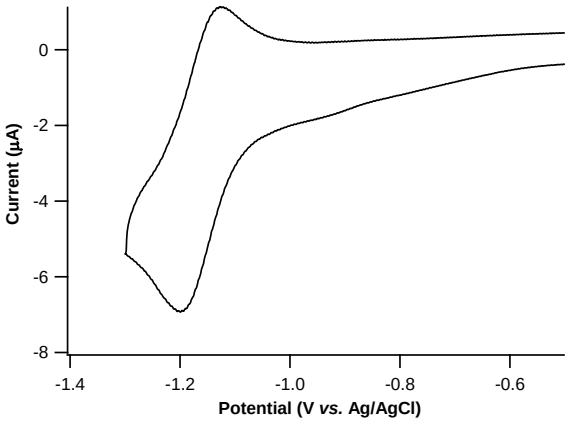

Figure 3.15 – Reduction voltammogram of **[Ir-Py]**$^{+}$ (0.1 V/s).

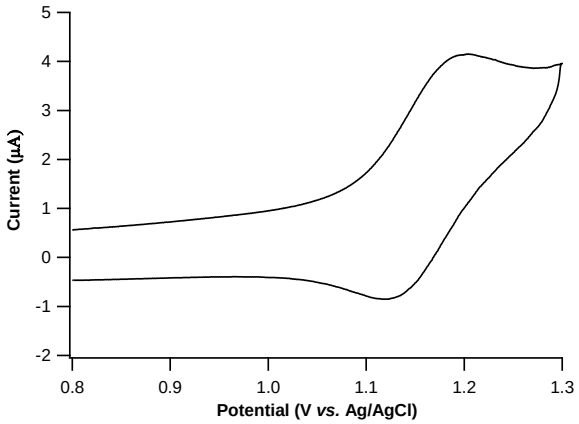

Figure 3.16 – Oxidation voltammogram of **[Ir-Py]**$^{+}$ (0.1 V/s).

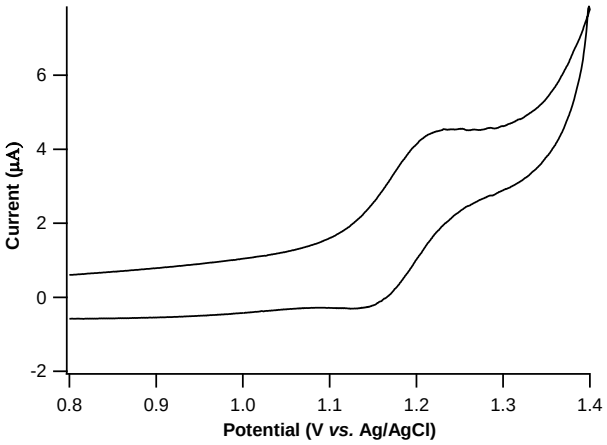

Figure 3.17 – Oxidation voltammogram of **[Ir-Py-Me]**$^{2+}$ (0.1 V/s).

3.5.4 Computational data

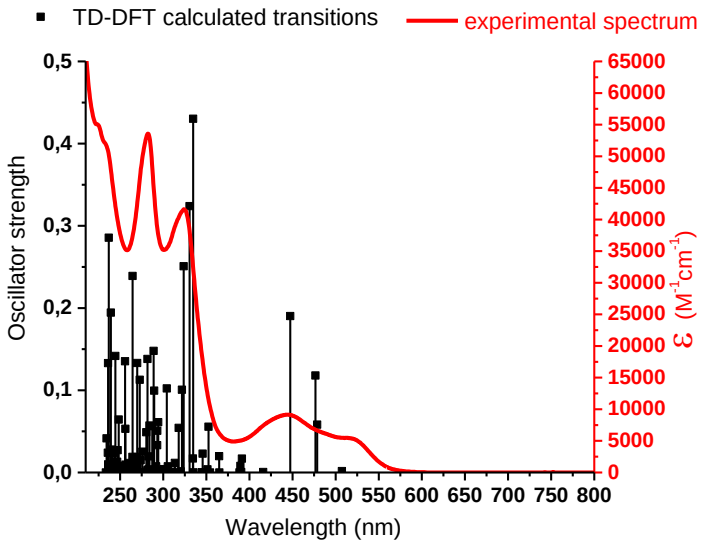

Figure 3.18 – Experimental spectra and calculated transitions for **[Ir-Py]**$^{+}$ in MeCN.

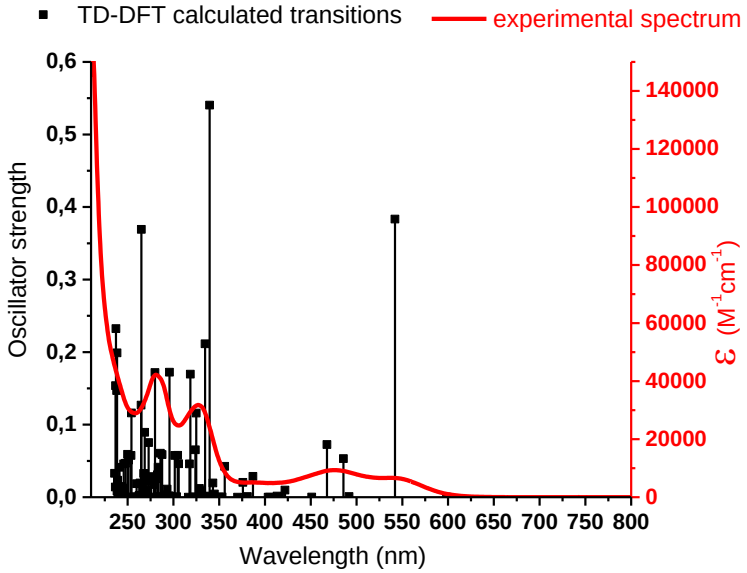

Figure 3.19 – Experimental and calculated transitions for **[Ir-Py-Me]**$^{2+}$ in MeCN.

Table 3.3 – Representation of the orbitals LUMO+4 through to HOMO-4 with the contributions of the different fragments of **[Ir-Py]**$^{+}$.

Orbital (energy)	Groups contribution
LUMO+4 (-1.52eV) 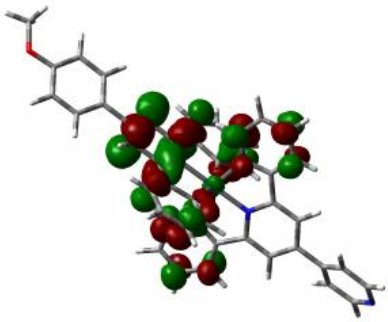	Ir : 2% MeOtppy : 68% Pytpy : 30%
LUMO+3 (-1.66eV) 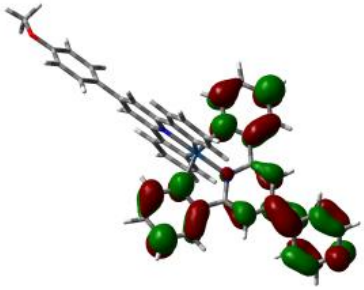	Ir : 0% MeOtppy : 1% Pytpy : 99%
LUMO+2 (-1.87eV) 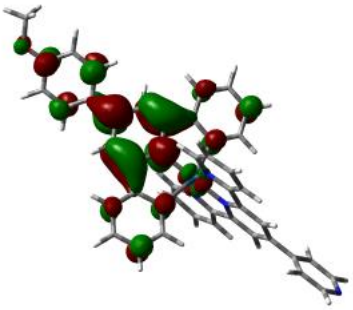	Ir : 3% MeOtppy : 96% Pytpy : 1%

Orbital (energy)	Groups contribution
LUMO+1 (-2.5eV) 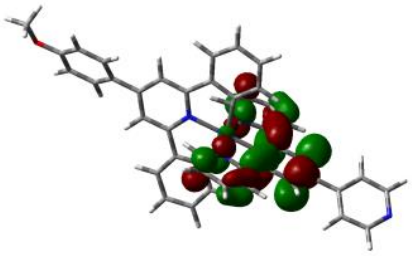	Ir : 2% MeOtppy : 0% Pytpy : 98%
LUMO (-2.63eV) 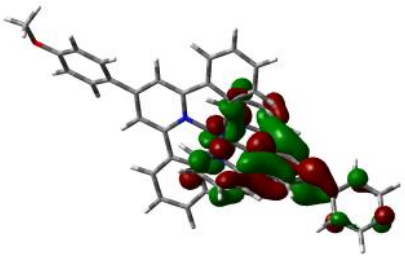	Ir : 8% MeOtppy : 7% Pytpy : 85%
HOMO (-5.78eV) 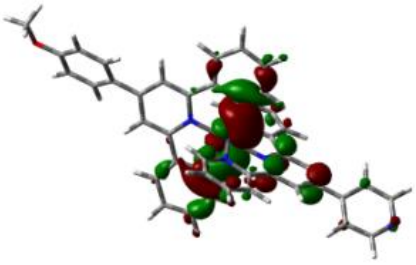	Ir :32% MeOtppy : 44% Pytpy : 24%

Orbital (energy)	Groups contribution
HOMO-1 (-5.79eV) 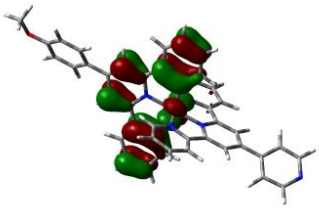	Ir : 22% MeOtppy : 74% Pytpy : 4%
HOMO-2 (-6.06eV) 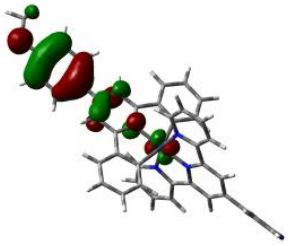	Ir : 6% MeOtppy : 93% Pytpy : 1%
HOMO-3 (-6.43eV) 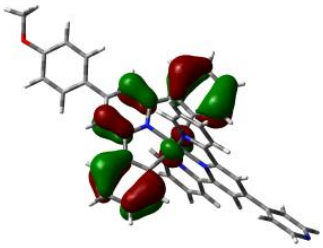	Ir : 10% MeOtppy : 87% Pytpy : 3%
HOMO-4 (-6.69eV) 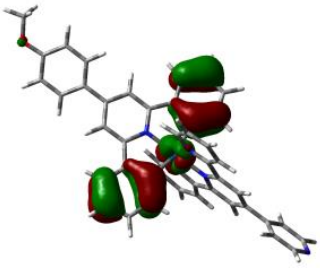	Ir : 11% MeOtppy : 85% Pytpy : 4%

Table 3.4 – Representation of the orbitals LUMO+4 through to HOMO-4 with the contributions of the different fragments of **[Ir-Py-H]**$^{2+}$.

Orbital (energy)	Groups contribution
LUMO+4 (-1.84 eV) 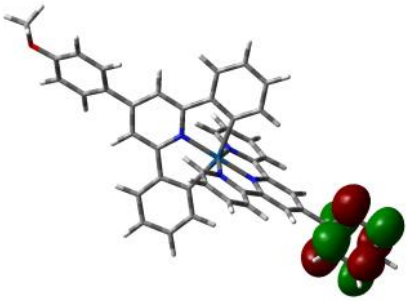	Ir : 0% MeOtppy : 0% Pytpy : 100%
LUMO+3 (-1.95 eV) 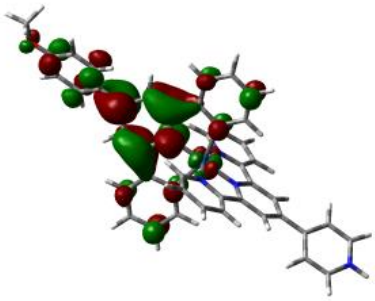	Ir : 3% MeOtppy : 96% Pytpy : 1%
LUMO+2 (-2.42 eV) 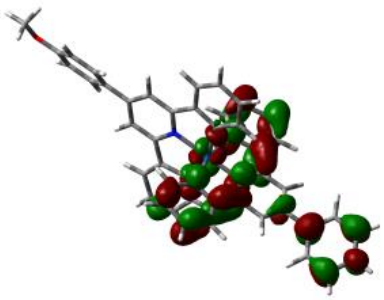	Ir : 4% MeOtppy : 4% Pytpy : 92%

Orbital (energy)	Groups contribution
LUMO+1 (-2.7 eV) 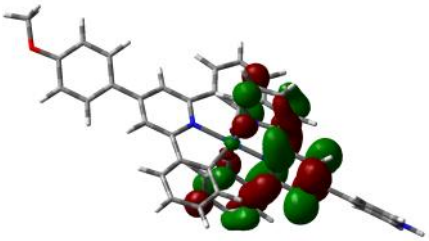	Ir : 2% MeOtppy : 0% Pytpy : 98%
LUMO (-3.33 eV) 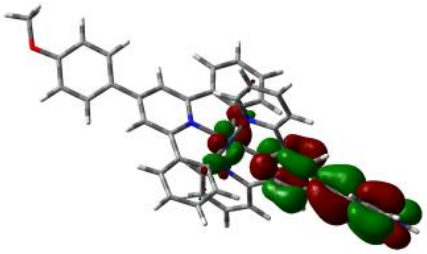	Ir : 6% MeOtppy : 4% Pytpy : 90%
HOMO (-5.90 eV) 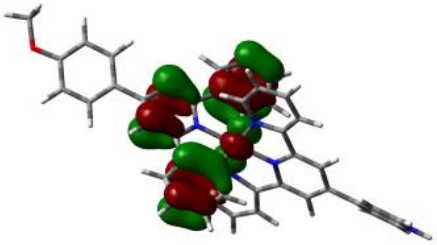	Ir :20% MeOtppy : 77% Pytpy : 3%

Orbital (energy)	Groups contribution
HOMO-1 (-5.94 eV)	
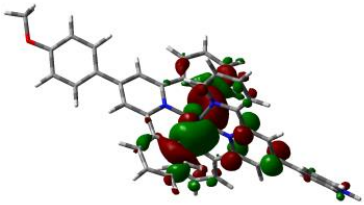	Ir : 30% MeOtppy : 45% Pytpy : 25%
HOMO-2 (-6.11 eV)	
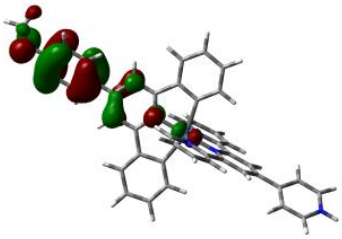	Ir : 4% MeOtppy : 95% Pytpy : 1%
HOMO-3 (-6.52 eV)	
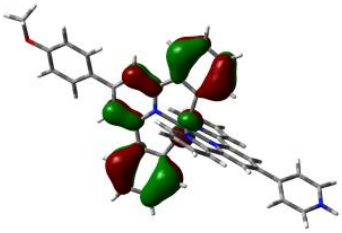	Ir : 11% MeOtppy : 87% Pytpy : 2%
HOMO-4 (-6.79 eV)	
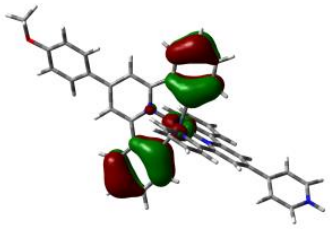	Ir : 8% MeOtppy : 89% Pytpy : 3%

Table 3.5 – Representation of the orbitals LUMO+4 through to HOMO-4 with the contributions of the different fragments of **[Ir-Py-Me]**$^{2+}$.

Orbital (energy)	Groups contribution
LUMO+4 (-1.81 eV) 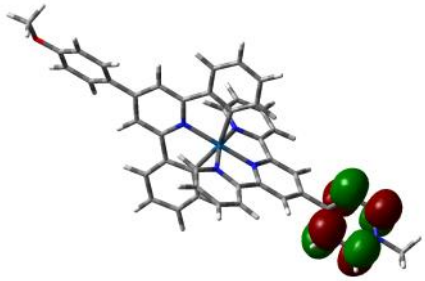	Ir : 0% MeOtppy : 0% Pytpy : 100%
LUMO+3 (-1.95 eV) 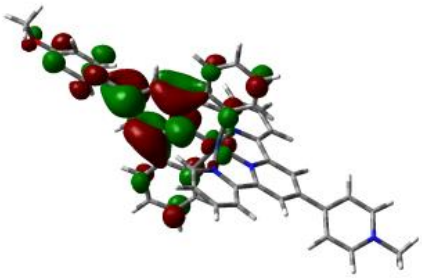	Ir : 3% MeOtppy : 96% Pytpy : 1%
LUMO+2 (-2.40 eV) 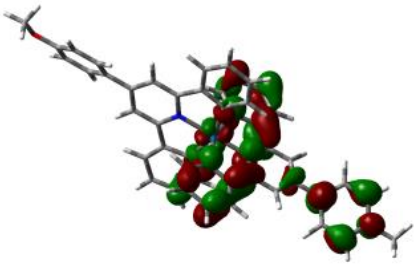	Ir : 4% MeOtppy : 4% Pytpy : 92%

Orbital (energy)	Groups contribution
LUMO+1 (-2.68 eV) 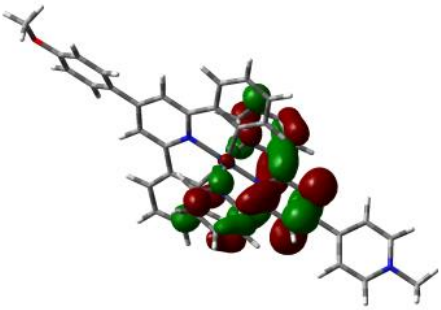	Ir : 2% MeOtppy : 0% Pytpy : 98%
LUMO (-3.27 eV) 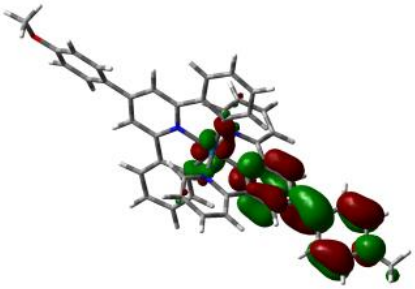	Ir : 6% MeOtppy : 4% Pytpy : 90%
HOMO (-5.89 eV) 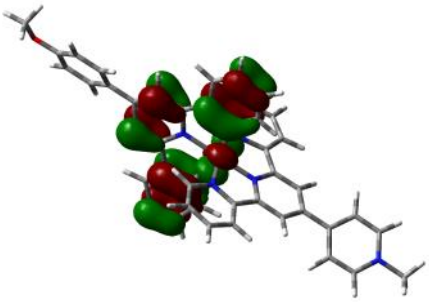	Ir :20% MeOtppy : 77% Pytpy : 3%

Orbital (energy)	Groups contribution
HOMO-1 (-5.93 eV) 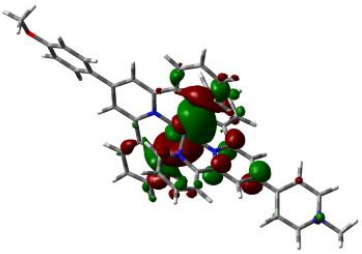	Ir : 30% MeOtppy : 45% Pytpy : 25%
HOMO-2 (-6.10 eV) 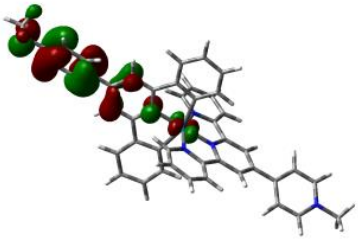	Ir : 4% MeOtppy : 95% Pytpy : 1%
HOMO-3 (-6.51eV) 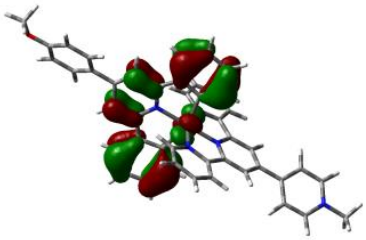	Ir : 11% MeOtppy : 87% Pytpy : 2%
HOMO-4 (-6.78 eV) 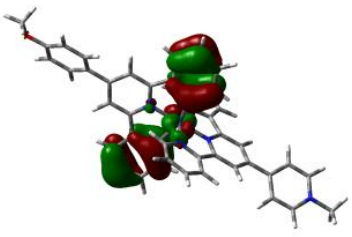	Ir : 8% MeOtppy : 89% Pytpy : 3%

Chapter 4 - Hydrogen Photo-Evolution From a Green Absorbing Ir(III)-Co(III) dyad

4.1 Foreword

In the previous section, we have demonstrated that $\mathbf{[IrN_4C_2]^+}$ complexes can be spectroscopically and electrochemically tuned upon protonation/methylation of pendant functional groups. These assumptions were supported by DFT and TD-DFT calculations. This study reveals that electronic transitions in the visible range correspond to a vectorial electron transfer from the electron-rich iridium fragment (MeO-tppy-Ir) to the electron poor 4′-Py-tpy ligand which has been termed MLLCT.

As a result, the $\mathbf{[Ir\text{-}Py]^+}$ complex can be combined with a suitable catalyst *via* the pendant pyridine to provide a supramolecular assembly able to photo-induce charge separation and therefore evolve molecular hydrogen (Figure 1.1). At this stage, we have scanned and assessed available catalysts able to reduce protons into hydrogen. Initially, platinum(II) complexes were considered to be covalently connected to $\mathbf{[Ir\text{-}Py]^+}$. This choice was dictated by the fact that these complexes are among the most efficient catalyst to carry out hydrogen photo-production experiments.[41,170,171] In addition, their covalent anchoring to photosensitizers has already been achieved recently.[42,172,173] In light of these considerations, some attempts were performed to tether platinum(II) complexes on $\mathbf{[Ir\text{-}Py]^+}$. However, the synthesis of these supramolecules turned out to be difficult despite our efforts. In addition to this synthetic issue, Pt(II) complexes remain expensive as the other noble transition metal. This is why we have turned to another emerging catalyst.

Recently, some cobalt derivatives (Figure 4.1) have drawn chemist's attention to act as an efficient and cheap catalysts for the reduction of proton into molecular hydrogen.[174-178] The advantage of these compounds arises from the cobalt-containing vitamin B_{12}, also termed cobalamin, which has been proved among the most efficient molecular electrocatalysts for H_2

evolution.[179] Accordingly, the mimic of vitamin B_{12} has led to the synthesis of cobalt bis-glyoximato complexes, also called cobaloximes (Figure 4.1).

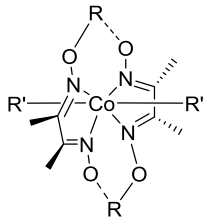

R = H or BF_2
R' = H_2O, CH_3CN, DMF

Figure 4.1 – Examples of cobalt catalysts used for hydrogen evolution.

Cobaloximes are easily prepared and efficient for hydrogen photo-evolution. Their covalent grafting has been recently achieved on a Ir(III) tris-bidentate complex (Figure 4.2).[36] To the best of our knowledge, this system is the most efficient supramolecular system based on cobaloxime complexes. However, the stability of this assembly remains relatively low although higher than that of Ru(II)-based devices.[180]

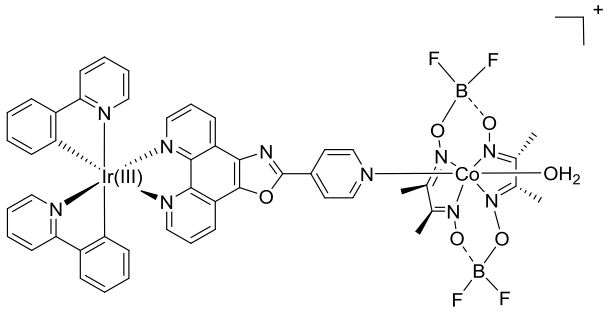

Figure 4.2 – Supramolecular iridium-cobalt dyad for hydrogen photo-production.[36]

The general mechanisms for light-driven H_2-evolution catalyzed by cobalt systems are depicted in Figure 4.3. The process starts with the absorption of a photon by the photosensitizer (PS) yielding to PS* excited

state. From this state, a reductive quenching of the PS* by the sacrificial electron donor (D) leads to the reduced PS^-, which subsequently gives an electron to the catalyst to generate the active Co^I species. Alternatively, an oxidative photoinduced electron transfer from the PS* to the cobalt complex as an electron acceptor provides the Co^I state. A second electron transfer between the sacrificial electron donor (D) and the oxidized PS^+ takes place, thus regenerating the PS. In the case of the Co^{III} catalysts, a primary photoinduced electron transfer step is required to generate the Co^{II} complex which is further reduced to the Co^I state.

The establishment of one mechanism rather than the other is not trivial and essentially depends on the redox properties of the different couples (PS^*/PS^-, PS^+/PS, Co^{III}/Co^{II}, Co^{II}/Co^I, $D^{\bullet+}/D$) together with their relative concentration.

In addition, electrons entering in the catalytic cycle may come from a dark (thermal) process (Figure 4.3) which is different from the light-induced process. Indeed, in most of these photo-catalytic experiments, the sacrificial electron donor is an amine such as the triethylamine (TEA) or the triethanolamine (TEOA). After electron transfer to the PS (either PS* or PS^+), the subsequent radical cation formed is well known to decompose in the medium.[181,182]

The electrons brought either by photo-induced or dark processes provide the Co^I species. The protonation of this intermediate implies the formation of a $cobalt^{III}$ hydride unit from which a hydrogen molecule is released. It is worthwhile to mention that this mechanism is a simplified one since it is still debated in the litterature.[28]

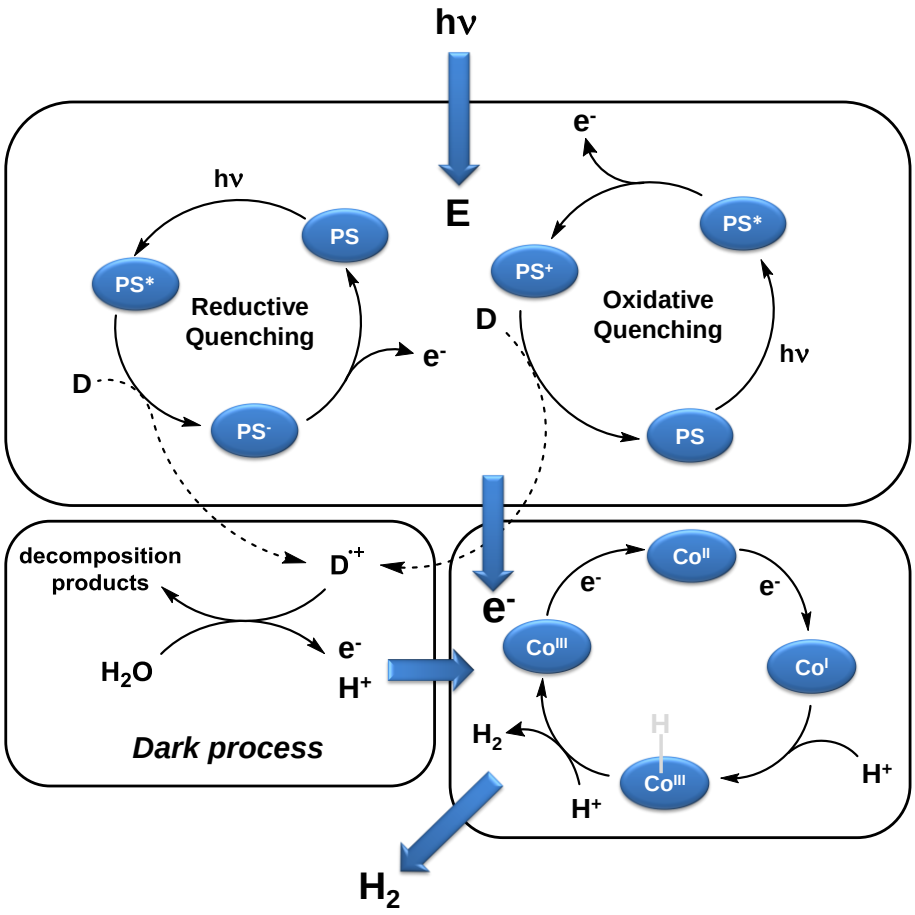

Figure 4.3 – Processes involved in light-driven H_2-evolution catalyzed by cobalt complexes (adapted from [28]).

4.2 Main topics addressed in the publication

With respect to the results highlighted in the Chapter 3, it seems reasonable to postulate that **[Ir-Py]**$^+$ can act as an efficient and (photo)stable photosensitizer (PS).

This section describes the synthesis, characterization and catalytic performance of an **[Ir-Py]**$^+$-cobaloxime supramolecular dyad for hydrogen evolution. On the one hand, the purpose of this work was to confirm that the

photophysical scheme proposed in the Chapter 3 may be extended to understand spectroscopic and electrochemical properties of the dyad. On the other hand, we wanted to evidence the photocatalytic activity of the system and optimize experimental conditions.

Numerous hydrogen photo-evolution experiments were carried out with **[Ir-Py]**$^{+}$ as charge injector and cobaloximes such as represented in Figure 4.1. However, solely the most significant ones are gathered in the publication.

Journal

Angewandte Chemie, International Edition **2015**, *to be submitted*.

Title

Hydrogen Photo-Evolution From a Green Absorbing Ir(III)-Co(III) dyad

Authors

Alexandre JACQUES,[a] Olivier SCHOTT,[b] Koen ROBEYNS,[a] Garry S. HANAN[b] and Benjamin ELIAS[a*]

Affiliations

[a] Université catholique de Louvain, Institut de la Matière Condensée et des Nanosciences, Place Louis Pasteur 1, L4.01.02, B-1348, Louvain-la-Neuve, Belgium.

[b] Département de Chimie, Pavillon J.-A. Bombardier, 5155 Chemin de la Rampe, Université de Montréal, Montréal, Québec, Canada, H3T 2B1.

4.3 Introduction

The future of a sustainable energy supply relies on profound scientific and technological breakthroughs providing efficient systems for the conversion and storage of renewable energy sources such as solar energy.[3] A photocatalytic hydrogen evolution reaction (HER) appears to be a promising solution to this issue.[183] Within a molecular approach, several components are usually required for efficient HERs: a catalyst (cat), a photosensitizer (PS), a sacrificial electron donor and a source of protons. For several years, cobalt derivatives have drawn considerable attention as efficient and inexpensive compounds[28] when compared to colloidal platinum[26,184,185] and palladium[186] catalysts. The catalyst and the PS may be either added as separate entities or as covalently linked dinuclear complexes prior to homogeneous catalysis. For instance, cobaloxime derivatives have been associated with transition metal-based photosensitizers such as platinum,[170,171] ruthenium[187-189] or rhenium[37,190-192] complexes. Recently, several Ru-Co dyads covalently connected to each other have been developed and were shown to have improved photocatalytic activity as compared to independent units.[31,36,180] In addition, Ir/Co dyads[36,193] have also been designed in order to benefit from the superiority of Ir(III) complexes in term of photophysical and electrochemical tunability.[51,194-200]

In these photosystems, the archetypical bidentate $[Ir(ppy)_2(bpy)]^+$ complexes (Figure 4.4, ppy = 2-phenylpyridine, bpy = 2-2′-bipyridine) were frequently used as photosensitizers in excess to increase the TurnOver Number (TON, *i.e.* the number of moles of substrate that a mole of catalyst can convert before becoming inactivated) of the catalytic cycle. To the best of our knowledge, supramolecular Ir/Co assemblies with terdentate ligands have not been described yet. A homoleptic $[Ir(phbpy)_2]^+$ complex (Figure 4.4, phbpy = 6-phenyl-2,2′-bipyridine) was used as a separate

photosensitizer in a bimolecular reaction in association with a palladium colloidal catalyst and shows a higher stability compared to their bidentate equivalents.[132] As opposed to $[Ir(ppy)_2(bpy)]^+$ in which the LUMO is bpy centered and the HOMO is located on the Ir/ppy fragment, $[Ir(phbpy)_2]^+$ has cyclometalating units onto each of its two ligands (Figure 4.4), hence having dramatic effect on the photophysics of the resulting complex. In addition, strongly donating ligands have also been shown to be effective in energy and electron transfer.[122-128,154,155,201-203]

In this work, the iridium bis-terdentate $[Ir(4'\text{-Py-tpy})(4'\text{-MeO-tppy})]^+$ (Figure 4.4, 4′-Py-tpy = 4′-(4-pyridinyl)-2,2′;6′,2″ terpyridine and 4′-MeO-tppy = 2,6-diphenyl-4-(4′-methoxyphenyl)pyridine) (termed hereafter **$[Ir\text{-}Py]^+$**) complex has two cyclometalling sites on the same terdentate ligand, centering the LUMO on the N^N^N tridentate ligand. The absorption of **$[Ir\text{-}Py]^+$** is red-shifted compared to $[Ir(ppy)_2(bpy)]^+$ and $[Ir(phbpy)_2]^+$, allowing a wider range of the visible light to be harvested with a significant absorptivity. In addition, the pendant pyridine moiety allows for an easy covalent tethering of a cobaloxime onto the terpyridine ligand, offering an efficient assembly for directional electron transfer required for HERs.

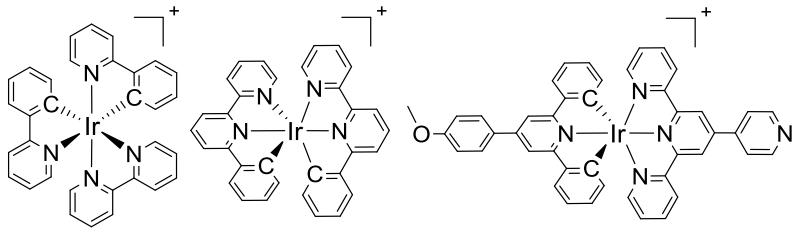

Figure 4.4 – Bis-cyclometalated Ir(III) bidentate and tridentate complexes used for HERs.

4.4 Results and discussion

4.4.1 Synthesis

The synthesis of complex **[Ir-Py-Co]**$^{+}$ was achieved by replacing a chloro ligand from **[Co(dmgH)(dmgH$_2$)Cl$_2$]**$^{+}$ (where dmgH$_2$ and dmgH are dimethylglyoxime and dimethylglyoximate, respectively) by free pyridine of the previously described **[Ir-Py]**$^{+}$ complex.[204]

*4.4.2 X-Ray structure of the **[Ir-Py-Co]**$^{+}$ complex*

Crystals suitable for X-ray crystal diffraction were obtained by slow diffusion of tetrahydrofuran into an acetonitrile solution of the compound at room temperature (Figure 4.5).

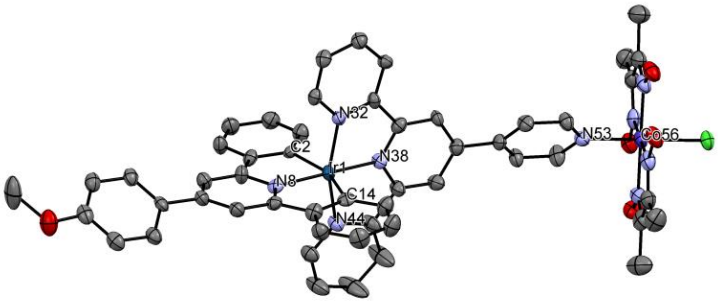

Figure 4.5 – ORTEP representation of **[Ir-Py-Co]**$^{+}$ at the 50% probability level. Hydrogen atoms, counter ions, and co-crystallised solvent molecules have been omitted for clarity.

The solid-state structure reveals that the cobalt complex coordinates to the pyridine which is twisted by 32° with respect to the terpyridine ring. For the iridium moiety, distances and angles between atoms are in agreement with data described for the similar [[(4′-(4-bromophenyl)-2:2′,6′:2″-terpyridine)Ir(2,6-diphenyl-4-(4-tolyl)pyridine)](NO$_3$)] complex.[101] As a result, the Ir-C bonds (Ir(1)-C(2) = 2.071(7) Å and Ir(1)-C(14) = 2.117(10)

Å) are longer compared to the peripheral Ir-N distances (Ir(1)-N(32) = 2.022(5) Å and Ir(1)-N(44) = 2.044(5) Å) due to a strong mutual *trans* effect between both C(2) and C(14) cyclometalated carbons. The central Ir-N distances (Ir(1)-N(8) = 1.988(15) Å and Ir(1)-N(38) = 1.921(5) Å) are shorter when compared to the peripheral Ir-C and Ir-N ones which is in agreement with distances measured for previous similar structures.[101] These shorter Ir-N distances may be explained by the mutual weaker *trans* effect between both N(8) and N(38) pyridine nitrogens. The diphenylpyridine ring and the methoxyphenyl are twisted by 35° to one another.

The six-coordinated cobalt(III) metal is chelated by two dmgHs, a chloride and the bridging pyridine. The bond distances and angles in **[Ir-Py-Co]**$^+$ (Co(56)-N(53) = 1.967(5) Å) are in agreement with those measured for $[Co(dmgH)_2PyCl]$[205], $[Co(dmgH)_2(4\text{-}CN\text{-}Py)Cl]$[206] and $[Co(dmgH)_2(4\text{-}MeO_2C\text{-}Py)Cl]$[171] (with Co-$N_{pyridine}$ distances = 1.959 Å, 1.963 Å, 1.959 Å, respectively) revealing that the structure of the dinuclear complex is not significantly affected when compared with the separate Ir(III) and Co(III) units. These data confirm the supramolecular structure of the dyad in the ground state.

4.4.3 Electrochemistry

The electrochemical data measured for **[Ir-Py-Co]**$^+$ in acetonitrile are gathered in Table 4.1. Values obtained for $[Ir(ppy)_2(bpy)](PF_6)$ and $[Ir(phbpy)_2](PF_6)$ and **[Ir-Py](PF$_6$)** are also given for comparison purposes. For the dinuclear complex, a reversible oxidation wave is observed at + 1.21 V corresponding to the oxidation of the cyclometalated iridium fragment (Ir-C^N^C). This value is slightly more positive than that found for similar **[Ir-Py]**$^+$ complex due to electron withdrawing effect of the cobalt moiety but more negative as compared to $[Ir(ppy)_2(bpy)]^+$ and $[Ir(phbpy)_2]^+$ since two

cyclometalated carbons belong to the same ligand and therefore render it more electron rich.

In the case of **[Ir-Py-Co]$^{+}$**, an irreversible one-electron-reduction wave at - 0.30 V corresponding to the reduction of Co(III) in Co(II) is observed. This value suggests that solvolysis of the Co(III)-Cl bond occurs in solution similarly to that noticed for a Ru-Co complex.[180] At more negative potential, two reversible reduction waves centered at - 0.93 V and - 1.08 V correspond to the Co(II)/(I) reduction and to the reduction of the terpyridine moiety, respectively. These values are slightly less negative than those measured for the parent complexes [Co(III)(dmgH)$_2$(py)Cl] (-0.98 V)[178] and **[Ir-Py]$^{+}$** (-1.16 V) due to the electron withdrawing nature of the metal centers in the assembly as compared to the separate complexes.

Table 4.1 – Electrochemical data[a] of [Ir(ppy)$_2$(bpy)]$^{+}$, [Ir(phbpy)$_2$]$^{+}$, **[Ir-Py]$^{+}$**, **[Ir-Py-Me]$^{2+}$**, **[Ir-Py-Co]$^{+}$** and [Co(III)(dmgH)$_2$(py)Cl] in acetonitrile. (ir) = irreversible.

	[Ir(ppy)$_2$(bpy)]$^{+}$	[Ir(phbpy)$_2$]$^{+}$	[Ir-Py]$^{+}$	[Ir-Py-Me]$^{2+}$	[Ir-Py-Co]$^{+}$[b]	[Co(III)(dmgH)$_2$(py)Cl][178]
E_{ox}	+ 1.29 (84)	+ 1.31 (83)	+ 1.16 (70)	+1.19 (62)	+ 1.21 (58)	+0.15[c]
E_{red}	- 1.36 (66)	- 1.38 (66);	- 1.16 (72)	-0.71 (73); -1.14 (71)	- 0.30 (ir); - 0.93 (54); - 1.08 (50)	-0.59;[c] -0.98[c]

[a]Potentials are given in V *vs.* Ag/AgCl. [b]Electrochemical data were measured with Bu_4NClO_4 0.1 M at 100 mV/s. For reversible waves, the difference between the anodic and cathodic peak potential (mV) is given in parentheses. [c]Measured in DMF.

4.4.4 Spectroscopic properties

The absorption and emission spectra in acetonitrile are shown in Figure 4.6. The corresponding spectroscopic data are gathered in Table 4.2. For **[Ir-Py-Co]**$^+$, based on previous studies on cyclometalated Ir(III) complexes, intense absorption bands between 282-325 nm are ascribed to Ligand Centered transitions (LC).[100] Absorption bands also appear in the visible with two maxima at *ca.* 455 nm and 525 nm. These transitions correspond to MLLCT from the cyclometalated iridium fragment (Ir-C^N^C) to the terpyridine ligand. The energy of the transitions in the visible is red-shifted compared to $[Ir(ppy)_2(bpy)]^+$ and $[Ir(phbpy)_2]^+$ due to the much lower LUMO energy of the 4′-Py-tpy ligand as compared to bpy and phbpy. The lower energy absorption as compared to **[Ir-Py]**$^+$ is due to the electron-withdrawing effect of the cobalt(III) moiety which stabilizes the LUMO of the 4′-Py-tpy. The maximum emission wavelength of **[Ir-Py]**$^+$ is red-shifted to 705 nm in comparison with $[Ir(ppy)_2(bpy)]^+$ and $[Ir(phbpy)_2]^+$.

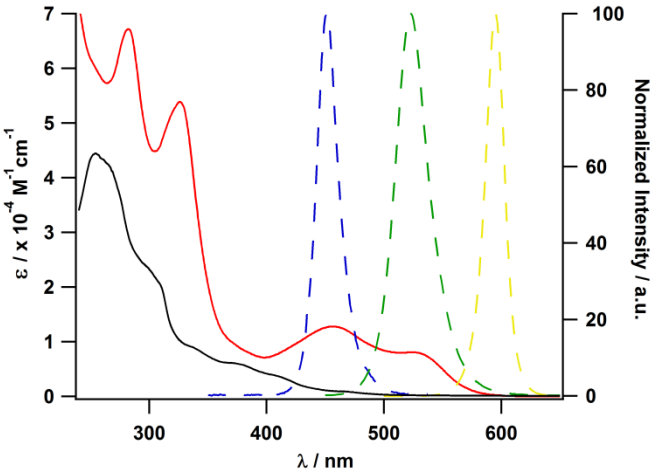

Figure 4.6 – Absorption spectra (solid lines) of **[Ir-Py-Co]**$^+$ (red) and $[Ir(ppy)_2(bpy)]^+$ (black) as well as emission spectra (dashed lines) of LEDs used as irradiation source (blue, green, yellow).

The quantum yield dramatically decreases from 3.9 % for $[Ir(phbpy)_2]^+$ and 9.3 % for $[Ir(ppy)_2(bpy)]^+$ to 0.64 % for **[Ir-Py]$^+$** whereas its excited state lifetime doubles or triples (1.05 μs) compared to the two other complexes. These observations are in agreement with the dramatic decrease in the radiative rate constant when two cyclometalated carbons are on the same ligand. Interestingly, **[Ir-Py-Co]$^+$** is not emissive at room temperature. This luminescence quenching could be due to a photo-induced electron transfer from the Ir(III) center to Co(III) unit.

Table 4.2 – Spectroscopic data of $[Ir(ppy)_2(bpy)]^+$, $[Ir(phbpy)_2]^+$, **[Ir-Py]$^+$** and [**Ir-Py-Co**]$^+$ in degassed acetonitrile at room temperature.

	$[Ir(ppy)_2(bpy)]^+$	$[Ir(phbpy)_2]^+$	**[Ir-Py]$^+$**	**[Ir-Py-Co]$^+$**
$\lambda_{max\ abs}$, nm (ε, $M^{-1}\ cm^{-1}$)	420 (2900), 375 (6000), 314 (16900), 265 (42500)	460 (1200)	514 (5500), 445 (9100), 324 (41600), 283 (53600)	527 (8100), 457 (12800), 326 (53900), 282 (67100)
$\lambda_{max\ Em}$ under air at 293 K	602	580	705	- [c]
τ (μs)	0.28	0.55	1.05	- [c]
Φ[a] (Ar)	0.093	0.039	0.006	- [c]
k_r (x 10^3 s^{-1})[b]	338.2	70.9	6.1	- [c]

[a]Quantum yield was measured under air using $[Ru(bpy)_3]^{2+}$ as reference Φ_{ref} = 0.028 in H_2O,[140] λ_{Exc} = 450 nm, 293 K. [b]Radiative rate constant under argon at 293 K ($k_r = \Phi / \tau$). [c]No emissive.

4.4.5 Hydrogen Photo-Evolution Experiments

The spectroscopic and electrochemical data suggest that **[Ir-Py-Co]$^+$** is the ideal candidate to evolve molecular hydrogen under irradiation as compared to other Ir(III) derivatives. First, photo-induced electron transfer will be directed from the cyclometalated/Ir fragment towards the terpyridine ligand, which is the LUMO of ^{1}MLLCT excited state and is closer to the cobalt catalyst. More importantly, the electronic transitions are extended up to 600 nm with appreciable molar absorptivity which should allow hydrogen photoproduction to occur at lower energy when compared to the classic Ir(III) complexes of 2-phenyl-pyridine. In order to prove this effect, three light-emitting diodes (LEDs) with narrow wavelengths centered at 451 nm, 522 nm and 595 nm were used for HER. To compare the activity of **[Ir-Py-Co]$^+$**, a non-coordinated system of $[Ir(ppy)_2(bpy)]^+$ with $[Co(dmgH)_2PyCl]$ in equal ratio was analyzed in parallel experiments (Table 4.3).

The photocatalytic HERs show no evidence for an induction time under blue and green irradiation for both systems, which suggests that the same molecular systems are involved in the photocatalytic reaction. In addition, dynamic light scattering studies do not reveal the presence of nanoparticles before nor after the examined HERs (data not shown). Using blue light at 451 nm, **[Ir-Py-Co]$^+$** system reaches a TON of 225 over 35 hours *vs*. a TON of 22 for $[Ir(ppy)_2(bpy)]^+$ and $[Co(dmgH)_2PyCl]$ over 0.5 h, at which time the latter catalyst system is inactive (Figure 4.7). The rate of activity for **[Ir-Py-Co]$^+$** is about one order of magnitude greater than the reference complex and it lasts up to 66 hours, which is unusually long for Ir(III) and Co(III)/Co(II) systems (Table 4.4).

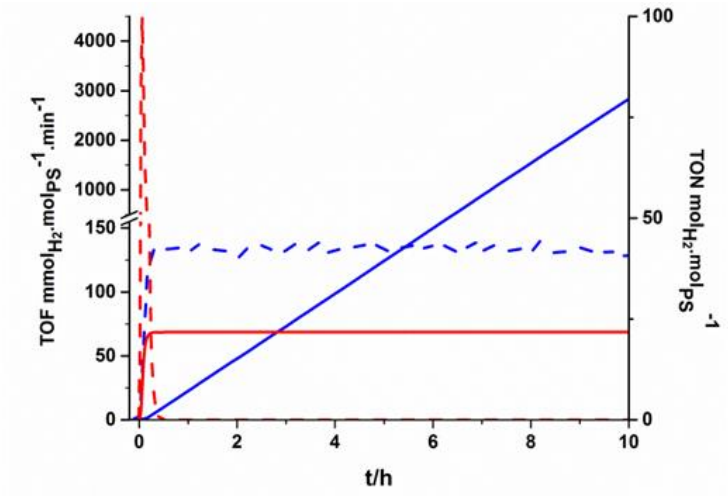

Figure 4.7 – Hydrogen evolution of **[Ir-Py-Co]**$^+$ (blue) and $[Ir(ppy)_2(bpy)]^+$ with $[Co(dmgH)_2PyCl]$ (red). Solid line: Turn Over Number, dashed line: TurnOver Frequencies. Irradiation centered at 451 nm (See Figure 4.6).

The rate of activity for **[Ir-Py-Co]**$^+$ remains constant within 130 $mmol_{H2}.mol_{PS}^{-1}.min^{-1}$ during the first 15 hours. When the lamp is turned on, $[Ir(ppy)_2(bpy)]^+$ rapidly reaches its maximum of activity at *ca.* 4500 $mmolH_2.mol_{PS}^{-1}.min^{-1}$ before a rapid decrease involving the decomposition of system (Figure 4.7), albeit with a lower overall TON compared to **[Ir-Py-Co]**$^+$ (Table 4.4). Additionally, when 4 equivalents of $dmgH_2$ are added to the reaction mixture, **[Ir-Py-Co]**$^+$ reaches a TON of 440 (66 h) (Table 4.4). The ratio of Ir/Co is an important parameter for the stability of the $[Ir(ppy)_2(bpy)]^+$ and $[Co(dmgH)_2PyCl]$ system, as the TurnOver Frequency (TOF, *i.e.* the turnover per time unit) quickly decreases after half an hour if an excess of photosensitizer is not used. Clearly the use of an excess of the expensive $[Ir(ppy)_2(bpy)]^+$ photosensitizer is not optimal.

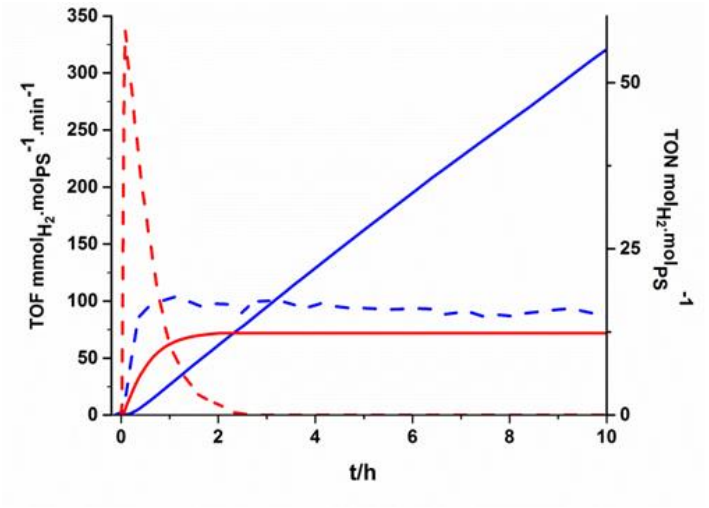

Figure 4.8 – Hydrogen evolution of **[Ir-Py-Co]**$^+$ (blue) and $[Ir(ppy)_2(bpy)]^+$ with $[Co(dmgH)_2PyCl]$ (red). Solid line: Turn Over Number, dashed line: TurnOver Frequency. Irradiation centered at 522 nm (See Figure 4.6).

The molar absorptivity of both systems is lower using green light irradiation (522 nm) which also results in a concomitant decrease in hydrogen production (Figure 4.8): a TON of 113 after 25 hours for **[Ir-Py-Co]**$^+$ and a TON of 12 for the reference system $[Ir(ppy)_2(bpy)]^+$ and $[Co(dmgH)_2PyCl]$. The decrease in TOF_{max} is remarkably different, since the reference system drops by over 4000 and **[Ir-Py-Co]**$^+$ decreases by only 30 over the full 25 h. The **[Ir-Py-Co]**$^+$ system is inferior in comparison with blue irradiation but stays still homogeneous at 95 $mmolH_2.mol_{PS}^{-1}.min^{-1}$ during 10 hours. For the bidentate model system, however, the rate does not decay as rapidly as for blue light. Under yellow irradiation centered at 595 nm, **[Ir-Py-Co]**$^+$ starts a low production of hydrogen (TOF = 4 mmol/mol/min) after 5 h and no activity is detected for $[Ir(ppy)_2(bpy)]^+$ (Table 4.4).

Table 4.3 – Performances of dissociated Ir/Co photocatalytic systems for hydrogen production.

Entry	PS	Cat	PS/Cat	Solvent	Sacrificial Electron Donor	TON mol $_{H2}$.mol$_{PS}^{-1}$ (irradiation time in hour)	TOF$_{max}$ mmol$_{H2}$.mol$_{PS}^{-1}$.min^{-1}	Irradiation source	Ref
1	$[Ir(ppy)_2(bpy)]^+$	$Co(DOH)_2pnBr_2$	1/1	MeCN:H_2O, 1:1	TEA [c] 10 %	307 (5 h)	nd	Xenon lamp >400 nm (500 W)	[207]
2	$[Ir(ppy)_2(bpy)]^+$	$Co(DOH)_2pnBr_2$ + 2 PPh_3	1/1	MeCN:H_2O, 1:1	TEA [c] 10 %	696 (10 h)	nd	Xenon lamp >400 nm (500 W)	[207]
3	$[Ir(ppy)_2(bpy)]^+$	$Co(dmgH)_2ClPyr$	1/1	MeCN	TEOA 1 mol.L^{-1} [d]	22 (0.5 h)	4496	Blue LED (451 nm)	In this work
4	$[Ir(ppy)_2(bpy)]^+$	$Co(dmgH)_2ClPyr$	1/1	MeCN	TEOA 1 mol.L^{-1} [d]	12 (2 h)	337	Green LED (522 nm)	In this work
5	$[Ir(ppy)_2(bpy)]^+$	$Co(dmgH)_2ClPyr$	1/1	MeCN	TEOA 1 mol.L^{-1} [d]	0	0	Yellow LED (595 nm)	In this work

[a] [PS] = 10^{-4} mol.L^{-1}. [b] [Cat] = 10^{-4} mol.L^{-1}. [c] $pH_{apparent}$ = 10, HCl as acid source. [d] 0.1 M HBF_4 (48% in water) as acid source.

Table 4.4 – Performances of Ir-Co assembly for hydrogen production.

Entry	Ir-Co assembly	Cat/PS	Solvent	Sacrificial Electron Donor ([ ] in $mol.L^{-1}$)	TON $mol_{H2}.mol_{PS}^{-1}$ (irradiation time in hour)	TOF_{max} $mmol_{H2}.mol_{PS}^{-1}.min^{-1}$	Irradiation source	Ref
1	$[(ppy)_2Ir(L\text{-}pyr)Co(dmgBF_2)_2(OH_2)]^{+}$ [a]	1/1	Acetone	TEA [c] (0.66)	210 (15 h)	nd	Mercury lamp (150 W) filter cut off λ >380 nm	[36]
2	[Ir-Py-Co]$^{+}$ [b]	1/1	MeCN	TEOA [d] (1.00)	224 (35 h)	169	Blue LED (451 nm)	In this work
3	[Ir-Py-Co]$^{+}$ [b] + 4 eq. $dmgH_2$	1/1	MeCN	TEOA [d] (1.00)	440 (66 h)	170	Blue LED (451 nm)	In this work
4	[Ir-Py-Co]$^{+}$ [b]	1/1	MeCN	TEOA [d] (1.00)	113 (25 h)	104	Green LED (522 nm)	In this work
5	[Ir-Py-Co]$^{+}$ [b]	1/1	MeCN	TEOA [d] (1.00)	3 (17 h) [e]	8	Yellow LED (595 nm)	In this work

[a][Ir-Co] = 5.5 x 10^{-4} $mol.L^{-1}$. [b][Ir-Co] = 1.0 x 10^{-4} $mol.L^{-1}$. [c] 0.33 $mol.L^{-1}$ in Et_3NH^{+}/Et_3N as acid source. [d] 0.1 $mol.L^{-1}$ HBF_4 as acid source. [e]5h of induction time.

Although the switch from blue to green light lowers the overall TON of the **[Ir-Py-Co]**$^{+}$ system, it is still much more efficient than the bidentate system after 5 hours at which time the latter has effectively no activity. The **[Ir-Py-Co]**$^{+}$ system has low but sustainable activity from the start of the photoreaction until the end which suggests that tridentate systems are much more stable with Ir(III) than Ru(II).[34] The low quantum yield of **[Ir-Py]**$^{+}$ could be relative to this slow photo-induced electron transfer rate compared to $[Ir(ppy)_2(bpy)]^{+}$. The pendant pyridine of **[Ir-Py]**$^{+}$ could act as electron relay from PS to catalyst, as it is the linker between both entities[208] and the coordination site for cobaloxime. Coordination of cobaloxime to the PS appears to be a crucial factor for the efficiency and stability of system.

4.5 Conclusions

In summary, the new **[Ir-Py-Co]**$^{+}$ dyad presents much greater robustness as compared to the bidentate equivalent for $[Ir(ppy)_2(bpy)]^{+}$ when examining HER at equivalent quantities of Ir photosensitizer and Co catalyst. The bis-cyclometalating ligand gives a HOMO with both M and L nature which is relatively high in energy while maintaining a low energy LUMO due to the terpyridine ligand in the role of ancillary ligand of the Ir(III) complex. This shift in ligand composition as compared to phenyl-bipyridines allows i) greater control of the direction of the MLLCT transition towards the Co catalyst and ii) HER to occur at lower energy when compared to the classic Ir(III) compounds. Further investigation of the robustness of these new photocatalysts is underway.

4.6 Experimental Section

4.6.1 Synthesis of complexes

Synthesis of $Co((dmgH)(dmgH_2))Cl_2$[209]

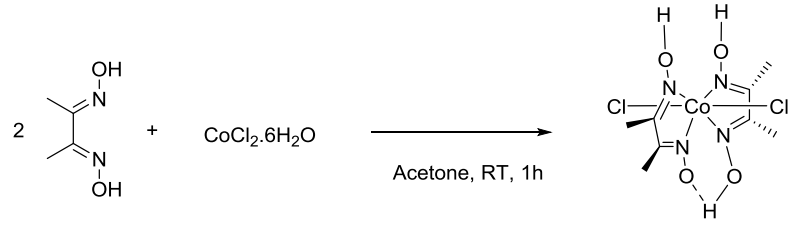

Dimethylglyoxime (89 mg, 0.77 mmol) was added to a solution of cobaltous chloride hexahydrate (50 mg, 0.39 mmol) in acetone (5 ml). The mixture was stirred at room temperature for 15 minutes and the green precipitate was filtreted and washed with acetone. Yield: 51% (70 mg).

Synthesis of $Co(II)(dmgBF_2)_2(H_2O)_2$[210]

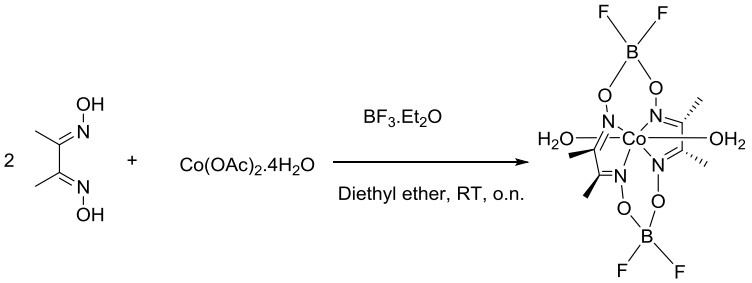

To a solution of $Co(OAc)_2.4H_2O$ (200 mg, 0.8 mmol) and dimethylglyoxime (186 mg, 1.6 mmol) in diethyl ether (15 mL) was added dropwise $BF_3.Et_2O$ (1 mL) under Ar. The mixture was stirred at room temperature overnight. The precipitate was filtered and washed with cold water to give a brown-red solid. Yield: 40% (135 mg).

Synthesis of [Ir-Py-Co](PF$_6$)

Et_3N (2.2 µl, 0.016 mmol) was added to a solution of $Co(dmgH)(dmgH_2)Cl_2$ (6.0 mg, 0.016 mmol) in MeOH (2 mL). The mixture was stirred at room temperature for 10 min. until a brown solution was obtained. **[Ir-Py]**$^+$ (14.4 mg, 0.015 mmol) in CH_2Cl_2 was dropwisely added to this solution and the mixture was stirred at room temperature for 1h30. A stream of air was passed through the red solution and Et_2O was added to precipitate the crude product. The dark red precipitate was isolated by filtration and purified by column chromatography on SiO_2 (CH_2Cl_2/MeOH (95/5)). The first eluted orange band was recovered and the solvent evaporated. The red powder was washed with water and dried under vacuum to afford **[Ir-Py-Co]**$^+$ (11 mg, 58 %). ^{1}H NMR (acetone-d_6, 500 MHz) (Figure 4.9) : δ (ppm), 9.47 (s, 2H, $H_{3'}$ and $H_{5'}$ of tpy-C_6H_5N), 9.01 (d, 2H, H_3 of tpy-C_6H_5N, J_{H3-H4} = 8.1 Hz), 8.50 (d, 2H, H_a of tpy-C_6H_5N, J_{Ha-Hb} = 6.8 Hz) 8.49 (s, 2H, $H_{3'}$ and $H_{5'}$ of tppy-OMe), 8.34 (d, 2H, H_b of tpy-C_6H_5N, J_{Hb-Ha} = 6.8 Hz), 8.22 (d, 2H, H_b of tppy-OMe, J_{Hb-Ha} = 8.8 Hz), 8.16-8.11 (m, 4H, H_3 of tppy-OMe and H_4 tpy-C_6H_5N), 8.11 (d, 2H, H_6 of tpy-C_6H_5N, J_{H6-H5} = 5.8 Hz), 7.48 (ddd, 2H, H_5 of tpy-C_6H_5N-Me, J_{H5-H4} = 7.2 Hz, J_{H5-H6} = 5.8 Hz, J_{H5-H3} = 1.2 Hz), 7.25 (d, 2H, H_a of tppy-OMe, J_{Ha-Hb} = 8.8 Hz), 6.97 (td, 2H, H_4 of tppy-OMe, $J_{H4-H5\ (H3)}$ = 7.3 Hz, J_{H4-H6} = 1.2 Hz), 6.70 (td, 2H, H_5 of tppy-OMe, $J_{H5-H4\ (H6)}$ = 7.3 Hz, J_{H5-H3} = 1.1 Hz), 6.20 (dd, 2H, H_6 of tppy-OMe, J_{H6-H5} = 7.3 Hz, J_{H6-H4} = 0.8 Hz), 3.97 (s, 3H, OMe), 2.42 (s, 12H, dmg^{2-}). HRMS (ESI): m/z calculated for $[C_{52}H_{45}ClN_9O_5{}^{193}Ir^{59}Co - PF_6]^+$, 1162.2188; found: 1162.2186.

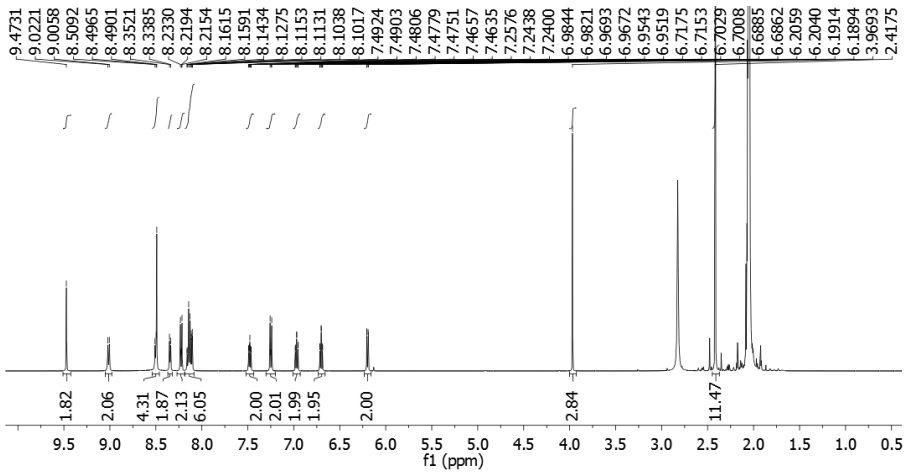

Figure 4.9 – ^{1}H NMR of **[Ir-Py-Co](PF6)** (500 MHz, Acetone).

Synthesis of [Ir-Py-CoBF$_2$](PF$_6$)

Typically, **[Ir-Py](PF$_6$)** (10 mg, 0.01 mmol) and [Co(dmgBF$_2$)(H$_2$O)$_2$] (4.3 mg, 0.01 mmol) were dissolved in acetone (5 mL) and stirred at room temperature for 3h under Argon. The crude product was fully precipitated by added Et$_2$O (5 mL), filtered and washed with Et$_2$O (three times) to afford a red powder (13 mg, 93 %). HRMS (ESI): m/z calculated for $[C_{54}H_{47}N_{10}O_5F_2Co^{11}B^{193}Ir]^{2+}$, 1216.2753; found: 1216.2712 (Only one BF$_2$ was detected and H$_2$O was replaced by CH$_3$CN (solvent used for mass analysis)).

4.6.2 HRMS of ***[Ir-Py-Co]$^{+}$***

For $C_{52}H_{45}O_5N_9$ $^{35}Cl^{59}Co^{193}Ir$

Measured mass: 1162.2186

Calculated mass: 1162.2188

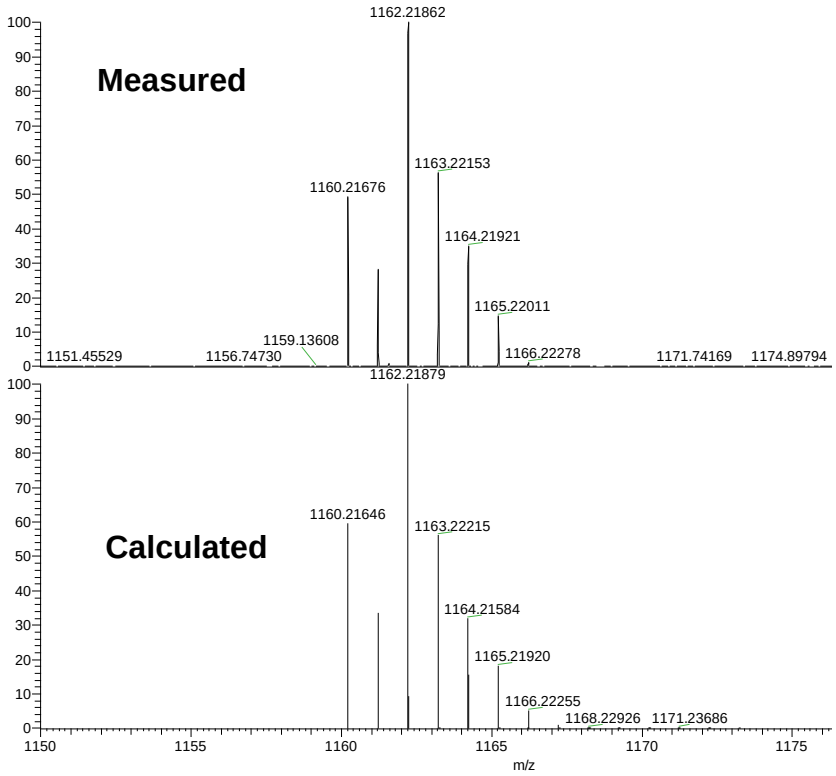

4.6.3 X-Ray Structure Determination

The X-ray data were collected at 100(2) K on a 4-circle Supernova goniometer system equipped with an Atlas CCD detector, using Cu-Kα radiation (mirrors). Diffraction images were integrated by Crysalis and an analytical face-indexed absorption correction was applied. The structure was solved by SHELX97 and refined by full-matrix least squares on $|F^2|$ with SHELXL-2014/7. Non-hydrogen atoms were anisotropically refined and hydrogen atoms were placed on calculated positions in riding mode with temperature factors fixed at 1.2 times Ueq of the parent atoms.

The 4′-MeO-tppy ligand was found to be disordered, with the methoxy group – in both cases in plane with the attached phenyl ring – pointing to opposite sides. In the figure below (Figure 4.10), the disordered 4′-MeO-tppy is shown in different shades of gray. The refined occupancies amount to a 48(dark gray)/52(light gray) ratio. A partial occupied water molecule was found to occupy the void inbetween two neighboring 4′-MeO-tppy ligands (in opposited conformations). The positive charge on the Ir atom is counterbalance by a 66/34 mixture of PF_6^- and Cl^- anions respectively.

The crystal packing contains cavities, which are occupied by solvent molecules; it was found that these sites consist of a mixture of THF and CH_2Cl_2 in a 66/34 ratio.

CCDC 1419882 contains the supplementary crystallographic data for this X-Ray crystal structure. These data can be obtained free of charge from The Cambridge Crystallographic Data Centre via www.ccdc.cam.ac.uk/getstructures.

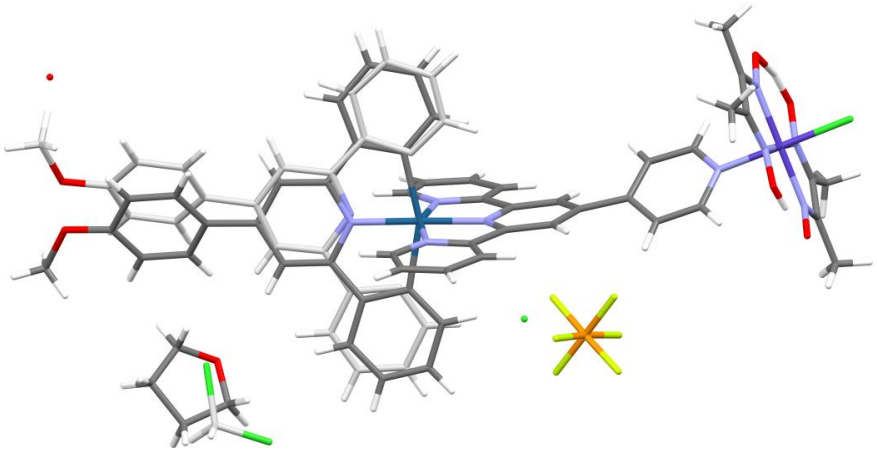

Figure 4.10 – Stick representation of **[Ir-Py-Co]**$^{+}$ showing the observed disorder of the 4′-MeO-tppy ligand (light and dark gray), the mixed anion site PF_6^- and Cl^- (green sphere), and the mixed solvent site, the CH_2Cl_2 carbon is shown in light gray to differentiate from the THF molecule.

Table 4.5 – Crystal and structure refinement data for **[Ir-Py-Co]**$^{+}$.

	[Ir-Py-Co]$^{+}$
Empirical formula	C54.70 H50.40 Cl2.21 Co F3.91 Ir N9 O6.04 P0.65
Formula weight	1354.58
Temperature (K)	100(2)
Wavelength (Å)	1.54184 Å
Crystal system	Monoclinic
Space group	C2/c
a (Å)	41.8168(16)
b (Å)	8.6483(5)
c (Å)	31.4674(8)
β (°)	94.124(3)
Volume (Å^3)	11350.6(8)
Z	8
Density (calculated) (Mg/m^3)	1.585
Absorption coefficient (mm^{-1})	8.488
F(000)	5412
Crystal size (mm^3)	0.205 x 0.188 x 0.049
Reflections collected	22696
Independent reflections	10292
Data / restraints / parameters	10292 / 543 / 961
GoF	1.020
$R_1(F)$ [I >2σ(I)]	0.0551
$wR(F^2)$ [I >2σ(I)]	0.1477
$R_1(F)$ (all data)	0.0656
$wR(F^2)$ (all data)	0.1597
Largest diff. peak and hole (e.Å^{-3})	2.281/-1.329

Table 4.6 – Selected bond lengths [Å] and angles (deg) for **[Ir-Py-Co]**$^{+}$.

	[Ir-Py-Co]$^{+}$
Ir(1)-C(2)	2.071(7)
Ir(1)-N(8)	1.988(15)
Ir(1)-C(14)	2.117(10)
Ir(1)-N(32)	2.022(5)
Ir(1)-N(38)	1.921(5)
Ir(1)-N(44)	2.044(5)
Co(56)-N(53)	1.967(5)
Co(56)-N(58)	1.893(6)
Co(56)-N(64)	1.902(5)
Co(56)-N(66)	1.890(6)
Co(56)-N(72)	1.892(5)
Co(56)-Cl(57)	2.236(2)
C(2)-Ir(1)-N(8)	80.0(5)
C(2)-Ir(1)-C(14)	158.5(5)
N(8)-Ir(1)-C(14)	78.5(5)
C(2)-Ir(1)-N(32)	94.8(5)
C(2)-Ir(1)-N(38)	99.5(3)
C(2)-Ir(1)-N(44)	87.2(5)
N(8)-Ir(1)-N(32)	100.7(13)
N(8)-Ir(1)-N(38)	178.7(12)
N(8)-Ir(1)-N(44)	98.9(13)
N(58)-Co(56)-Cl(57)	88.7(2)
N(58)-Co(56)-N(53)	90.8(2)
N(64)-Co(56)-Cl(57)	90.4(2)
N(64)-Co(56)-N(58)	80.7(2)
N(72)-Co(56)-N(66)	81.9(2)
N(66)-Co(56)-Cl(57)	91.0(2)
N(72)-Co(56)-Cl(57)	89.3(2)
N(72)-Co(56)-N(58)	98.8(2)
N(53)-Co(56)-N(72)	90.3(2)
C10-C11-C20-C21[a]	32.5
C40-C41-C50-C51[a]	35.2

[a]Dihedral angles between terdentate ligands and aryl group.

Chapter 5 - Selective DNA Purine Base Photo-Oxidation by bis-Terdentate Ir(III) Polypyridyl and Cyclometalated Complexes

5.1 Foreword

In the former section, we have demonstrated that Ir(III) cyclometalated bis-terdentate complexes ($\mathbf{[IrN_4C_2]^+}$) can be incorporated in a supramolecular dyad and photo-induce electron transfer to the cobalt catalyst for the reduction of protons into hydrogen. The remarkable photo-stability of our Ir(III) derivatives motivated us to develop novel applications requiring some stable electronic photo-injectors. In the supramolecular structures described previously, an organic ligand (4′-Py-tpy) (Subunit B in Figure 1.1) connects the Ir(III) and Co(III) moieties. This linker plays a crucial role in photo-induced electron transfer phenomena. Its structure can therefore be modified to generate more efficient processes. For instance, the solubility of our systems in water should be maximized since they have to be operative *in fine* in the widely available aqueous solvent.

In this context, the oligonucleotides represent excellent candidates to act as linker (Part B in Figure 1.1) in such structures. Indeed, DNA is water-soluble, can be synthetized in a controlled manner and transports electrical charges.[115,116]

DNA charge transport chemistry has been studied for a long time and is now relatively well understood.[116,117,211,212] The long-lasting interest of the scientific community in the charge migration in DNA was due to its relevance for the mechanism of DNA oxidative damage and repair.[213] DNA charge transport can be fast and occurs over long molecular distances if the reaction is triggered by oxidants or reductants that are properly coupled to the base-pair stack. This evidence suggested that the double-stranded DNA can exhibit a "wire-like" behaviour.[214,215] Nowadays, the DNA charge mobility has also been extended to design other nanoscale devices.[216-218]

DNA-mediated charge-transfer processes can be regarded as either *oxidative hole transfer* or *reductive electron transfer* reactions.[219] This formally means that either positive or negative charges are injected in the double strand. Both processes are in fact electron-transfer reactions. However, the differenciation is necessary with respect to the molecular orbitals that are involved.

DNA hole transport has attracted enormous research efforts over the three last decades due to its importance for the oxidative damage which causes mutagenesis and carcinogenesis.[220] On the other hand, the complementary DNA reductive electron transfer has remained considerably underdeveloped relative to the understanding of hole-transfer processes.[221] This disinterest partially arises from lack of proper photoreductants displaying close interactions towards DNA. Indeed, reductive chemistry on DNA has been essentially demonstrated using organic reductants such as phenothiazine,[221] flavin[222] or aromatic amines.[223,224] However, these reductants adopt different interaction modes with the double-stranded DNA compared to metallointercalators.

5.2 Main topics addressed in the publication

Recently, direct comparisons of hole and electron transport were performed using a charge injector able to selectively oxidize or reduce DNA bases by taking advantage of the powerful photochemistry of bidentates Ir(III) bis-cyclometalated complexes.[225]

The purpose of this chapter is to compare $\mathbf{[IrN_4C_2]^+}$ and $\mathbf{[IrN_6]^{3+}}$ complexes as DNA charge photo-injectors. We anticipated that the different photoelectrochemical properties of both complexes should induce: (i) a reductive electron transfer process for the bis-cyclometalated complex and (ii) holes injection in the case of $\mathbf{[IrN_6]^{3+}}$. Before studying Ir(III)-DNA

interactions, we have investigated the behaviour of both complexes alone then in the presence of each DNA bases to gain insight into the feasibility of the charges photo-injection in the double strand.

As before, we introduced methoxy group to induce vectorial electronic transition but also a carboxylic acid function to subsequently covalently tether the complexes to synthetic oligonucleotides.

Journal

Inorganic Chemistry **2014**, *53*, 1507-1512.

Title

Selective DNA Purine Base Photo-Oxidation by bis-Terdentate Ir(III) Polypyridyl and Cyclometalated Complexes.

Authors

Alexandre JACQUES,[a] Andrée KIRSCH-DE MESMAEKER,[b] Benjamin ELIAS*[a]

Affiliations

[a] Université catholique de Louvain, Institut de la Matière Condensée et des Nanosciences, Place Louis Pasteur 1, L4.01.02, B-1348, Louvain-la-Neuve, Belgium.

[b] Université libre de Bruxelles, Service de Chimie Organique et Photochimie, CP160/08, 50 Av F. D. Roosevelt, B-1050, Brussels, Belgium.

Abstract

Two bis-terdentate Ir(III) complexes with polypyridyl and cyclometalated ligands have been prepared and characterized. Their spectroscopic and electrochemical behaviour has been studied and a photophysical scheme addressing their properties is proposed. Different types of excited states have been considered to account for the deactivation processes in each complex. Interestingly, in the presence of mono- or polynucleotides, a photo-induced electron transfer process from a DNA purine base (i.e. guanine or adenine) to the excited complex is shown through luminescence quenching experiments. For the first time, this work reports evidence for selective DNA purine bases oxidation by excited Ir(III) bis-terdentate complexes.

5.3 Introduction

Polyazaaromatic transition metal complexes have gained considerable interest these past decades. Their use as catalyst in water splitting process,[41,170,197] therapeutic agent in several cancer treatments,[226-228] or photoprobes of biological media[219,229-232] is well established. Among all transition metals available, Ir(III) is one of the most interesting element for building complexes.[233,234] Indeed, it allows the synthesis of multiple polypyridyl and cyclometalled complexes with bidentate or terdentate ligands. Ir(III) is capable of forming stable mono-, bis- and tris-cyclometalated complexes, and up to three C-donor sites can be coordinated onto the metal center. The C/N ratio present in the first coordination sphere can thus be varied from 0/6 to 3/3, hence providing an excellent means to tune the photoredox properties of the resulting complexes. For instance, tris-bidentate Ir(III) complexes made of two ppy (ppy = 2-phenylpyridine) and an imidazo[4,5-f][1,10]phenanthroline have a C/N = 2/4 and are specific anion sensors.[56,235] Upon replacement of the imidazolo ligand by an intercalative ligand dppz (dppz = dipyrido[3,2-a:2′,3′-c]phenazine), the

resulting luminescent Ir(III) has been used to study DNA mediated hole and electron transfer.[225,236] Recently, it has been shown that a luminescent bis-terdentate Ir(III) complex made exclusively of terpyridine type-like ligands (C/N = 0/6) exhibits intercalation between DNA base-pairs.[237] The luminescence of this complex is quenched in the presence of a guanine moiety *via* a photo-induced electron transfer process, showing the high oxidizing ability of the excited state. Although displaying spectroelectrochemical properties enabling photoreactions towards DNA, Ir(III) complexes have only been scarcely used as such in the literature.

Therefore, in this paper, we present the comprehensive study of two novel Ir(III) complexes obtained from the coordination of either two terpyridyl like ligands (*i.e.* $[Ir(4'\text{-COOH-Phtpy})(4'\text{-MeO-Phtpy})]^{3+}$ (4′-COOH-Phtpy = 4′-(4-carboxyphenyl)-2,2′:6′,2″-terpyridine and 4′-MeO-Phtpy = 4′-(4-methoxyphenyl)-2,2′:6′,2″-terpyridine) called hereafter **$[IrN_6\text{-COOH}]^{3+}$** for sake of clarity – Figure 5.1) or one terpyridyl and one triphenylpyridyl ligands (*i.e.* $[Ir(4'\text{-COOH-Phtpy})(4'\text{-MeO-tppy})]^{+}$ (4′-MeO-tppy = 2,6-diphenyl-4-(4′-methoxyphenyl)pyridine) called hereafter **$[IrN_4C_2\text{-COOH}]^{+}$** for sake of clarity – Figure 5.1). Their photophysics and photochemistry have been investigated. Although both complexes display very similar structural features, their photoredox behaviour towards DNA bases and the excited state involved in the electron transfer process is quite different depending on the coordination sphere. Using luminescence measurements in the absence and in the presence of several DNA building blocks, synthetic or natural DNA, we were able to show that these complexes selectively photo-oxidize purine nucleobases (*i.e.* adenine and guanine) whereas no nucleobases reduction occurs under irradiation. This paper represents, to the best of our knowledge, one of the very few studies addressing photo-induced electron transfer processes between excited bis-terdentate Ir(III) complexes and DNA bases.

5.4 Results

5.4.1 Synthesis

The synthesis of both complexes was achieved in two steps by heating Ir(III) chloride salts with the desired ligand in ethylene glycol according to methodologies previously described.[73,98] It is worth mentioning that the synthesis of **[IrN$_4$C$_2$-COOH]$^+$** requires harsher conditions than **[IrN$_6$-COOH]$^{3+}$**, as expected from the greater inertness of the cyclometalated ligand. **[IrN$_6$-COOH]$^{3+}$** and **[IrN$_4$C$_2$-COOH]$^+$** display very similar structural features. Thanks to the derivatization on the 4′-position, they have several symmetry elements, hence circumventing the problem of the occurrence of geometrical isomers as encountered for tris-bidentate arrangements. Both complexes have thus been unambiguously characterized by ^{1}H NMR spectroscopy and high-resolution mass spectrometry (HRMS) (See experimental section).

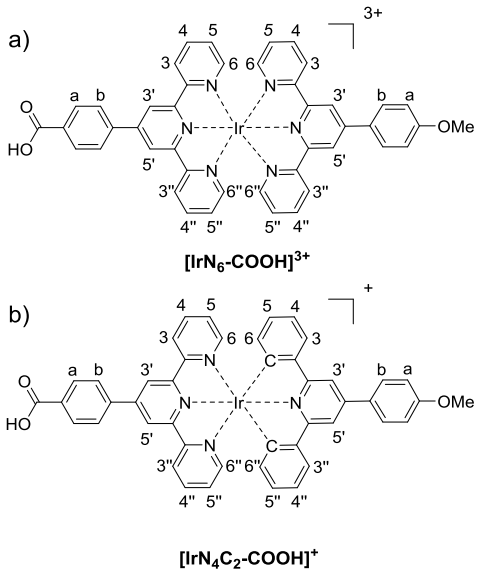

Figure 5.1 – Structure of Ir(III) complexes: a) **[IrN$_6$-COOH]$^{3+}$** ([Ir(4′-COOH-Phtpy)(4′-MeO-Phtpy)]$^{3+}$) and b) **[IrN$_4$C$_2$-COOH]$^+$** ([Ir(4′-COOH-Phtpy)(4′-MeO-tppy)]$^+$).

5.4.2 Electrochemistry

The redox potentials of both complexes were determined by cyclic voltammetry measurements. The data are gathered in Table 5.1. The **[IrN_6-COOH]$^{3+}$** displays two irreversible one-electron reduction waves at -0.81 V *vs.* Ag/AgCl and -1.22 V *vs.* Ag/AgCl respectively (Figure 5.2).

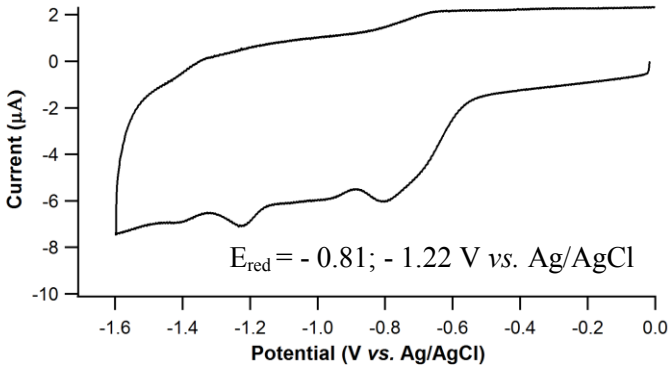

Figure 5.2 – Reduction voltammogram of **[IrN_6-COOH]$^{3+}$** (0.1 V/s).

No oxidation process could be detected up to + 2.2 V *vs.* Ag/AgCl, suggesting that the oxidation is highly energetic and probably metal centered. In contrast, **[IrN_4C_2-COOH]$^{+}$** is characterized by one reversible reduction and one reversible oxidation wave, at -1.24 V *vs.* Ag/AgCl and +1.14 V *vs.* Ag/AgCl respectively (Figures 5.3-5.4).

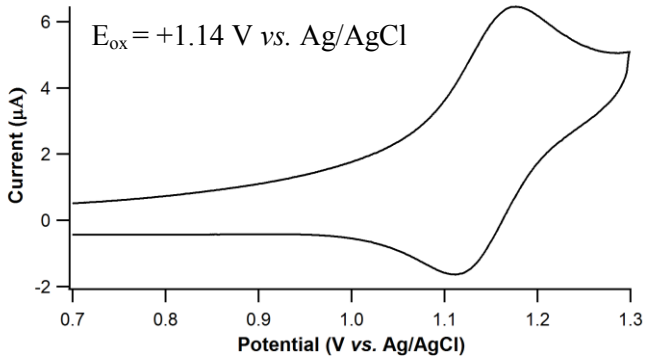

Figure 5.3 – Oxidation voltammogram of **[IrN_4C_2-COOH]$^{+}$** (0.1 V/s).

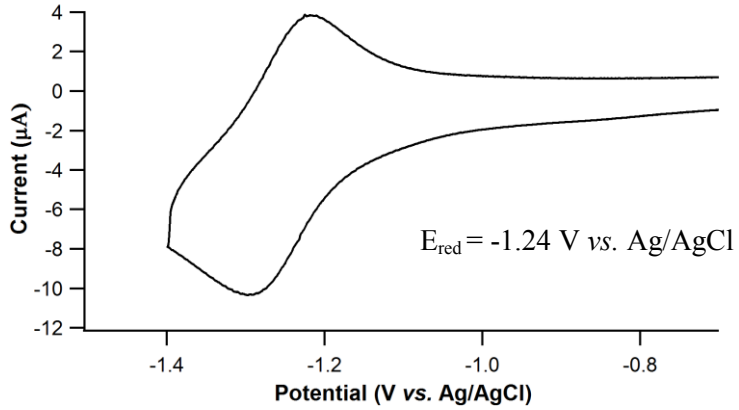

Figure 5.4 – Reduction voltammogram of **[IrN$_4$C$_2$-COOH]**$^+$ (0.4 V/s).

The oxidation of **[IrN$_4$C$_2$-COOH]**$^+$ is probably due to the cyclometalated iridium fragment (Ir-C^N^C). The potentials in the excited state (namely E_{ox}* and E_{red}*)[238] for both complexes have been estimated from the ground state redox potentials and the energy of the excited state corresponding to the maximum of the emission spectrum at 298K, *i.e.* $\lambda_{max\ Em}$ = 568 nm (2.19 eV) for **[IrN$_6$-COOH]**$^{3+}$ and $\lambda_{max\ Em}$ = 528 nm (2.36 eV) for **[IrN$_4$C$_2$-COOH]**$^+$. Not surprisingly, **[IrN$_6$-COOH]**$^{3+}$ is strongly oxidizing (E_{red}* = +1.38 V *vs.* Ag/AgCl) in its excited state.

5.4.3 Absorption and Emission Spectroscopy

Absorption and emission spectra in CH_3CN under air at room temperature for both complexes are shown in Figure 5.5. Table 5.2 gathers the corresponding data. For both complexes, absorption (ε > 30,000 M^{-1} cm^{-1}) bands in UV region tailing into the visible are observed.

Table 5.1 – Electrochemical data measured at room temperature in DMF for **[IrN$_6$-COOH]$^{3+}$** and in CH_3CN for **[IrN$_4$C$_2$-COOH]$^+$** with Bu_4NClO_4 0.1 M as supporting electrolyte; (r) = reversible, (ir) = irreversible, (Δ E_p) (the peak-to-peak separation) is close to 59 mV.

	[IrN$_6$-COOH]$^{3+}$	**[IrN$_4$C$_2$-COOH]$^+$**
E_{ox} (V *vs.* Ag/AgCl)	> 2.2	1.14 (r, ΔE_p = 58 mV)
E_{red} (V *vs.* Ag/AgCl)	-0.81 (ir) ; -1.22 (ir)	-1.24 (r, ΔE_p = 54 mV)
E_{ox}* (V *vs.* Ag/AgCl)	/	-1.22
E_{red}* (V *vs.* Ag/AgCl)	1.38	1.12

[IrN$_6$-COOH]$^{3+}$ and **[IrN$_4$C$_2$-COOH]$^+$** emit in CH_3CN under air ($\Phi \sim 10^{-3}$). A broad band emission centered around 568 nm ($\tau_{RT, Air}$ = 470 ns) is observed for **[IrN$_6$-COOH]$^{3+}$** whereas **[IrN$_4$C$_2$-COOH]$^+$** exhibits a dual band emission, centered at 528 nm ($\tau_{RT, Air}$ = 1 μs) and 697 nm ($\tau_{RT, Air}$ = 260 ns).

Although there is almost no emission band shift between CH_3CN and water, the excited state lifetimes are affected upon solvent change and increase by a factor of two or three in water for both complexes. It is worth mentioning that in air-equilibrated solvent, a decrease in luminescence intensity with respect to degassed solutions is observed, showing a sensitization of $^1O_2$ by excited Ir(III) complexes. Because all of our experiments have been carried out under the same conditions, the influence of oxygen is kept constant and is therefore not further investigated in the present manuscript.

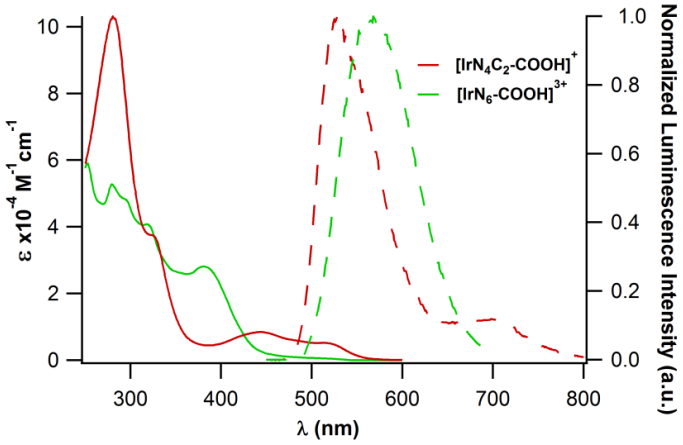

Figure 5.5 – Absorption (solid lines) and emission (dashed lines - $\lambda_{exc} = 350$ nm) for **[IrN$_6$-COOH]$^{3+}$** (green) and **[IrN$_4$C$_2$-COOH]$^{+}$** (red) complexes in CH_3CN under air at room temperature.

5.4.4 Luminescence behaviour of Ir(III) complexes in the presence of deoxynucleotides

With respect to the excited state potentials of Ir(III) complexes and the ability of some DNA-bases to act as an electron donor or acceptor, a photo-oxidative or photo-reductive electron transfer process could be thermodynamically possible between the excited complex and some DNA building-blocks (deoxynucleotides). Thanks to the ability of Ir complexes to emit in aqueous solution, monitoring the luminescence in the presence of increased concentration of a given nucleotide can be performed. It is worth mentioning that all the experiments presented here were carried out with nucleobase concentrations far below the aggregation and self-association limit.[239] In addition, due to the poor solubility of **[IrN$_4$C$_2$-COOH]$^{+}$** in pure water, 10 % CH_3CN (vol/vol) were added for each experiment with deoxynucleotides. Figure 5.6 shows the relative emission decrease of both **[IrN$_6$-COOH]$^{3+}$** and **[IrN$_4$C$_2$-COOH]$^{+}$** upon increased concentrations of deoxyguanosine-5′-monophosphate (dGMP). It is striking that solely the

higher energy emission band (λ_{em} = 514 nm) for **[IrN$_4$C$_2$-COOH]$^+$** is quenched whereas the other band (λ_{em} = 682 nm) is not affected by the presence of dGMP. A linear Stern-Volmer relation in luminescence intensity can be obtained from these data (Figure 5.6 – inset), suggesting that pure dynamic quenching[67] of the excited state of both **[IrN$_6$-COOH]$^{3+}$** and **[IrN$_4$C$_2$-COOH]$^+$** is occuring in the presence of dGMP.

Table 5.2 – Absorption and luminescence data for the Ir(III) complexes

		[IrN$_6$-COOH]$^{3+}$	**[IrN$_4$C$_2$-COOH]$^+$**	
λ max $_{Abs}$ (nm - ε*10^{-3} M^{-1} cm^{-1}) in CH$_3$CN		382 (28.1), 319 (40.8), 279 (52.7), 252 (59.0)	512 (5.2), 439 (8.4), 325 (37.4), 281 (102.8)	
λ max $_{Em}$[a] (nm) under air at 298K	CH$_3$CN	568	528	697
	H$_2$O[b]	560	514	682
λ max $_{Em}$[a] (nm - 77K)	EtOH/MeOH (4/1)	505	505	663
τ(μs) under air at 298K	CH$_3$CN	0.47	1.00	0.26
	H$_2$O[b]	1.31	1.76	0.39
Φ[c]	CH$_3$CN	0.0010	0.0055	0.0006
	H$_2$O[b]	0.0019	0.0291	0.0227
k_r (10^3 s^{-1})[d]	CH$_3$CN	2.2	5.5	2.3

[a]Excitation wavelength = 350 nm. [b]**[IrN$_4$C$_2$-COOH]$^+$** was dissolved in H$_2$O/CH$_3$CN (90/10) mixture due to its low solubility in water. [c]Quantum yield (± 5%) was measured under air using [Ru(bpy)$_3$]$^{2+}$ as reference Φ_{ref} = 0.028 in H$_2$O,[140] λ_{Exc} = 420 nm, 293 K. [d]Radiative rate constant at 298 K ($k_r = \Phi/\tau$).

In the presence of deoxyadenosine-5′-monophosphate (dAMP), a luminescence quenching and decrease of the excited state lifetime (τ_0/τ >1) is observed only for **[IrN$_6$-COOH]$^{3+}$**. However, in that case, a negative deviation from the Stern-Volmer linear relation in intensity is observed

(Figure 5.7). This presumably shows that the luminescence quenching of **[IrN$_6$-COOH]$^{3+}$** in the presence of dAMP is more complicated than a simple dynamic diffusion between the excited complex and dAMP monomers.[67] Addition of dCMP or dTMP to **[IrN$_6$-COOH]$^{3+}$** or **[IrN$_4$C$_2$-COOH]$^{+}$** did not affect their luminescence behaviour excluding thus any photoinduced process involving these nucleobases.

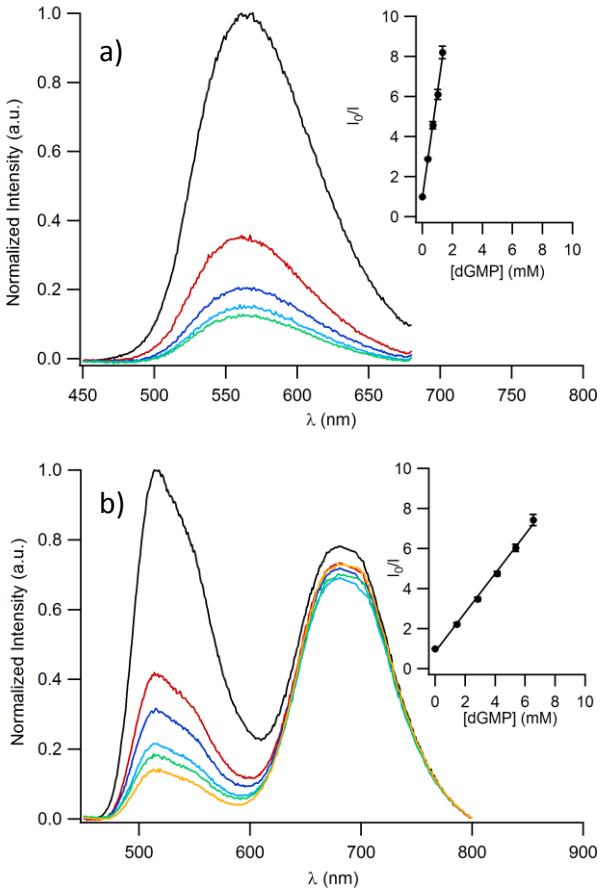

Figure 5.6 – Luminescence spectra (λ_{exc} = 350 nm) of: a) **[IrN$_6$-COOH]$^{3+}$** and b) **[IrN$_4$C$_2$-COOH]$^{+}$** in the presence of increased concentration of dGMP (TRIS Buffer 50 mM pH = 7.4, RT)[240]. Inset : Stern-Volmer plots obtained upon addition of dGMP for a) **[IrN$_6$-COOH]$^{3+}$** and b) **[IrN$_4$C$_2$-COOH]$^{+}$** measured at λ_{em} = 563 nm and λ_{em} = 514 nm respectively.

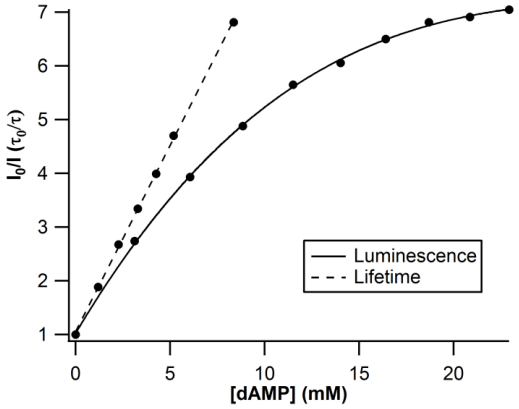

Figure 5.7 – Stern-Volmer plots measured using excited state luminescence lifetime (dashed line) and luminescence intensity (solid line) of **$[IrN_6\text{-}COOH]^{3+}$** upon increased concentration of dAMP (TRIS Buffer 50 mM pH = 7.4, RT) at λ_{em} = 563 nm (λ_{exc} = 350 nm).

5.4.5 Luminescence behaviour of $[IrN_6\text{-}COOH]^{3+}$ in presence of polynucleotides

Due to the relatively low solubility of **$[IrN_4C_2\text{-}COOH]^{+}$** in aqueous buffer, we have decided to limit our study of the influence of polynucleotides on the spectroscopic properties of the complex to **$[IrN_6\text{-}COOH]^{3+}$**.

Although no significant change in the absorption spectra of **$[IrN_6\text{-}COOH]^{3+}$** is observed when interacting with the polynucleotide, its luminescence is dramatically altered. Figure 5.8 shows the relative luminescence intensity changes I/I_0 for **$[IrN_6\text{-}COOH]^{3+}$** upon addition of selected polynucleotides. Two distinct behaviours are observed. In the presence of GC base-pairs containing polynucleotides (*i.e.* [poly(dG-dC)$_2$] – 100% GC base-pairs – and CT-DNA – 42% GC base-pairs[241]), a luminescence quenching is observed. In contrast, in the presence of AT base-pairs containing polynucleotides (*i.e.* [poly(dA-dT)$_2$] or [poly(dA)-poly(dT)]

– 100% AT base-pairs), a somewhat more complex behaviour is observed with a strong luminescence increase followed by a plateau value of $I/I_0 \approx 3$ for $[poly(dA\text{-}dT)_2]$, or followed by a decrease for [poly(dA)-poly(dT)].

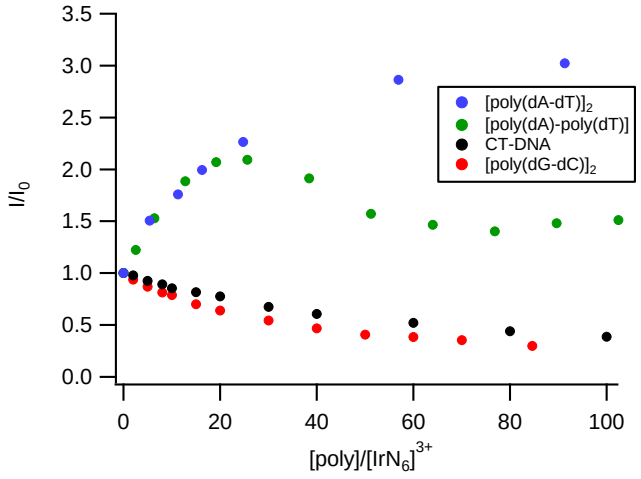

Figure 5.8 – Relative luminescence intensity of **$[IrN_6\text{-}COOH]^{3+}$** measured at λ_{em} = 560 nm in presence of increased concentrations of $[poly(dA\text{-}dT)]_2$ (blue circle), [poly(dA)-poly(dT)] (green circle), CT-DNA (black circle) and $[poly(dG\text{-}dC)]_2$ (red circles). All the measurements were performed with a constant complex concentration of 32 µM in a 50 mM TRIS-HCl buffer aqueous solution (pH = 7.4) with NaCl 50 mM (λ_{exc} = 350 nm).

5.5 Discussion

5.5.1 Photophysics of the complexes alone in solution

Ir(III) complexes are well known in the literature for their rich photophysics and photochemistry. Indeed, due to a strong spin-orbit coupling and an important influence of the ancillary ligands, a mixture of different excited states usually participates to the radiative deactivation of the complex. In the case of $[Ir(tpy)_2]^{3+}$ and related compounds, it has been shown that the emission arises from a ligand-centred (^{3}LC) excited state,

with a small but non-negligible contribution of an ^{3}MLCT (metal-to-ligand charge transfer) excited state.[73]

For **[IrN$_6$-COOH]$^{3+}$**, change in solvent polarity (*i.e.* from CH_3CN to water) does not influence the emission maximum, in agreement with a ^{3}LC excited state. However, the luminescence at room temperature in a polar fluid solvent is unstructured, decays in about 1 μs and is blue-shifted at 77K (Table 5.2), which is more in favor of an ^{3}MLCT excited state. In addition, the k_r value ($\approx 10^3$ s^{-1}) is relatively high, and usually such values are much smaller for pure ^{3}LC states.[69] Therefore, we propose that the lowest excited state in **[IrN$_6$-COOH]$^{3+}$** corresponds to a ^{3}LC centered on the electron poorest ligand *i.e.* $^3[\pi \rightarrow \pi^*$ (4′-COOH-Phtpy)] mixed with some ^{3}MLCT character $^3[d\pi(Ir) \rightarrow \pi^*$ (4′-COOH-Phtpy)].

In contrast, the cyclometalated compound **[IrN$_4$C$_2$-COOH]$^+$** displays a different photophysical behaviour. Compared to **[IrN$_6$-COOH]$^{3+}$**, the absorption is shifted to the red in agreement with the greater donating ability of the cyclometalated ligand. In addition, a dual emission is observed. According to experimental[101] and theoretical[100] data, Ir(III) complexes made from terdentate cyclometalated ligands usually have an emitting state corresponding to a metal/ligand-to-ligand charge transfer (MLLCT), often combined with other ^{3}LC/^{3}MLCT excited states. In the case of **[IrN$_4$C$_2$-COOH]$^+$**, the emission at $\lambda_{em} \approx 520$ nm is similar to that of **[IrN$_6$-COOH]$^{3+}$** described above. Therefore, we ascribe this transition to a mixture ^{3}LC/^{3}MLCT *i.e.* $^3[d\pi(Ir) \rightarrow \pi^*$ (4′-COOH-Phtpy) and π (4′-COOH-Phtpy) $\rightarrow$ π^* (4′-COOH-Phtpy)]. The most bathochromic band (λ_{em} = 697 nm) is believed to correspond to a ^{3}MLLCT *i.e.* ^{3}[cyclometalated iridium fragment (Ir-C^N^C) $\rightarrow \pi^*$ (4′-COOH-Phtpy)]. Indeed, the emission at 77K is poorly resolved, in agreement with a CT process.[69] Moreover, addition of protons

(*e.g.* HNO_3 2M – Figure 5.9) in the solution leads to a complete disappearance of this ^{3}MLLCT emission, probably arising from the protonation of the –OMe group hence inhibiting any CT processes involving the electron donating Ir-C^N^C fragment.

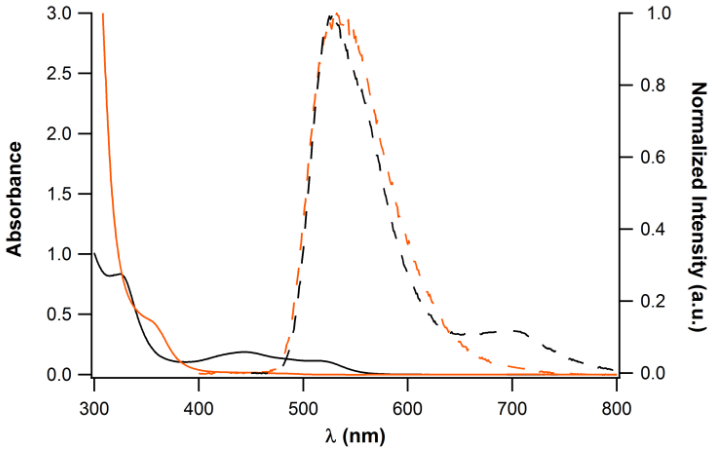

Figure 5.9 – Absorption (solid line) and emission (dashed line) (λ_{exc} = 350 nm) for **[IrN$_4$C$_2$-COOH]$^+$** under air in CH_3CN before (black) and after (orange) addition of HNO_3 2M.

5.5.2 *Photochemical behaviour in the presence of mono- and polynucleotides*

Although the total emission of **[IrN$_6$-COOH]$^{3+}$** is quenched in the presence of a G unit, solely one emission band of **[IrN$_4$C$_2$-COOH]$^+$** undergoes a quenching process upon addition of GMP (Figure 5.6). Based on thermodynamic considerations, this luminescence quenching for both complexes could be ascribed to a photo-induced electron transfer process from the G unit to the excited complexes (equations 1 and 2).

[IrN$_6$-COOH]$^{3+}$* + G → **[IrN$_6$-COOH]$^{2+}$** + G$^{\bullet+}$ (equation 1)

[IrN$_4$C$_2$-COOH]$^+$* + G → **[IrN$_4$C$_2$-COOH]** + G$^{\bullet+}$ (equation 2)

Indeed, although the G oxidation potential has been debated for a long time in the literature, it is generally accepted that E_{ox} of isolated G is close to + 1.10 V *vs.* Ag/AgCl and even less positive when stacked to other G units (E_{ox} [poly(dG-dC)$_2$] < + 0.85 V *vs.* Ag/AgCl).[242] Considering the oxidation power of the excited state of **[IrN$_6$-COOH]$^{3+}$** and using the empirical Rehm-Weller equation,[50] it is expected that process 1 will be exergonic by about 0.3 eV. In the case of **[IrN$_4$C$_2$-COOH]$^{+}$**, solely the most energetic emission band (λ_{em} = 514 nm) is quenched via a photo-reductive electron transfer (equation 2), favored by less than 0.1 eV based on thermodynamic assumptions. The low oxidizing power of the less energetic excited state (MLLCT) does not allow any G oxidation. Efficient quenching in the presence of G units is also in agreement with the high value of the quenching rate constant (k_q) obtained from the Stern-Volmer plot of **[IrN$_6$-COOH]$^{3+}$** and **[IrN$_4$C$_2$-COOH]$^{+}$** with dGMP (*vide supra* - Stern-Volmer plots, Figure 5.6 – inset, k_q = 3.9 x 10^9 $M^{-1}s^{-1}$ for **[IrN$_6$-COOH]$^{3+}$** and 5.3 x 10^8 $M^{-1}s^{-1}$ for **[IrN$_4$C$_2$-COOH]$^{+}$**), both close to the diffusion limit.

The behaviour of **[IrN$_6$-COOH]$^{3+}$** in the presence of A units is less common. The emission lifetimes dramatically decrease upon addition of dAMP, evidencing an efficient quenching of the excited state with a k_q = 5.3 x 10^8 M^{-1} s^{-1} (Figure 5.7). However, a deviation from the linearity of the Stern-Volmer relation for the emission intensity (I_0/I) is observed (Figure 5.7). This usually arises when static quenching is operative but in that particular case, an upward curvature is observed. Instead for **[IrN$_6$-COOH]$^{3+}$**, a downward curvature indicates that other processes have to be taken into account. A similar behaviour has been reported in the literature for the fluorescence quenching of doxorubicin in the presence of AMP.[243] Two conformers (*i.e.* with one or two intramolecular H-bonded hydrophenolic moieties) of doxorubicin in the ground state with different accessibility to the quencher were shown to be responsible for the emission quenching

behaviour. In the present case, (de)protonation of the carboxylic acid moiety could generate two ground states with a different quenching constant by dAMP. Experiments at different pH in buffered aqueous solution showed that the proton concentration of the medium has only a small influence on the quenching behaviour (Figure 5.10).

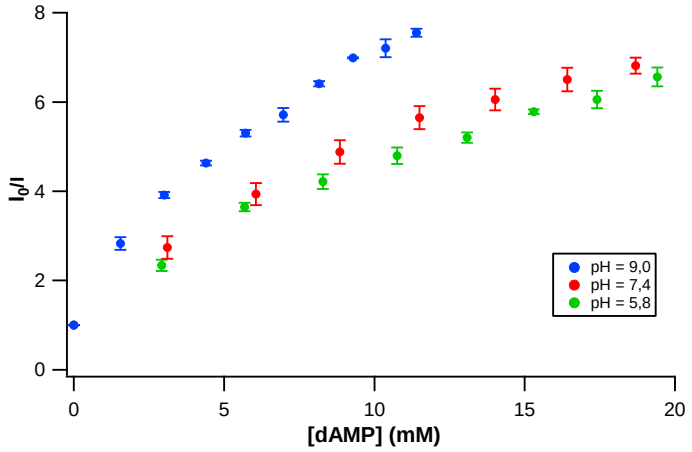

Figure 5.10 – Stern-Volmer plots measured using luminescence intensity of **[IrN$_6$-COOH]$^{3+}$** upon increased concentration of dAMP (TRIS Buffer 50 mM, RT) at λ_{em} = 560 nm (λ_{exc} = 350 nm) at different pH.

Moreover, converting the acid function into an ester does not allow to obtain a straight line graph even if the I_0/I absolute values differ from acid form (Figures 5.11-5.12). Therefore, it is likely that the behaviour of **[IrN$_6$-COOH]$^{3+}$** in the presence of dAMP originates from the complex mixture of excited states participating to the emission, each state being successively reductively quenched by dAMP with different rate constants. In the presence of oligonucleotides, the change of luminescence of **[IrN$_6$-COOH]$^{3+}$** strongly depends on the nature of the nucleobases content. In agreement with the behaviour observed in the presence of dGMP, quenching of excited **[IrN$_6$-COOH]$^{3+}$** with [poly(dG-dC)]$_2$ or CT-DNA would arise from the photo-induced electron transfer process from a G unit of the polynucleotide to the

excited complex, hence generating an oxidative damage within the DNA double helix. The plateau value, reflecting the quenching efficiency, does not seem to depend on the percentage of GC of the polynucleotide, in contrast to G photo-oxidizing Ru(II) complexes.[241] This shows that the quenching of the excited state of **[IrN$_6$-COOH]$^{3+}$** is highly efficient, in agreement with its very high oxidation power when irradiated by light.

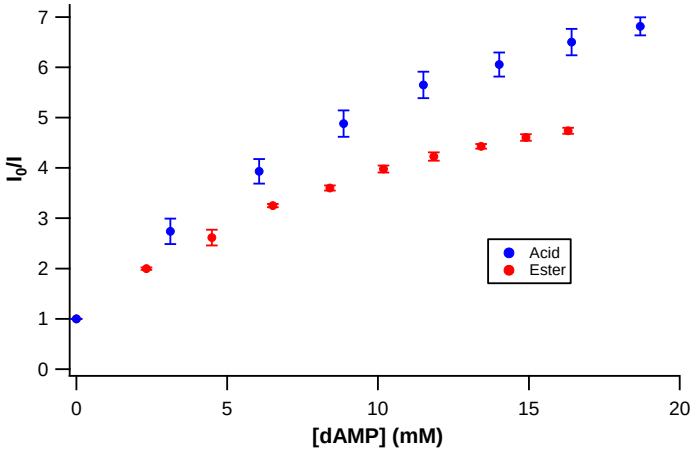

Figure 5.11 – Comparison of Stern-Volmer plots measured using luminescence intensity of **[IrN$_6$-COOH]$^{3+}$** (Acid) and **[Ir(4′-COOMe-Phtpy)(4′-MeO-Phtpy)]$^{3+}$** (Ester) upon increased concentration of dAMP (TRIS Buffer 50 mM pH = 7.4, RT) at λ_{em} = 560 nm (λ_{exc} = 350 nm).

In contrast, in the presence of adenine rich polynucleotides such as [poly(dA-dT)]$_2$ or [poly(dA)-poly(dT)], a luminescence increase is recorded, in spite of a sufficiently reducing power of A for quenching the excited state of **[IrN$_6$-COOH]$^{3+}$** (*vide supra* – Figure 5.7). The luminescence of the complex in the presence of these specific polynucleotides probably originates from two antagonist processes: *i)* protection of the complex from the solvent molecules and from oxygen by the DNA hydrophobic environment (*via* intercalation or groove binding for instance), resulting in

luminescence increase and *ii)* quenching by the A moieties, resulting in luminescence decrease.

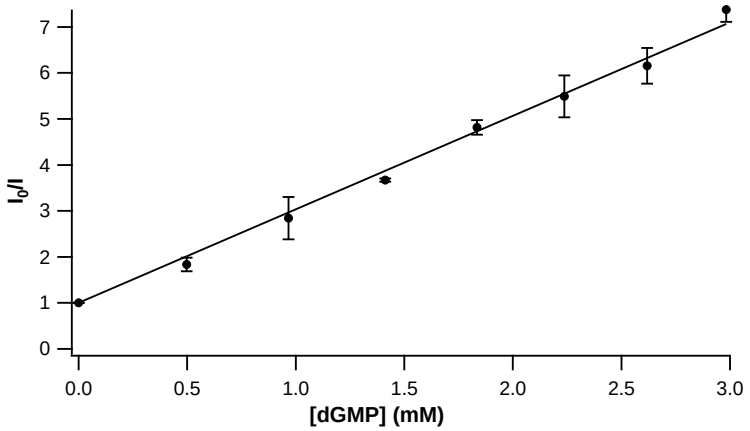

Figure 5.12 – Stern-Volmer plot measured using luminescence intensity of **[Ir(4′-COOMe-Phtpy)(4′-MeO-Phtpy)]**$^{3+}$ (ester) upon increased concentration of dGMP (TRIS Buffer 50 mM pH = 7.4, RT) at λ_{em} = 560 nm (λ_{exc} = 350 nm).

In the case of the alternating copolymeric [poly(dA-dT)]$_2$, the luminescence enhancement is monotonic, reflecting a constant involvement of both processes at any [poly]/[IrN$_6$-COOH]$^{3+}$ ratio, with the protection effect being predominant. For the homopolymeric [poly(dA)-poly(dT)], a different behaviour is observed, this could originate from a different type of interaction with the double helix, depending on the polynucleotide loading level by the complex (Figure 5.8). Thus because of these structural changes, at [poly]/[IrN$_6$-COOH]$^{3+}$ > 40, the quenching by the A units would become predominant as compared to their protection, which would account for the inflection observed in the titration curve.

5.6 Conclusion

We managed to synthesize two new bis-terdendate Ir(III) complexes. Both have been obtained thanks to successive addition of the ligands on the metal center. The spectroscopic and electrochemical data revealed that several excited states contribute to the overall luminescence. Oxidative quenching of the **$[IrN_6\text{-}COOH]^{3+}$** emission in the presence of dGMP or dAMP confirms the high oxidizing ability of the excited complex. The behaviour of **$[IrN_4C_2\text{-}COOH]^{+}$** is less common. Indeed, a selective quenching of the most energetic excited state is observed in the presence of dGMP. No quenching in the presence of dTMP or dCMP was evidenced for both complexes. This shows that these two Ir(III) complexes are not sufficiently reducing (or oxidizing) in their excited state to reduce (or oxidize) thymine or cytosine derivatives. Therefore, selective oxidative electron transfer processes involving DNA purine bases can be triggered upon irradiation of these new Ir(III) complexes.

ASSOCIATED CONTENT

Supporting Information. Synthetic details and HRMS data for all the complexes. This material is available free of charge via the Internet at http://pubs.acs.org.

ACKNOWLEDGMENT

The authors gratefully acknowledge the *Fonds National pour la Recherche Scientifique* (F.R.S.-FNRS), the *Fonds pour la Formation à la Recherche dans l'Industrie et dans l'Agriculture* (F.R.I.A.), the *Région Wallonne*, the *Université catholique de Louvain* and the *Prix Pierre et Colette Bauchau* for financial support. We are also grateful to L. Marcélis and L. Troian-Gautier for their scientific help.

5.7 Experimental Section

5.7.1 Materials and instrumentation

4′-Methoxyphenyl-2,2′;6′,2″-terpyridine[76] (4′-MeO-Phtpy), [(4′-COOMe-Phtpy)$IrCl_3$][98], [(4′-COOH-Phtpy)$IrCl_3$][244] and 2,6-diphenyl-4-(4′-methoxyphenyl)pyridine[157] (4′-MeO-tppy) were prepared as previously described. Deoxynucleotides (dGMP, dAMP, dCMP and dTMP) were purchased from Sigma-Aldrich (purity ≥ 99%) and used without further purification. Calf Thymus DNA (CT-DNA) was purchased from Sigma-Aldrich and [poly(dG-dC)]$_2$, [poly(dA-dT)]$_2$ and [poly(dA)-poly(dT)] were purchased from Amersham Bioscience. Polynucleotides phosphate concentrations were determined spectroscopically ($\varepsilon_{260\,nm}$ = 6600 M^{-1} for CT-DNA,[245] $\varepsilon_{262\,nm}$ = 6600 M^{-1} for [poly(dA-dT)]$_2$,[246] $\varepsilon_{260\,nm}$ = 6000 M^{-1} for [poly(dA)-poly(dT)][247] and $\varepsilon_{254\,nm}$ = 8400 M^{-1} for [poly(dG-dC)]$_2$).[248] ^{1}H NMR experiments were performed in CD_3CN on a Bruker AC-300 Avance II (300 MHz) or on a Bruker AM-500 (500 MHz). The chemical shifts (given in ppm) were measured versus the residual peak of solvent as the internal standard. HRMS were recorded on a Q-Extractive orbitrap from ThermoFisher. Samples were ionized by ESI (capillary temperature: 250 °C, vaporizer temperature: 250 °C, sheath gas flow rate: 20). UV-vis absorption spectra were recorded on a Shimadzu UV-1700. Room temperature fluorescence spectra were recorded on Varian Cary Eclipse. Luminescence lifetimes were measured with a modified Applied Photophysics laser kinetic spectrometer by exciting the samples at 355 nm with a Nd-YAG pulsed laser (Continuum NY 61-10). Emitted light as a function of time was detected with a R-928 Hamamatsu photomultiplier tube whose output was applied to a digital oscilloscope (Hewlett-Packard HP 54200A) interfaced with a Dell Dimension DE051 computer. Signals were averaged over at least 16 shots and corrected for baseline. Igor 6.1 software was used for the decay

analyses. Cyclic voltammetry was carried out in a one-compartment cell, using a glassy carbon disk working electrode (approximate area = 0.03 cm^2), a platinum wire as counter electrode and an Ag/AgCl electrode as reference electrode. The potential of the working electrode was controlled by an Autolab PGSTAT 100 potentiostat through a PC interface. The cyclic voltammograms were recorded with a sweep rate of 100 $mV.s^{-1}$, either in dried acetonitrile (Acros, HPLC grade) or in dried DMF (Sigma-Aldrich, HPLC grade). Tetrabutylammonium perchlorate (0.1 M) was used as supporting electrolyte and the samples were purged by argon before each measurement.

5.7.2 Synthesis of $[IrN_6\text{-}COOH]^{3+}$ *(acid and ester forms) and* $[IrN_4C_2\text{-}COOH]^{+}$ *complexes*

[Ir(4′-COOH-Phtpy)(4′-MeO-Phtpy)]$(PF_6)_3$ ([IrN_6-COOH]$(PF_6)_3$)

A suspension of [(4′-COOH-Phtpy)$IrCl_3$] (24 mg, 0.037 mmol) and 4′-MeO-Phtpy (12 mg, 0.037 mmol) was heated to 170°C in degassed ethylene glycol (2.5 mL) in the dark and under Ar for 30 min. After cooling, aqueous NH_4PF_6 was added to precipitate the crude product. The pure complex was isolated by column chromatography on Al_2O_3 (acetone/water, from 100/0 to 90/10), which yielded the complex $[IrN_6\text{-}COOH]^{3+}$ (PF_6^- salt) as a yellow solid (40 mg, 82%). When the chloride salt was required for the experiments, counter-anion exchange was achieved upon addition of $^tBu_4N^+Cl^-$ to the PF_6^- salt dissolved in acetone. ^1H NMR (CD_3CN, 500 MHz) (Figure 5.13) : δ (ppm), 9.11 (s, 2H, $H_{3'}$ and $H_{5'}$ of tpy-C_6H_4-COOH), 9.03 (s, 2H, $H_{3'}$ and $H_{5'}$ of tpy-C_6H_4-OMe), 8.72 (d, 2H, H_3 and $H_{3''}$ of tpy-C_6H_4-COOH, $J_{H3\text{-}H4}$ = 8.1 Hz), 8.70 (d, 2H, H_3 and $H_{3''}$ of tpy-C_6H_4-OMe, $J_{H3\text{-}H4}$ = 8.1 Hz), 8.40 (d, 2H, H_a of tpy-C_6H_4-COOH, $J_{Ha\text{-}Hb}$ = 8.4 Hz), 8.28 (d, 2H, H_b of tpy-C_6H_4-COOH, $J_{Hb\text{-}Ha}$ = 8.4 Hz), 8.25-8.20 (m, 6H, H_4 and $H_{4''}$ of both tpys, H_b of tpy-C_6H_4-OMe), 7.70 (dd, 2H, H_6 and $H_{6''}$ of tpy-C_6H_4-COOH, $J_{H6\text{-}H5}$ = 4.9 Hz, $J_{H6\text{-}H4}$ =

0.9 Hz), 7.68 (dd, 2H, H_6 and $H_{6''}$ of tpy-C_6H_4-OMe, J_{H6-H5} = 4.9 Hz, J_{H6-H4} = 0.9 Hz), 7.51-7.46 (m, 4H, H_5 and $H_{5''}$ of both tpys), 7.34 (d, 2H, H_a of tpy-C_6H_4-OMe, J_{Ha-Hb} = 8.8 Hz), 3.99 (s, 3H, OMe). HRMS (ESI): m/z calculated for $[C_{44}H_{32}N_6O_3{}^{193}IrP_2F_{12} - PF_6]^+$, 1175.1443; found: 1175.1429, m/z calculated for $[C_{44}H_{32}N_6O_3{}^{193}Ir - 3PF_6]^{3+}$, 295.0716; found: 295.0723.

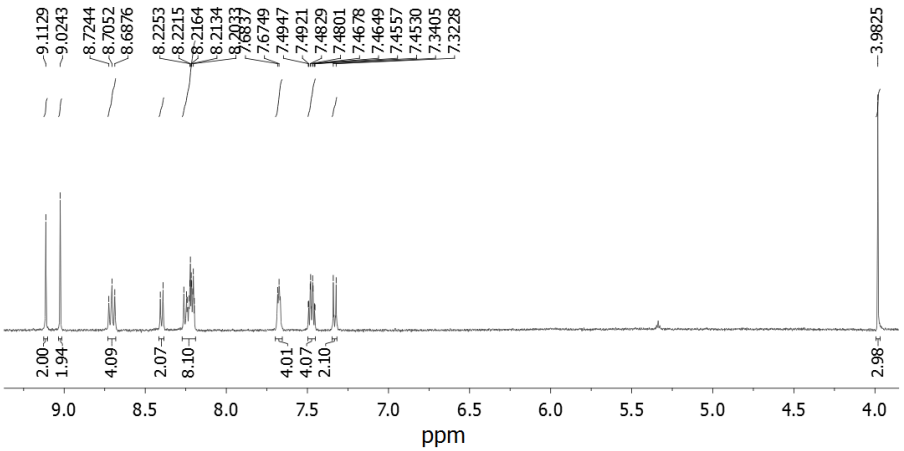

Figure 5.13 – ^{1}H NMR spectrum of **[IrN$_6$-COOH]$^{3+}$** (500 MHz, CD_3CN).

[Ir(4′-COOH-Phtpy)(4′-MeO-tppy)](NO$_3$) ([IrN$_4$C$_2$-COOH](NO$_3$))

A mixture of [(4′-COOMe-Phtpy)$IrCl_3$] (98 mg, 0.15 mmol), 4′-MeO-tppy (54 mg, 0.16 mmol) and $AgNO_3$ (125 mg, 0.74 mmol) was refluxed in degassed ethylene glycol (13 mL) in the dark and under Ar for 22h. On cooling, the mixture was filtered through Celite to remove AgCl. The Celite was washed with MeOH, subsequently evaporated. Water was added and the aqueous layer was extracted with $CHCl_3$ (3x). The organic solutions were combined and evaporated to dryness. The crude product was purified by column chromatography on SiO_2 (CH_3CN/saturated aqueous KNO_3 (10/1)). The first eluted orange band was recovered and the solvent evaporated. The resulting red solid was saponified in a mixture MeOH (30 mL)/1M NaOH (20 mL) and the solution was heated to 80°C for 3h. After cooling, the

solution was adjusted to pH = 7 with 2M HCl and solvents evapored. The solid was purified by column chromatography on SiO_2 (CH_3CN/saturated aqueous KNO_3 (10/1)). The red powder was washed with water and dried under vacuum to afford **$[IrN_4C_2$-COOH$]^+$** with 40% yield (63 mg). ^1H NMR (CD_3CN, 300 MHz) (Figure 5.14) : δ (ppm), 9.00 (s, 2H, $H_{3'}$ and $H_{5'}$ of tpy-C_6H_4-COOH), 8.67 (d, 2H, H_3 and $H_{3''}$ of tpy-C_6H_4-COOH, J_{H3-H4} = 7.8 Hz), 8.36 (d, 2H, H_a of tpy-C_6H_4-COOH, J_{Ha-Hb} = 8.6 Hz), 8.29 (s, 2H, $H_{3'}$ and $H_{5'}$ of tppy-OMe), 8.28 (d, 2H, H_b of tpy-C_6H_4-COOH, J_{Hb-Ha} = 8.6 Hz), 8.13 (d, 2H, H_b of tppy-OMe, J_{Hb-Ha} = 8.4 Hz), 8.03-7.96 (m, 4H, H_4 and $H_{4''}$ of tpy-C_6H_4-COOH and H_3 and $H_{3''}$ of tppy-OMe), 7.89 (d, 2H, H_6 of and $H_{6''}$ tpy-C_6H_4-COOH, J_{H6-H5} = 5.1 Hz), 7.31-7.24 (m, 4H, H_5 and $H_{5''}$ of tpy-C_6H_4-COOH and H_a of tppy-OMe), 7.01 (td, 2H, H_4 and $H_{4''}$ of tppy-OMe, $J_{H4-H5\ (H3)}$ = 7.4 Hz, J_{H4-H6} = 1.1 Hz), 6.78 (td, 2H, H_5 and $H_{5''}$ of tppy-OMe, $J_{H5-H4\ (H6)}$ = 7.3 Hz, J_{H5-H3} = 1.0 Hz), 6.28 (dd, 2H, H_6 and $H_{6''}$ of tppy-OMe, J_{H6-H5} = 7.3 Hz, J_{H6-H4} = 0.9 Hz), 3.97 (s, 3H, OMe). HRMS (ESI): m/z calculated for $[C_{46}H_{32}N_4O_3{}^{193}Ir - NO_3]^+$, 881.2098; found: 881.2088.

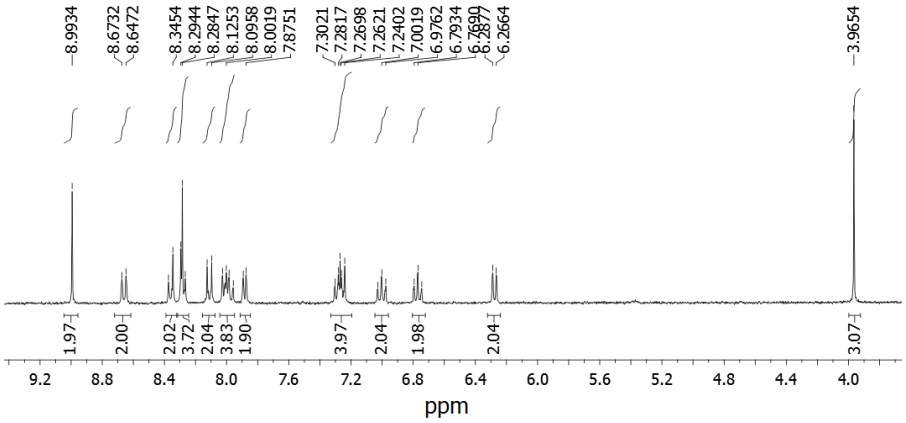

Figure 5.14 – ^1H NMR spectrum of **$[IrN_4C_2$-COOH$]^+$** (300 MHz, CD_3CN).

Synthesis of [Ir(4′-COOMe-Phtpy)(4′-MeO-Phtpy)](PF$_6$)$_3$ (ester)

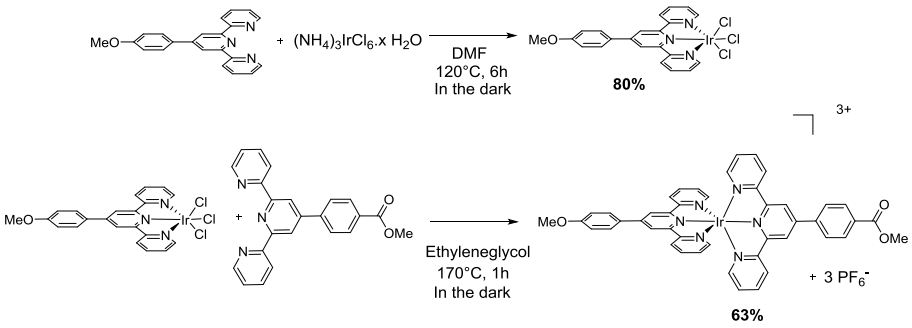

Scheme 5.1 – Synthetic route followed to yield ester.

[(4′-MeO-Phtpy)IrCl$_3$] $(NH_4)_3IrCl_6$ (200 mg, 0.42 mmol) and 4′-MeO-Phtpy (142 mg, 0.42 mmol) was heated to 120°C in DMF (5 mL) in the dark and under Ar for 6h. After cooling, the crude product was successively washed with H_2O, EtOH and $CHCl_3$ and dried under vacuum. The product is obtained as a red powder (215 mg, 80%). ^{1}H NMR (DMSO-d$_6$, 300 MHz) : δ (ppm), 9.22 (dd, 2H, H_6 and $H_{6''}$, $J_{H6\text{-}H5}$ = 5.6 Hz, $J_{H6\text{-}H4}$ = 1.0 Hz), 9.06 (s, 2H, $H_{3'}$ and $H_{5'}$), 8.91 (d, 2H, H_3 and $H_{3''}$, $J_{H3\text{-}H4}$ = 7.7 Hz), 8.30 (td, 2H, H_4 and $H_{4''}$, $J_{H4\text{-}H3(H5)}$ = 7.8 Hz, $J_{H4\text{-}H6}$ = 1.5 Hz), 8.23 (d, 2H, H_b, $J_{Hb\text{-}Ha}$= 8.3 Hz), 7.96 (ddd, 2H, H_5 and $H_{5''}$, $J_{H5\text{-}H4}$ = 7,7 Hz, $J_{H5\text{-}H6}$ = 5.6 Hz, $J_{H5\text{-}H3}$ = 1.3 Hz), 7.24 (d, 2H, H_a, $J_{Ha\text{-}Hb}$= 8.3 Hz), 3.94 (s, 3H, H, OMe).

[Ir(4′-COOMe-Phtpy)(4′-MeO-Phtpy)](PF$_6$)$_3$ A suspension of [(4′-MeO-Phtpy)IrCl$_3$] (24 mg, 0.038 mmol) and 4′-COOMe-Phtpy (16 mg, 0.042 mmol) was heated to 170°C in degassed ethylene glycol (2 mL) in the dark and under Ar for 1h. After cooling, aqueous NH_4PF_6 was added to precipitate the crude product. The pure product was isolated by column chromatography on Al_2O_3 (acetone/water, from 100/0 to 90/10), which yielded the complex as

a yellow solid (32 mg, 63%). ^{1}H NMR (CD_3CN, 500 MHz) (Figure 5.15): δ (ppm), 9.11 (s, 2H, $H_{3'}$ and $H_{5'}$ of tpy-C_6H_4-COOMe), 9.04 (s, 2H, $H_{3'}$ and $H_{5'}$ of tpy-C_6H_4-OMe), 8.72 (d, 4H, H_3 and $H_{3''}$ of both tpy's, J_{H3-H4} = 8.1 Hz), 8.41 (d, 2H, H_a of tpy-C_6H_4-COOMe, J_{Ha-Hb} = 8.3 Hz), 8.30 (d, 2H, H_b of tpy-C_6H_4-COOMe, J_{Hb-Ha} = 8,4 Hz), 8.24-8.21 (m, 6H, H_4 and $H_{4''}$ of both tpy's, H_b of tpy-C_6H_4-OMe), 7.70 (dd, 2H, H_6 and $H_{6''}$ of tpy-C_6H_4-COOMe, J_{H6-H5} = 4.9 Hz, J_{H6-H4} = 0.9 Hz), 7.68 (dd, 2H, H_6 and $H_{6''}$ of tpy-C_6H_4-OMe, J_{H6-H5} = 4.9 Hz, J_{H6-H4} = 0.9 Hz), 7.52-7.48 (m, 4H, H_5 and $H_{5''}$ of both tpy's), 7.34 (d, 2H, H_a of tpy-C_6H_4-OMe, J_{Ha-Hb} = 8.9 Hz), 4.00 (s, 6H, Me of ester and OMe). HRMS (ESI): m/z calculated for $[C_{45}H_{34}N_6O_3{}^{193}IrP_2F_{12} - PF_6]^+$, 1189.1600; found: 1189.1600, m/z calculated for $[C_{44}H_{32}N_6O_3{}^{193}Ir - 3PF_6]^{3+}$, 299.7435; found: 299.7442.

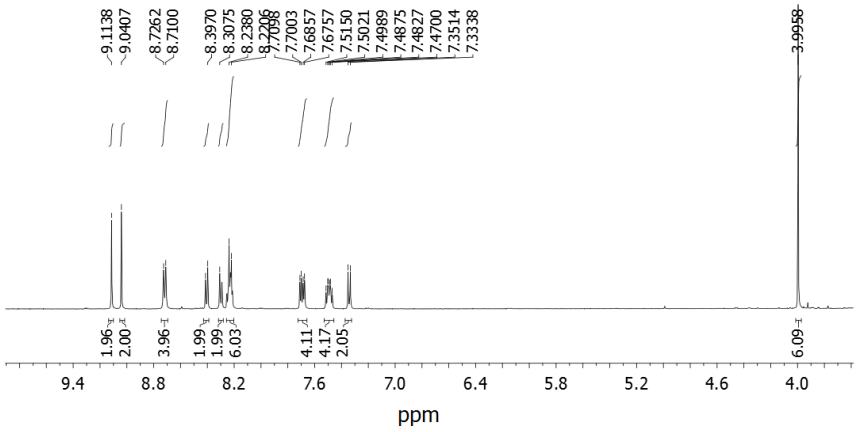

Figure 5.15 – ^{1}H NMR spectrum of **[Ir(4′-COOMe-Phtpy)(4′-MeO-Phtpy)]$^{3+}$** (ester) (500 MHz, CD_3CN).

5.7.3 Absorption and Emission spectra of [Ir(4'-COOMe-Phtpy)(4'-MeO-Phtpy)]$^{3+}$ (ester)

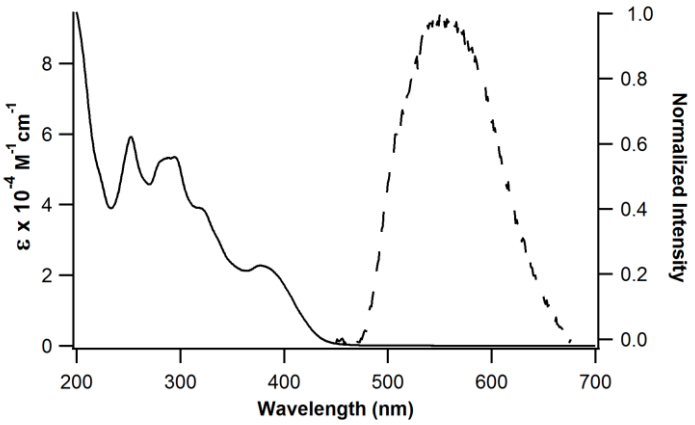

Figure 5.16 – Absorption (solid line) and emission (dashed line) (λ_{exc} = 350 nm) for **[Ir(4′-COOMe-Phtpy)(4′-MeO-Phtpy)]$^{3+}$** (ester) under air in CH_3CN.

5.7.4 Synthesis of other Ir(III) bis-terpyridine complexes

Different attempts have been made to modulate spectroscopic and electrochemical properties of Ir(III) bis-terpyridine complexes. Our idea was to modify one of tpy ligand by adding an increasing number of electron-donor groups (MeO) without changing the other tpy ligand. However, this strategy does not allow to conveniently tune the spectroscopic properties. The synthesis of these derivatives and their spectroscopic data are now presented.

Synthesis of [Ir(tpy)Cl$_3$)][73]

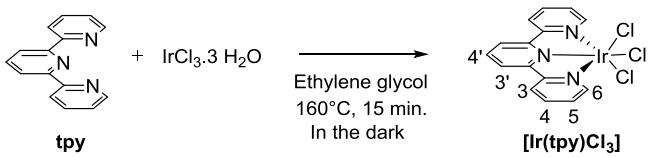

Typically, a suspension of tpy (132 mg, 0.56 mmol) and $IrCl_3.3H_2O$ (208 mg, 0.56 mmol) was heated at 160°C in degassed ethylene glycol (5 mL) under Argon for 15 minutes. The mixture was cooled to room temperature and washed with H_2O MilliQ (2x), EtOH and Et_2O to afford a red powder with a yield of 60% (180 mg). ^1H NMR (DMSO-d_6, 500 MHz) : δ (ppm), 9.24 (dd, 2H, H_6, J_{H6-H5} = 5.5 Hz, J_{H6-H4} = 1.1 Hz), 8.80 (d, 2H, H_3, J_{H3-H4} = 7.8 Hz), 8.76 (d, 2H, $H_{3'}$, $J_{H3'-H4'}$ = 8.0 Hz), 8.31 (td, 2H, H_4, $J_{H4-H3(H5)}$ = 7.8 Hz, J_{H4-H6} = 1.5 Hz), 8.27 (t, 1H, $H_{4'}$, $J_{H4'-H3'}$ = 8.0 Hz), 8.00 (ddd, 2H, H_5, J_{H5-H4} = 7.8 Hz, J_{H5-H6} = 5.6 Hz, J_{H5-H3} = 1.3 Hz).

Synthesis of [Ir(tpy)(4′-X-tpy)](3PF_6)

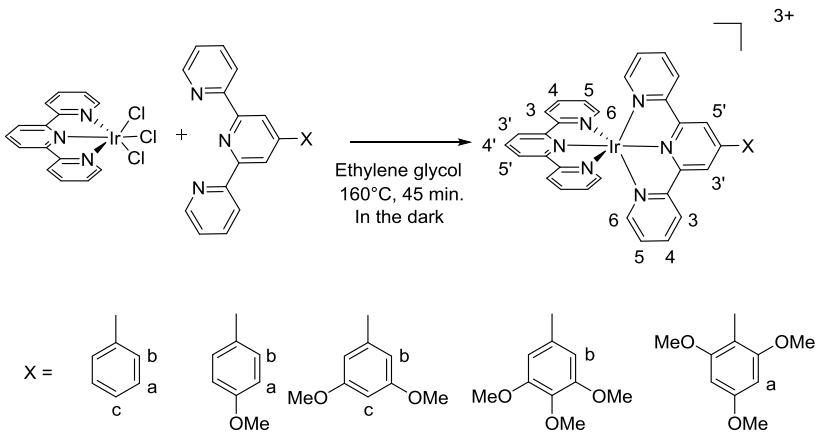

Typically, a suspension of [Ir(tpy)Cl_3] (1 equiv.) and 4′-X-Phtpy (1 equiv.) was heated at 160 °C for 45 minutes in degassed ethylene glycol (5 mL) under Ar. The mixture was cooled to room temperature and the precipitate (by-product) was isolated by centrifugation. The supernatant was recovered and the addition of an excess of NH_4PF_6 precipitated the crude product. This latter was washed with H_2O MilliQ (three times) and purified by column chromatography on Al_2O_3 (elution gradient: hexane-acetone/acetone/acetone-H_2O, 35:65/100/95:5) to afford the pure product as a yellow (orange) powder.

[Ir(tpy)(Phtpy)](3PF$_6$) (X = Ph)[249]

Yield: 25 %. (Yellow powder) ^{1}H NMR (acetone-d$_6$, 500 MHz) : δ (ppm), 9.59 (s, 2H, H$_{3'}$ and H$_{5'}$ of tpy-C$_6$H$_4$-H), 9.27 (d, 2H, H$_{3'}$ and H$_{5'}$ of tpy, $J_{H3'-H4'}$ = 8.3 Hz), 9.20 (dd, 2H, H$_3$ of tpy-C$_6$H$_4$-H, J_{H3-H4} = 7.7 Hz, J_{H3-H5} = 1.0 Hz), 9.00 (t, 1H, H$_{4'}$ of tpy, $J_{H4'-H3'}$ = 8.3 Hz), 8.98 (dd, 2H, H$_3$ of tpy, J_{H3-H4} = 8.0 Hz, J_{H3-H5} = 1.0 Hz), 8.41 (td, 2H, H$_4$ of tpy-C$_6$H$_4$-H, $J_{H4-H3\ (H5)}$ = 7.7 Hz, J_{H4-H6} = 1.1 Hz), 8.39 (td, 2H, H$_4$ of tpy, $J_{H4-H3\ (H5)}$ = 8.0 Hz, J_{H4-H6} = 1.1 Hz), 8.32 (m, 2H, H$_b$), 8.26 (dd, 2H, H$_6$ of tpy-C$_6$H$_4$-H, J_{H6-H5} = 5.7 Hz, J_{H6-H4} = 1.1 Hz), 8.18 (dd, 2H, H$_6$ of tpy, J_{H6-H5} = 5.7 Hz, J_{H6-H4} = 1.1 Hz), 7.78 (m, 3H, H$_a$ and H$_c$ of tpy-C$_6$H$_4$-H), 7.65 (ddd, 4H, H$_5$ of both tpy's, J_{H5-H4} = 7.7 Hz, J_{H5-H6} = 5.7 Hz, J_{H5-H3} = 1.0 Hz).

[Ir(tpy)(4′-MeO-Phtpy)](3PF$_6$) (X = 4-MeO-Ph)

Yield: 37 %. (Yellow powder) ^{1}H NMR (acetone-d$_6$, 500 MHz) : δ (ppm), 9.54 (s, 2H, H$_{3'}$ and H$_{5'}$ of tpy-C$_6$H$_4$-OMe), 9.26 (d, 2H, H$_{3'}$ and H$_{5'}$ of tpy, $J_{H3'-H4'}$ = 8.3 Hz), 9.18 (d, 2H, H$_3$ of tpy-C$_6$H$_4$-OMe, J_{H3-H4} = 7.4 Hz), 8.99 (t, 1H, H$_{4'}$ of tpy, $J_{H4'-H3'}$ = 8.3 Hz), 8.97 (d, 2H, H$_3$ of tpy, J_{H3-H4} = 7.5 Hz), 8.38 (m, 4H, H$_4$ of both tpy's), 8.34 (d, 2H, H$_b$ of tpy-C$_6$H$_4$-OMe, J_{Hb-Ha} = 8.7 Hz), 8.26 (dd, 2H, H$_6$ of tpy-C$_6$H$_4$-OMe, J_{H6-H5} = 5.7 Hz, J_{H6-H4} = 0.9 Hz), 8.16 (dd, 2H, H$_6$ of tpy, J_{H6-H5} = 5.7 Hz, J_{H6-H4} = 0.9 Hz), 7.64 (m, 4H, H$_5$ of both tpy's), 7.32 (d, 2H, H$_a$ of C$_6$H$_4$-OMe, J_{Ha-Hb} = 8.7 Hz), 4.00 (s, 3H, OMe).

[Ir(tpy)(4′-(3,5-diMeO-Phtpy))](3PF$_6$) (X = 3,5-diMeO-Ph)

Yield: 30 %. (Yellow powder) ^{1}H NMR (acetone-d$_6$, 500 MHz) : δ (ppm), 9.49 (s, 2H, H$_{3'}$ and H$_{5'}$ of tpy-C$_6$H$_3$-2OMe), 9.24 (d, 2H, H$_{3'}$ and H$_{5'}$ of tpy, $J_{H3'-H4'}$ = 8.3 Hz), 9.15 (dd, 2H, H$_3$ of tpy-C$_6$H$_3$-2OMe, J_{H3-H4} = 8.2 Hz, J_{H3-H5} = 0.7 Hz), 8.97 (t, 1H, H$_{4'}$ of tpy, $J_{H4'-H3'}$ = 8.3 Hz), 8.96 (dd, 2H, H$_3$ of tpy, J_{H3-H4} = 8.2 Hz, J_{H3-H5} = 0.7 Hz), 8.34 (m, 4H, H$_4$ of both tpy's), 8.20 (dd, 2H, H$_6$ of tpy-C$_6$H$_3$-2OMe, J_{H6-H5} = 5.7 Hz, J_{H6-H4} = 0.9 Hz), 8.15 (dd, 2H, H$_6$ of

tpy, J_{H6-H5} = 5.7 Hz, J_{H6-H4} = 0.9 Hz), 7.63 (m, 4H, H_5 of both tpy's), 7.40 (d, 2H, H_b of tpy-C_6H_3-2OMe, J_{Hb-Ha} = 2.2 Hz), 6.86 (d, 2H, H_c of tpy-C_6H_3-2OMe, J_{Hc-Hb} = 2.2 Hz), 3.99 (s, 6H, 2OMe).

[Ir(tpy)(4′-(3,4,5-triMeO-Phtpy))](3PF$_6$) (X = 3,4,5-triMeO-Ph)

Yield: 23 %. (Yellow powder) ^{1}H NMR (acetone-d_6, 500 MHz) : δ (ppm), 9.49 (s, 2H, $H_{3'}$ and $H_{5'}$ of tpy-C_6H_2-3OMe), 9.27 (d, 2H, $H_{3'}$ and $H_{5'}$ of tpy, $J_{H3'-H4'}$ = 8.3 Hz), 9.07 (d, 2H, H_3 of tpy-C_6H_2-3OMe, J_{H3-H4} = 7.5 Hz), 8.99 (t, 1H, $H_{4'}$ of tpy, $J_{H4'-H3'}$ = 8.3 Hz), 8.98 (d, 2H, H_3 of tpy, J_{H3-H4} = 7.5 Hz), 8.39 (m, 4H, H_4 of both tpy's), 8.21 (dd, 2H, H_6 of tpy-C_6H_2-3OMe, J_{H6-H5} = 5.7 Hz, J_{H6-H4} = 0.9 Hz), 8.16 (dd, 2H, H_6 of tpy, J_{H6-H5} = 5.7 Hz, J_{H6-H4} = 0.9 Hz), 7.64 (m, 4H, H_5 of both tpy's), 7.32 (s, 2H, H_b of tpy-C_6H_3-2OMe), 4.04 (s, 6H, 2OMe), 3.91 (s, 3H, OMe).

[Ir(tpy)(4′-(2,4,6-triMeO-Phtpy))](3PF$_6$) (X = 2,4,6-triMeO-Ph)

Yield: 12 %. (Orange powder) ^{1}H NMR (acetone-d_6, 500 MHz) : δ (ppm), 9.28 (s, 2H, $H_{3'}$ and $H_{5'}$ of tpy-C_6H_2-3OMe), 9.23 (d, 2H, $H_{3'}$ and $H_{5'}$ of tpy, $J_{H3'-H4'}$ = 8.3 Hz), 8.97 (t, 5H, H_3 of both tpy's and $H_{4'}$ of tpy, $J_{H4'-H3'}$ = $J_{H3-H4(H5)}$ = 8.3 Hz), 8.38 (m, 2H, H_4 of tpy-C_6H_2-3OMe), 8.33 (m, 2H, H_4 of tpy), 8.17 (dd, 2H, H_6 of tpy-C_6H_2-3OMe, J_{H6-H5} = 5.7 Hz, J_{H6-H4} = 0.9 Hz), 8.12 (dd, 2H, H_6 of tpy, J_{H6-H5} = 5.7 Hz, J_{H6-H4} = 0.9 Hz), 7.67 (m, 2H, H_5 of tpy-C_6H_2-3OMe), 7.59 (m, 2H, H_5 of tpy), 6.58 (s, 2H, H_a of tpy-C_6H_3-2OMe), 4.00 (s, 3H, OMe), 3.99 (s, 6H, 2OMe).

5.7.5 Spectroscopic data of others Ir(III) bis-terpyridine complexes

The Figure 5.17 gathers absorption and emission spectra of novel Ir(III) bis-terpyridine complexes bearing some electron-donating methoxy group(s) (MeO). We expected that absorption and emission properties would be tuned upon addition of one or several MeO groups leading to more and more photo-reducing complexes when further electron-donating groups (MeO)

were added. Although absorption properties were clearly modified upon addition of methoxy groups, the emission spectra were almost unaltered upon these modifications. Unfortunately, the addition of one MeO group or several ones furnished similar spectroscopic properties. Therefore, this strategy was given up for the modification of the close coordinating sphere (C/N ratio).

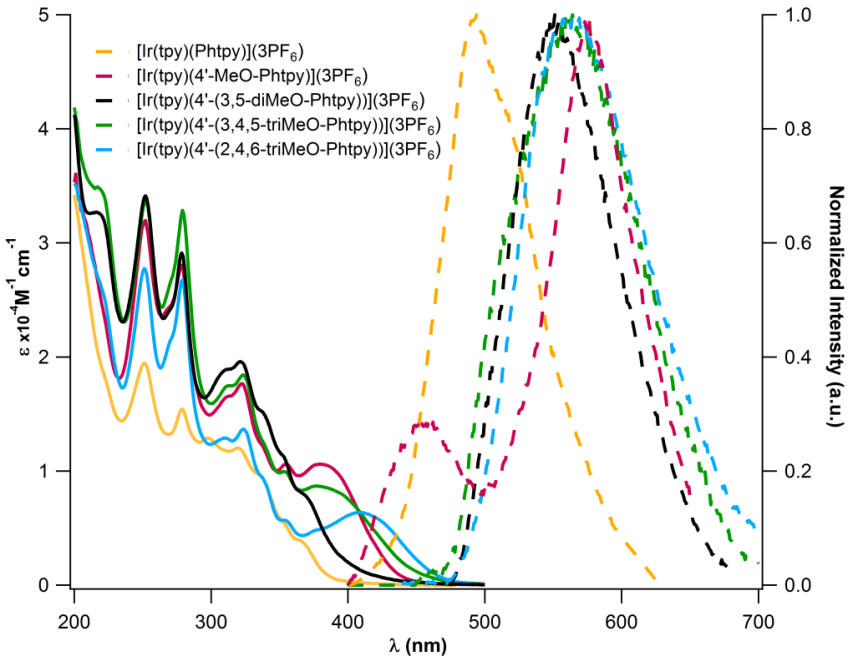

Figure 5.17 – Absorption and emission (λ_{Exc} = 350 nm) spectra of [Ir(tpy)(Phtpy)](3PF$_6$), [Ir(tpy)(4′-MeO-Phtpy)](3PF$_6$), [Ir(tpy)(4′-(3,5-diMeO-Phtpy))](3PF$_6$), [Ir(tpy)(4′-(3,4,5-diMeO-Phtpy))](3PF$_6$) and [Ir(tpy)(4′-(2,4,6-diMeO-Phtpy))](3PF$_6$) in CH_3CN under air.

Chapter 6 - Grafting of Ir(III) Polypyridyl Complexes on graphene and application in photocatalysis

6.1 Introduction

The use of solar energy for the synthesis of complex organic molecules has remained unexplored for a long time.[250] Photochemical synthesis has long been considered as the field of a small community of scientists rather than a powerful universal tool in standard organic synthesis.[251,252] Several reasons explain this relative disregard. First, organic molecules mostly absorb the UV light that is not abundant (around 3%) in the solar radiation that penetrates the earth atmosphere.[253] In addition, UV photons are high in energy and therefore may lead to undesirable photo-decomposition especially when some weak bonds are present. In spite of these limitations, several examples of classic syntheses of complex targets include photo-chemical key steps.

Recently, visible light photo-redox catalysis has received much more attention from synthetic organic chemists.[254] This renewed interest clearly arises from the ability of organic dyes as well as transition metal complexes to trigger single electron transfer (SET) processes upon photo-excitation with visible light. As mentioned in the introduction, transition metal complexes become more oxidant and more reductive in the excited state. Therefore, some of them may react either as an oxidant or as a reducer depending on involved substrates.

Up to now, the majority of photocatalysts consists in either polypyridinic ruthenium(II) (such as $[Ru(bpy)_3]^{2+}$) or iridium(III) (such as *fac*-$[Ir(ppy)_3]$) complexes (Figure 6.1) even if some copper and gold complexes have also been recently reported.[255,256]

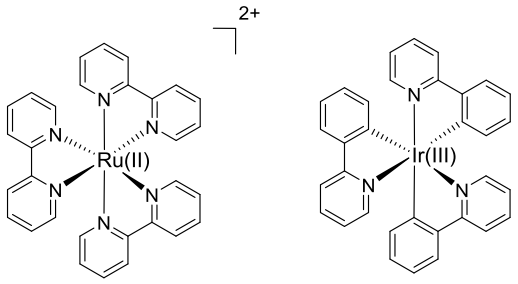

Figure 6.1 – Structure of some common photocatalysts.

These complexes share several features essential to properly achieve the photocatalysis. They absorb visible light and subsequent excited states are quite stable and long-lived, hence providing time to react with substrates. To the best of our knowledge, only bidentate-based complexes have been investigated. As previously discussed, their terdentate equivalents exhibit more interesting properties such as ease of functionalization and better thermal stability. In addition, Ir(III) bis-terdentate complexes also meet the conditions to be good photocatalysts. We focused on $\mathbf{[IrN_6]^{3+}}$ complexes especially for their more convenient synthesis and their high oxidation power in the excited state as compared to $\mathbf{[IrN_4C_2]^{+}}$ ones. Four $\mathbf{[IrN_6]^{3+}}$ complexes bearing different functionalized groups have been prepared (Figure 6.2). They have been chosen to allow subsequent grafting on solid support in order to recover the catalyst by filtration. Reduced graphene oxide (rGO) and graphene oxide (GO) have been designated as solid support because of their unique electronic and structural properties.[257-259] Although homogeneous photocatalysis supported on GO has already been developed for reactions such as carbon dioxide reduction[260,261] or degradation of rhodamine B,[262] supported visible-light photo-redox catalysis applied to more controlled organic reactions has scarcely been described despite its potential significance.[263]

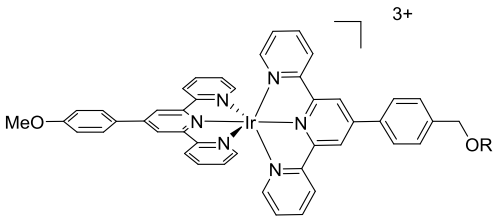

[IrN$_6$-OH]$^{3+}$: R = H,
[IrN$_6$-Br]$^{3+}$: R = COCBr(CH$_3$)$_2$,
[IrN$_6$-IPr]$^{3+}$: R = COCH(CH$_3$)$_2$,
[IrN$_6$-Pyrene]$^{3+}$: R = CO(CH$_2$)$_3$-Pyrene

Figure 6.2 – Structures of studied **[IrN$_6$]$^{3+}$** complexes.

A described model reaction[264] was used to test our photocatalytic systems (Scheme 6.1): the radical cyclization of 2-bromo-2-(pent-4-enyl)malonate. This synthesis has been selected because only one easily analyzable major product is obtained upon irradiation in the presence of the photocatalyst $[Ru(bpy)_3]^{2+}$.

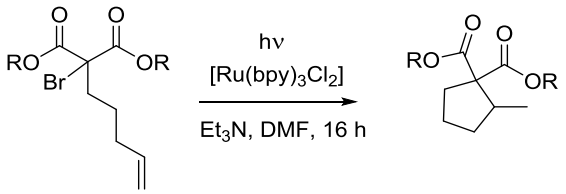

Scheme 6.1 – Model reaction: radical cyclization of 2-bromo-2-(pent-4-enyl)malonate.

The aim of this project was first to evidence the efficiency of terdentate complexes **[IrN$_6$]$^{3+}$** in homogeneous photocatalysis. Secondly, their covalent and non-covalent grafting on solid support was investigated. This will allow a comparison of both homogeneous and supported homogeneous photocatalysis in the same experimental conditions.

6.2 Results

6.2.1 Synthesis of $[IrN_6]^{3+}$ complexes

The synthesis of **$[IrN_6\text{-}OH]^{3+}$** was achieved in two steps according to well established methods.[244] This latter complex was used to obtain **$[IrN_6\text{-}Br]^{3+}$** and **$[IrN_6\text{-}IPr]^{3+}$** with good yields by esterification with the corresponding acyl halide in acetonitrile (Scheme 6.2). In addition, **$[IrN_6\text{-}OH]^{3+}$** was also coupled to 1-pyrenebutyric acid providing a complex (**$[IrN_6\text{-}Pyrene]^{3+}$**) able to non-covalently interact with graphene by π-π stacking (Scheme 6.2).[247] All four complexes were characterized by X-ray crystallography, ^{1}H NMR and High-Resolution Mass Spectrometry (HRMS).

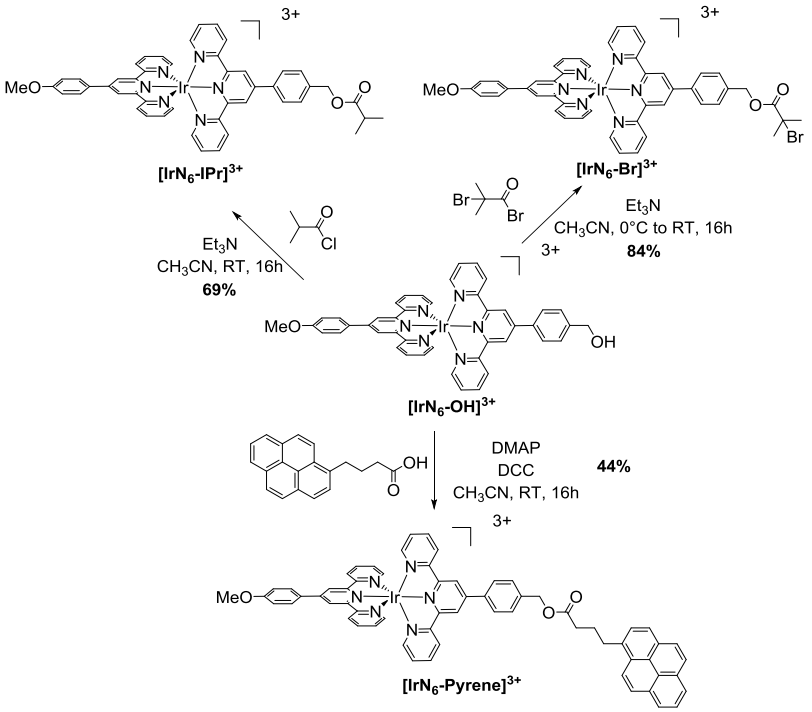

Scheme 6.2 – Synthesis and structures of **$[IrN_6\text{-}OH]^{3+}$**, **$[IrN_6\text{-}Br]^{3+}$**, **$[IrN_6\text{-}IPr]^{3+}$** and **$[IrN_6\text{-}Pyrene]^{3+}$**.

6.2.2 X-Ray structures of $[IrN_6]^{3+}$ complexes

Crystals suitable for X-Ray crystal diffraction were obtained for three of the complexes by slow diffusion of tetrahydrofuran into acetonitrile solution of compound at room temperature (Figure 6.3). Despite our efforts, we did not manage to obtain suitable crystals for the **$[IrN_6\text{-Pyrene}]^{3+}$** complex. The complex **$[IrN_6\text{-OH}]^{3+}$** crystallized in the monoclinic space group (C2/c) whereas both **$[IrN_6\text{-Br}]^{3+}$** and **$[IrN_6\text{-IPr}]^{3+}$** crystallized in the triclinic space group (P-1). X-Ray experimental data are collected in Table 6.1. Selected bond distances and angles for the analyzed complexes are gathered in Table 6.2. The Ir-N distances are close to each other for all the compounds although slightly longer for **$[IrN_6\text{-Br}]^{3+}$**. A detailed discussion concerning X-Ray crystal structure is given in the experimental section. The values obtained are in good agreement with previously related structures of $[Ir(tpy)_2]^{3+}$ [73] and other similar Ir(III) bis-terpyridine complexes.[244]

Complexes based on 2′,2′:6′,2″-terpyridines usually form a two-dimensional packing structure (termed “tpy embrace”) driven by the outer pyridyl rings.[265] This arrangement is here disrupted due to the presence of the bulky phenyl groups.[266] For **$[IrN_6\text{-OH}]^{3+}$**, the rings remain essentially coplanar but a staggered motif is adopted that extends out of the two-dimensional plane (Figure 6.4). For **$[IrN_6\text{-IPr}]^{3+}$** and **$[IrN_6\text{-Br}]^{3+}$**, this arrangement is not observed possibly due to steric hindrance induced by the bulkier lateral chain.

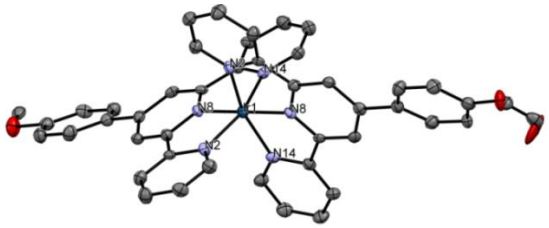

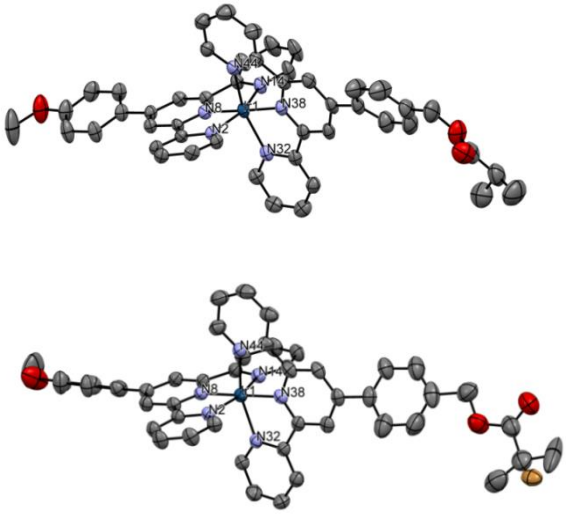

Figure 6.3 – ORTEP view (from top to bottom) of **[IrN$_6$-OH]$^{3+}$**, **[IrN$_6$-IPr]$^{3+}$** and **[IrN$_6$-Br]$^{3+}$**. Only one position of the terminal methoxy group is shown. Ellipsoids are shown at the 50 % probability level. Hydrogen atoms, hexafluorophosphate anions and solvent molecules have been omitted for clarity.

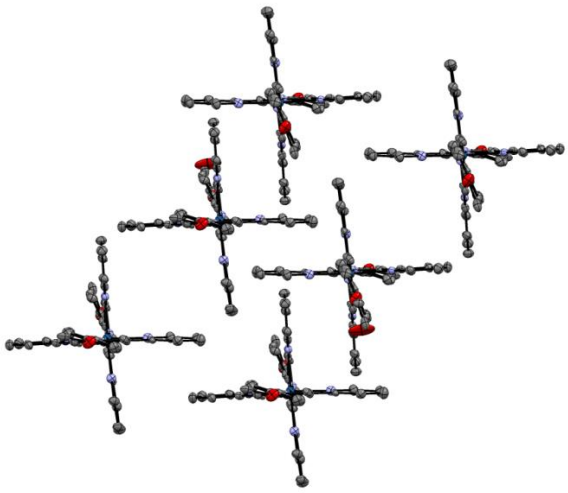

Figure 6.4 – Distorted "tpy embrace" packing for **[IrN$_6$-OH]$^{3+}$**. Hydrogen atoms, hexafluorophosphate anions and acetonitrile have been omitted for clarity.

Table 6.1 – Crystal data and structure refinement for **[IrN$_6$-OH]$^{3+}$**, **[IrN$_6$-Br]$^{3+}$** and **[IrN$_6$-IPr]$^{3+}$**.

	[IrN$_6$-OH]$^{3+}$	**[IrN$_6$-Br]$^{3+}$**	**[IrN$_6$-IPr]$^{3+}$**
Empirical formula	$C_{48}H_{40}F_{18}IrN_8O_2P_3$	$C_{50}H_{42.36}Br_{0.64}F_{18}IrN_7O_3P_3$	$C_{56}H_{56}F_{18}IrN_6O_5P_3$
Formula weight	1387.99	1467.84	1520.17
Temperature (K)	100(2)	150(2)	150(2)
Wavelength (Å)	0.71073	0.71073	0.71073
Crystal system	Monoclinic	Triclinic	Triclinic
Space group	C2/c	P-1	P-1
a (Å)	14.6270(6)	11.9202(6)	12.6649(6)
b (Å)	16.4793(6)	15.5826(8)	13.5583(8)
c (Å)	21.3062(9)	18.1183(9)	19.3416(4)
α (°)	90	111.056(5)	99.555(3)
β (°)	105.536(4)	93.837(4)	99.142(3)
γ (°)	90	96.700(4).	110.037(5)
Volume (Å^3)	4948.1(3)	3097.7(3)	2992.3(2)
Z	4	2	2
Density (calculated) (Mg/m^3)	1.863	1.574	1.687
Absorption coefficient (mm^{-1})	2.915	2.746	2.421
F(000)	2736	1444	1516
Crystal size (mm^3)	0.439 x 0.076 x 0.049	0.44 x 0.20 x 0.16	0.27 x 0.15 x 0.11
Reflections collected	15559	26729	43889
Independent reflections	4521	11432	11111
Data / restraints / parameters	4521 / 245 / 383	11432 / 28 / 764	11111 / 328 / 902
GoF	1.003	1.072	1.040
R_1(F) [I >2σ(I)]	0.0404	0.0477	0.0342
wR(F^2) [I >2σ(I)]	0.0677	0.1224	0.0847
R_1(F) (all data)	0.0587	0.0538	0.0377
wR(F^2) (all data)	0.0729	0.1284	0.0867
Largest diff. peak and hole (e.Å^{-3})	1.130/-0.668	2.252/-1.371	0.978/-0.791

Table 6.2 – Selected bond lengths [Å] and angles (deg) for **$[IrN_6\text{-}OH]^{3+}$**, **$[IrN_6\text{-}Br]^{3+}$** and **$[IrN_6\text{-}IPr]^{3+}$**.

	$[IrN_6\text{-}OH]^{3+}$	**$[IrN_6\text{-}Br]^{3+}$**	**$[IrN_6\text{-}IPr]^{3+}$**
Ir(1)-N(2)	2.055(4)	2.061(4)	2.055(3)
Ir(1)-N(8)	1.981(3)	1.988(5)	1.981(3)
Ir(1)-N(14)	2.051(4)	2.062(4)	2.055(3)
Ir(1)-N(32) (or N(2')[a])	2.055(4)	2.055(5)	2.065(3)
Ir(1)-N(38) (or N(8')[a])	1.981(3)	1.990(5)	1.980(3)
Ir(1)-N(44) (or N(14')[a])	2.051(4)	2.065(5)	2.049(3)
N(2)-Ir(1)-N(8)	79.41(14)	79.73(18)	80.06(12)
N(2)-Ir(1)-N(14)	159.45(13)	159.81(19)	159.71(12)
N(8)-Ir(1)-N(14)	80.08(14)	80.09(19)	80.04(13)
N(2)-Ir(1)-N(32)	92.96(15)	90.02(18)	93.33(12)
N(2)-Ir(1)-N(38)	103.30(14)	101.22(18)	99.80(12)
N(2)-Ir(1)-N(44)	90.5(2)	93.91(19)	88.36(13)
N(8)-Ir(1)-N(32)	97.25(14)	100.59(19)	102.20(13)
N(8)-Ir(1)-N(38)	176.2(2)	179.06(17)	178.27(13)
N(8)-Ir(1)-N(44)	103.30(14)	99.87(19)	97.98(13)
C10-C11-C20-C21[b]	19.3	27.1	15.5
C40-C41-C50-C51[b]	19.3	27.9	26.1

[a]For **$[IrN_6\text{-}OH]^{3+}$**, N(32), N(38) and N(44) respectively equals to N(2′), N(8′) and N(14′) due to symmetry. This also applies to angles. [b]Dihedral angles between terpyridine rings and aryl group.

6.2.3 Electrochemistry

The redox potentials of **$[IrN_6]^{3+}$** complexes were measured by cyclic voltammetry method. Data are collected in Table 6.3. The **$[IrN_6]^{3+}$** complexes display two irreversible one-electron reduction waves ascribed to successive reduction of both ligands. These reduction potentials are not altered after chemical modifications on the complex. An irreversible one-electron oxidation is observed for **$[IrN_6\text{-}OH]^{3+}$** possibly due to oxidation of benzylic alcohol. No oxidation process occurs for two other complexes up to + 1.8 V *vs.* Ag/AgCl which are believed to take place at higher potentials. It is worthwhile to mention that the solubility of the four complexes is relatively weak in acetonitrile. Therefore, adsorption on the glassy carbon disk prevents any easy measurements and leads to reproducibility issues.

Table 6.3 – Electrochemical data measured at room temperature in CH_3CN for **$[IrN_6]^{3+}$** complexes (10^{-5} mol/L) with Bu_4NClO_4 0.1 M as supporting electrolyte.

Complexes	**$[IrN_6\text{-}OH]^{3+}$**	**$[IrN_6\text{-}Br]^{3+}$**	**$[IrN_6\text{-}IPr]^{3+}$**	**$[IrN_6\text{-}Pyrene]^{3+}$**
E_{ox} (V *vs.*Ag/AgCl)	1.24 (ir)	> 1.8	>1.8	>1.8
E_{red} (V *vs.* Ag/AgCl)	- 0.88 (ir), - 1.29 (ir)	- 0.78 (ir), - 1.23 (ir)	- 0.83 (ir), - 1.34 (ir)	- 0.88 (ir), - 1.38 (ir)

6.2.4 Spectroscopic properties

Absorption and emission spectra in CH_3CN under air at room temperature for four complexes are shown in Figure 6.5. Table 6.4 gathers the corresponding data. For all the complexes, absorption (ε > 25,000 M^{-1} cm^{-1}) bands in UV region tailing into the visible are observed. In the case of **$[IrN_6\text{-}Pyrene]^{3+}$**, well-resolved absorption bands ascribed to pyrene

$^1\pi-\pi^*$ transitions emerge as well. **$[IrN_6\text{-}OH]^{3+}$**, **$[IrN_6\text{-}Br]^{3+}$** and **$[IrN_6\text{-}IPr]^{3+}$** complexes emit in CH_3CN under air ($\Phi \sim 10^{-3}$) whereas no luminescence (λ_{exc} = 350 nm) is monitored for **$[IrN_6\text{-}Pyrene]^{3+}$**. This quenching effect possibly arises from a photo-induced electron transfer from the pyrene unit to **$[IrN_6]^{3+}$** even though no additional experiments have been performed so far to determine the nature of this luminescence quenching. A broad band emission centered on 560 nm is observed for three luminescent complexes.

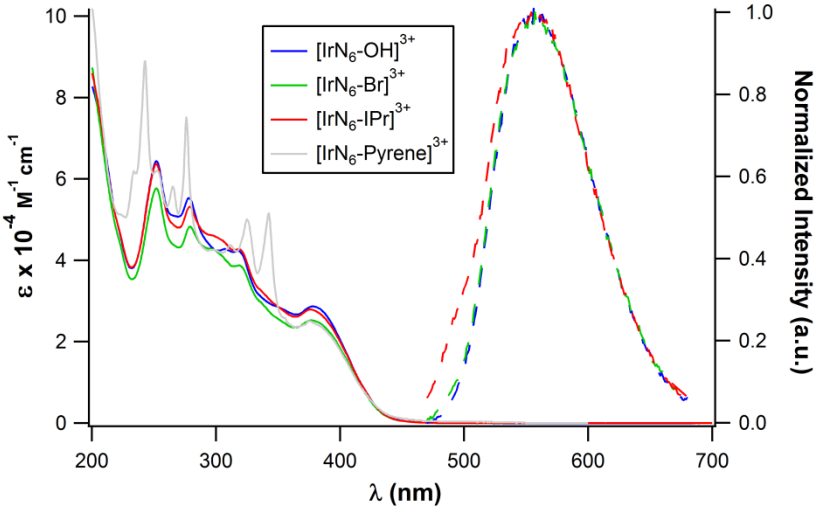

Figure 6.5 – Absorption (solid line) and emission (dashed line) (λ_{exc} = 350 nm) for **$[IrN_6\text{-}OH]^{3+}$**, **$[IrN_6\text{-}Br]^{3+}$**, **$[IrN_6\text{-}IPr]^{3+}$** and **$[IrN_6\text{-}Pyrene]^{3+}$** under air in CH_3CN.

The excited state lifetimes are close to 2 µs under argon and relatively sensitive to oxygen ($\tau \sim 0.8$ µs under air). All three complexes display some very close spectroscopic data evidencing the low influence of chemical modifications on the tpy unit.

Table 6.4 – Absorption and luminescence data for the Ir(III) complexes.

Complexes	$[IrN_6\text{-}OH]^{3+}$	$[IrN_6\text{-}Br]^{3+}$	$[IrN_6\text{-}IPr]^{3+}$	$[IrN_6\text{-}Pyrene]^{3+}$
λ_{max}/nm (ε*10^{-3} $M^{-1}cm^{-1}$)	378 (28.7), 318 (42.2), 307 (42.8), 278 (55.3), 252 (64.4)	377 (25.3), 319 (38.8), 299 (42.6), 279 (48.3), 252 (57.7)	376 (27.9), 319 (42.8), 298 (46.1), 279 (53.1), 252 (63.4)	376 (25.1), 342 (51.6), 325 (50.1), 311 (43.7), 276 (75.1), 265 (58.2), 253 (62.0), 243 (88.9), 234 (61.9)
λ max $_{Em}$[a] at 298 K	559	561	562	-[b]
λ max $_{Em}$[c] at 77 K	510	511	507	-[b]
τ[a] under air (μs)	0.82	0.80	0.71	-[b]
τ[a] under Ar (μs)	2.28	2.37	1.75	-[b]
Φ[d] under air	0.006	0.003	0.005	-[b]
Φ[d] under Ar	0.008	0.004	0.007	-[b]

[a]Measured in CH_3CN. λ_{exc} = 350 nm. [b]Not emissive. [c]Measured in a mixture EtOH/MeOH (4/1). [d]Quantum yield (± 5%) was measured under air using $[Ru(bpy)_3]^{2+}$ as reference Φ_{ref} = 0.028 in H_2O.[140]

6.2.5 Homogeneous photocatalysis

This part of the study was conducted in close collaboration with Christophe RUBAY (Prof B. ELIAS) for his Ph.D. thesis. Therefore, only the main results are discussed here. For homogeneous and supported homogeneous photocatalyses, all the reactions were carried out in the same conditions (Scheme 6.3) in order to compare the results in terms of yield or conversion.

[IrN$_6$-OH]$^{3+}$ as well as **[IrN$_6$-IPr]$^{3+}$** were shown to be efficient homogeneous photocatalysts for the model reaction under Ar using triethylamine as a sacrificial electron donor in DMF (**[IrN$_6$-Br]$^{3+}$** was not tested because of its labile C-Br bond under these conditions). However, the reaction leads to at least two different products (**2** and **3** in Scheme 6.3). In addition, the nature of irradiation lamps has a dramatic effect on the photocatalytic efficiency. The fluocompact and halogen lamps gave poor conversion while LEDs lamp significantly improves the photocatalytic efficiency. This result possibly arises from the substantially lower amount of UV irradiation provided by LEDs lamps with respect to the other kind of lamps. After optimization with the LEDs lamp, the conversion after 16 h into the product **3** (monitored by ^{1}H NMR experiments) reached 88 % and 91 % respectively for **[IrN$_6$-OH]$^{3+}$** and **[IrN$_6$-IPr]$^{3+}$**. The photoredox catalysis does not work when **[IrN$_6$-Pyrene]$^{3+}$** was used. This result highlights the requirement of a long-lived excited state to trigger photocatalysis.

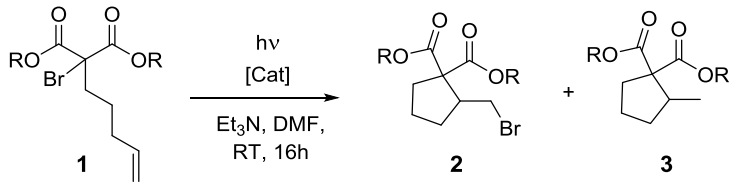

[Cat] =		
[IrN$_6$-OH]$^{3+}$	12%	88%
[IrN$_6$-IPr]$^{3+}$	9%	91%
[IrN$_6$-Pyrene]$^{3+}$	0%	0%

Scheme 6.3 – Five-membered ring cyclization with **[IrN$_6$-OH]$^{3+}$** and **[IrN$_6$-IPr]$^{3+}$** and **[IrN$_6$-Pyrene]$^{3+}$** as photocatalyst.

6.2.6 Grafting of Ir(III) complexes on GO and rGO

The covalent grafting of **[IrN$_6$]$^{3+}$** was achieved by Florence PENNETREAU (Prof. S. HERMANS and Prof. O. RIANT-UCL/MOST). Several strategies were investigated. First, the covalent grafting of **[IrN$_6$-**

Br]$^{3+}$ on rGO by Cu(I)-based radical coupling (Scheme 6.4) was tested.[267] Unfortunately, the quantity of grafted iridium(III) invariably remains low whichever the conditions used (maximum atomic concentration of 0.034 % of Ir(III) measured by XPS).

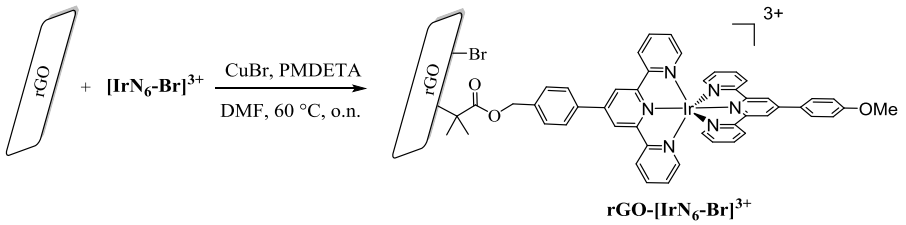

Scheme 6.4 – First synthetic approach to yield supported **[IrN$_6$]**$^{3+}$ complex on rGO.

As a result, another grafting method was used (Scheme 6.5): the coupling between **[IrN$_6$-OH]**$^{3+}$ and acyl chloride functions of activated GO.[268] This strategy turned out to be much more efficient with a significant loading of catalyst on GO. After treatment of GO by thionyl chloride, the atomic concentration (determined by XPS analysis) in chlorine equals 1.77 %. The subsequent coupling with **[IrN$_6$-OH]**$^{3+}$ in acetonitrile at 60 °C led to the covalently grafted **GO-[IrN$_6$-OH]**$^{3+}$.

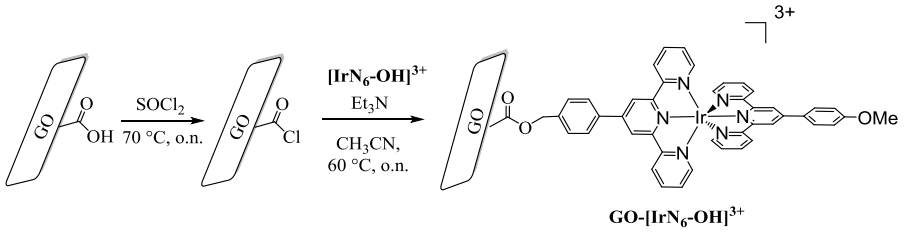

Scheme 6.5 – Synthetic strategy for covalent grafting of **[IrN$_6$-OH]**$^{3+}$ on GO.

After functionalization, XPS spectra revealed the expected apparition of both nitrogen (atomic concentration = 2.97 %) and iridium peaks (atomic concentration = 0.42 %) belonging to the complex (XPS

analyses were repeated three times with good reproducibility). As a result, the N/Ir ratio was found at 6.99. This value is close to the expected ratio of 6 witnessing the conservation of the **$[IrN_6\text{-}OH]^{3+}$** structure. The Ir4f XPS spectrum (Figure 6.6) showed two characteristic peaks, the $Ir4f_{5/2}$ peak centered at 66.8 eV and the $Ir4f_{7/2}$ centered at 64.0 eV. In addition, bulk elemental analyses further confirmed the presence of iridium (1.23 wt %, 0.0064 % molar) and nitrogen (1.02 wt %, 0.0728 % molar).

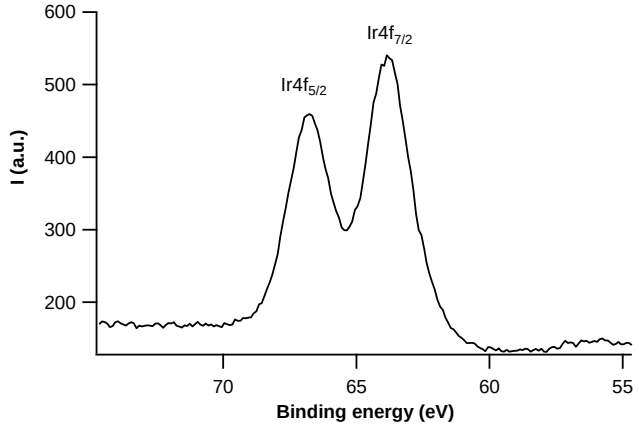

Figure 6.6 – Zoom on the Ir4f peak of the XPS spectrum of **GO-$[IrN_6\text{-}OH]^{3+}$**.

6.2.7 Supported homogeneous photocatalysis

Unlike **rGO-$[IrN_6\text{-}Br]^{3+}$**, the functionalized **GO-$[IrN_6\text{-}OH]^{3+}$** photocatalyses the model reaction. This result highlights that a minimum quantity of **$[IrN_6]^{3+}$** should be anchored on rGO to perform the photo-reaction. The conversion was lower (46 % of **3** and 6 % of **2**) as compared with homogeneous **$[IrN_6\text{-}OH]^{3+}$** catalyst (88 %). However, after filtration and washing, XPS analysis showed that a large amount of Iridium(III) was still tethered to the GO. The recycled catalyst was reused and the conversion was maintained at 45 % for the product **3** for the second use. However, when the anchoring of **$[IrN_6\text{-}OH]^{3+}$** on GO was further attempted, the resulting catalyst worked only once. After recycling, the conversion dramatically

decreases and only low amount of Ir(III) was still linked to the support. This effect could be due to:

- decomplexation of ligands on Ir(III)
- leaching during the photocatalysis
- destructive interactions when catalysis occurs

This deleterious behaviour is still under investigation. It has been discovered that the solvent plays an important role. When replacing DMF by dichloromethane, the photocatalysis conversion was lower. However, the recycling was much more efficient with a large amount of Ir(III) recovered on GO.

Although **[IrN$_6$-Pyrene]$^{3+}$** was not luminescent at room temperature, the photocatalysis has been nevertheless tried. As expected, almost no reaction occurred since conversion barely reached 2 %. We suspected that π–π stacking interactions between pyrene moiety and graphene may induce a particular effect. *De facto*, the **[IrN$_6$-Pyrene]$^{3+}$**/rGO mixture led to a conversion of 40 % (20 times better than without graphene). This behaviour results probably from π–π stacking interactions between rGO and pyrene moiety preventing the quenching of luminescence observed for the free complex. As a consequence, the restored excited state may have sufficiently long lifetime to photocatalyze the cyclization. These results brought to light that the supported photocatalysis remains very complicated to address despite some obvious advances. To the best of our knowledge, this work represents one of the first examples of a controlled organic reaction achieved by supported homogeneous photocatalysis with **[IrN$_6$]$^{3+}$** complexes.

6.3 Conclusions

Four heteroleptic **[IrN$_6$]$^{3+}$** complexes were synthetized and fully characterized. With emission lifetimes close to 2 µs under argon,

[IrN$_6$-OH]$^{3+}$ and **[IrN$_6$-IPr]$^{3+}$** efficiently photocatalyze the radical cyclization of 2-bromo-2-(pent-4-enyl)malonate in contrast to the non-luminescent **[IrN$_6$-Pyrene]$^{3+}$**. The easy functionalization of terdentate ligands as compared with bidentate ones led to efficient covalent grafting of **[IrN$_6$-OH]$^{3+}$** and non-covalent grafting of **[IrN$_6$-Pyrene]$^{3+}$** by π–π stacking interactions on rGO. The resulting **GO-[IrN$_6$-OH]$^{3+}$** catalyst retained an activity as supported photocatalyst despite a less effective conversion. However, this catalyst may be recovered and reused without any significant change in conversion values although some reproducibility issues occured. In contrast, **rGO-[IrN$_6$-Pyrene]$^{3+}$** catalyst becomes active as supported catalyst whereas no reaction occurred with the free **[IrN$_6$-Pyrene]$^{3+}$**.

6.4 Experimental section

6.4.1 Synthesis of complexes

[IrN$_6$-OH](3PF$_6$)

A suspension of [(4′-MeO-Phtpy)IrCl$_3$] (58 mg, 0.091 mmol) and 4′-CH$_2$OH-Phtpy (34 mg, 0.100 mmol) was heated to 170 °C in degassed ethylene glycol (2 mL) in the dark under Ar for 30 min. After cooling, aqueous NH_4PF_6 was added to precipitate the crude product. The pure product was isolated by column chromatography on Al_2O_3 (acetone/water, from 100/0 to 90/10), which yielded the complex as a yellow solid (115 mg, 97%). ^{1}H NMR (CD_3CN, 300 MHz) (Figure 6.7): δ (ppm), 9.09 (s, 2H, H$_{3'}$ and H$_{5'}$ of tpy-C$_6$H$_4$-CH$_2$OH), 9.04 (s, 2H, H$_{3'}$ and H$_{5'}$ of tpy-C$_6$H$_4$-OMe), 8.72 (d, 4H, H$_3$ and H$_{3''}$ of both tpys, J_{H3-H4} = 8.0 Hz), 8.25-8.18 (m, 8H, H$_4$ and H$_{4''}$ of both tpys, H$_b$ of tpy-C$_6$H$_4$-OMe and H$_b$ of tpy-C$_6$H$_4$-CH$_2$OH), 7.78 (d, 2H, H$_a$ of tpy-C$_6$H$_4$-CH$_2$OH, J_{Ha-Hb} = 8.4 Hz), 7.71-7.68 (m, 4H, H$_6$ and H$_{6''}$ of both tpys), 7.48 (m, 4H, H$_5$ and H$_{5''}$ of both tpys), 7.34 (d, 2H, H$_a$ of tpy-C$_6$H$_4$-OMe, J_{Ha-Hb} = 8.9 Hz), 4.82 (d, 2H, CH$_2$-OH, J_{CH2-OH} = 5.6 Hz), 4.00 (s, 3H, OMe), 3.49 (t, 1H, -OH, J_{HO-CH2} = 5.7 Hz). HRMS (ESI): m/z

calculated for $[C_{44}H_{34}N_6O_2{}^{193}IrP_2F_{12}]^+$, 1161.1651; found: 1161.1657, m/z calculated for $[C_{44}H_{34}N_6O_2{}^{193}IrPF_6]^{2+}$, 508.1002; found: 508.1005, m/z calculated for $[C_{44}H_{34}N_6O_2{}^{193}Ir]^{3+}$, 290.4119; found: 290.4119.

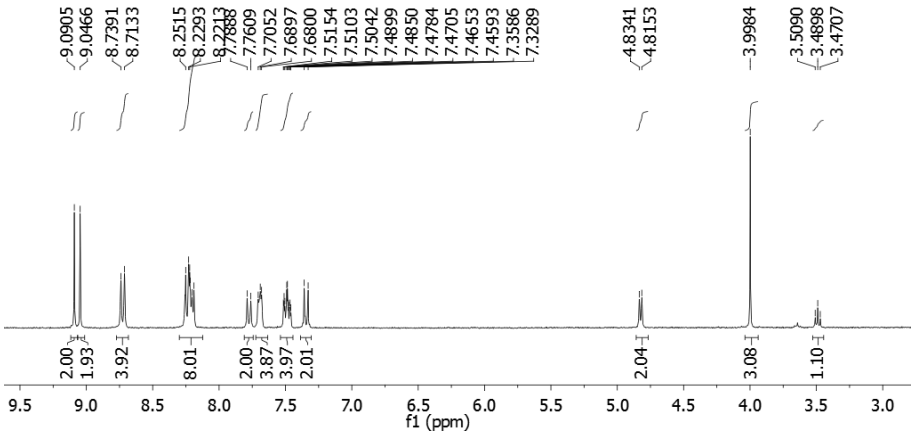

Figure 6.7 – ^{1}H NMR spectrum of **[IrN$_6$-OH](3PF$_6$)** (300 MHz, CD_3CN).

[IrN$_6$-Br](3PF$_6$)

To **[IrN$_6$-OH](3PF$_6$)** (50 mg, 0.038 mmol) and Et_3N (0.1 mL, 0.76 mmol) dissolved in dry acetonitrile (14 mL) was added 2-bromo-2-methylpropionyl bromide (0.047 mL, 88 mg, 0.38 mmol) at 0 °C under Ar. The reaction was warmed up to room temperature over 16h. Aqueous NH_4PF_6 (2 mL) was added to quench the reaction and solvent removed. The orange powder was washed with water, EtOH and Et_2O. Recrystallization using CH_3CN-THF yielded the pure complex as yellow-orange solid (46 mg, 84%). ^{1}H NMR (CD_3CN, 300 MHz) (Figure 6.8) : δ (ppm), 9.09 (s, 2H, $H_{3'}$ and $H_{5'}$ of tpy-C_6H_4-$CH_2OCOC(CH_3)_2Br$), 9.04 (s, 2H, $H_{3'}$ and $H_{5'}$ of tpy-C_6H_4-OMe), 8.72 (d, 4H, H_3 and $H_{3''}$ of both tpys, J_{H3-H4} = 8.2 Hz), 8.27-8.19 (m, 8H, H_4 and $H_{4''}$ of both tpys, H_b of both tpys), 7.84 (d, 2H, H_a of tpy-C_6H_4-$CH_2OCOC(CH_3)_2Br$, J_{Ha-Hb} = 8.3 Hz), 7.70 (dd, 4H, H_6 and $H_{6''}$ of both tpys, J_{H6-H5} = 5.5 Hz, J_{H6-H4} = 0.9 Hz), 7.53-7.45 (m, 4H, H_5 and $H_{5''}$ of both tpys), 7.34 (d, 2H, H_a of tpy-C_6H_4-OMe, J_{Ha-Hb} = 8.9 Hz), 5.43 (s, 2H, CH_2), 4.00

(s, 3H, OMe), 2.02 (s, 6H, -$(CH_3)_2$Br). HRMS (ESI): m/z calculated for $[C_{48}H_{39}N_6O_3Br^{193}IrP_2F_{12}]^+$, 1309.1174; found: 1309.1164, m/z calculated for $[C_{48}H_{39}N_6O_3Br^{193}IrPF_6]^{2+}$, 582.0764; found: 582.0760, m/z calculated for $[C_{48}H_{39}N_6O_3Br^{193}Ir]^{3+}$, 339.7293; found: 339.7291.

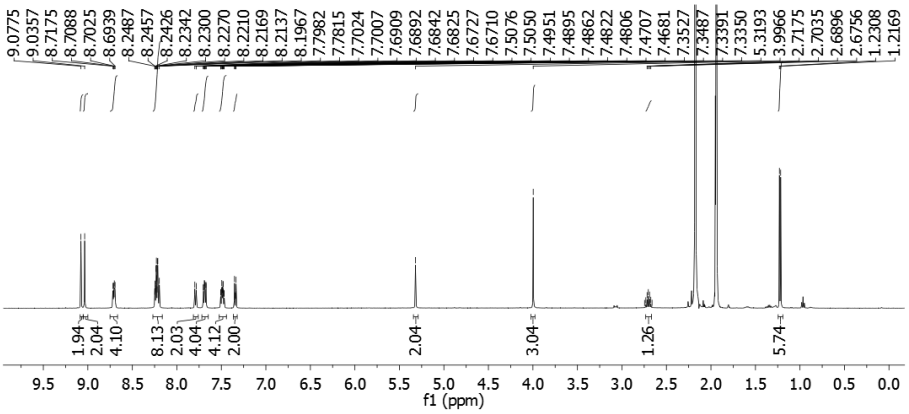

Figure 6.8 – ^{1}H NMR of **[IrN_6-IPr](3PF_6)** (300 MHz, CD_3CN).

[IrN_6-IPr](3PF_6)

To **[IrN_6-OH](3PF_6)** (25 mg, 0.019 mmol) and Et_3N (0.416 mL, 3.80 mmol) dissolved in dry acetonitrile (8 mL) was added isobutyryl chloride (0.202 mL, 203 mg, 1.90 mmol) at room temperature under Argon. The reaction was stirred for 16h. Aqueous NH_4PF_6 (2 mL) was added to quench the reaction and solvent removed. The yellow powder was washed with water, EtOH and Et_2O. Recrystallization using CH_3CN-THF yielded the pure complex as yellow solid (18 mg, 69%). ^{1}H NMR (CD_3CN, 300 MHz) (Figure 6.9) : δ (ppm), 9.08 (s, 2H, $H_{3'}$ and $H_{5'}$ of tpy-C_6H_4-$CH_2OCOCH(CH_3)_2$), 9.04 (s, 2H, $H_{3'}$ and $H_{5'}$ of tpy-C_6H_4-OMe), 8.71 (d, 2H, H_3 and $H_{3''}$ of tpy-C_6H_4-OMe, J_{H3-H4} = 7.5 Hz), 8.70 (d, 2H, H_3 and $H_{3''}$ of tpy-C_6H_4-$CH_2OCOCH(CH_3)_2$, J_{H3-H4} = 7.5 Hz) 8.25-8.19 (m, 8H, H_4 and $H_{4''}$ of both tpys, H_b of both tpys), 7.79 (d, 2H, H_a of tpy-C_6H_4-$CH_2OCOCH(CH_3)_2$, J_{Ha-Hb} = 8.4 Hz), 7.70 (dd, 2H, H_6 and $H_{6''}$ of tpy-C_6H_4-

OMe, J_{H6-H5} = 5.7 Hz, J_{H6-H4} = 0.9 Hz), 7.68 (dd, 2H, H_6 and $H_{6''}$ of tpy-C_6H_4-$CH_2OCOCH(CH_3)_2$, J_{H6-H5} = 5.7 Hz, J_{H6-H4} = 0.9 Hz), 7.51-7.46 (m, 4H, H_5 and $H_{5''}$ of both tpys), 7.34 (d, 2H, H_a of tpy-C_6H_4-OMe, J_{Ha-Hb} = 8.9 Hz), 5.32 (s, 2H, CH_2), 4.00 (s, 3H, OMe), 2.02 (s, 6H, -$(CH_3)_2$Br). HRMS (ESI): m/z calculated for $[C_{48}H_{40}N_6O_3{}^{193}IrP_2F_{12}]^+$, 1231.2069; found: 1231.2075, m/z calculated for $[C_{48}H_{40}N_6O_3{}^{193}IrPF_6]^{2+}$, 543.1211; found: 543.1215, m/z calculated for $[C_{48}H_{40}N_6O_3{}^{193}Ir]^{3+}$, 313.7592; found: 313.7590.

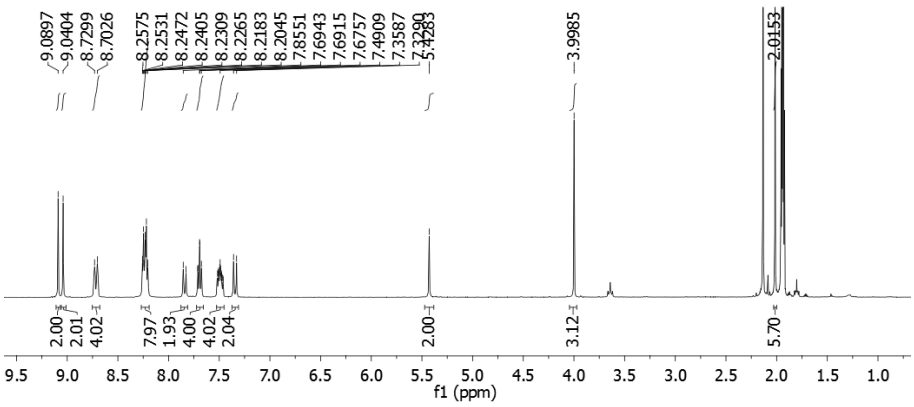

Figure 6.9 – ^{1}H NMR of **[IrN$_6$-Br](3PF$_6$)** (CD_3CN, 300 MHz).

[IrN$_6$-Pyrene](3PF$_6$)

To **[IrN$_6$-OH](3PF$_6$)** (30 mg, 0.023 mmol) dissolved in dry acetonitrile (8 mL) was successively added 1-pyrenebutyric acid (7 mg, 0.025 mmol), dimethylaminopyridine (DMAP) (1 mg, 0.007 mmol) and N,N'-dicyclohexylcarbodiimide (DCC) (5 mg, 0.025 mmol) at room temperature under Argon. The reaction was stirred for 16h. An excess of tetrabutyl ammonium chloride ($^tBu_4NCl$) was added to precipitate the crude product. After filtration, the solid was purified by a column chromatography on SiO_2 (Eluent: $CH_3CN/H_2O/KNO_{3aq\ sat}$ (90/9/1)) to afford an orange powder (16 mg, 44%). ^{1}H NMR (CD_3CN, 500 MHz) (Figure 6.10) : δ (ppm), 9.05 (s, 2H, $H_{3'}$ and $H_{5'}$ of tpy-C_6H_4-$CH_2OCO(CH_2)_3$-Pyrene), 9.04 (s, 2H, $H_{3'}$ and $H_{5'}$ of tpy-C_6H_4-OMe), 8.72 (d, 2H, H_3 and $H_{3''}$ of tpy-C_6H_4-OMe, J_{H3-H4} = 7.5

Hz), 8.66 (d, 2H, H_3 and $H_{3''}$ of tpy-C_6H_4-$CH_2OCO(CH_2)_3$-Pyrene, J_{H3-H4} = 7.5 Hz), 8.40 (d, 1H, H_{pyr}, $J_{Hpyr-Hpyr}$ = 9.3 Hz), 8.27-8.17 (m, 12H, H_4 and $H_{4''}$ of both tpys, H_b of both tpys, H_{pyr}), 8.14 (d, 1H, H_{pyr}, $J_{Hpyr-Hpyr}$ = 9.0 Hz), 8.11 (d, 1H, H_{pyr}, $J_{Hpyr-Hpyr}$ = 9.0 Hz), 8.02 (t, 1H, H_{pyr}, $J_{Hpyr-Hpyr}$ = 7.7 Hz), 7.99 (d, 1H, H_{pyr}, $J_{Hpyr-Hpyr}$ = 7.7 Hz), 7.80 (d, 2H, H_a of tpy-C_6H_4-$CH_2OCO(CH_2)_3$-Pyrene, J_{Ha-Hb} = 8.3 Hz), 7.70 (dd, 2H, H_6 and $H_{6''}$ of tpy-C_6H_4-OMe, J_{H6-H5} = 5.7 Hz, J_{H6-H4} = 0.9 Hz), 7.68 (dd, 2H, H_6 and $H_{6''}$ of tpy-C_6H_4-$CH_2OCO(CH_2)_3$-Pyrene, J_{H6-H5} = 5.7 Hz, J_{H6-H4} = 0.9 Hz), 7.53-7.47 (m, 4H, H_5 and $H_{5''}$ of both tpys), 7.37 (d, 2H, H_a of tpy-C_6H_4-OMe, J_{Ha-Hb} = 8.9 Hz), 5.35 (s, 2H, CH_2), 4.02 (s, 3H, OMe), 3.46 (t, 2H, CH_2, $J_{CH2-CH2}$ = 7.9 Hz), 2.65 (t, 2H, CH_2, $J_{CH2-CH2}$ = 7.1 Hz), 2.27-2.20 (m, 2H, CH_2). HRMS (ESI): m/z calculated for $[C_{64}H_{48}N_6O_3{}^{193}IrP_2F_{12}]^+$, 1431.2695; found: 1431.2694, m/z calculated for $[C_{64}H_{48}N_6O_3{}^{193}IrPF_6]^{2+}$, 643.1524; found: 643.1525, m/z calculated for $[C_{64}H_{48}N_6O_3{}^{193}Ir]^{3+}$, 380.4467; found: 380.4468.

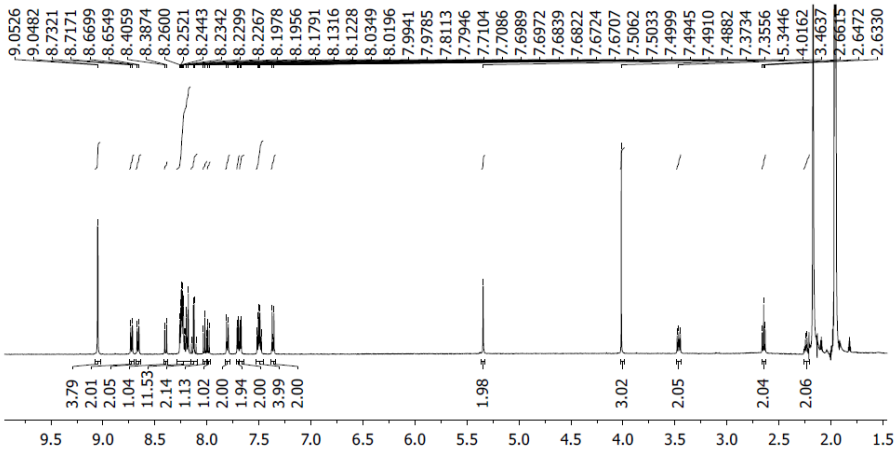

Figure 6.10 – ^{1}H NMR of **[IrN_6-Pyrene](3PF_6)** (CD_3CN, 500 MHz).

6.4.2 X-Ray Structures Determination

For **[IrN_6-Br]$^{3+}$** and **[IrN_6-IPr]$^{3+}$**, reflection data were measured on a MAR345 image plate using MoKα (λ= 0.71069Å) radiation, Rigaku Ultra X18 generator. For **[IrN_6-OH]$^{3+}$**, reflection data were measured on an Atlas

detector using MoKα (λ= 0.71069Å) radiation, Supernova X-ray source. An orange crystal (0.44 x 0.22 x 0.16 mm^3), a yellow-greenish crystal (0.27 x 0.15 x 0.11 mm^3) and an orange needle like crystal (0.439 x 0.076 x 0.049 mm^3) were respectively chosen for **$[IrN_6\text{-}Br]^{3+}$**, **$[IrN_6\text{-}IPr]^{3+}$** and **$[IrN_6\text{-}OH]^{3+}$**. They were flash cooled to 150K for **$[IrN_6\text{-}Br]^{3+}$** and **$[IrN_6\text{-}IPr]^{3+}$** and to 100 K for **$[IrN_6\text{-}OH]^{3+}$** in a nitrous gas flow prior to the data collection. Two datasets (phi scans) were measured on the same crystal, the data were individually integrated and corrected for absorption by the CrysalisPRO[270] program and both datasets data were scaled (not merged) together by xprep. See Table 6.1 for crystallographic and refinement details. The structure was solved by direct methods[271] SHELXS97 and refined by full-matrix block least-squares on F^2 using SHELXL97. All non-hydrogen atoms were refined anisotropically. The hydrogen atoms were placed at calculated positions and refined isotropically with temperature factors fixed at 1.2 $U_{(eq)}$ of the parent atom (1.5 $U_{(eq)}$ for methyl groups). A selected list of bonds and angles for compounds **$[IrN_6\text{-}Br]^{3+}$**, **$[IrN_6\text{-}IPr]^{3+}$** and **$[IrN_6\text{-}OH]^{3+}$** can be found above. The data have been deposit with the Cambridge Crystallographic Data Centre respectively for **$[IrN_6\text{-}IPr]^{3+}$** and **$[IrN_6\text{-}OH]^{3+}$**).

- ✓ **$[IrN_6\text{-}OH](3PF_6)$**

The **$[IrN_6\text{-}OH]^{3+}$** complex is found onto a crystallographic 2-fold axis mapping both terpyridine ligands onto each other, their dihedral angle being 86.43(4)°. The phenyl ring is rotated 19.30(11)° with respect to the terpyridine plane. The Ir(III) complex is counterbalanced by PF_6^- anions, one of which is found onto a 2-fold axis. An acetonitrile solvent molecule was equally found in the asymmetric unit.

- ✓ **[IrN_6-IPr]($3PF_6$)** and **[IrN_6-Br]($3PF_6$)**

The asymmetric **[IrN_6-Br]$^{3+}$** complex is coordinated by two tridentate chelating terpyridines angled at 86.37(6)°. The phenyl ring holding the methoxy group makes an angle of 27.07(19)° with the terpyridine plane; on the opposite side the angle is found to be nearly identical (27.9(2)°). Both extremities of the ligands show disorder. The methoxy group is found in the plane of the attached phenyl ring, with the methyl group either at a torsion angle of -15.4° (73%) or 167.4° (27%) for C27-O26-C23-C22. On the brominated terpyridine, the Br atom is only partially occupied (64%), indicating that the Br bond easily ruptures. The Ir(III) complex is counterbalance by three PF_6^- anions. An acetonitrile solvent molecule was equally found in the asymmetric unit. Two cavities are found inside the unit cell and were treated by the platon SQUEEZE algorithm to account for disordered solvent molecules inside these voids. A total of 132 electrons were treated this way over a total volume of 652 $Å^3$; this accounts for acetonitrile molecules disordered over multiple sites and possibly Br atoms as a result of the photo-degradation of the C-Br bond.

The asymmetric **[IrN_6-IPr]$^{3+}$** complex is coordinated by two tridentate chelating terpyridines angled at 89.85(6). The phenyl ring holding the methoxy group makes an angle of 15.49(18)° with the terpyridine plane; on the opposite side the angle is found to be 26.5(6)° similar to the angle found in **[IrN_6-Br]$^{3+}$**. For both complexes, a head-to-tail arrangement is found (Figure 6.11).

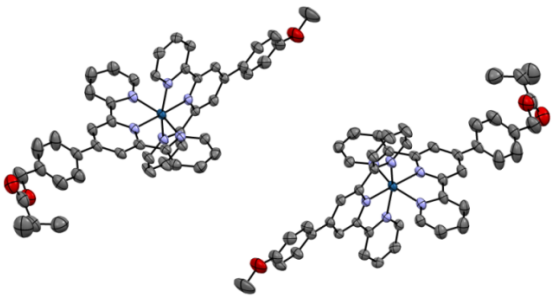

Figure 6.11 – Head-to-Tail arrangement for **[IrN$_6$-IPr]$^{3+}$** (also observed for **[IrN$_6$-Br]$^{3+}$**).

When superimposing compounds **[IrN$_6$-Br]$^{3+}$** and **[IrN$_6$-IPr]$^{3+}$** (Figure 6.12), the RMS deviation is 0.3138 Å with the maximum deviation (1.3551Å) found at the isopropyl unit (Br atom was ignored during RMS calculations in Mercury[272]).

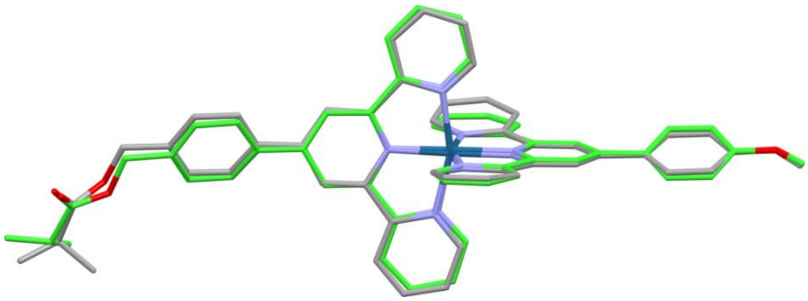

Figure 6.12 – Superimposition of **[IrN$_6$-Br]$^{3+}$** and **[IrN$_6$-IPr]$^{3+}$**. For **[IrN$_6$-Br]$^{3+}$**, the carbon atoms are shown in green, hydrogen atoms and the Br atom (**[IrN$_6$-Br]$^{3+}$**) are omitted for clarity.

Chapter 7 - Access to functionalized luminescent Multi-2,2′:6′,2′′-terpyridine ligands

7.1 Foreword

Unlike the previous chapters, this one has somewhat taken us away from the photochemistry of Ir(III) complexes. Initially encouraged by the results obtained in Chapter 4 for the hydrogen photo-evolution, we have designed an acetyl-quaterpyridine intermediate (represented in light grey in Scheme 7.1) to target a supramolecule bearing two Ir(III) cores for only one cobalt catalyst moiety. The hypothesis was that two electron injectors should be more efficient that only one. This project stems from the fact that cobalt bis(iminopyridine) complexes are highly active electrocatalysts for water reduction.[273] Their synthesis is straightforwardly achieved *via* condensation of 1,3-diaminopropane with two equivalents of derivatized 2-acetylpyridine templated by $[Co(CH_3CN)_6]^{2+}$ in acetonitrile at room temperature (Scheme 7.1). Unfortunately, the harsch conditions required to synthesize $\mathbf{[IrN_4C_2]^+}$ complexes (*vide infra*) lead to degradation of the acetyl subunit even if protected as an acetal. As a result, a fully different use of the acetyl-quaterpyridine was investigated.

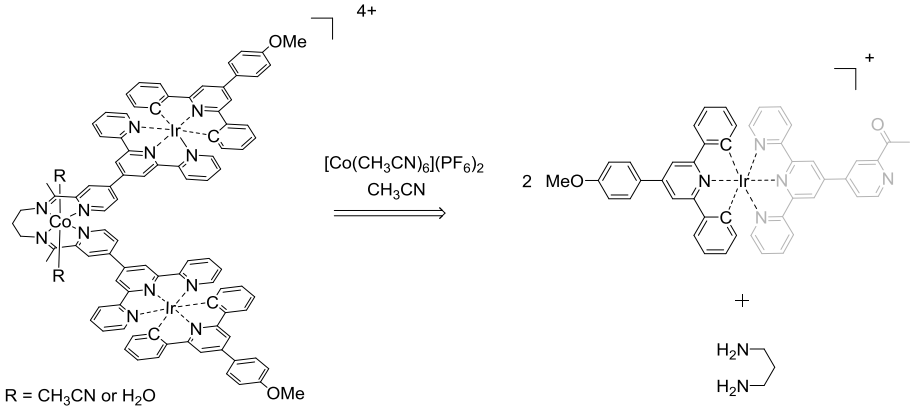

Scheme 7.1 – Retrosynthetic scheme considered to obtain a supramolecular Ir(III)-Co(II) triad for hydrogen photo-evolution.

7.2 Main topics addressed in the publication

The designed acetyl-quaterpyridine may react with various functional groups due to its own derivatization. For example, the formation of an imine was initially envisaged in order to reach a bis-terpyridine ligand useful to connect different transition metals (Scheme 7.1).

In the frame of the supramolecular chemistry, the "acetyl-pyridine" moiety can also enable access to new "tri-terpyridine" scaffolds by applying the Kröhnke synthesis[274] which has been plentifully exploited to synthesize terpyridines.[275] This strategy requires the use of the acetyl-pyridine, an aromatic aldehyde, a base and an ammoniacal source.

This Chapter presents the development of the methodology as well as its scope and boundaries. The numerous functional groups successfully anchored to the "tri-terpyridine" scaffold pave the way to diverse applications in the field of supramolecular chemistry.

Journal

Journal of Organic Chemistry **2015**, *80*, 11143-11148.

Title

Access to functionalized luminescent multi-2,2′:6′,2″-terpyridine ligands

Authors

Alexandre JACQUES, Simon CERFONTAINE and Benjamin ELIAS*

Affiliations

Université catholique de Louvain, Institut de la Matière Condensée et des Nanosciences, Place Louis Pasteur 1, L4.01.02, B-1348, Louvain-la-Neuve, Belgium.

Abstract

A one-pot synthesis of substituted multi-2,2':6',2" terpyridines (multi-tpy) has been achieved using an acetyl-quaterpyridine precursor with various aryl aldehydes in basic media. This strategy enables ready access to functionalized tri-terpyridines. Utilizing a Suzuki-type cross-coupling, larger structures such as tetra- or even hexa-tpy were obtained from our tri-tpy precursor. These macromolecular units are ideal building blocks for the construction of transition metal-based supramolecular assemblies.

7.3 Introduction

2,2′:6′,2″-Terpyridines (tpy) have become some of the most useful N/C-coordinating ligand for building transition metal complexes. Indeed, interesting spectro-electrochemical, magnetic and structural properties arise in the resulting assemblies, which can be useful in several fields of endeavour,[275] especially in supramolecular chemistry.[276] For example, supramolecular aggregates made up of metal-tpy subunits have been widely studied.[277-281] Tpy-polymer based structures have also led to numerous applications ranging from Polymer Light-Emitting Diodes (PLED's)[282,283] to the development of advanced multiblock copolymers.[284,285] The increasing interest for tpy ligands originates from their reproducible syntheses and their ease of functionalization. Numerous methods have been described and continuously improved affording an increasing number of readily available derivatized tpy. More recently, multi-tpy based ligands have been developed and used as luminescence sensors[286] and in self-assembled supramolecular systems (2D and 3D architectures).[287-289] Thus far, the multi-tpy systems have usually been obtained from thiol[286] or palladium cross-coupling strategies,[290-292] in which only a few functional groups were introduced.

Herein, we report an approach to overcome this issue based on a one-pot strategy using a common easily accessible precursor. Accordingly, novel tpy scaffolds bearing various substituents have been obtained and their spectroscopic properties studied. To demonstrate the strength and versatility of our synthetic approach, larger structures bearing four or six tpy units have been prepared with these new functionalized ligands. The structural and photophysical features of our new macromolecular units open doors to applications in different fields. For instance, they can be used as building blocks for the construction of transition metal-based supramolecular assemblies.

7.4 Results and Discussion

Usually, the tpy motif is obtained through a one-pot Kröhnke synthesis, in which key-intermediates are required. In our case, a key precursor (**5**) for the synthesis of multi-tpy has been synthesized in 5 steps (Scheme 7.2), starting from methyl-2-acetylisonicotinate **1**. The acetal derivative **2** is then reduced by sodium borohydride in refluxing EtOH to yield the corresponding alcohol **3**. Aldehyde **4** was obtained upon treatment of **3** using a Swern oxidation. The synthesis of the key intermediate tpy **5** was adapted from a procedure developed by Schubert *et al.*[77] leading to the acetal-tpy **4′** followed by an aqueous acidic treatment. It is worth mentioning that this strategy was easily applied to multigrams scale.

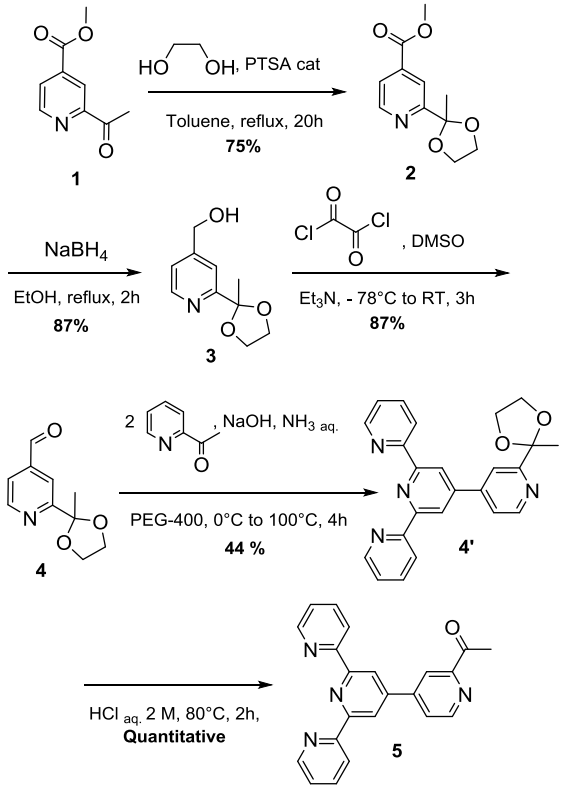

Scheme 7.2 – Synthetic route followed to generate the intermediate **5**.

Our one-pot strategy toward functionalized luminescent multi-tpy is presented in Scheme 7.3. Acetyl-pyridine **5** reacts with aromatic aldehydes in the presence of potassium hydroxide through a Claisen-Schmidt aldol condensation and subsequent 1,4-Michael addition. The central pyridine ring is obtained from the reaction of the 1,5-dione intermediate with concentrated aqueous ammonia, in a sealed tube at 100 °C in EtOH. Upon reflux at atmospheric pressure, only very low conversion was observed. The reaction also works in MeOH despite lower quantities of pure products being recovered. Typically, after 10 minutes of reaction, complete dissolution of tpy **5** was observed. The tri-tpy derivatives **7a-h** smoothly precipitated from the reaction mixture and were easily recovered by filtration.

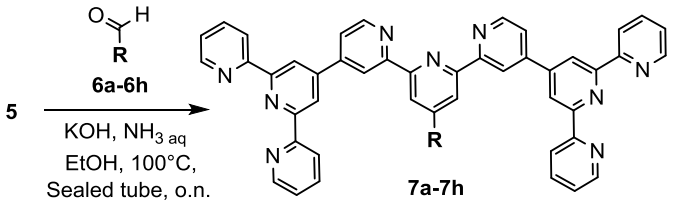

Scheme 7.3 – One-pot synthesis of tri-tpy.

For purification, the crude product was suspended in large amount of EtOH, sonicated, heated at reflux then filtrated or purified by column chromatography depending on the nature of the substituent.

Thanks to the versatility of our synthetic approach, different substituted aromatic aldehydes (**6a-6h**) can be used for the synthesis of multi-tpy (Table 7.1). The various pendant functional groups on the central pyridine core show the ease of structural modification and renders our method advantageous and competitive compared to multi-tpy based strategies, which usually rely on metal-promoted cross-coupling or thiol chemistry.[290-292]

Table 7.1. Functionalized tri-tpy.

Entry	R	Yield (%)	$\lambda_{max\ abs}$ (nm - ε *10^{-3} M^{-1} cm^{-1})[a]	$\lambda_{max\ em}$ (nm)[a,b]	Φ_{em}[b]
7a		36	248 (93.6), 273 (sh, 65.4), 311 (sh, 30.6)	366	0.20
7b	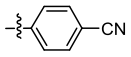	18	249 (59.5), 270 (sh, 48.6), 314 (sh, 18.4)	365	0.17
7c	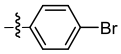	31	247 (75.8), 275 (sh, 59.5), 313 (sh, 26.0)	366	0.23
7d	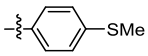	62	241 (97.1), 282 (63.0), 295 (sh, 59.5), 310 (sh, 55.7)	404	0.05
7e	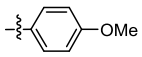	40	245 (89.4), 283 (69.7), 294 (sh, 65.0)	368	0.12
7f	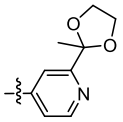	25	243 (88.3), 278 (sh, 47.0), 313 (sh, 35.6)	366	0.14
7g	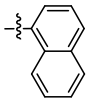	51	242 (90.4), 283 (54.1), 295 (sh, 49.5), 313 (sh, 35.6)	368	0.21
7h	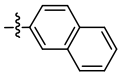	52	250 (103.3), 269 (sh, 85.2), 294 (sh, 60.9), 315 (sh, 38.8)	374	0.27
7i[c]	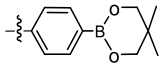	68	-[d]	-[d]	-[d]
7j[c]		-[e]	-[e]	-[e]	-[e]

[a]Measured in CH_2Cl_2 at RT. [b]Quantum yield was measured under air using quinine sulfate as reference Φ_{ref} = 0.546 in aqueous 0.5 M H_2SO_4,[293] λ_{Exc} = 250 nm, 293 K. [c]**7i** was obtained upon treatment of **7c** with bis(neopentyl glycolato)diboron. [d]Spectroscopic properties were not measured due to difficulties in the purification of **7i**. [e]The compound **7j** was totally insoluble in the common organic solvent, hence no spectroscopic data could be measured.

It is worth mentioning that aldehydes bearing electron rich groups (*e.g.* **6e**, **6g**, **6h** - Table 7.1) lead to better yields although the reason for these results remains unclear with respect to the mechanism of the reaction. Interestingly, the solubility of the novel tri-tpy was strongly modulated by the nature of the functional groups, ranging from poorly soluble for **7a-c** (typically saturated in the 1 mmol.L^{-1} range in CH_2Cl_2) to moderately soluble for **7d-i** (typically saturated in the 10 mmol.L^{-1} range in CH_2Cl_2). Strikingly, a completely insoluble product was obtained when 4-carboxaldehyde pyridine was used as an aromatic aldehyde (**7j** – Table 7.1).

In order to gain insight into the spectroscopic behaviour of our tri-tpy, their absorption and emission properties were examined. All the compounds exhibit broad absorption bands below *ca.* 350 nm with a maximum close to 250 nm (ε between 50,000 and 100,000 M^{-1} cm^{-1}) (See Figure 7.1 and Table 7.1). These bands are attributed to $^1\pi$-π^* transitions as observed for mono-tpy chromophores.[294] Moreover, each tri-tpy emits in CH_2Cl_2 at room temperature in air (Φ_{em} values between 0.05 and 0.27). The emission maximum is close to 370 nm except for **7d** which emits at a longer wavelength maximum ($\lambda_{max\ em}$ = 404 nm). Such a red-shifted emission has previously been reported in the literature for 4′-(4-methylthio)phenyl-2,2′;6′,2″-terpyridine[286] indicating that the thiomethyl group clearly induces a reduction in the HOMO-LUMO gap.

Based on these functionalized tri-tpy, a wide variety of multi-tpy structures become readily available. Initially, the use of terephthalaldehyde (dialdehyde) to reach a “hexa-tpy” was explored. However, a mixture of intermediates precipitated prior to completion of the reaction. As a result, another strategy relying on coupling reactions was investigated and turned out to be more successful. The Suzuki coupling was chosen due to the ease of preparation of organoboron derivatives, its usual relatively high stability

and the low toxicity of by-products.[295] Homocoupling[17] of **7c** was achieved in good yield *via* a one-pot tandem Miyaura boronic ester formation and subsequent Suzuki coupling (Scheme 7.4).

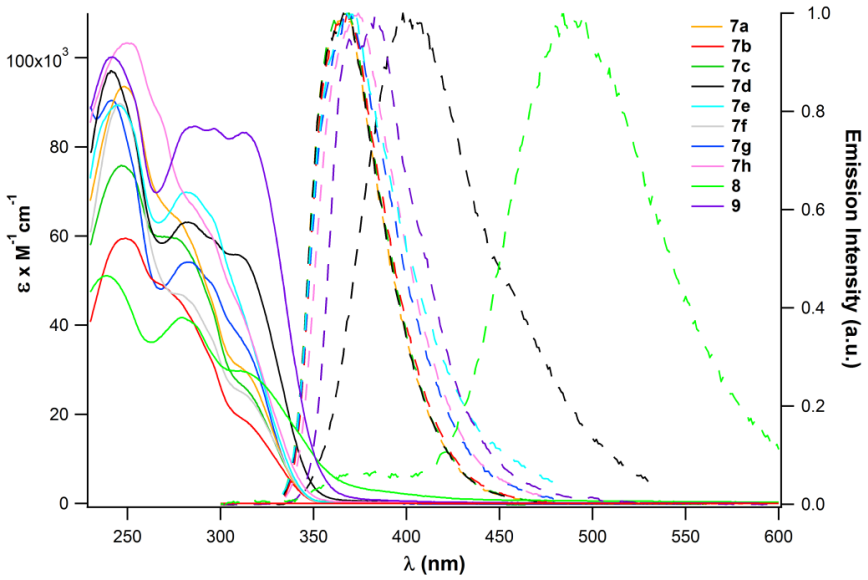

Figure 7.1 – Absorption and emission spectra of **7a-h**, **8** and **9** in CH_2Cl_2 under air at room temperature (λ_{Exc} = 250 nm).[296]

The resulting luminescent ($\lambda_{max\ em}$ = 484 nm, Φ_{em} = 0.07 in CH_2Cl_2 under air) hexa-tpy product **8** possesses a unique structure. However, its poor solubility prevents its ease of use. To tackle this issue, the tetra-tpy **9** was also synthetized by a Suzuki coupling[297] between the brominated ligand **7c** and the readily available 4′-boronatophenyl-2,2′:6′,2″-terpyridine[298] with good yield (Scheme 7.5). Alternatively, the boronate ester **7i** was prepared upon treatment of **7c** with the commercially available bis(neopentyl-glycolato)diboron. Suzuki coupling of **7i** with 4′-bromophenyl-2,2′:6′,2″-terpyridine[299] also gave the product **9** ($\lambda_{max\ em}$ = 383 nm, Φ_{em} = 0.29 in CH_2Cl_2 under air) showing the versatility of our new synthetic protocol. As

expected, this product exhibits a relatively high solubility compared to the hexa-tpy **8**.

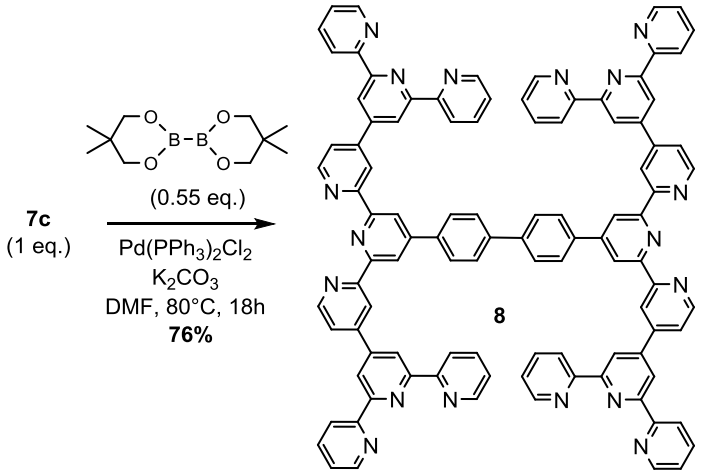

Scheme 7.4 – Synthetic scheme for the hexa-tpy.

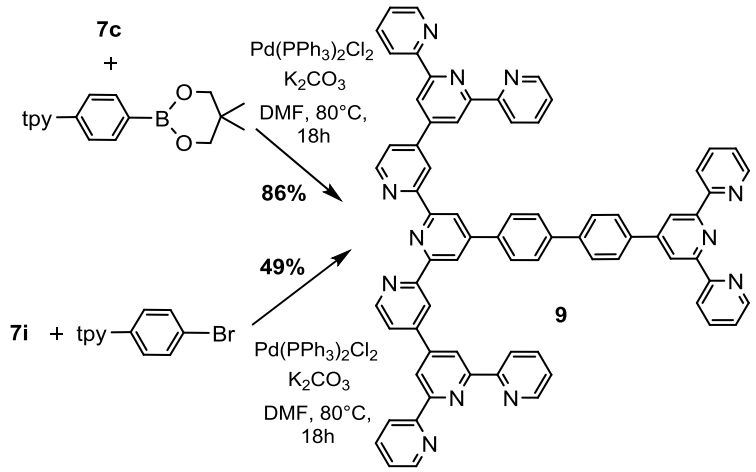

Scheme 7.5 – Synthetic scheme for the tetra-tpy.

7.5 Conclusion

In conclusion, this paper demonstrates our efforts in expanding the classical terpyridine synthetic scheme in order to build novel multi-tpy ligands. The functionalization of these scaffolds was successfully achieved

in a straightforward manner by selection of the desired aldehydes. We took advantage of this versatility to synthetize tetra- and hexa-tpy by utilizing the Suzuki-Miyaura coupling. As a result, the design and synthesis of supramolecular assemblies such as metallo-supramolecular polymers has become feasible using our synthetic methodology.

ASSOCIATED CONTENT

Supporting Information

^{1}H NMR, ^{13}C NMR and ^{1}H-^{1}H COSY NMR spectra, absorption and emission spectra of tri-tpy, tetra-tpy and hexa-tpy. This material is available free of charge via the Internet at http://pubs.acs.org.

ACKNOWLEDGMENT

The authors gratefully acknowledge the *Fonds National pour la Recherche Scientifique* (F.R.S.-FNRS), the *Fonds pour la Formation à la Recherche dans l'Industrie et dans l'Agriculture* (F.R.I.A.), the *Région Wallonne*, the *Université catholique de Louvain* and the *Prix Pierre et Colette Bauchau* for financial support.

7.6 Experimental Section

NMR experiments were performed in $CDCl_3$ and CD_2Cl_2 on a Bruker AC-300 Avance II (300 MHz) or on a Bruker AM-500 (500 MHz). The chemical shifts (given in ppm) were measured versus the residual peak of solvent as the internal standard. HRMS were recorded on a Q-Extractive orbitrap from ThermoFisher. Samples were ionized by ESI (capillary temperature: 250 °C, vaporizer temperature: 250 °C, sheath gas flow rate: 20). UV-vis absorption spectra were recorded on a Shimadzu UV-1700. Room temperature fluorescence spectra were recorded on Varian Cary Eclipse. IR absorption spectra were recorded as a liquid deposition on a ZnSe crystal on a

Shimadzu FTIR 8400 Spectrophotometer from 4000 cm^{-1} to 600 cm^{-1}. Methyl 2-acetylisonicotinate **1** was prepared according to literature procedure.[300]

Synthesis of Methyl 2-acetylisonicotinate[300] (1)

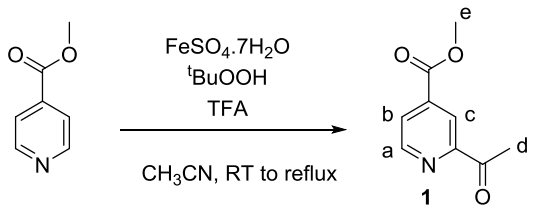

Methyl isonicotinate (25.00 g, 182 mmol) was added to a solution of paraldehyde (120.26 g, 910 mmol) in CH_3CN (350 ml) at room temperature. To this solution was added $FeSO_4 \cdot 7H_2O$ (0.809 g, 2.9 mmol), TFA (20.98 g, 184 mmol) and 70% ^tBuOOH (32.44 g, 360 mmol). The mixture was heated to reflux for 4 h leading to a brown solution. The solvent was removed under reduced pressure, and the residue was taken up in saturated aqueous $NaHCO_3$ (100 mL), then extracted with AcOEt (4×200 mL). The combined organic fractions were dried over $MgSO_4$, combined and freed of solvent under reduced pressure. The dark brown residue was purified by chromatography column on SiO_2 (EtOAc/Hexane (1/3)) to afford off-white needles (17.00 g, 52%). The ^1H NMR spectrum agreed with that in the literature.[301] ^1H NMR (300 MHz, $CDCl_3$) δ (ppm), 8.84 (dd, 1H, H_a, J_{Ha-Hb} = 4.9 Hz, J_{Ha-Hc} = 0.8 Hz), 8.56 (dd, 1H, H_c, J_{Hc-Hb} = 1.6 Hz, J_{Hc-Ha} = 0.8 Hz), 8.03 (dd, 1H, H_b, J_{Hb-Ha} = 4.9 Hz, J_{Hb-Hc} = 1.6 Hz), 3.99 (s, 3H, H_e), 2.76 (s, 3H, H_d).

Methyl 2-(2-methyl-1,3-dioxolan-2-yl)isonicotinate (2)

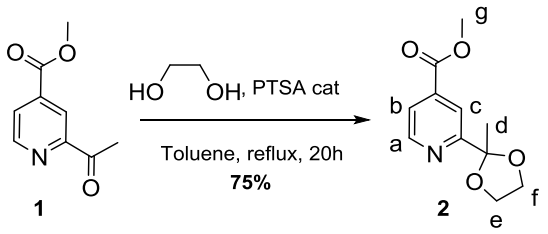

Ethylene glycol (0.56 mL, 10.08 mmol, 1.5 equiv) and PTSA (0.030 g, 0.17 mmol, 0.03 equiv) were added to methyl 2-acetylisonicotinate (1.200 g, 6.72 mmol, 1 equiv) in anhydrous toluene (25 mL). The mixture was refluxed for 20 h with a Dean Stark trap. A 0.05 M NaOH solution (20 mL) was added and aqueous layer was extracted with AcOEt (3 x 25 mL). Organic layers were combined, dried over $MgSO_4$ and solvents removed. The brown residue was purified by column chromatography on SiO_2 (eluent: cyclohexane/ethyl acetate (2/1)) to give a white powder with 75 % yield (1.120 g). The ^1H NMR spectrum agreed with that found in literature.[301] ^1H NMR ($CDCl_3$, 300 MHz) : δ (ppm), 8.80 (dd, 1H, H_a, J_{Ha-Hb} = 5.0 Hz, J_{Ha-Hc} = 0.7 Hz), 8.10 (dd, 1H, H_c, J_{Hc-Hb} = 1.5 Hz, J_{Hc-Ha} = 0.6 Hz), 7.78 (dd, 1H, H_b, J_{Hb-Ha} = 5.0 Hz, J_{Hb-Hc} = 1.6 Hz), 4.12 (m, 2H, H_e), 3.97 (s, 3H, H_g), 3.90 (m, 2H, H_f), 1.75 (s, 3H, H_d). MS (APCI) m/z: 224.2 $[M+H]^+$.

(2-(2-methyl-1,3-dioxolan-2-yl)pyridin-4-yl)methanol (3)

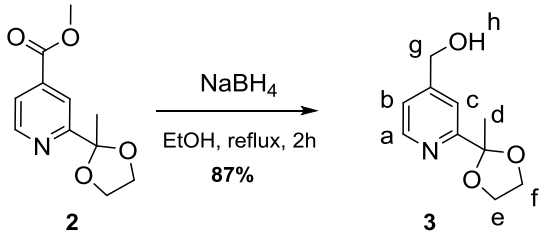

Ester **2** (1.120 g, 5.02 mmol, 1 equiv) was stirred in EtOH (50 mL) up to solid dissolved. $NaBH_4$ (570 mg, 15.05 mmol, 3 equiv) was added and the

mixture was refluxed for 2h. The reaction was quenched with water (20 mL) and EtOH removed under vacuum. Aqueous layer was extracted with CH_2Cl_2 (4 x 25 mL). Organic layers were combined, dried over $MgSO_4$ and solvent removed. Colorless oil was obtained with 94 % yield (920 mg). The ^{1}H NMR spectrum agreed with that found in literature.[302] ^{1}H NMR ($CDCl_3$, 300 MHz) : δ (ppm), 8.60 (d, 1H, H_a, J_{Ha-Hb} = 5.0 Hz), 7.56 (s, 1H, H_c), 7.25 (d, 1H, H_b, J_{Hb-Ha} = 4.9 Hz), 5.30 (s, 1H, H_h), 4.78 (s, 2H, H_g), 4.10 (m, 2H, H_e), 3.88 (m, 2H, H_f), 1.73 (s, 3H, H_d).

2-(2-methyl-1,3-dioxolan-2-yl)isonicotinaldehyde (4)

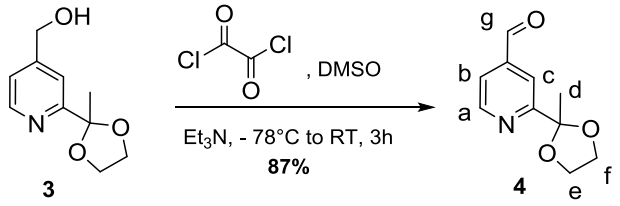

DMSO (0.34 mL, 4.80 mmol, 2.4 equiv) was added to oxalyl chloride (0.34 mL, 4.00 mmol, 2 equiv) in anhydrous CH_2Cl_2 (15 mL) at -78°C. Alcohol **3** (390 mg, 2.00 mmol, 1 equiv) dissolved in anhydrous CH_2Cl_2 (3 mL) was added and the mixture was allowed to react for 45 minutes at – 78°C until a white salt was obtained. Et_3N (1.35 mL, 10.00 mmol, 5 equiv) was added and the reaction warmed to room temperature over 1h30min. CH_2Cl_2 (50 mL) was added and washed with Brine (50 mL) and water (2 x 50 mL). The organic phase was dried over $MgSO_4$ and the solvent removed under vacuum. The crude product was purified by flash chromatography on SiO_2 (cyclohexane/AcOEt (1/1)) to afford colorless oil with 70% yield (272 mg). ^{1}H NMR ($CDCl_3$, 500 MHz) : δ (ppm), 10.10 (s, 1H, H_g), 8.90 (d, 1H, H_a, J_{Ha-Hb} = 4.8 Hz), 7.97 (dd, 1H, H_c, J_{Hc-Hb} = 1.4 Hz, J_{Hc-Ha} = 1.0 Hz), 7.65 (dd, 1H, H_b, J_{Hb-Hc} = 4.9 Hz, J_{Hb-Ha} = 1.5 Hz), 4.14 (m, 2H, H_e), 3.91 (m, 2H, H_f), 1.96 (s, 3H, H_d). ^{13}C NMR ($CDCl_3$, 125 MHz) : δ 191.7, 163.4, 151.1, 142.4,

121.5, 118.5, 108.4, 77.4, 65.3, 25.5. HRMS (APCI): m/z calculated for $[C_{10}H_{12}NO_3 + H]^+$, 194.0812; found: 194.0813.

4′-(2-(2-methyl-1,3-dioxolan-2-yl)pyridine-4-yl)-2′,2′:6′,2′′-terpyridine (4′)

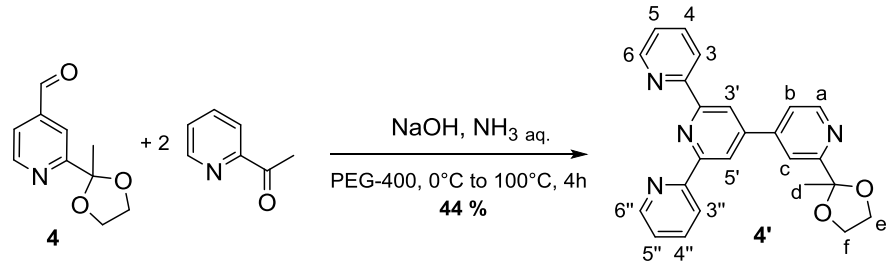

Acetal-pytpy **4′** was prepared using an adapted literature procedure.[77] 2-Acetylpyridine (2.133 g, 1.975 mL, 17.6 mmol, 2 equiv) was added to a stirred suspension of NaOH (0.704 g, 17.6 mmol, 2 equiv) in PEG-400 (10 mL) at 0 °C. After 5 min, aldehyde **4** (1.700 g, 8.8 mmol, 1 equiv) was added and the reaction mixture was kept at 0 °C for 2 h. Then a concentrated solution of NH_3 aq. (10 mL) was added and the suspension was heated at 100 °C for 15 min. During this period, product formed as an off-white precipitate. The product was filtrated, washed with H_2O (200 mL) and recrystallized from EtOH to yield pure product (1.533 g, 44 %). ^{1}H NMR ($CDCl_3$, 300 MHz) : δ (ppm), 8.79 (dd, 1H, H_a, J_{Ha-Hb} = 5.1 Hz, J_{Ha-Hc} = 0.7 Hz), 8.78 (s, 2H, $H_{3'}$ and $H_{5'}$), 8.75 (ddd, 2H, H_6, J_{H6-H5} = 4.8 Hz, J_{H6-H4} = 1.7 Hz, J_{H6-H3} = 0.7 Hz), 8.69 (dd, 2H, H_3, J_{H3-H4} = 8.0 Hz, J_{H3-H5} = 1.0 Hz), 8.04 (dd, 1H, H_c, J_{Hc-Hb} = 1.7 Hz, J_{Hc-Ha} = 0.7 Hz), 7.91 (td, 2H, H_4, $J_{H4-H3(H5)}$ = 7.8 Hz, J_{H4-H6} = 1.8 Hz), 7.73 (dd, 1H, H_b, J_{Hb-Ha} = 5.0 Hz, J_{Hb-Hc} = 1.8 Hz), 7.39 (ddd, 2H, H_5, J_{H5-H4} = 7.5 Hz, J_{H5-H6} = 4.8 Hz, J_{H5-H3} = 1.1 Hz), 4.15 (m, 2H, H_f), 3.95 (m, 2H, H_e), 1.81 (s, 3H, H_d). ^{13}C NMR ($CDCl_3$, 75 MHz) : δ (ppm), 162.2, 156.5, 155.8, 150.4, 149.3, 148.0, 146.9, 137.2, 124.3, 121.6,

121.2, 119.0, 117.6, 108.8, 65.2, 25.8. HRMS (APCI): m/z calculated for $[C_{24}H_{20}N_4O_2 + H]^+$, 397.1659 ; found: 397.1658.

1-(6′-(2-pyridine-2-yl)-[2,2′:6′,2″-terpyridin]-2″-yl]ethan-1-one (5)

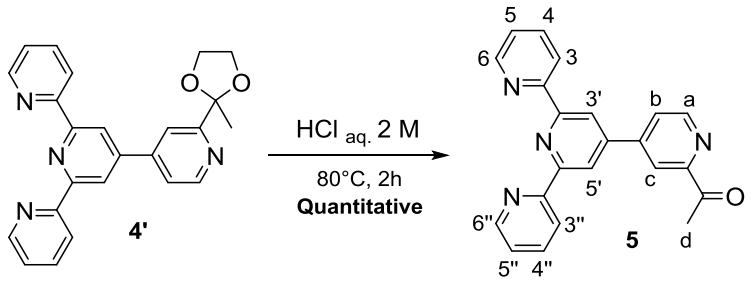

Acetal-pytpy **4′** (1.000 g, 2.55 mmol, 1 equiv) was dissolved in $HCl_{aq.}$ 2 M (5 mL) and the mixture was heated at 80 °C for 2h. After cooling, saturated $NaHCO_{3aq}$ was added to neutralize the reaction. Aqueous layer was extracted with CH_2Cl_2 (three times). The organic layers were combined, dried over $MgSO_4$ and solvent removed to give a white powder with a quantitative yield (890 mg). ^{1}H NMR ($CDCl_3$, 300 MHz) : δ (ppm), 8.82 (dd, 1H, H_a, J_{Ha-Hb} = 5.1 Hz, J_{Ha-Hc} = 0.7 Hz), 8.80 (s, 2H, $H_{3'}$ and $H_{5'}$), 8.73 (ddd, 2H, H_6, J_{H6-H5} = 4.8 Hz, J_{H6-H4} = 1.7 Hz, J_{H6-H3} = 0.8 Hz), 8.66 (dd, 2H, H_3, J_{H3-H4} = 8.0 Hz, J_{H3-H5} = 1.0 Hz), 8.55 (dd, 1H, H_c, J_{Hc-Hb} = 1.8 Hz, J_{Hc-Ha} = 0.7 Hz), 7.97 (dd, 1H, H_b, J_{Hb-Ha} = 5.1 Hz, J_{Hb-Hc} = 1.8 Hz), 7.89 (td, 2H, H_4, $J_{H4-H3(H5)}$ = 7.8 Hz, J_{H4-H6} = 1.8 Hz), 7.38 (ddd, 2H, H_5, J_{H5-H4} = 7.5 Hz, J_{H5-H6} = 4.8 Hz, J_{H5-H3} = 1.2 Hz), 2.80 (s, 3H, H_d). ^{13}C NMR ($CDCl_3$, 75 MHz): δ (ppm), 200.1, 156.7, 155.7, 154.5, 150.0, 149.3, 147.3, 146.9, 137.1, 125.1, 124.3, 121.5, 119.8, 118.8, 26.2. IR (thin film): υ_{max} = 3053, 3011, 1697, 1583, 1566, 1537, 1468, 1410, 1389, 1352, 1283, 1267, 1248, 1213, 1124, 1092, 1072, 1041, 989, 964, 891, 845, 789, 733, 671, 660 cm^{-1}. HRMS (APCI): m/z calculated for $[C_{22}H_{17}N_4O + H]^+$, 353.1397 ; found: 353.1396.

General procedure for tri-tpy's 7a-h

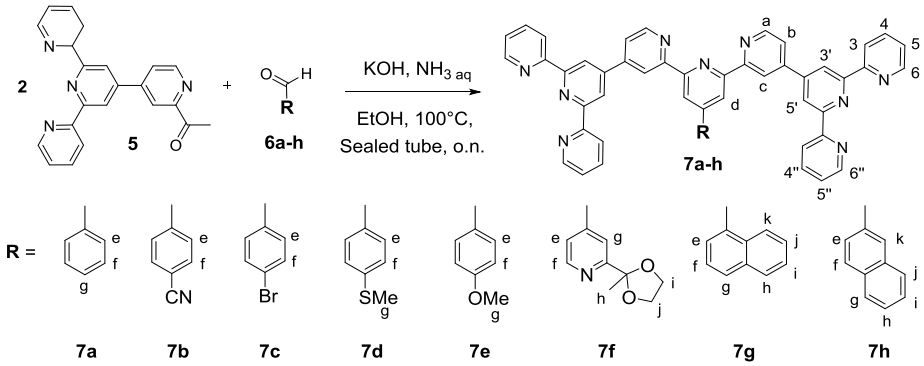

Acetyl-pytpy **5** (200 mg, 0.568 mmol, 2 equiv) was added in a solution of the corresponding benzaldehyde **6a-6c** (0.284 mmol, 1 equiv), potassium hydroxide (31.9 mg, 0.568 mmol) and aqueous ammonia (28%, 2 mL, 92.3 mmol) in absolute EtOH (10 mL). The mixture was heated for 18 h at 100 °C into a sealed tube. The off-white precipitate was filtered and washed with warm EtOH.

7a-c. A suspension of crude product was sonicated for 15 min in EtOH (100 mL) and the mixture refluxed then filtered. This procedure was repeated three times. The resulting white powder was dried to afford the pure tri-tpy.

7d-h. The crude product was purified by chromatography column on neutral alumina with a CH_2Cl_2/MeOH (95/5) mixture as the eluent.

Compound 7a. Yield: 36 % (80 mg). (White powder)

^{1}H NMR ($CDCl_3$, 500 MHz) : δ (ppm), 9.18 (d, 2H, H_c, $J_{Hc\text{-}Hb}$ = 1.0 Hz), 8.84 (s, 4H, $H_{3'}$ and $H_{5'}$), 8.81 (d, 2H, H_a, $J_{Ha\text{-}Hb}$ = 5.0 Hz), 8.76 (s, 2H, H_d), 8.44 (d, 4H, H_3 and $H_{3''}$, $J_{H3\text{-}H4}$ = 7.9 Hz), 8.37 (d, 4H, H_6 and $H_{6''}$, $J_{H6\text{-}H5}$ = 4.7 Hz), 7.97 (dd, 2H, H_e, $J_{He\text{-}Hf}$ = 8.5 Hz, $J_{He\text{-}Hg}$ = 1.4 Hz), 7.80 (dd, 2H, H_b, $J_{Hb\text{-}Ha}$ = 5.0 Hz, , $J_{Hb\text{-}Hc}$ = 1.8 Hz), 7.74 (td, 4H, H_4 and $H_{4''}$, $J_{H4\text{-}H5(H3)}$ = 7.7 Hz, $J_{H4\text{-}H6}$ = 1.8 Hz), 7.56 (t, 2H, H_f, $J_{Hf\text{-}He(Hg)}$ = 7.4 Hz), 7.50 (t, 1H, Hg $J_{Hg\text{-}Hf}$ = 7.3

Hz), 7.16 (ddd, 4H, H_5 and $H_{5''}$, J_{H5-H4} = 7.4 Hz, J_{H5-H6} = 4.7 Hz, J_{H5-H3} = 1.1 Hz). ^{13}C NMR ($CDCl_3$, 75 MHz) : δ (ppm), 157.0, 156.1, 155.8, 155.7, 149.7, 149.0, 147.9, 147.0, 138.6, 137.6, 136.6, 129.1, 127.5, 123.8, 121.8, 121.0, 120.0, 119.4, 118.9. IR (thin film): υ_{max} = 1582, 1566, 1539, 1468, 1396, 1356, 1246, 1076, 1042, 988, 887, 839, 791, 735, 696 cm^{-1}. HRMS (APCI): m/z calculated for $[C_{51}H_{33}N_9 + H]^+$, 772.2932 ; found: 772.2934.

Compound 7b. Yield: 18 % (36 mg). (White powder)

^1H NMR ($CDCl_3$, 500 MHz) : δ (ppm), 9.16 (d, 2H, H_c, J_{Hc-Hb} = 1.1 Hz), 8.78 (s, 4H, $H_{3'}$ and $H_{5'}$), 8.76 (d, 2H, H_a, J_{Ha-Hb} = 5.0 Hz), 8.68 (s, 2H, H_d), 8.41 (d, 4H, H_3 and $H_{3''}$, J_{H3-H4} = 7.9 Hz), 8.34 (d, 4H, H_6 and $H_{6''}$, J_{H6-H5} = 4.7 Hz), 8.01 (d, 2H, H_f, J_{Hf-He} = 8.4 Hz), 7.84 (d, 2H, H_e, J_{He-Hf} = 8.4 Hz), 7.76 (dd, 2H, H_b, J_{Hb-Ha} = 5.0 Hz, , J_{Hb-Hc} = 1.7 Hz), 7.71 (td, 4H, H_4 and $H_{4''}$, $J_{H4-H5(H3)}$ = 7.7 Hz, J_{H4-H6} = 1.7 Hz), 7.13 (ddd, 4H, H_5 and $H_{5''}$, J_{H5-H4} = 7.3 Hz, J_{H5-H6} = 4.7 Hz, J_{H5-H3} = 1.0 Hz). IR (thin film): υ_{max} = 2924, 2851, 2228, 1584, 1566, 1541, 1466, 1356, 1259, 1076, 1051, 1018, 837, 791, 733 cm^{-1}. HRMS (APCI): m/z calculated for $[C_{52}H_{32}N_{10} + H]^+$, 797.2884 ; found: 797.2885. Note: the compound **7b** was found to be too insoluble to record a carbon NMR.

Compound 7c. Yield: 31 % (72 mg). (White powder)

^1H NMR ($CDCl_3$, 500 MHz) : δ (ppm) 9.22 (d, 2H, H_c, J_{Hc-Hb} = 1.3 Hz), 8.87-8.84 (m, 6H, H_a, $H_{3'}$ and $H_{5'}$), 8.76 (s, 2H, H_d), 8.48 (d, 4H, H_3 and $H_{3''}$, J_{H3-H4} = 7.9 Hz), 8.38 (dd, 4H, H_6 and $H_{6''}$, J_{H6-H5} = 4.6 Hz, J_{H6-H4} = 0.7 Hz), 7.84 (d, 4H, H_b and H_e, J_{He-Hf} = 8.2 Hz), 7.76 (td, 4H and $H_{4''}$, H_4, $J_{H4-H5(H3)}$ = 7.7 Hz, J_{H4-H6} = 1.7 Hz), 7.69 (d, 2H, H_f, J_{Hf-He} = 8.5 Hz), 7.18 (ddd, 4H, H_5 and $H_{5''}$, J_{H5-H4} = 7.4 Hz, J_{H5-H6} = 4.7 Hz, J_{H5-H3} = 1.0 Hz). ^{13}C NMR ($CDCl_3$, 125 MHz) : δ (ppm), 156.5, 156.0, 155.6, 155.5, 149.7, 148.9, 147.0, 145.7, 137.1, 136.5, 132.1, 128.9, 123.7, 121.9, 120.9, 119.9, 118.9, 118.8. IR (thin

film): υ_{max} = 2928, 2843, 1582, 1566, 1541, 1466, 1394, 1354, 1259, 1074, 1038, 1018, 889, 791, 731 cm^{-1}. HRMS (APCI): m/z calculated for $[C_{51}H_{32}N_9{}^{79}Br+ H]^+$, 850.2037 ; found: 850.2034.

Compound 7d. Yield: 62 % (142 mg). (Clear yellow powder)

^1H NMR ($CDCl_3$, 500 MHz) : δ (ppm) 8.96 (d, 2H, H_c, J_{Hc-Hb} = 0.8 Hz), 8.62 (s, 4H, $H_{3'}$ and $H_{5'}$), 8.58 (d, 2H, H_a, J_{Ha-Hb} = 4.9 Hz), 8.49 (s, 2H, H_d), 8.25 (d, 4H, H_6 and $H_{6''}$, J_{H6-H5} = 4.1 Hz), 8.22 (d, 4H, H_3 and $H_{3''}$, J_{H3-H4} = 7.9 Hz), 7.82 (d, 2H, H_e, J_{He-Hf} = 8.3 Hz), 7.58 (td, 4H and $H_{4''}$, H_4, $J_{H4-H5(H3)}$ = 7.8 Hz, J_{H4-H6} = 1.7 Hz), 7.57 (m, 2H, H_b), 7.39 (d, 2H, H_f, J_{Hf-He} = 8.3 Hz), 7.02 (ddd, 4H, H_5 and $H_{5''}$, J_{H5-H4} = 7.4 Hz, J_{H5-H6} = 4.9 Hz, J_{H5-H3} = 0.7 Hz), 2.61 (s, 3H, H_g). ^{13}C NMR ($CDCl_3$, 125 MHz): δ (ppm) 156.8, 155.8, 155.6, 155.5, 149.4, 148.8, 147.7, 146.9, 140.1, 136.4, 135.0, 127.7, 126.6, 123.6, 121.7, 120.9, 120.0, 118.8, 118.6, 15.7. IR (thin film): υ_{max} = 3053, 2920, 2851, 1582, 1566, 1537, 1499, 1468, 1394, 1356, 1246, 1124, 1095, 1076, 1040, 988, 887, 839, 820, 791, 735, 669 cm^{-1}. HRMS (APCI): m/z calculated for $[C_{52}H_{35}{}^{32}S_1N_9 + H]^+$, 818.2809; found: 818.2809.

Compound 7e. Yield: 40 % (90 mg). (White powder)

^1H NMR ($CDCl_3$, 500 MHz) : δ (ppm) 9.00 (s, 2H, H_c), 8.68 (s, 4H, $H_{3'}$ and $H_{5'}$), 8.63 (d, 2H, H_a, J_{Ha-Hb} = 4.9 Hz), 8.54 (s, 2H, H_d), 8.32-8.26 (m, 8H, H_3, $H_{3''}$, H_6 and $H_{6''}$), 7.88 (d, 2H, H_e, J_{He-Hf} = 8.6 Hz), 7.66-7.60 (m, 6H, H_b, H_4 and $H_{4''}$), 7.08-7.04 (m, 6H, H_f, H_5 and $H_{5''}$), 3.94 (s, 3H, H_g). ^{13}C NMR ($CDCl_3$, 125 MHz) : δ (ppm) 160.6, 157.0, 155.9, 155.6, 155.5, 149.5, 149.3, 148.9, 147.8, 146.9, 136.5, 130.9, 128.7, 123.7, 121.7, 121.0, 120.0, 118.8, 118.6, 114.4, 55.6. IR (thin film): υ_{max} = 3053, 3013, 2955, 2922, 2853, 1609, 1582, 1566, 1539, 1516, 1468, 1396, 1356, 1292, 1263, 1252, 1180, 1116, 1076, 1040, 987, 887, 831, 791, 735, 704, 658 cm^{-1}. HRMS (APCI): m/z calculated for $[C_{52}H_{35}O_1N_9 + H]^+$, 802.3037; found: 802.3037.

Compound 7f. Yield: 25 % (60 mg). (White powder)

^{1}H NMR ($CDCl_3$, 500 MHz) : δ (ppm) 9.08 (d, 2H, H_c, J_{Hc-Hb} = 0.9 Hz), 8.82 (dd, 1H, H_f, J_{Hf-He} = 5.0 Hz, J_{Hf-Hg} = 0.6 Hz), 8.74 (s, 4H, $H_{3'}$ and $H_{5'}$), 8.71 (d, 2H, H_a, J_{Ha-Hb} = 5.0 Hz), 8.65 (s, 2H, H_d), 8.35 (d, 4H, H_3 and $H_{3''}$, J_{H3-H4} = 7.9 Hz), 8.31 (dd, 4H, H_6 and $H_{6''}$, J_{H6-H5} = 4.5 Hz, J_{H6-H4} = 0.6 Hz), 8.08 (dd, 1H, H_g, J_{Hg-He} = 1.7 Hz, J_{Hg-Hf} = 0.6 Hz), 7.73-7.70 (m, 3H, H_e and H_b), 7.68 (td, 4H, H_4 and $H_{4''}$, $J_{H4-H5(H3)}$ = 7.7 Hz, J_{H4-H6} = 1.7 Hz), 7.11 (ddd, 4H, H_5 and $H_{5''}$, J_{H5-H4} = 7.4 Hz, J_{H5-H6} = 4.7 Hz, J_{H5-H3} = 1.0 Hz), 4.21 (m, 2H, H_j), 4.02 (m, 2H, H_i), 1.87 (s, 3H, H_h). ^{13}C NMR ($CDCl_3$, 125 MHz) : δ (ppm) 162.6, 156.6, 156.4, 156.2, 155.8, 150.8, 149.9, 149.2, 147.9, 147.6, 147.3, 147.1, 136.8, 124.0, 122.3, 121.4, 121.2, 120.4, 119.4, 119.1, 117.8, 109.2, 65.6, 26.1. IR (thin film): υ_{max} = 3053, 2955, 2928, 1582, 1566, 1539, 1468, 1445, 1394, 1356, 1265, 1200, 1123, 1076, 1040, 988, 887, 839, 791, 735, 702, 669 cm^{-1}. HRMS (APCI): m/z calculated for $[C_{54}H_{38}O_2N_{10} + H]^+$, 859.3252; found: 859.3252.

Compound 7g. Yield: 51 % (104 mg). (White powder)

^{1}H NMR ($CDCl_3$, 500 MHz) : δ (ppm) 9.20 (d, 2H, H_c, J_{Hc-Hb} = 0.7 Hz), 8.87-8.84 (s, 4H, $H_{3'}$ and $H_{5'}$), 8.75 (s, 2H, H_a, J_{Ha-Hb} = 4.9 Hz), 8.66 (s, 2H, H_d), 8.48 (d, 4H, H_3 and $H_{3''}$, J_{H3-H4} = 7.9 Hz), 8.39 (dd, 4H, H_6 and $H_{6''}$, J_{H6-H5} = 4.5 Hz, J_{H6-H4} = 0.6 Hz), 8.09-8.06 (m, 1H, H_k), 7.99-7.95 (m, 2H, H_h and H_e), 7.80 (dd, 2H, H_b, J_{Hb-Ha} = 4.9 Hz, J_{Hb-Hc} = 1.7 Hz), 7.76 (td, 4H, H_4 and $H_{4''}$, $J_{H4-H5(H3)}$ = 7.7 Hz, J_{H4-H6} = 1.7 Hz), 7.67 (dd, 1H, H_g, J_{Hg-Hf} = 7.0 Hz, J_{Hg-He} = 1.2 Hz), 7.61 (dd, 1H, H_f, J_{Hf-He} = 7.1 Hz, J_{Hf-Hg} = 7.0 Hz), 7.63-7.58 (m, 2H, H_i and H_j), 7.17 (ddd, 4H, H_5 and $H_{5''}$, J_{H5-H4} = 7.4 Hz, J_{H5-H6} = 4.7 Hz, J_{H5-H3} = 1.0 Hz). ^{13}C NMR ($CDCl_3$, 125 MHz) : δ (ppm) 157.1, 156.3, 155.8, 155.6, 150.0, 149.1, 148.0, 147.1, 136.8, 133.9, 133.6, 131.2, 128.9, 128.6, 127.7, 127.3, 126.8, 126.2, 125.8, 125.5, 123.9, 123.0, 122.0, 121.1, 120.0, 119.0. IR (thin film): υ_{max} = 3053, 3008, 2955, 2922, 2853, 1584, 1566,

1539, 1468, 1396, 1356, 1263, 1122, 1074, 1041, 988, 889, 839, 791, 777, 739 cm^{-1}. HRMS (APCI): m/z calculated for $[C_{55}H_{35}N_9 + H]^+$, 822.3088; found: 822.3082.

Compound 7h. Yield: 52 % (122 mg). (Off-white powder)

^{1}H NMR ($CDCl_3$, 500 MHz) : δ (ppm) 9.01 (s, 2H, H_c), 8.66 (s, 4H, $H_{3'}$ and $H_{5'}$), 8.63 (s, 2H, H_d), 8.61 (d, 2H, H_a, J_{Ha-Hb} = 4.9 Hz), 8.36 (d, 1H, H_k, J_{Hk-He} = 1.0 Hz), 8.27-8.23 (m, 8H, H_3, $H_{3''}$, H_6 and $H_{6''}$), 8.02-7.90 (m, 4H, H_e, H_f, H_g and H_j) 7.60-7.56 (m, 4H, H_b, H_h and H_i), 7.58 (td, 4H and $H_{4''}$, H_4, $J_{H4-H5(H3)}$ = 7.6 Hz, J_{H4-H6} = 1.5 Hz), 7.02 (dd, 4H, H_5 and $H_{5''}$, J_{H5-H4} = 7.1 Hz, J_{H5-H6} = 4.9 Hz). ^{13}C NMR ($CDCl_3$, 125 MHz) : δ (ppm) 157.1, 156.1, 155.9, 155.7, 149.8, 149.0, 147.8, 147.1, 136.6, 135.8, 133.7, 133.7, 128.9, 128.8, 127.9, 126.9, 126.8, 126.7, 125.2, 123.8, 121.9, 121.0, 120.1, 119.5, 118.9. IR (thin film): υ_{max} = 3030, 1582, 1566, 1539, 1468, 1396, 1367, 1340, 1263, 1122, 1074, 1040, 988, 887, 856, 791, 746, 737, 704, 652 cm^{-1}. HRMS (APCI): m/z calculated for $[C_{55}H_{35}N_9 + H]^+$, 822.3088; found: 822.3087.

4'''-(4-(5,5-dimethyl-1,3,2-dioxaborinan-2-yl)phenyl)-6',6'''''-di(pyridin-2-yl)-2,2':4',4'':2'',2''':6''',2'''':4'''',4''''':2''''',2''''''-sepipyridine (7i)

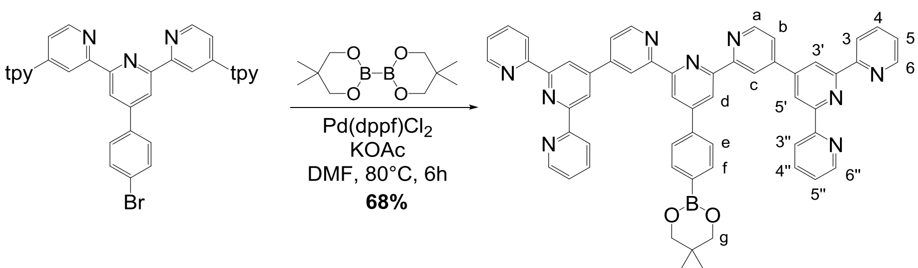

7c 7i

A Schlenk tube was charged with $Pd(dppf)Cl_2$ (3.4 mg, 0.0042 mmol, 0.05 equiv), KOAc (24.6 mg, 0.251 mmol, 3 equiv), **7c** (74.0 mg, 0.084 mmol, 1 equiv.) and bis(neopentyl glycolato)diboron (28.4 mg, 0.126 mmol, 1.5

equiv) and flushed with Argon. Anhydrous DMF (8 ml) was added and the reaction mixture was degassed by five freeze-pump-thaw cycles. The mixture was heated for 6h at 80°C under argon. The DMF was evaporated. The crude mixture was dissolved with dichloromethane (250 ml) and filtered over Celite. The resulting solution was washed five times with deionized water (100 ml). The dichloromethane was removed by evaporation to give an off-white product with 68% yield (50 mg). ^{1}H NMR ($CDCl_3$, 500 MHz) : δ (ppm), 9.17 (d, 2H, H_c, J_{Hc-Hb} = 1.4 Hz), 8.84-8.79 (m, 8H, H_a, H_f, $H_{3'}$and $H_{5'}$), 8.76 (s, 2H, H_d), 8.44 (d, 4H, H_3 and $H_{3''}$, J_{H3-H4} = 7.9 Hz), 8.36 (d, 4H, H_6 and $H_{6''}$, J_{H6-H5} = 4.9 Hz), 7.97 (d, 2H, H_e , J_{He-Hf} = 1.8 Hz), 7.79 (dd, 2H, H_b , J_{Hb-Ha} = 5.0 Hz, J_{Hb-Hc} = 1.4 Hz), 7.74 (td, 4H, H_4 and $H_{4''}$, $J_{H4-H3(H5)}$ = 7.7 Hz, J_{H4-H6} = 1.7 Hz), 7.16 (ddd, 4H, H_5 and $H_{5''}$, J_{H5-H4} = 7.7 Hz, J_{H5-H6} = 5.0 Hz, J_{H5-H3} = 1.1 Hz), 3.84 (s, 4H, H_g), 1.08 (s, 6H, H_f). ^{13}C NMR (125 MHz, CD_2Cl_2): δ (ppm), 156.0, 155.5, 155.3, 154.9, 148.9, 148.5, 147.8, 146.6, 136.2, 134.4, 126.1, 123.4, 121.4, 120.6, 119.8, 118.5, 72.6, 31.9, 21.7. IR (thin film): υ_{max} = 2964, 2928, 1584, 1566, 1541, 1468, 1420, 1394, 1356, 1315, 1308, 1261, 1132, 1076, 1040, 1020, 987, 908, 837, 791, 735 cm^{-1}. HRMS (ESI): m/z calculated for $[C_{56}H_{44}O_2N_9{}^{11}B+H]^+$, 884.3627; found: 884.3634.

4,4'-bis(6',6''''-di(pyridin-2-yl)-[2,2':4',4'':2'',2''':6''',2'''':4'''',4''''':2''''',2'''''-sepipyridin]-4'''-yl)-1,1'-biphenyl (8)

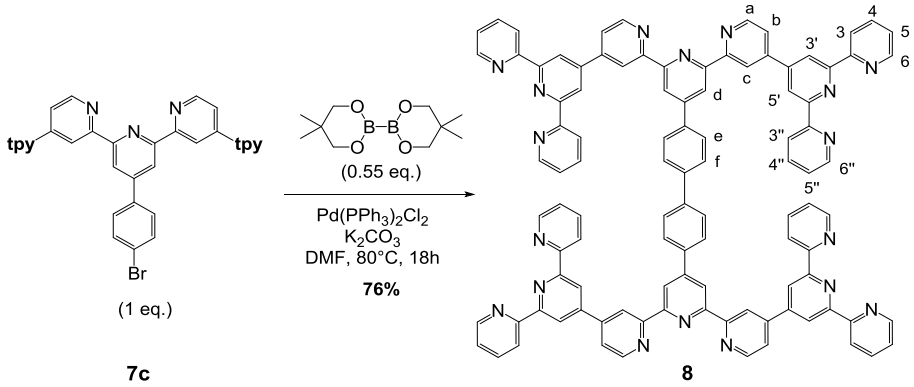

A Schlenk tube was charged with $Pd(PPh_3)_2Cl_2$ (3.0 mg, 0.0042 mmol, 0.05 equiv), K_2CO_3 (35.2 mg, 0.254 mmol, 3 equiv), **7c** (75.0 mg, 0.085 mmol, 1 equiv.) and bis(neopentyl glycolato)diboron (10.5 mg, 0.046 mmol, 0.55 equiv) and flushed with Argon. DMF (10 ml) was added and the reaction mixture was degassed by five freeze-pump-thaw cycles. The mixture was heated for 18h at 80°C under argon. The reaction mixture was centrifuged and the resulting solid was washed with water, ethanol and chloroform. An off-white powder was obtained with 76 % yield (32.6 mg). ^{1}H NMR ($CDCl_3$/$(CF_3)_2CHOH$:9/1, 500 MHz) : δ (ppm), 8.83 (d, 4H, H_a, J_{Ha-Hb} = 5.4 Hz), 8.81 (s, 4H, H_c), 8.60 (d, 8H, H_6 and $H_{6''}$, J_{H6-H5} = 5.2 Hz), 8.53 (s, 8H, $H_{3'}$ and $H_{5'}$), 8.48 (s, 4H, H_d), 8.43 (d, 8H, H_3 an $H_{3''}$, J_{H3-H4} = 7.9 Hz), 8.07 (m, 16H, H_b, H_e or H_f, H_4 and $H_{4''}$), 7.90 (d, 4H, H_e or H_f, J_{He-Hf} = 8.3 Hz), 7.59 (dd, 4H, H_5 an $H_{5''}$, J_{H5-H6} = 5.2 Hz, J_{H5-H4} = 7.9 Hz). IR (thin film): υ_{max} = 2959, 2920, 2905, 2851, 1584, 1568, 1558, 1541, 1521, 1506, 1472, 1456, 1418, 1396, 1362, 1339, 1261, 1096, 1078, 1040, 1020, 791, 773, 669, 656 cm^{-1}. HRMS (ESI): m/z calculated for $[C_{102}H_{64}N_{18}+H]^+$, 1541.5634 ;

found:1542.5617. Note: the compound **8** was found to be too insoluble to record a carbon NMR.

4'''-(4'-([2,2':6',2''-terpyridin]-4'-yl)-[1,1'-biphenyl]-4-yl)-6',6''''-di(pyridin-2-yl)-2,2':4',4'':2'',2''':6''',2'''':4'''',4''''':2''''',2'''''-sepipyridine (9)

A:

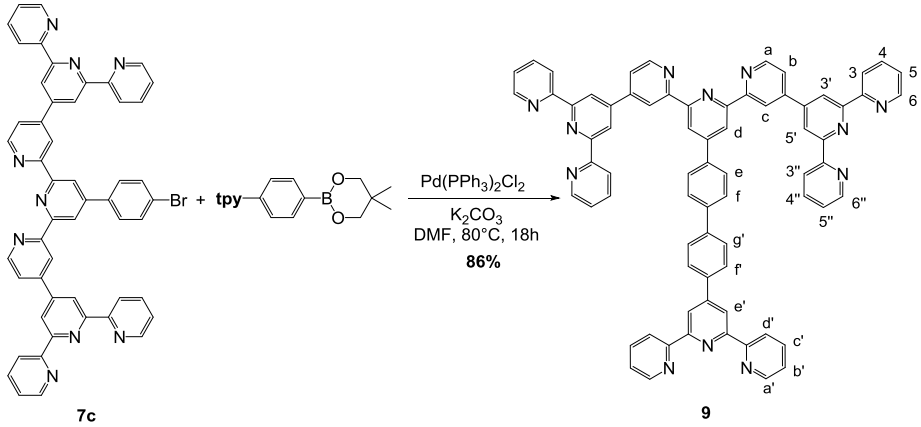

A Schlenk tube was charged with $Pd(PPh_3)_2Cl_2$ (3.1 mg, 0.0043 mmol, 0.05 equiv), K_2CO_3 (36.1 mg, 0.261 mmol, 3 equiv), **7c** (77.0 mg, 0.087 mmol, 1 equiv.) and 4′-boronatophenyl-2,2′:6′,2″-terpyridine (55.0 mg, 0.131 mmol, 1.5 equiv) and flushed with Argon. DMF (10 ml) was added and the reaction mixture was degassed by five freeze-pump-thaw cycles. The mixture was heated for 18h at 80°C under argon. The DMF was removed by rotary evaporation. The crude mixture was washed successively with water and ethanol and centrifuged. An off-white powder was obtained with 86 % yield (78 mg). ^{1}H NMR ($CDCl_3$, 500 MHz) : δ (ppm), 9.12 (s, 2H, H_c,), 8.80 (m, 10H, H_a, $H_{a'}$, $H_{e'}$, $H_{3'}$ and $H_{5'}$), 8.68 (d, 2H, $H_{d'}$, $J_{Hd'-Hc'}$ = 8.1 Hz), 8.36 (d, 4H, $H_{3'}$ and $H_{3''}$, J_{H3-H4} = 7.8 Hz), 8.33 (d, 4H, H_6 and $H_{6''}$, J_{H6-H5} = 4.7 Hz), 8.05 (dd, 4H, H_f and $H_{g'}$, J_{Hf-He} = 8.2 Hz, $J_{Hf-Hg'}$ = 1.8 Hz), 7.88 (td, 2H, $H_{c'}$, $J_{Hc'-Hb'}$

$_{(d')}$ = 7.7 Hz, $J_{Hc'-Ha'}$ = 1.6 Hz), 7.84 (d, 4H, H_e and $H_{f'}$, J_{He-Hf} = 8.3 Hz), 7.72 (dd, 2H, H_b, J_{Hb-Ha} = 5.1 Hz, $J_{Hb-Hc'}$ = 1.8 Hz), 7.68 (td, 4H, H_4 and $H_{4''}$, $J_{H4-H3(5)}$ = 7.8 Hz, J_{H4-H6} = 1.8 Hz), 7.36 (ddd, 2H, $H_{b'}$, $J_{Hb'-Hc'}$ = 7.7 Hz, $J_{Hb'-Ha'}$ = 4.6 Hz, $J_{Hb'-Hd'}$ = 1.2 Hz), 7.36 (ddd, 2H, $H_{b'}$, $J_{Hb'-Hc'}$ = 7.7 Hz, $J_{Hb'-Ha'}$ = 4.6 Hz, $J_{Hb'-Hd'}$ = 1.2 Hz), 7.10 (ddd, 4H, H_5 and $H_{5''}$, J_{H5-H4} = 7.8 Hz, $J_{H5-H6'}$ = 4.6 Hz, J_{H5-H3} = 1.4 Hz). ^{13}C NMR (125 MHz, $CDCl_3$) : δ (ppm), 157.3, 156.6, 156.4, 156.3, 156.1, 155.9, 150.0, 149.6, 149.2, 148.1, 147.3, 137.3, 136.8, 128.2, 128.0, 124.2, 124.0, 122.1, 121.8, 121.3, 120.3, 119.4, 119.2, 119.1. IR (thin film): υ_{max} = 3055, 3005, 2922, 1584, 1566, 1539, 1506, 1466, 1394, 1356, 1265, 1123, 1074, 988, 885, 837, 818, 789, 764, 745, 733 cm^{-1}. HRMS (ESI): m/z calculated for $[C_{72}H_{46}N_{12} + H]^+$, 1079.4041; found:1079.4030.

B:

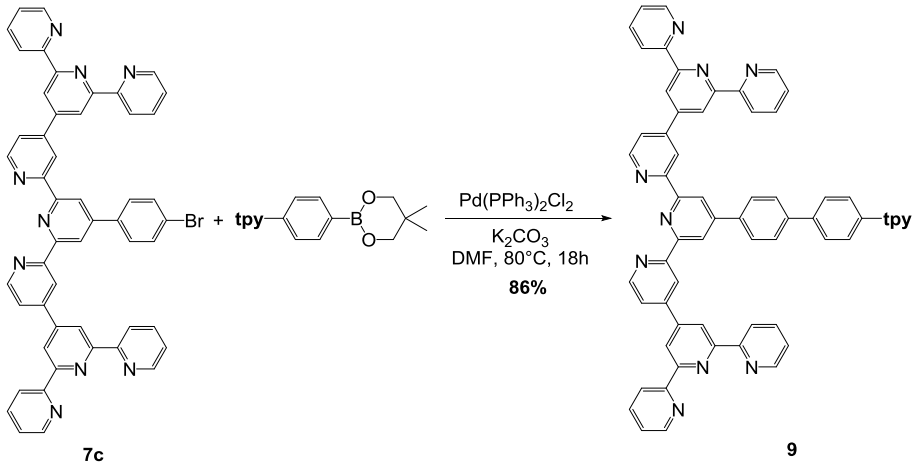

A Schlenk tube was charged with $Pd(PPh_3)_2Cl_2$ (2.0 mg, 0.0028 mmol, 0.05 equiv), K_2CO_3 (23.6 mg, 0.171 mmol, 3 equiv), **7i** (50.4 mg, 0.057 mmol, 1 equiv.) and 4′-bromophenyl-2,2′:6′,2″-terpyridine (3320 mg, 0.085 mmol, 1.5 equiv) and flushed with Argon. DMF (10 ml) was added and the reaction mixture was degassed by five freeze-pump-thaw cycles. The mixture was heated for 18h at 80°C under argon. The DMF was removed by rotary

evaporation. The crude mixture was washed successively with water and ethanol and centrifuged. An off-white powder was obtained with 49 % yield (30 mg).

Chapter 8 - Conclusions and prospects

8.1 General conclusions

This Ph.D. thesis first aimed at investigating Ir(III) bis-terdentate complexes with either $[Ir(N^N^N)_2]^{3+}$ (**$[IrN_6]^{3+}$**) or $[Ir(N^N^N)(C^N^C)]^{+}$ (**$[IrN_4C_2]^{+}$**) structures in terms of their spectroelectrochemical properties (Figure 8.1). Since the bis-cyclometalated character of **$[IrN_4C_2]^{+}$** induces less energetic electronic transitions and higher photo-reducing power with respect to **$[IrN_6]^{3+}$**, we proposed to develop applications to take advantage of their intrinsic properties.

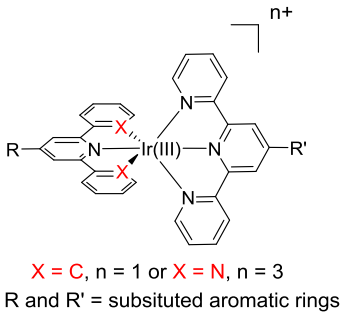

Figure 8.1 – Structure of Ir(III) complexes investigated.

Whereas **$[IrN_6]^{3+}$** displays some well known spectroscopic and electrochemical features and therefore did not require further efforts, the **$[IrN_4C_2]^{+}$** properties have been fully investigated by both theoretical and experimental approaches. As a result, **[Ir-Py]$^{+}$** and **[Ir-Py-Me]$^{2+}$** bearing a methoxy and a pyridine have been synthesized and studied. They exhibit important spectroscopic sensitivity to acids such as acetic or trifluoroacetic acid (Figure 8.2). This behaviour was rationalized based on their HOMO, HOMO-1 and LUMO relative energies. Depending on the acid strength and concentration, solely pyridine or both methoxy and pyridine may be protonated. Furthermore, spectroscopic modification upon addition of acids reveals that **$[IrN_4C_2]^{+}$** complexes have higher affinity for the stronger trifluoroacetic acid. With respect to the electrochemistry of the complexes,

these observations are in agreement with MLLCT transition in which electron goes from the electron rich cyclometalated iridium fragment (Ir-N^C^N) to the terpyridine ligand (N^N^N) upon irradiation. These results represent the first experimental evidence that some MLLCT character exists for $[Ir(N^N^N)(C^N^C)]^+$ as previously predicted from TD-DFT calculations by Scandola *et al.*[100]. This unusual behaviour for Ir(III) bis-terdentates complexes permit to design supramolecular structures requiring directional electron transfer.

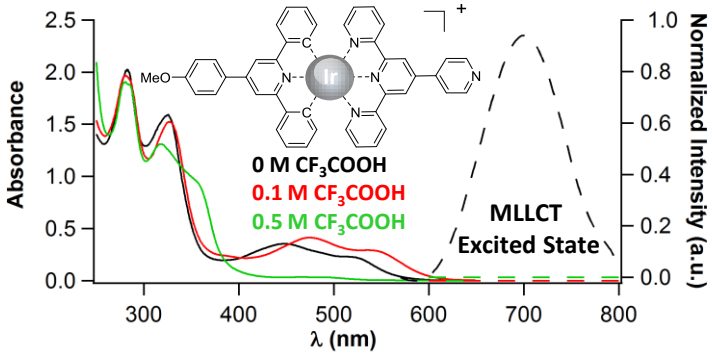

Figure 8.2 – Modification of spectroscopic properties of **[Ir-Py]**$^+$ upon addition of trifluoroacetic acid.

As a consequence, we investigated the coordination of **[Ir-Py]**$^+$ with cobaloximes leading to dinuclear structure (Figure 8.3) for which the vectorial electron transfer from the Ir(III) center to Co(III) unit properly occurs. It turns out that the hydrogen evolution was very sensitive to the experimental conditions. The best results were obtained in acetonitrile with triethanolamine as sacrificial electron donor and tetrafluoroboric acid as proton source (TON = 225, 35 h, Blue LEDs). Moreover, it has been evidenced that the catalytic activity can be improved by adding excess of dimethylglyoxime ligand to regenerate the cobalt moiety. In these conditions, the activity is significantly higher (TON = 440, 66 h, Blue

LEDs). The catalytic activity was maintained when the less energetic green light was used (TON = 113, 25 h) but became marginal upon yellow irradiation (TON = 3, 17 h). Interestingly, our system presents higher robustness and efficiency with respect to a reference system containing $[Ir(ppy)_2bpy]^+$ and $[Co(dmgH)_2PyCl]$ as photosensitizer and catalyst, respectively. For this latter system, the inactivation was relatively fast and the overall efficiency was lower when compared with our system (TON = 22, 0.5 h, Blue LEDs; TON = 12, 2 h, Green LEDs; TON = 0, 17 h, Yellow LEDs). These results proved that our photosensitizer was very photostable as predicted. To the best of our knowledge, our Ir(III)-cobalt dyad presents the best efficiency (TON) and photostability with respect to other supramolecular cobalt-based systems for hydrogen evolution described so far.[28] This successful outcome witnesses that the vectorial electron transfer works well between the Ir(III) and Co(III) moieties despite its relative slowness as compared with systems relying on Ir(III) tris-bidentate complexes.

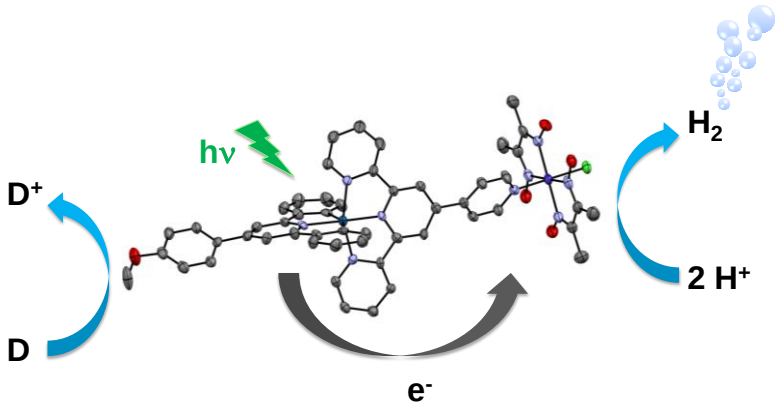

Figure 8.3 – Supramolecular Ir(III)-Co(III) dyad for hydrogen photo-evolution.

Based on the ability of our complexes to photo-induce electron transfer, we broaden the scope to study their interaction with DNA. We were

also interested in comparing $[IrN_4C_2]^+$ and $[IrN_6]^{3+}$ complexes in terms of electron transfer efficiency. Therefore, two complexes (*e.g.* $[IrN_6\text{-}COOH]^{3+}$ and $[IrN_4C_2\text{-}COOH]^+$) differing only by their C/N ratio and bearing a carboxylic acid were prepared (Figure 8.4). Their photo-reactivity with each deoxynucleobase was assessed by luminescence quenching experiments. It was found that the most photo-oxidizing $[IrN_6\text{-}COOH]^{3+}$ can remove an electron from guanine and adenine bases under irradiation while $[IrN_4C_2\text{-}COOH]^+$ may only oxidize guanine. Furthermore, $[IrN_4C_2\text{-}COOH]^+$ displays an intriguing spectroscopic behaviour with a dual emission, the most energetic band ascribed to ^{3}LC/^{3}MLCT transition centered on terpyridine part and the other band attributed to ^{3}MLLCT from cyclometalated iridium fragment to terpyridine. When $[IrN_4C_2\text{-}COOH]^+$ was left with guanine derivative, only the most energetic transition was quenched which is in agreement with some thermodynamic considerations. After these preliminary studies, interactions between $[IrN_6\text{-}COOH]^{3+}$ and DNA revealed that only guanine containing polynucleotides induce electron transfer upon irradiation. Without guanine, DNA protects the complex from external environment inducing an increase of the luminescence.

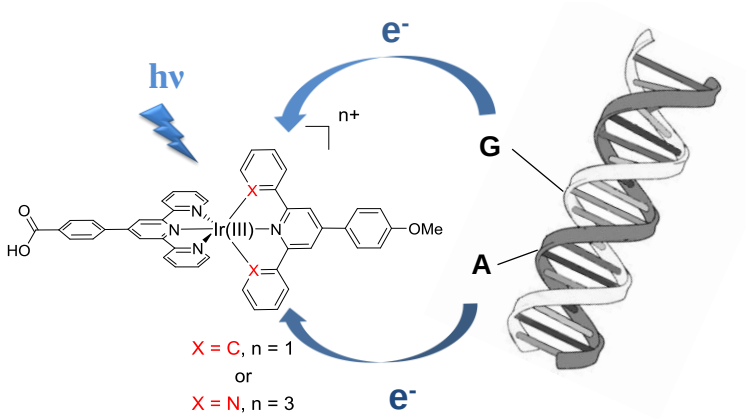

Figure 8.4 – Photo-induced electron transfer occurring between $[IrN_6\text{-}COOH]^{3+}$ (or $[IrN_4C_2\text{-}COOH]^+$) and DNA deoxynucleobases.

To further demonstrate the usefulness of our systems, we showed that photo-initiated organic transformations can be achieved by choosing substrate holding a relatively labile C-Br bond. Hence, the photocatalysis with our Ir(III) complexes have been extended to organic synthesis. For ease of synthesis in larger quantity, $[Ir(N\text{^}N\text{^}N)_2]^{3+}$ structures have been chosen. Therefore, four complexes (**$[IrN_6]^{3+}$**) were synthesized and their photocatalytic activity was demonstrated in homogeneous systems. Moreover, the grafting of **$[IrN_6]^{3+}$** on graphene source for "heterogeneous" catalyst was achieved. The best catalyst loading was realized for the esterification of rGO with **$[IrN_6\text{-}OH]^{3+}$**. The resulting catalyst displays an interesting activity for the cyclization reaction. In addition, it may be easily recovered and recycled for several runs despite reproducibility problems. Furthermore, the non-covalent π-π stacking interactions of **$[IrN_6\text{-}Pyrene]^{3+}$** with rGO led to an unexpected switch off/on effect of the catalysis for ring cyclization. The catalytic efficiency is qualitatively summarized in the Figure 8.5.

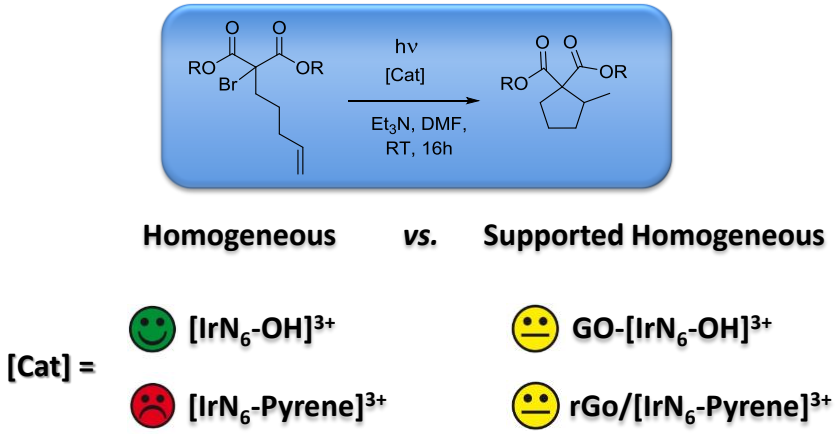

Figure 8.5 – Qualitative summary of radical cyclization conversion using **$[IrN_6\text{-}OH]^{3+}$**, **$[IrN_6\text{-}Pyrene]^{3+}$** in both homogeneous and graphene supported homogeneous photocatalysis.

The last part of our Ph.D. thesis manuscript deals with the exploratory development of a novel method to couple several terpyridine moieties (Scheme 8.1). The methodolody was successfully applied from a prepared terpyridine acetyl-pyridine moiety leading to fully conjugated and luminescent tri-terpyridine ligands. Compared to other procedures, the originality of the approach was the ease of functionalization of the central part. Various functional groups including electron donors (OMe, SMe), acceptors (CN, acetal-pyridine), halide (Br) and aromatic systems with extended conjugation (naphtalenes) were used to validate the method. Subsequent Suzuki-Miyaura cross-coupling between either two tri-tpys properly functionalized or tri-tpy and tpy provided respectively hexa-terpyridine or tetra-terpyridine evidencing the relevance of the strategy to reach larger scaffolds.

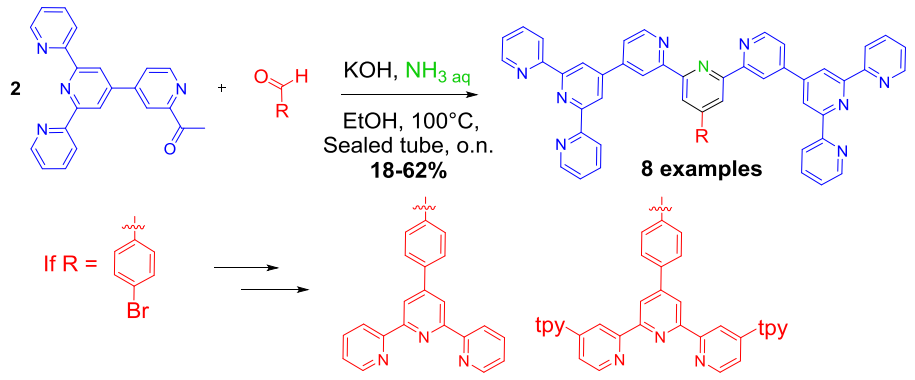

Scheme 8.1 – Synthetic methodology developed to reach multi-tpy scaffolds.

8.2 Prospects

From the results unveiled in this work, this is clear that further efforts can be provided to take advantage of the specificity of studied complexes.

The $[Ir(N^N^N)(C^N^C)]^+$ structure widely absorbs in the visible range. In addition, the anchoring of an electron withdrawing group on **$[Ir\text{-}Py]^+$** (such as proton, methyl or cobalt center) results in red-shifted electronic transitions. Therefore, it would be interesting to assess the impact of modifications on both the cyclometalated (C^N^C) and terpyridine (N^N^N) ligands with donor or acceptor groups in order to cover the whole visible spectrum as it has been achieved for tris-bidentate Ir(III) complexes.

As a consequence, the resulting Ir(III) bis-terdentate structures could be tested in hydrogen photo-evolution experiments to exploit the less energetic colors of the visible spectrum. In addition, functionalization of $[Ir(N^N^N)(C^N^C)]^+$ complexes could affect the quantum yield in a positive way to speed up photocatalytic activity while keeping their remarkable photo-stability. However, it remains complicated to predict which substitutions would foster such interesting properties.

In Chapter 5, we have evidenced that photo-induced electron transfer occurs from both $[Ir(N^N^N)(C^N^C)]^+$ and $[Ir(N^N^N)_2]^{3+}$ and DNA bases. Unfortunately, only holes are injected indicating that the photo-reducing power is not sufficient. Nevertheless, the covalent anchoring of **$[IrN_6\text{-}COOH]^{3+}$** and **$[IrN_4C_2\text{-}COOH]^+$** should be performed especially to make this latter complex fully water soluble. In this case, the hydrogen photo-production could be tested if the tethering of a suitable catalyst is achieved. Another strategy could consist of targeting an oxidation reaction instead of a reduction since positive charges injection is triggered upon

irradiation. However, in this case, the catalyst will have to be different and to match with the considered reaction.

Overall, harsch synthetic conditions deeply limit the functionalization of studied Ir(III) complexes. During this Ph.D. thesis, some attemps have been unsuccessfully tried to favor deprotonation of the bis-cyclometalated ligand for example by addition of bases. The discovery of significantly milder conditions would represent an important advance in the field since that would enable to add some more sensitive functional groups.

The novel multi-terpyridine-based structures pave the way to numerous applications in different research area. For instance, we showed that tri-tpy could be covalently coupled to other ligands providing multiple chelation sites (tetra- and hexa-tpy). Nevertheless, the access to these large structures relies on additional palladium cross-coupling reactions. A simple method to reach such molecules in one step from our quaterpyridine precursor could be achieved by the use of terephtaldehyde instead of mono-benzaldehydes (Scheme 8.2). Some synthetic trials were carried out to obtain this structure. However, the intermediates were not soluble in our conditions preventing the completion of the reaction. The addition of a co-solvent helping the dissolution of these intermediates while maintaining insolubility of the product can solve this issue.

In addition, thiols chemistry starting from the thiomethyl tri-terpyridines may also be applied (Scheme 8.3). According to our observations, the presence of sulfur-based multi-tpy ligands tends to increase the solubility of the system allowing a larger range of applications.

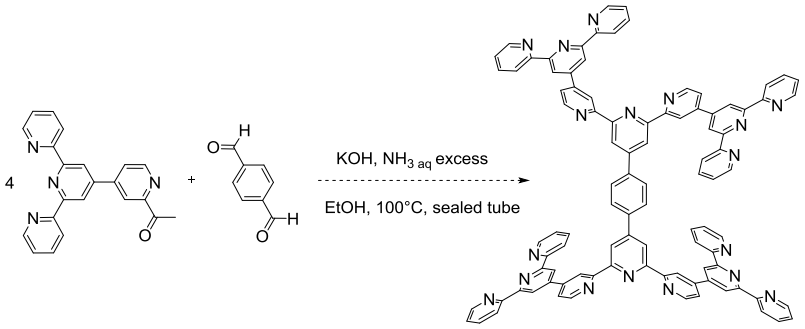

Scheme 8.2 – Potential one-pot synthesis of other "hexa-terpyridine" using terephtaldehyde as bridging precursor.

The control of the architecture based on the interplay of ligands and transition metals is essential and allowed to reach colorful assemblies from terpyridines such as cycles, grids, racks, helicates or roxatanes.[303-311] Our novel functionalized structures should be convenient to design such three-dimensional architectures. The incorporation of convenient metals with our hexa-tpy structure may lead to supramolecular assemblies (Figure 8.6) with potential interesting properties. The scope and limitations of these novel structures are currently investigated in the Ph.D. thesis of Simon CERFONTAINE (Prof. B. ELIAS).

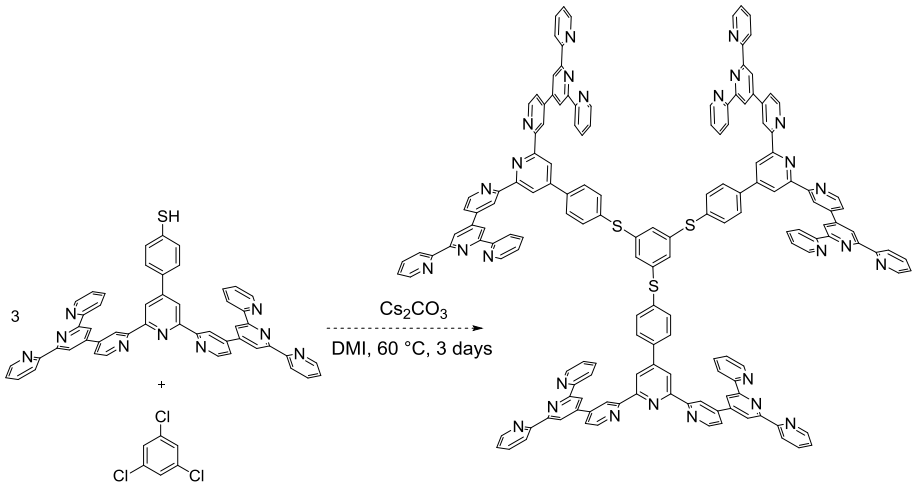

Scheme 8.3 – Potential synthesis of "nona-terpyridine" using thiols chemistry.

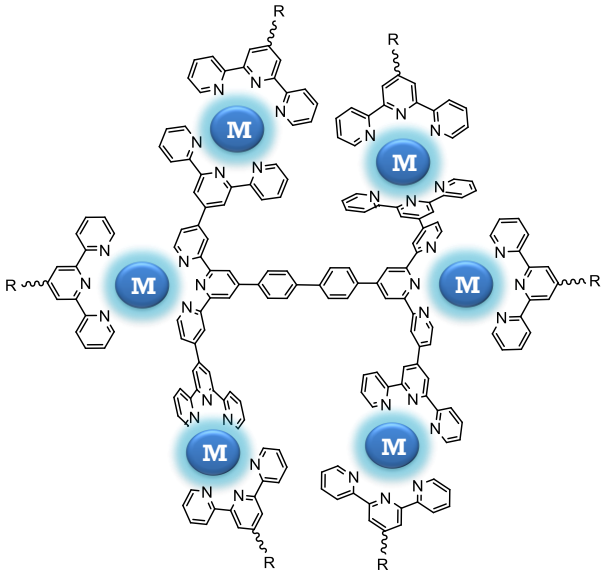

Figure 8.6 – Potential metallo-assembly based on our hexa-tpy structure.

Chapter 9 - Instrumental techniques

9.1 Nuclear Magnetic Resonance (^{1}H and ^{13}C NMR)

^{1}H and ^{13}C NMR spectra have been recorded on a Bruker AC-300 Avance II (^{1}H: 300 MHz), a Varian GEMINI-2000 (^{1}H : 300 MHz, ^{13}C: 75 MHz) or a Bruker AM-500 (^{1}H : 500 MHz, ^{13}C: 125 MHz). Spectra were obtained in $CDCl_3$, CD_3CN, DMSO-d_6, D_2O and $(CD_3)_2CO$. The chemical shifts (given in ppm) were measured versus the residual peak of solvent as the internal standard. The constants coupling (J) are given in Hertz. ^{13}C NMR spectra were obtained with broadband proton decoupling. Multiplicity is given as follows: s = singlet, d = doublet, t = triplet, q = quadruplet, m = multiplet, br = broad.

9.2 Mass Spectrometry

HRMS were recorded on a Q-Extractive orbitrap from ThermoFisher. Samples were ionized either by ESI or by APCI (positive mode) (capillary temperature: 250 °C, vaporizer temperatures: 250 °C or 400 °C, sheath gas flow rate: 20).

9.3 Elemental Analysis

The elemental analyses (C, H, N) of the Ir(III) bis-terdentate complexes were realized by MEDAC Ltd., UK.

9.4 UV-vis Absorption Spectrophotometry

UV-vis absorption spectra were recorded on a Shimadzu UV-1700. Data were converted and transferred to a PC computer. A halogen lamp from Narva-light (12V/20 W) was used to generate light in the visible range. Near-UV light was produced from a Shimadzu deuterium lamp.

9.5 Determination of Molar Extinction Coefficient

Molar extinction coefficients were determined by measuring absorbance of different solutions with known complex concentrations in the appropriate solvent (by weighting). A linear relation was found when absorbance of these solutions in function of concentration was plotted. The molar extinction coefficient was given by the slope of this plot according to the Beer-Lambert equation ($A = \varepsilon.l.C$ where A is the absorbance of the solution, ε is the molar extinction coefficient, l is the optical path length and C is the concentration).

9.6 Emission Spectroscopy

Room temperature luminescence spectra were recorded on Varian Cary Eclipse. Excitation source was a Xe lamp and a phototube was used for detection. Luminescence emission at 77 K was recorded on a FluoroLog3 FL3-22 from Jobin Yvon equipped with an 18V 450W Xenon Short Arc lamp and an R928P photomultiplier, using an Oxford Instrument Optistat DN nitrogen cryostat controlled by an Oxford Intelligent Temperature Controller (ITC503S) instrument. Data were converted and transferred to a PC computer.

9.7 Luminescence Lifetime

Luminescence lifetimes were measured with a modified Applied Photophysics laser kinetic spectrometer by exciting the samples at 355 nm with a Nd-YAG pulsed laser (Continuum NY 61-10). Emitted light as a function of time was detected with a R-928 Hamamatsu photomultiplier tube whose output was applied to a digital oscilloscope (Hewlett-Packard HP 54200A) interfaced with a Dell Dimension DE051 computer. Signals were averaged over at least 16 shots and corrected for baseline. Igor 6.1 software was used for the decay analyses.

9.8 Determination of Quantum Yield

The luminescence quantum yield of a complex *i*, Φ_i, is determined by comparison with a reference complex. In our case, $[Ru(bpy)_3]^{2+}$ in water under air was used as reference $\Phi_{ref} = 0.028$.[140] The luminescence quantum yield of the complex *i* is given by the equation:

$$\Phi_i = \Phi_{ref} \frac{A_{ref}}{A_i} \frac{\int I_i \, d\nu}{\int I_{ref} \, d\nu} \frac{\eta_i^2}{\eta_{ref}^2} \quad \text{(equation 1)}$$

where I_{ref} and I_i are respectively the emission intensity of the reference and the complex *i*, A_{ref} and A_i are the optical density of the reference and the complex *i* solutions at the same wavelength excitation, and η_{ref} and η_i are the refractive index of solvents.

9.9 Cyclic Voltammetry

Cyclic voltammetry was carried out in a one-compartment cell, using a glassy carbon disk working electrode (approximate area = 0.03 cm^2), a platinum wire as counter electrode and an Ag/AgCl electrode as reference electrode. The potential of the working electrode was controlled by an Autolab PGSTAT 100 potentiostat through a PC interface. The cyclic voltammograms were recorded with a sweep rate of 100 or 400 $mV.s^{-1}$, either in dried acetonitrile (Acros, HPLC grade) or in dried DMF (Sigma-Aldrich, HPLC grade). Tetrabutylammonium perchlorate (0.1 M) was used as supporting electrolyte and the samples were purged by argon before each measurement.

9.10 Photochemical Reactor description and photo-production of hydrogen experiments

All these experiments were warried out in Montreal (Canada) in the laboratory of Prof. Garry Hanan. The experimental set-up has been widely developed and continuously improved by Dr. Daniel Chartrand.

In a typical experiment, the prepared solutions each containing up to 5 mL solution were kept in the dark and thoroughly degassed by Ar carrier gas bubbling into the solution until no oxygen was detected by gas chromatography. The vials contained a Teflon stirrer and were agitated during the whole experiment. The samples were fitted in a carousel submerged inside a thermostated borosilicate waterbath at 20.0 ± 0.3 °C and interchangeable light sources consisting of a 90 x 1 watt LED UFO lamp (Nanning LvXing Lighting Electronics Co.Ltd) centered at the wished wavelength (see Figure 9.1, Figure 9.2 and Table 9.1 for more details on emission band wavelength available).

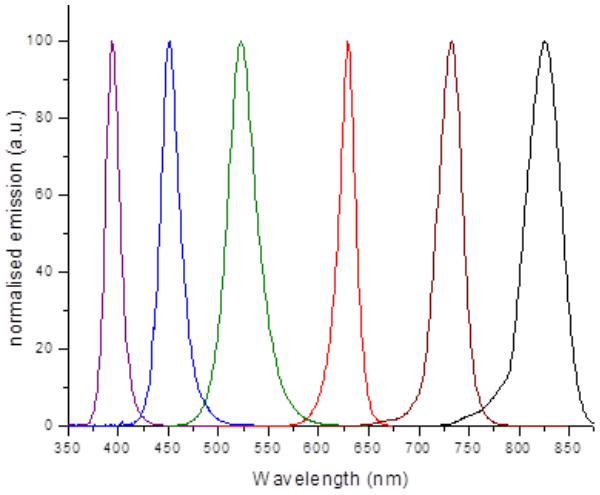

Figure 9.1 – Emission spectra of the lamps available for hydrogen photo-production.

Table 9.1 – Emission characterics of the lamps used.

	UV	**Blue**	**Green**	**Red**	**Near-IR**
$\lambda_{max\ Em}$ (nm)	390	460	560	630	730
$\lambda_{max\ Em}$ (cm^{-1})	25641	21739	17857	15873	13699
$\Delta\lambda$ (nm)	80	150	170	125	150

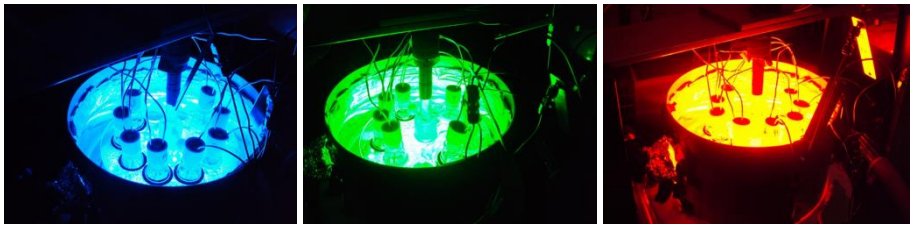

Figure 9.2 – Lamps setup for irradiation experiments.

The flow was monitored at defined time intervals (typically 4 minutes) and the resulting H_2 rates of production were integrated over time to yield the total quantity of molecular hydrogen evolved.

9.11 Hydrogen measurement description

The general setup for flow analysis is presented in Figure 9.3. Gas chromatograms were recorded using a gas chromatograph (GC) (Perkin Elmer Clarus-480) with a TCD detector, argon as the carrier gas a 7' HayeSep N60/80 pre-column and a 2 mL injection loop. The gas flow was set 10 mL/min. Samples solutions were prepared in a standard 20 mL headspace vials and sealed with a rubber septum. These latter were connected to an Argon flow of about 10 mL/min (adjusted with manual flow controller (Porter, 1000)) and referenced with a digital flowmeter (Perkin Elmer FlowMark)) and were pre-bubbled in pure solvent. This flow passed through a 2 mL overflow protection vial, then through a 3-way selection valve (Clippard) before being sent to the GC sample loop. A microprocessor

(Arduino Uno) coupled with custem PC interface allowed for timed injections of both channels in alternation. For calibration of H_2 production rate at a specific Argon flow, a syringe pump (New Era Pump) equipped with a gas-tight syringe (SGE) and a 26s gauge needle (Hamilton) was used to bubble different rates of pure hydrogen gas into the the sample, to a minimum of 0.5 µl/min. This gave a linear fit for peak area for H_2 versus the flow rates of H_2 used in the experiments. For general calibration, stock cylinders of known concentration of H_2 in Argon replaced the Argon flow (inserted at the pre-bubbler, to keep the vapor matrix consistent). The measured results, independent of flow rate (under the same pressure) can be easily converted into a rate of hydrogen following the equation 2.

H_2 rate (µL/min) = [H_2 standard] (ppm) x Ar flow rate (L/min) (equation 2)

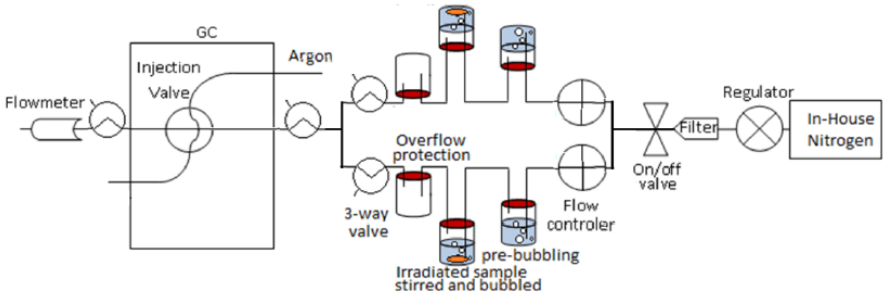

Figure 9.3 – General setup for flow analysis of hydrogen (adapted from [312]).

Chapter 10 - Annexes

10.1 Synthesis of terdentate ligands

Several pioneer methods have been described for the synthesis of terpyridines derivatives.[274,313,314] The most straightforward is a modern Kröhnke procedure developed by G. Hanan *et al.*[76] and therefore this methodology was usually used (Scheme 10.1).

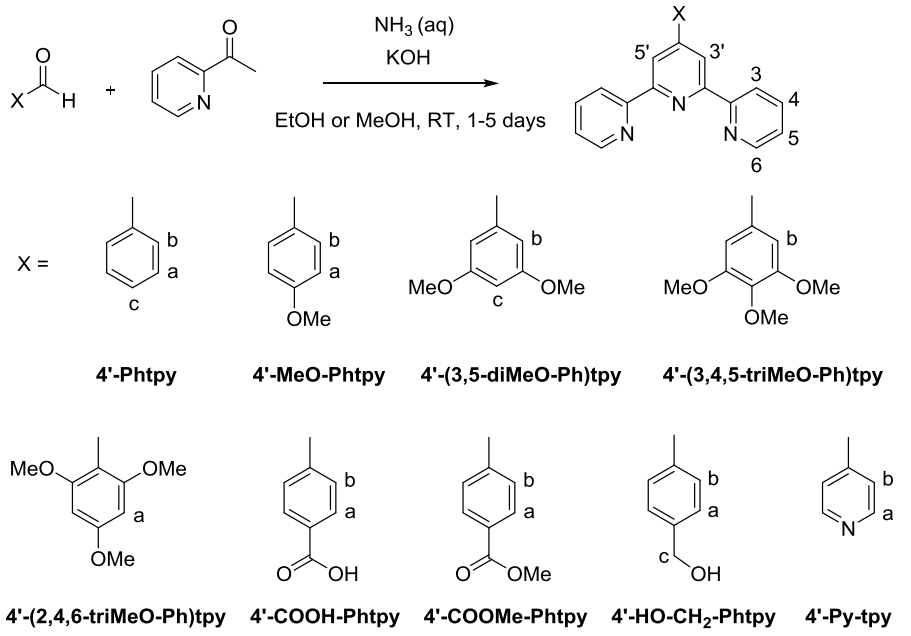

Scheme 10.1 – Synthesis and structures of tpy-based ligands.

Typically, 2-acetylpyridine (2 equiv.) was added in a solution of the corresponding benzaldehyde (1 equiv.), potassium hydroxide (2 equiv.) and aqueous ammonia (28%, excess) in absolute EtOH. The mixture was stirred for 1 to 5 days at room temperature. The off-white precipitate was filtered and washed with cold EtOH. The crude product is recrystallized from warm EtOH to afford the pure product.

For **4′-COOH-Phtpy**,[315] the crude product (after filtration) was dissolved in a MeOH/H_2O (80/20) mixture at 40 °C and the pH was adjusted to 2 by

using 1 M HCl_{aq}. The resulting white precipitate was filtered and washed with cold MeOH.

4′-Phenyl-2,2′:6′,2′′-terpyridine (4′-Phtpy)[102]

Yield: 24%. (White Powder) ^{1}H NMR ($CDCl_3$, 300 MHz) : δ (ppm), 8.73 (s, 2H, $H_{3'}$ and $H_{5'}$), 8.70 (m, 2H, H_6), 8.68 (dd, 2H, H_3, J_{H3-H4} = 8.0 Hz, J_{H3-H5} = 1.0 Hz), 7.91 (m, 2H, H_b), 7.87 (td, 2H, H_4, $J_{H4-H5(H3)}$ = 7.9 Hz, J_{H4-H6} = 1.7 Hz), 7.52 (m, 3H, H_a and H_c), 7.35 (ddd, 2H, H_5, J_{H5-H4} = 7.5 Hz, J_{H5-H6} = 4.8 Hz J_{H5-H3} = 1.0 Hz).

4′-(4-MethoxyPhenyl)-2,2′:6′,2′′-terpyridine (4′-MeO-Phtpy)[316]

Yield: 27%. (White Crystals) ^{1}H NMR ($CDCl_3$, 300 MHz) : δ (ppm), 8.72 (d, 2H, H_6, J_{H6-H5} = 4.8 Hz), 8.70 (s, 2H, $H_{3'}$ and $H_{5'}$), 8.66 (d, 2H, H_3, J_{H3-H4} = 8.0 Hz), 7.93 (d, 4H, H_4 and H_b), 7.34 (ddd, 2H, H_5, J_{H5-H4} = 7.4 Hz, J_{H5-H6} = 4.8 Hz J_{H5-H3} = 1.1 Hz), 7.02 (d, 2H, H_a, J_{Ha-Hb} = 8.8 Hz), 3.88 (s, 3H, OMe).

4′-(3,5-diMethoxyPhenyl)-2,2′:6′,2′′-terpyridine (4′-3,5-diMeO-Phtpy)[317]

Yield: 23%. (White powder) ($CDCl_3$, 300 MHz) : δ (ppm), 8.72 (d, 2H, H_6, J_{H6-H5} = 4.5 Hz), 8.69 (s, 2H, $H_{3'}$ and $H_{5'}$), 8.66 (d, 2H, H_3, J_{H3-H4} = 8.0 Hz), 7.87 (td, 2H, H_4, $J_{H4-H5(H3)}$ = 7.7 Hz, J_{H4-H6} = 1.6 Hz), 7.35 (ddd, 2H, H_5, J_{H5-H4} = 7.7 Hz, J_{H5-H6} = 4.5 Hz, J_{H5-H3} = 1.6 Hz), 7.01 (d, 2H, H_b, J_{Hb-Ha} = 2.2 Hz), 6.56 (t, 1H, H_a, J_{Ha-Hb} = 2.2 Hz), 3.89 (s, 6H, 2 OMe).

4′-(3,4,5-triMethoxyPhenyl)-2,2′:6′,2′′-terpyridine (4′-3,4,5-triMeO-Phtpy)[318]

Yield: 30%. (White powder) ($CDCl_3$, 300 MHz) : δ (ppm), 8.72 (d, 2H, H_6, J_{H6-H5} = 4.9 Hz), 8.67 (s, 2H, $H_{3'}$ and $H_{5'}$), 8.66 (d, 2H, H_3, J_{H3-H4} = 7.2 Hz), 7.88 (t, 2H, H_4, $J_{H4-H5(H3)}$ = 7.2 Hz), 7.36 (dd, 2H, H_5, J_{H5-H4} = 7.2 Hz, J_{H5-H6} = 4.9 Hz), 7.07 (s, 2H, H_b), 3.99 (s, 6H, 2 OMe), 3.92 (s, 3H, 1 OMe).

4′-(2,4,6-triMethoxyPhenyl)-2,2′:6′,2″-terpyridine (4′-2,4,6-triMeO-Phtpy)[77]

Yield: 28%. (Yellow powder) ($CDCl_3$, 300 MHz) : δ (ppm), 8.67 (d, 2H, H_6, J_{H6-H5} = 5.2 Hz), 8.65 (d, 2H, H_3, J_{H3-H4} = 7.6 Hz), 8.41 (s, 2H, $H_{3'}$ and $H_{5'}$), 7.84 (td, 2H, H_4, $J_{H4-H5(H3)}$ = 7.6 Hz, J_{H4-H6} = 1.6 Hz), 7.29 (ddd, 2H, H_5, J_{H5-H4} = 7.6 Hz, J_{H5-H6} = 5.2 Hz, J_{H5-H3} = 1.3 Hz), 6.21 (s, 2H, H_a), 3.87 (s, 6H, 2 OMe), 3.72 (s, 3H, 1 OMe).

4′-(4-CarboxyPhenyl)2,2′:6′,2″-terpyridine (4′-COOH-Phtpy)[315]

Yield: 50 %. (White needles) ^{1}H NMR (DMSO-d_6, 500 MHz) : δ (ppm), 8.90-8.82 (m, 6H, H_3, H_6, $H_{3'}$ and $H_{5'}$), 8.25 (td, 2H, H_4, $J_{H4-H5(H3)}$ = 7.9 Hz), 8.19 (d, 2H, H_a, J_{Ha-Hb} = 8.4 Hz), 8.15 (d, 2H, H_b, J_{Hb-Ha} = 8.4 Hz), 7.72-7.68 (m, 2H, H_5).

4′-(4-MethoxycarbonylPhenyl)2,2′:6′,2″-terpyridine (4′-COOMe-Phtpy)[77]

Yield: 14 %. (White powder) ^{1}H NMR ($CDCl_3$, 300 MHz) : δ (ppm), 8.76 (s, 2H, $H_{3'}$ and $H_{5'}$), 8.74 (d, 2H, H_6, J_{H6-H5} = 4.8 Hz), 8.69 (d, 2H, H_3, J_{H3-H4} = 8.0 Hz), 8.18 (d, 2H, H_a, J_{Ha-Hb} = 8.4 Hz), 7.97 (d, 2H, H_b, J_{Hb-Ha} = 8.4 Hz), 7.90 (td, 2H, H_4, $J_{H4-H5(H3)}$ = 7.8 Hz, J_{H4-H6} = 1.8 Hz), 7.37 (ddd, 2H, H_5, J_{H5-H4} = 7.3 Hz, J_{H5-H6} = 4.5 Hz, J_{H5-H3} = 0.9 Hz), 3.97 (s, 3H, OMe).

The synthesis of the **4′-COOMe-Phtpy** ligand requires the preparation of **4-(Methoxycarbonyl)benzaldehyde** as precursor. The synthesis of this compound is presented below.

4-(Methoxycarbonyl)benzaldehyde[319]

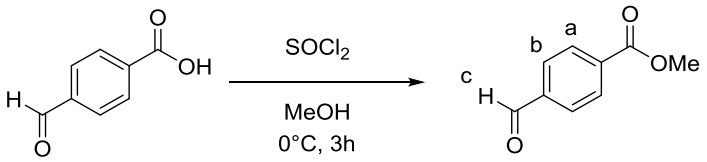

4-Carboxybenzaldehyde (1.000 g, 6.66 mmol) was stirred in dry MeOH (70 mL) until complete dissolution of the solid (10 minutes). Thionyl chloride was slowly added at 0 °C and the mixture was stirred for further 3h at 0°C. The solvent was evaporated. The residue was recovered with CH_2Cl_2 and washed with brine (three times). The organic layer was dried over $MgSO_4$ and the solvent removed under vacuum. The yellow oil was recrystallized in hexane to afford white crystals. Yield: 49 % (530 mg). ^{1}H NMR ($CDCl_3$, 300 MHz) : δ (ppm), 10.10 (s, 1H, H_c), 8.20 (d, 2H, H_a, J_{Ha-Hb} = 8.4 Hz), 7.95 (d, 2H, H_b, J_{Hb-Ha} = 8.4 Hz), 3.96 (s, 3H, OMe).

[4-(2,2′:6′,2′′-terpyridin-4′-yl)phenyl]methanol (4′-HO-CH_2-Phtpy)[320]

Yield: 30%. (Off-white powder) ^{1}H NMR ($CDCl_3$, 300 MHz) : δ (ppm), 8.75 (s, 2H, $H_{3'}$ and $H_{5'}$), 8.74 (d, 2H, H_6, J_{H6-H5} = 5.8 Hz), 8.68 (d, 2H, H_3, J_{H3-H4} = 8.0 Hz), 7.93 (d, 2H, H_b, J_{Hb-Ha} = 8.3 Hz), 7.90 (td, 2H, H_4, $J_{H4-H5(H3)}$ = 7.9 Hz, J_{H4-H6} = 1.7 Hz), 7.52 (d, 2H, H_a, J_{Ha-Hb} = 8.3 Hz), 7.37 (ddd, 2H, H_5, J_{H5-H4} = 7.4 Hz, J_{H5-H6} = 4.8 Hz, J_{H5-H3} = 1.1 Hz), 4.80 (s, 2H, H_c).

The synthesis of the **4′-HO-CH_2-Phtpy** ligand was achieved from the not commercially available **4-Hydroxymethylbenzaldehyde.** The preparation of this precursor is reported hereafter.

4-Hydroxymethylbenzaldehyde[321]

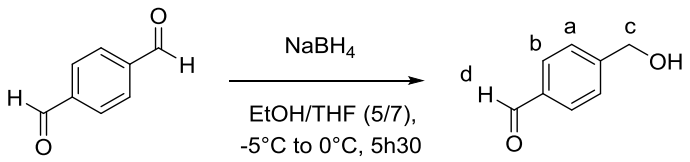

$NaBH_4$ (0.170 g, 3.7 mmol) was slowly added at –5 °C with continuous stirring for 30 min to a solution of dialdehyde (2.0 g, 15.0 mmol) in a mixture of absolute EtOH (25 mL) and THF (35 mL). The mixture was stirred for 5h30, while the temperature was maintained in an interval of 0-5 °C. Then the reaction mixture was neutralized with 2 M HCl to pH = 5, the solvents were evaporated, water (20 mL) was added to the residue and products were extracted with AcOEt (three times). Combined organic extracts were dried with $MgSO_4$ and the solvent was evaporated. The product was purified by column chromatography (SiO_2) using an AcOEt/hexane (1/1) as eluent to afford the pure product as yellow crystals (1.189 g, 58%). ^{1}H NMR ($CDCl_3$, 300 MHz) : δ (ppm), 10.01 (s, 1H, H_d), 7.88 (d, 2H, H_b, J_{Hb-Ha} = 8.1 Hz), 7.54 (d, 2H, H_a, J_{Ha-Hb} = 8.1 Hz, 2H), 4.81 (s, H_d, 2H).

4′-((4-pyridinyl)-2,2′;6′,2′′-terpyridine (4′-Py-tpy)[322]

Yield: 39%. (Off-white powder) ^{1}H NMR ($CDCl_3$, 300 MHz) : δ (ppm), 8.80-8.77 (m, 4H, $H_{3'}$, $H_{5'}$ and H_a), 8.75 (d, 2H, H_6, J_{H6-H5} = 4.8 Hz), 8.69 (d, 2H, H_3, J_{H3-H4} = 8.0 Hz), 7.93 (d, 2H, H_b, J_{Hb-Ha} = 8.3 Hz), 7.92 (td, 2H, H_4, $J_{H4-H5(H3)}$ = 7.7 Hz, J_{H4-H6} = 1.8 Hz), 7.88 (d, 2H, H_b, J_{Hb-Ha} = 6.2 Hz), 7.40 (ddd, 2H, H_5, J_{H5-H4} = 7.5 Hz, J_{H5-H6} = 4.8 Hz J_{H5-H3} = 1.2 Hz).

(4′-(4-methyl-pyridinio)-2,2′;6′,2″-terpyridine)([4′-Me-Py-tpy]$^{+}$)[139]

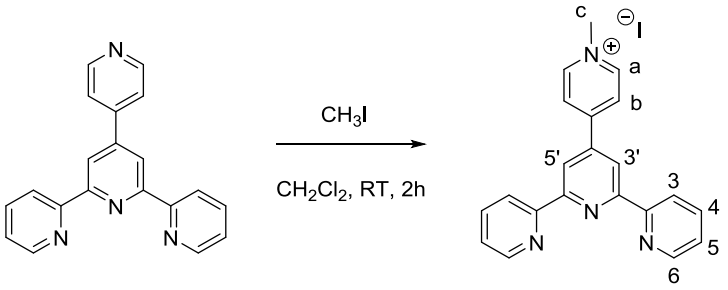

Iodomethane (0.161 mL, 2.6 mmol) was dropwisely added to **4′-Py-tpy** (300 mg, 0.97 mmol) dissolved in dry CH_2Cl_2 under Argon. The mixture was stirred for 16h at room temperature. The yellow iodide salt was filtered and washed with CH_2Cl_2. Yield: 86 % (378 mg). ^{1}H NMR (DMSO-d_6, 300 MHz) : δ (ppm), 9.16 (d, 2H, H_a, J_{Ha-Hb} = 6.8 Hz), 8.92 (s, 2H, $H_{3'}$ and $H_{5'}$), 8.86-8.76 (m, 4H, H_6 and H_b), 8.72 (d, 2H, H_3, J_{H3-H4} = 7.9 Hz), 8.09 (td, 2H, H_4, $J_{H4-H5(H3)}$ = 7.8 Hz, J_{H4-H6} = 1.7 Hz), 7.60 (ddd, 2H, H_5, J_{H5-H4} = 7.4 Hz, J_{H5-H6} = 4.8 Hz J_{H5-H3} = 1.0 Hz), 4.43 (s, 3H, H_c).

Synthesis of 4′-MeO-tppy[102]

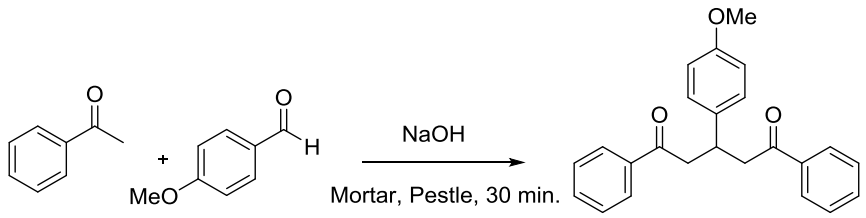

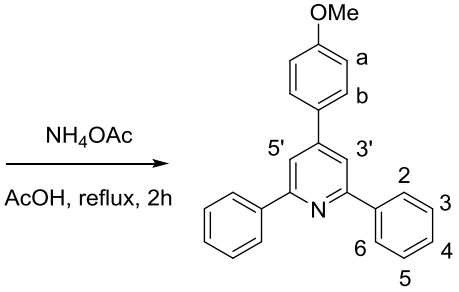

Para-anisaldehyde (0.500 g, 3.67 mmol), acetophenone (0.882 g, 7.34 mmol) and NaOH (0.294 g, 7.34 mmol) were grinded by using a mortar and pestle until a yellow oily mixture was obtained (*ca.* 30 min). The product was dissolved in acetone, transferred to a flask and solvent removed under vacuum. Glacial acetic acid (10 mL) and ammonium acetate (3g, excess) were added and heated to reflux for 3h. The crude product was filtered, washed with water and purified by column chromatography on SiO_2 (Hexane/AcOEt (9/1)) to afford pure product as colorless crystals. Yield: 0.285 g (23 %). ^{1}H NMR (300 MHz, $CDCl_3$): δ (ppm), 8.20 (d, 4H, $H_{2'}$, $H_{2''}$, $H_{6'}$ and $H_{6''}$, $J_{H2'-H3'}$ = 6.9 Hz), 7.87 (s, 2H, $H_{3'}$ and $H_{5'}$), 7.72 (d, 2H, H_b, J_{Hb-Ha} = 8.8 Hz), 7.50 (m, 6H, $H_{3'}$, $H_{3''}$, $H_{4'}$, $H_{4''}$, $H_{5'}$ and $H_{5''}$), 7.06 (d, 2H, H_a, J_{Ha-Hb} = 8.8 Hz), 3.90 (s, 3H, OMe).

10.2 Additional computational data (Chapter 3)

Table 3.6 – The 100 lowest singlet–singlet and 10 lowest singlet–triplet obtained from the TD-DFT/singlets and the TD-DFT/triplets output files for **[Ir-Py]$^+$** at the S_0-optimized geometry.

S_0 to S^x	Wavelength (nm)	Oscillator Strength	Major contribution(s)
1	507.30	0.0017	H-1->LUMO (95%)
2	478.63	0.0582	HOMO->L+1 (98%)
3	476.55	0.118	H-1->L+1 (33%), HOMO->LUMO (63%)
4	447.33	0.1903	H-1->L+1 (65%), HOMO->LUMO (32%)
5	415.93	0.0005	H-2->LUMO (84%)
6	391.32	0.0169	H-2->L+1 (25%), H-1->L+2 (65%)
7	390.45	0.0005	HOMO->L+2 (92%)
8	389.54	0.008	H-2->L+1 (65%), H-1->L+2 (29%)
9	388.44	0.0001	H-3->LUMO (96%)
10	365.16	0	H-4->LUMO (81%), H-2->LUMO (10%)
11	364.82	0.0198	H-3->L+1 (97%)
12	354.29	0	H-5->LUMO (84%), H-4->LUMO (10%)
13	352.53	0.0557	HOMO->L+3 (91%)
14	351.28	0.0038	HOMO->L+4 (96%)
15	345.68	0.0229	H-1->L+3 (89%)
16	344.64	0.0003	H-4->L+1 (89%)
17	334.95	0.0001	H-5->L+1 (90%)
18	334.73	0.4302	H-2->L+2 (66%), H-1->L+4 (25%)
19	334.44	0.017	HOMO->L+5 (95%)
20	330.50	0.3239	H-2->L+2 (26%), H-1->L+4 (53%)
21	323.73	0.2508	H-1->L+4 (11%), H-1->L+5 (56%), HOMO->L+6 (20%)
22	321.73	0.1007	H-7->LUMO (29%), H-6->LUMO (50%)
23	320.22	0.0014	H-1->L+5 (20%), HOMO->L+6 (71%)
24	317.91	0.0543	H-3->L+2 (58%), H-2->L+4 (32%)
25	317.08	0.0001	H-9->LUMO (47%), H-8->LUMO (35%)
26	313.50	0.0117	H-1->L+6 (89%)
27	309.93	0.001	H-9->LUMO (31%), H-8->LUMO (40%)
28	306.70	0	H-2->L+3 (91%)
29	305.33	0.0074	H-12->LUMO (15%), H-9->L+1 (30%), H-8->L+1 (48%)
30	304.17	0.1022	H-3->L+2 (34%), H-2->L+4 (56%)

31	300.89	0.0006	H-9->L+1 (28%), H-8->L+1 (20%), HOMO->L+9 (19%)
32	300.69	0.0041	H-10->LUMO (83%)
33	297.29	0.0021	H-9->L+1 (20%), H-8->L+1 (14%), HOMO->L+9 (37%), HOMO->L+10 (13%)
34	294.14	0.0611	H-4->L+2 (72%)
35	293.10	0.0508	H-12->LUMO (28%), H-3->L+3 (21%), H-1->L+9 (18%)
36	293.04	0.0332	H-12->LUMO (19%), H-3->L+3 (14%), H-1->L+9 (31%), H-1->L+10 (12%)
37	292.16	0.0009	H-7->LUMO (51%), H-6->LUMO (32%)
38	291.82	0.0074	H-2->L+5 (82%)
39	289.53	0.0996	H-12->L+1 (12%), H-7->L+1 (16%), H-6->L+1 (31%), H-5->L+2 (11%), H-4->L+2 (22%)
40	288.86	0.1479	H-12->LUMO (21%), H-11->LUMO (10%), H-3->L+3 (56%)
41	287.24	0.0563	H-11->LUMO (84%)
42	283.95	0.0571	H-5->L+2 (66%)
43	282.82	0.0196	H-10->L+1 (43%), H-7->L+1 (34%)
44	282.76	0.0038	H-10->L+1 (26%), H-7->L+1 (30%), H-6->L+1 (26%)
45	281.67	0.1381	H-11->L+1 (41%), H-3->L+4 (32%)
46	281.56	0.0027	H-2->L+6 (87%)
47	280.46	0.0489	H-11->L+1 (44%), H-10->L+1 (20%), H-3->L+4 (27%)
48	276.61	0.0002	H-4->L+3 (87%)
49	275.89	0.0253	H-12->L+1 (48%), H-3->L+4 (16%)
50	273.86	0.0149	H-4->L+4 (87%)
51	272.74	0.1128	H-12->L+1 (13%), H-3->L+5 (70%)
52	271.10	0	H-5->L+3 (89%)
53	269.75	0.1332	H-5->L+4 (76%)
54	269.26	0.0002	H-9->L+2 (37%), H-8->L+2 (54%)
55	269.10	0.0189	H-7->L+2 (16%), H-2->L+9 (20%)
56	268.23	0.0151	H-7->L+2 (30%), H-6->L+2 (18%), H-2->L+10 (18%)
57	267.92	0.0062	H-3->L+6 (94%)
58	264.40	0.239	H-13->LUMO (93%)
59	264.33	0.019	H-4->L+5 (78%)
60	262.35	0.006	HOMO->L+7 (88%)
61	261.19	0.0003	HOMO->L+8 (60%), HOMO->L+9 (21%)
62	260.85	0.0016	H-7->L+2 (31%), H-6->L+2 (49%)
63	259.82	0.0116	H-5->L+5 (81%)
64	257.73	0.004	H-13->L+1 (82%)

65	256.26	0.0095	H-1->L+7 (76%)
66	256.17	0.0532	H-9->L+2 (14%), H-1->L+7 (19%), H-1->L+8 (41%)
67	255.74	0.1352	H-9->L+2 (33%), H-8->L+2 (22%), H-1->L+8 (20%)
68	255.31	0	H-4->L+6 (90%)
69	252.18	0.0042	H-10->L+3 (15%), H-7->L+3 (19%), H-6->L+3 (33%)
70	250.91	0.0001	H-5->L+6 (37%), HOMO->L+12 (52%)
71	250.60	0	H-5->L+6 (53%), HOMO->L+12 (36%)
72	249.52	0.0003	H-14->L+1 (11%), H-10->L+3 (47%)
73	248.93	0.0077	H-1->L+8 (15%), H-1->L+9 (15%), H-1->L+10 (61%)
74	248.33	0.0644	H-9->L+3 (32%), H-8->L+3 (54%)
75	248.24	0.0051	H-9->L+4 (37%), H-8->L+4 (55%)
76	247.19	0.0271	H-14->LUMO (74%), HOMO->L+11 (13%)
77	246.71	0.0004	H-9->L+3 (53%), H-8->L+3 (29%)
78	246.58	0.0131	H-12->L+2 (77%)
79	244.47	0.0037	H-9->L+4 (37%), H-8->L+4 (23%)
80	244.40	0.1418	H-14->L+1 (74%), H-6->L+3 (10%)
81	244.25	0.0121	HOMO->L+8 (19%), HOMO->L+10 (65%)
82	243.25	0.0234	H-7->L+4 (29%), H-6->L+4 (54%)
83	241.76	0.0029	H-7->L+4 (43%), H-6->L+4 (23%)
84	240.76	0.0279	H-7->L+2 (12%), H-2->L+8 (32%), H-2->L+10 (29%)
85	240.00	0.0022	H-9->L+5 (13%), H-8->L+5 (22%), HOMO->L+13 (46%), HOMO->L+14 (10%)
86	239.17	0.1944	H-8->L+5 (12%), H-1->L+12 (41%)
87	238.85	0.024	H-9->L+5 (26%), H-8->L+5 (27%), HOMO->L+13 (23%), HOMO->L+14 (12%)
88	238.77	0.0041	H-7->L+5 (18%), H-6->L+5 (30%), HOMO->L+11 (22%)
89	238.65	0.0001	H-15->LUMO (96%)
90	237.58	0.001	H-2->L+7 (96%)
91	237.20	0.0002	H-3->L+9 (48%), H-3->L+10 (17%)
92	237.07	0.0004	H-7->L+3 (56%), H-6->L+3 (34%)
93	236.80	0.2856	H-2->L+8 (33%), H-2->L+9 (23%), H-2->L+10 (17%), HOMO->L+11 (10%)
94	236.41	0	H-10->L+2 (96%)
95	236.24	0.0052	H-1->L+11 (44%), HOMO->L+11 (21%)
96	236.17	0.0098	H-1->L+11 (32%), HOMO->L+11 (24%)
97	236.00	0.133	H-9->L+5 (39%), H-8->L+5 (23%), H-1->L+12 (12%)
98	235.69	0.024	H-11->L+3 (78%)

99	234.23	0.0415	H-12->L+3 (15%), H-7->L+6 (18%), H-6->L+6 (31%), H-1->L+11 (15%)
100	233.40	0	H-11->L+2 (98%)

S_0 to T^x	**Wavelength (nm)**	**Oscillator Strength**	**Major contribution(s)**
1	623.44	0	HOMO->LUMO (95%)
2	528.62	0	H-1->LUMO (76%), HOMO->L+1 (15%)
3	512.45	0	H-1->LUMO (15%), HOMO->L+1 (82%)
4	484.23	0	H-1->L+1 (77%)
5	450.01	0	H-2->L+2 (21%), H-1->L+4 (32%), H-1->L+5 (12%)
6	440.34	0	H-1->L+2 (84%)
7	421.73	0	H-2->LUMO (76%)
8	417.24	0	H-7->L+1 (13%), H-6->L+1 (22%), H-1->L+1 (19%), HOMO->L+3 (12%)
9	404.51	0	H-2->L+2 (53%), H-1->L+4 (15%)
10	399.78	0	HOMO->L+2 (88%)

Table 3.7 – The 100 lowest singlet–singlet and 10 lowest singlet–triplet obtained from the TD-DFT/singlets and the TD-DFT/triplets output files for **[Ir-Py-H]$^{2+}$** at the S_0-optimized geometry.

S_0 to S^x	Wavelength (nm)	Oscillator Strength	Major contribution(s)
1	610.33	0.0002	HOMO->LUMO (93%)
2	549.91	0.3702	H-1->LUMO (95%)
3	501.59	0.001	H-2->LUMO (95%)
4	485.89	0.053	H-1->L+1 (97%)
5	468.68	0.0624	HOMO->L+1 (94%)
6	458.59	0.0001	H-3->LUMO (92%)
7	425.07	0.0097	HOMO->L+2 (91%)
8	422.49	0	H-5->LUMO (12%), H-4->LUMO (78%)
9	414.48	0.0039	H-1->L+2 (95%)
10	409.32	0	H-5->LUMO (77%), H-4->LUMO (16%)
11	405.88	0	H-2->L+1 (95%)
12	386.49	0.0291	HOMO->L+3 (97%)
13	380.03	0.0008	H-1->L+3 (98%)
14	376.49	0.0194	H-3->L+1 (97%)
15	372.78	0.0001	H-2->L+2 (80%)
16	360.19	0.0443	H-7->LUMO (91%)
17	353.88	0.0001	H-8->LUMO (73%), H-2->L+2 (14%)
18	353.63	0.0004	H-4->L+1 (87%)
19	346.88	0.0078	H-3->L+2 (91%)
20	343.92	0.0001	H-5->L+1 (87%), H-4->L+1 (11%)
21	342.68	0.0145	H-1->L+5 (94%)
22	341.27	0.4345	H-9->LUMO (59%), H-2->L+3 (29%)
23	341.14	0.0076	H-6->LUMO (92%)
24	338.45	0.0007	H-1->L+4 (96%)
25	334.76	0.2911	H-2->L+3 (49%), H-1->L+6 (16%), HOMO->L+5 (14%)
26	332.86	0.0011	H-1->L+6 (68%), HOMO->L+5 (15%)
27	331.49	0.0035	H-10->LUMO (29%), HOMO->L+4 (21%), HOMO->L+6 (44%)
28	331.39	0.0025	HOMO->L+4 (67%), HOMO->L+6 (11%)
29	328.37	0.0003	H-10->LUMO (19%), H-1->L+7 (68%)
30	326.24	0.0787	H-10->LUMO (35%), H-1->L+7 (28%), HOMO->L+6 (30%)
31	325.56	0.0114	H-4->L+2 (79%)

32	325.36	0.1009	H-9->LUMO (16%), H-2->L+3 (13%), HOMO->L+5 (48%)
33	318.29	0.1726	HOMO->L+7 (83%)
34	318.04	0.0026	H-5->L+2 (87%)
35	317.51	0.0453	H-3->L+3 (51%), H-2->L+5 (36%)
36	306.23	0.0232	H-8->L+1 (37%), H-2->L+4 (38%)
37	305.27	0.0284	H-8->L+1 (15%), H-3->L+3 (11%), H-2->L+4 (59%), H-2->L+5 (11%)
38	304.72	0.0532	H-8->L+1 (34%), H-3->L+3 (24%), H-2->L+5 (31%)
39	301.24	0.0507	H-9->L+1 (94%)
40	297.15	0.0008	H-2->L+6 (94%)
41	295.79	0.1534	H-10->L+1 (16%), H-7->L+1 (58%)
42	295.33	0.0013	H-2->L+7 (34%), H-1->L+9 (46%)
43	293.46	0.0016	H-6->L+1 (89%)
44	293.17	0.0102	H-2->L+7 (42%), H-1->L+9 (33%), HOMO->L+9 (10%)
45	292.92	0.0014	HOMO->L+9 (64%)
46	291.52	0.0009	H-4->L+3 (79%)
47	288.63	0.0654	H-7->L+2 (90%)
48	286.18	0.0261	H-11->LUMO (13%), H-9->L+2 (17%), H-5->L+3 (51%)
49	284.56	0.0018	H-3->L+4 (92%)
50	283.74	0	H-8->L+2 (80%)
51	282.99	0.0274	H-10->L+1 (23%), H-5->L+3 (15%), H-3->L+5 (37%)
52	281.89	0.2358	H-11->LUMO (74%)
53	280.66	0.0222	H-3->L+6 (94%)
54	278.97	0.0108	H-10->L+1 (45%), H-3->L+5 (28%)
55	275.95	0.011	H-9->L+2 (68%), H-5->L+3 (11%), H-3->L+5 (10%)
56	275.19	0.0001	H-6->L+2 (93%)
57	272.87	0.0717	H-3->L+7 (82%)
58	272.50	0.0222	H-4->L+5 (87%)
59	270.60	0.0093	H-6->L+3 (78%), H-2->L+11 (12%)
60	268.95	0.023	H-5->L+5 (13%), H-4->L+4 (50%)
61	268.24	0.0868	H-5->L+5 (56%), HOMO->L+8 (13%)
62	267.90	0.0328	H-4->L+4 (17%), HOMO->L+8 (62%)
63	267.08	0	H-4->L+6 (91%)
64	266.91	0.0286	H-8->L+9 (14%), H-5->L+9 (11%), H-4->L+4 (26%), H-2->L+9 (20%)
65	265.67	0.1248	H-10->L+2 (75%), HOMO->L+8 (13%)
66	264.72	0.3306	H-7->L+1 (10%), H-1->L+8 (76%)
67	264.20	0.0017	H-12->LUMO (94%)

68	263.69	0.0062	H-5->L+4 (84%)
69	263.47	0.0169	H-4->L+7 (72%)
70	262.26	0	H-5->L+6 (90%)
71	261.63	0	H-9->L+3 (90%)
72	259.66	0.0199	H-5->L+7 (85%)
73	256.78	0.0004	H-7->L+3 (84%)
74	256.04	0.0005	H-1->L+10 (75%)
75	255.57	0.0001	H-13->LUMO (94%)
76	253.88	0.1236	H-8->L+3 (60%), HOMO->L+10 (25%)
77	253.50	0.0548	H-8->L+3 (25%), HOMO->L+10 (57%)
78	251.06	0.0673	H-11->L+1 (87%)
79	248.40	0.0234	H-14->LUMO (15%), H-7->L+4 (79%)
80	247.23	0.0515	H-15->LUMO (84%)
81	246.81	0.0002	H-1->L+12 (84%)
82	246.16	0.0523	H-14->LUMO (58%), H-7->L+4 (17%)
83	245.74	0.0014	H-2->L+8 (93%)
84	245.54	0.0072	HOMO->L+11 (76%)
85	244.10	0.0006	H-6->L+5 (74%), H-6->L+7 (16%)
86	243.55	0.014	H-10->L+3 (74%), H-7->L+3 (11%)
87	242.00	0.0005	H-8->L+5 (69%)
88	241.53	0.0257	H-9->L+5 (85%)
89	241.09	0.0371	H-6->L+3 (15%), H-2->L+10 (15%), H-2->L+11 (40%)
90	240.19	0.0009	H-6->L+4 (95%)
91	239.85	0.0068	H-14->LUMO (12%), H-7->L+5 (61%)
92	239.15	0.0009	H-3->L+9 (69%)
93	238.60	0.078	H-1->L+11 (59%), HOMO->L+12 (10%)
94	238.41	0.003	H-8->L+6 (87%)
95	238.28	0.2035	H-7->L+6 (48%), H-1->L+13 (21%)
96	237.85	0.1166	H-8->L+7 (17%), H-1->L+11 (17%), HOMO->L+12 (29%)
97	237.12	0.2417	H-2->L+10 (49%), H-2->L+11 (17%)
98	236.84	0.0122	H-18->LUMO (73%)
99	236.68	0.0622	H-8->L+4 (53%), H-1->L+13 (12%)
100	236.49	0.1144	H-8->L+4 (24%), H-7->L+6 (14%), H-1->L+13 (31%), H-1->L+14 (15%)

S_0 to T^x	Wavelength (nm)	Oscillator Strength	Major contribution(s)
1	746.12	0	H-1->LUMO (88%)
2	627.80	0	HOMO->LUMO (89%)
3	522.48	0	H-1->L+1 (97%)
4	505.25	0	H-2->LUMO (92%)
5	493.51	0	HOMO->L+1 (81%)
6	464.37	0	H-3->LUMO (80%)
7	459.62	0	H-1->L+2 (85%)
8	448.71	0	H-2->L+3 (22%), HOMO->L+5 (27%), HOMO->L+7 (15%)
9	438.41	0	HOMO->L+3 (84%)
10	433.67	0	H-3->LUMO (12%), HOMO->L+2 (76%)

Table 3.8 – The 100 lowest singlet–singlet and 10 lowest singlet–triplet obtained from the TD-DFT/singlets and the TD-DFT/triplets output files for **[Ir-Py-Me]$^{2+}$** at the S_0-optimized geometry.

S_0 to S^x	Wavelength (nm)	Oscillator Strength	Major contribution(s)
1	598.29	0.0002	HOMO->LUMO (93%)
2	542.03	0.3834	H-1->LUMO (94%)
3	491.90	0.0008	H-2->LUMO (94%)
4	485.71	0.0532	H-1->L+1 (98%)
5	467.77	0.0725	HOMO->L+1 (93%)
6	451.03	0.0001	H-3->LUMO (91%)
7	421.80	0.0098	HOMO->L+2 (90%)
8	416.48	0	H-5->LUMO (12%), H-4->LUMO (76%)
9	413.18	0.0015	H-1->L+2 (95%)
10	404.91	0	H-2->L+1 (95%)
11	403.43	0	H-5->LUMO (76%), H-4->LUMO (17%)
12	386.83	0.0287	HOMO->L+3 (97%)
13	380.80	0.0008	H-1->L+3 (98%)
14	375.83	0.0205	H-3->L+1 (97%)
15	370.13	0	H-2->L+2 (82%)
16	355.97	0.0426	H-7->LUMO (89%)
17	353.18	0.0004	H-4->L+1 (87%)
18	350.08	0.0002	H-8->LUMO (75%), H-2->L+2 (12%)
19	344.79	0.0044	H-3->L+2 (84%)
20	343.45	0.0004	H-5->L+1 (86%), H-4->L+1 (10%)
21	343.21	0.0195	H-1->L+5 (86%)
22	339.59	0.5404	H-9->LUMO (48%), H-2->L+3 (42%)
23	336.61	0.0015	H-1->L+4 (97%)
24	336.23	0	H-6->LUMO (94%)
25	334.53	0.2115	H-2->L+3 (35%), H-1->L+6 (36%), HOMO->L+5 (11%)
26	332.95	0.0005	H-1->L+6 (52%), HOMO->L+5 (27%)
27	330.72	0.009	H-10->LUMO (13%), HOMO->L+6 (76%)
28	329.45	0.0006	HOMO->L+4 (93%)
29	328.38	0.012	H-1->L+7 (87%)
30	324.90	0.1159	H-9->LUMO (23%), H-2->L+3 (15%), HOMO->L+5 (48%)
31	324.04	0.0653	H-10->LUMO (70%), HOMO->L+6 (16%)

32	323.68	0.0005	H-4->L+2 (89%)
33	318.47	0.1695	HOMO->L+7 (83%)
34	317.54	0.0459	H-3->L+3 (52%), H-2->L+5 (36%)
35	316.32	0	H-5->L+2 (89%)
36	305.80	0.0461	H-8->L+1 (51%), H-3->L+3 (17%), H-2->L+5 (18%)
37	304.61	0.0577	H-8->L+1 (31%), H-3->L+3 (25%), H-2->L+5 (33%)
38	303.48	0.0007	H-2->L+4 (94%)
39	301.42	0.0575	H-9->L+1 (93%)
40	296.92	0.0011	H-2->L+6 (94%)
41	295.67	0.1722	H-10->L+1 (16%), H-7->L+1 (57%), H-4->L+3 (11%)
42	295.42	0.0018	H-2->L+7 (29%), H-1->L+9 (51%)
43	293.17	0.0111	H-2->L+7 (53%), H-1->L+9 (31%)
44	292.86	0.0002	H-6->L+1 (11%), HOMO->L+9 (63%)
45	292.77	0.0012	H-6->L+1 (80%)
46	291.54	0.0034	H-7->L+1 (10%), H-4->L+3 (78%)
47	287.60	0.0588	H-7->L+2 (89%)
48	285.70	0.0606	H-9->L+2 (15%), H-5->L+3 (61%)
49	283.38	0.0413	H-10->L+1 (11%), H-3->L+4 (38%), H-3->L+5 (31%)
50	282.54	0.0309	H-10->L+1 (12%), H-3->L+4 (56%), H-3->L+5 (15%)
51	282.38	0.0009	H-8->L+2 (77%)
52	280.50	0.0253	H-3->L+6 (93%)
53	279.81	0.1718	H-11->LUMO (83%)
54	278.82	0.0173	H-10->L+1 (44%), H-3->L+5 (29%)
55	275.70	0.0284	H-9->L+2 (71%)
56	273.95	0.0001	H-6->L+2 (93%)
57	272.90	0.0752	H-3->L+7 (82%)
58	272.60	0.0217	H-4->L+5 (87%)
59	270.45	0.0097	H-6->L+3 (78%), H-2->L+11 (12%)
60	268.59	0.0894	H-5->L+5 (57%), H-4->L+4 (10%)
61	268.17	0.0277	H-5->L+5 (17%), H-2->L+9 (10%), HOMO->L+8 (27%)
62	267.52	0.0327	H-4->L+4 (14%), HOMO->L+8 (58%)
63	267.06	0.0011	H-4->L+6 (88%)
64	266.28	0.012	H-4->L+4 (62%)
65	265.04	0.3692	H-1->L+8 (75%)
66	264.68	0.1269	H-10->L+2 (82%)
67	263.54	0.0196	H-4->L+7 (72%)

68	262.53	0.0025	H-5->L+4 (78%), H-5->L+6 (11%)
69	262.27	0.0001	H-9->L+3 (83%)
70	262.16	0.0004	H-5->L+4 (10%), H-5->L+6 (73%)
71	261.57	0	H-12->LUMO (97%)
72	259.68	0.0185	H-5->L+7 (82%)
73	257.03	0.0003	H-7->L+3 (85%)
74	256.46	0.0004	H-1->L+10 (75%)
75	254.07	0.1161	H-8->L+3 (58%), HOMO->L+10 (26%)
76	253.70	0.0575	H-8->L+3 (27%), HOMO->L+10 (55%)
77	253.05	0	H-13->LUMO (94%)
78	250.97	0.0512	H-11->L+1 (84%)
79	249.90	0.059	H-15->LUMO (72%)
80	247.67	0.0468	H-14->LUMO (25%), H-7->L+4 (62%)
81	247.13	0.0002	H-1->L+12 (85%)
82	245.79	0.0124	HOMO->L+11 (75%)
83	245.69	0.0459	H-14->LUMO (34%), H-7->L+4 (31%), H-2->L+8 (11%)
84	245.41	0.0066	H-2->L+8 (85%)
85	244.01	0.0005	H-6->L+5 (72%), H-6->L+7 (15%)
86	243.74	0.0146	H-10->L+3 (74%), H-7->L+3 (11%)
87	242.17	0.0052	H-9->L+5 (32%), H-8->L+5 (46%)
88	242.02	0.014	H-9->L+5 (59%), H-8->L+5 (23%)
89	241.09	0.0411	H-6->L+3 (16%), H-2->L+10 (15%), H-2->L+11 (40%)
90	240.36	0.0011	H-14->LUMO (11%), H-7->L+5 (58%)
91	238.98	0.0224	H-6->L+4 (23%), H-3->L+9 (34%), H-1->L+11 (12%)
92	238.94	0.0234	H-6->L+4 (13%), H-3->L+9 (31%), H-1->L+11 (30%)
93	238.88	0.0126	H-6->L+4 (55%), H-1->L+11 (28%)
94	238.45	0.0085	H-8->L+6 (83%)
95	238.37	0.1989	H-7->L+6 (46%), H-1->L+13 (23%)
96	237.98	0.147	H-8->L+7 (18%), HOMO->L+12 (36%)
97	237.21	0.2324	H-7->L+7 (14%), H-2->L+10 (42%), H-2->L+11 (15%)
98	236.76	0.1537	H-7->L+6 (22%), H-1->L+13 (41%), H-1->L+14 (22%)
99	236.50	0.014	H-9->L+6 (16%), H-7->L+5 (19%), H-7->L+7 (14%), H-2->L+10 (20%)
100	235.79	0.0329	H-8->L+4 (72%)

S_0 to T^x	Wavelength (nm)	Oscillator Strength	Major contribution(s)
1	731.51	0	H-1->LUMO (88%)
2	615.64	0	HOMO->LUMO (89%)
3	522.25	0	H-1->L+1 (98%)
4	495.68	0	H-2->LUMO (90%)
5	493.23	0	HOMO->L+1 (81%)
6	457.08	0	H-3->LUMO (77%)
7	455.50	0	H-1->L+2 (83%)
8	448.69	0	H-2->L+3 (21%), HOMO->L+5 (26%), HOMO->L+7 (15%)
9	438.55	0	HOMO->L+3 (84%)
10	429.90	0	H-3->LUMO (15%), HOMO->L+2 (74%)

10.3 Publications

Inorganic Chemistry

Article

pubs.acs.org/IC

Selective DNA Purine Base Photooxidation by Bis-terdentate Iridium(III) Polypyridyl and Cyclometalated Complexes

Alexandre Jacques, Andrée Kirsch-De Mesmaeker,† and Benjamin Elias*

Institut de la Matière Condensée et des Nanosciences, Université Catholique de Louvain, Place Louis Pasteur 2, Box L4.01.02, B-1348 Louvain-la-Neuve, Belgium

Supporting Information

ABSTRACT: Two bis-terdentate iridium(III) complexes with polypyridyl and cyclometalated ligands have been prepared and characterized. Their spectroscopic and electrochemical properties have been studied, and a photophysical scheme addressing their properties is proposed. Different types of excited states have been considered to account for the deactivation processes in each complex. Interestingly, in the presence of mono- or polynucleotides, a photoinduced electron-transfer process from a DNA purine base (i.e., guanine or adenine) to the excited complex is shown through luminescence quenching experiments. For the first time, this work reports evidence for selective DNA purine bases oxidation by excited iridium(III) bis-terdentate complexes.

INTRODUCTION

Polyazaaromatic transition-metal complexes have gained considerable interest these past decades. Their use as catalysts in the water splitting process,[1] therapeutic agents in several cancer treatments,[2] or photoprobes of biological media[3] is well-established. Among all transition metals available, iridium(III) is one of the most interesting elements for building complexes.[4] Indeed, it allows the synthesis of multiple polypyridyl and cyclometalated complexes with bidentate or terdentate ligands. Iridium(III) is capable of forming stable mono-, bis-, and tris-cyclometalated complexes, and up to three C-donor sites can be coordinated onto the metal center. The C/N ratio present in the first coordination sphere can thus be varied from 0/6 to 3/3, hence providing an excellent means to tune the photoredox properties of the resulting complexes. For instance, tris-bidentate iridium(III) complexes made of two PPY (PPY = 2-phenylpyridine) and an imidazo[4,5-*f*][1,10]phenanthroline have C/N = 2/4 and are specific anion sensors.[5] Upon replacement of the imidazolo ligand by an intercalative ligand dppz (dppz = dipyrido[3,2-*a*:2′,3′-*c*]phenazine), the resulting luminescent iridium(III) has been used to study DNA-mediated hole and electron transfer.[6] Recently, it has been shown that a luminescent bis-terdentate iridium(III) complex made exclusively of terpyridine-type-like ligands (C/N = 0/6) exhibits intercalation between DNA base pairs.[7] The luminescence of this complex is quenched in the presence of a guanine moiety via a photoinduced electron-transfer process, showing the high oxidizing ability of the excited state. Although displaying spectroelectrochemical properties enabling photoreactions toward DNA, iridium(III) complexes have only been scarcely used as such in the literature. Therefore, in this paper, we present the comprehensive study of two novel iridium(III) complexes obtained from the coordination of either two terpyridyl-like ligands {i.e., $[Ir(4'\text{-COOH-Phtpy})(4'\text{-MeO-Phtpy})]^{3+}$ [4′-COOH-Phtpy = 4′-(4-carboxyphenyl)-2,2′:6′,2″-terpyridine and 4′-MeO-Phtpy = 4′-(4-methoxyphenyl)-2,2′:6′,2″-terpyridine] called hereafter $[\mathbf{IrN_6}]^{3+}$ for the sake of clarity; Figure 1} or one terpyridyl and one triphenylpyridyl ligands {i.e., $[Ir(4'\text{-COOH-Phtpy})(4'\text{-MeO-tppy})]^{+}$ [4′-MeO-tppy = 2,6-diphenyl-4-(4′-methoxyphenyl)pyridine] called hereafter $[\mathbf{IrN_4C_2}]^{+}$ for the sake of clarity; Figure 1}. Their photophysics and photochemistry have been investigated. Although both complexes display very similar structural features, their photoredox behavior toward DNA bases and the excited state involved in the electron transfer process are quite different depending on the coordination sphere. Using luminescence measurements in the absence and presence of several DNA building blocks, synthetic or natural DNA, we were able to show that these complexes selectively photooxidize purine nucleobases (i.e., adenine and guanine), whereas no nucleobase reduction occurs under irradiation. This paper represents, to the best of our knowledge, one of the very few studies addressing photoinduced electron-transfer processes between excited bis-terdentate iridium(III) complexes and DNA bases.

EXPERIMENTAL SECTION

Materials and Instrumentation. 4′-(Methoxyphenyl)-2,2′:6′,2″-terpyridine[8] (4′-MeO-Phtpy), $[(4'\text{-COOMe-Phtpy})IrCl_3]$,[9] $[(4'\text{-COOH-Phtpy})IrCl_3]$,[10] and 2,6-diphenyl-4-(4′-methoxyphenyl)-pyridine[11] (4′-MeO-tppy) were prepared as previously described. Deoxynucleotides (dGMP, dAMP, dCMP, and dTMP) were

Received: October 1, 2013
Published: January 22, 2014

dx.doi.org/10.1021/ic402476b | Inorg. Chem. 2014, 53, 1507−1512

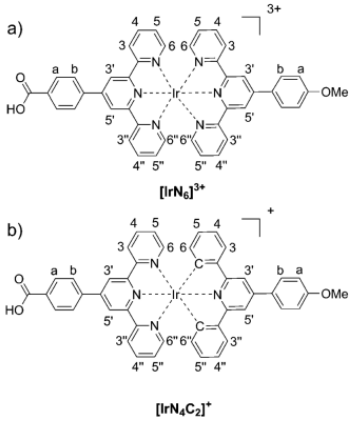

Figure 1. Structures of the iridium(III) complexes: (a) $[\mathbf{IrN_6}]^{3+}$; (b) $[\mathbf{IrN_4C_2}]^{+}$.

purchased from Sigma-Aldrich (purity ≥99%) and used without further purification. Calf thymus DNA (CT-DNA) was purchased from Sigma-Aldrich, and $[poly(dG\text{-}dC)]_2$, $[poly(dA\text{-}dT)]_2$, and [poly(dA)-poly(dT)] were purchased from Amersham Bioscience. Polynucleotide phosphate concentrations were determined spectroscopically ($\varepsilon_{260\ nm}$ = 6600 M^{-1} for CT-DNA,[12] $\varepsilon_{262\ nm}$ = 6600 M^{-1} for $[poly(dA\text{-}dT)]_2$,[13] $\varepsilon_{260\ nm}$ = 6000 M^{-1} for [poly(dA)-poly(dT)],[14] and $\varepsilon_{254\ nm}$ = 8400 M^{-1} for $[poly(dG\text{-}dC)]_2$).[15] ^{1}H NMR experiments were performed in CD_3CN on a Bruker AC-300 Avance II (300 MHz) or on a Bruker AM-500 (500 MHz). The chemical shifts (given in ppm) were measured versus the residual peak of the solvent as the internal standard. High-resolution mass spectrometry (HRMS) were recorded on a Q-Extractive orbitrap from ThermoFisher. Samples were ionized by electrospray ionization (ESI; capillary temperature = 250 °C, vaporizer temperature = 250 °C, sheath gas flow rate = 20). UV−vis absorption spectra were recorded on a Shimadzu UV-1700. Room temperature fluorescence spectra were recorded on a Varian Cary Eclipse instrument. Luminescence lifetimes were measured with a modified Applied Photophysics laser kinetic spectrometer by exciting the samples at 355 nm with a Nd:YAG pulsed laser (Continuum NY 61-10). Emitted light as a function of time was detected with a R-928 Hamamatsu photomultiplier tube whose output was applied to a digital oscilloscope (Hewlett-Packard HP 54200A) interfaced with a Dell Dimension DE051 computer. Signals were averaged over at least 16 shots and corrected for baseline. *Igor 6.1* software was used for decay analyses. Cyclic voltammetry was carried out in a one-compartment cell, using a glassy carbon disk working electrode (approximate area = 0.03 cm^2), a platinum wire counter electrode, and an Ag/AgCl reference electrode. The potential of the working electrode was controlled by an Autolab PGSTAT 100 potentiostat through a PC interface. The cyclic voltammograms were recorded with a sweep rate of 100 mV s^{-1}, either in dried acetonitrile (Acros, HPLC grade) or in dried *N*,*N*-dimethylformamide (DMF; Sigma-Aldrich, HPLC grade). Tetrabutylammonium perchlorate (0.1 M) was used as the supporting electrolyte, and the samples were purged by argon before each measurement.

[Ir(4′-COOH-Phtpy)(4′-MeO-Phtpy)]$(PF_6)_3$ ($[\mathbf{IrN_6}](PF_6)_3$). A suspension of [(4′-COOH-Phtpy)$IrCl_3$] (24 mg, 0.037 mmol) and 4′-MeO-Phtpy (12 mg, 0.037 mmol) was heated to 170 °C in degassed ethylene glycol (2.5 mL) in the dark and under argon for 30 min. After cooling, aqueous NH_4PF_6 was added to precipitate the crude product. The pure complex was isolated by column chromatography on Al_2O_3 (acetone/water, from 100/0 to 90/10), which yielded the complex $[\mathbf{IrN_6}]^{3+}$ (PF_6^- salt) as a yellow solid (40 mg, 82%). When the chloride salt was required for the experiments, counteranion exchange was achieved upon the addition of $^tBu_4N^+Cl^-$ to the PF_6^- salt dissolved in acetone. ^{1}H NMR (CD_3CN, 500 MHz): δ 9.11 (s, 2H, H_3' and H_5' of tpy-C_6H_4-COOH), 9.03 (s, 2H, H_3' and H_5' of tpy-C_6H_4-OMe), 8.72 (d, 2H, H_3 and H_3'' of tpy-C_6H_4-COOH, J_{H3-H4} = 8.1 Hz), 8.70 (d, 2H, H_3 and H_3'' of tpy-C_6H_4-OMe, J_{H3-H4} = 8.1 Hz), 8.40 (d, 2H, H_a of tpy-C_6H_4-COOH, J_{Ha-Hb} = 8.4 Hz), 8.28 (d, 2H, H_b of tpy-C_6H_4-COOH, J_{Hb-Ha} = 8.4 Hz), 8.25−8.20 (m, 6H, H_4 and H_4'' of both tpy's, H_b of tpy-C_6H_4-OMe), 7.70 (dd, 2H, H_6 and H_6'' of tpy-C_6H_4-OMe, J_{H6-H5} = 4.9 Hz, J_{H6-H4} = 0.9 Hz), 7.68 (dd, 2H, H_6 and H_6'' of tpy-C_6H_4-OMe, J_{H6-H5} = 4.9 Hz, J_{H6-H4} = 0.9 Hz), 7.51−7.46 (m, 4H, H_5 and H_5'' of both tpy's), 7.34 (d, 2H, H_a of tpy-C_6H_4-COOH, J_{Ha-Hb} = 8.8 Hz), 3.99 (s, 3H, OMe). HRMS (ESI). Calcd for $[C_{44}H_{32}N_6O_3{}^{193}IrP_2F_{12} - PF_6]^+$: *m*/*z* 1175.1443. Found: *m*/*z* 1175.1429. Calcd for $[C_{44}H_{32}N_6O_3{}^{193}Ir - 3PF_6]^{3+}$: *m*/*z* 295.0716. Found: *m*/*z* 295.0723.

[Ir(4′-COOH-Phtpy)(4′-MeO-tppy)](NO_3) ($[\mathbf{IrN_4C_2}](NO_3)$). A mixture of [(4′-COOMe-Phtpy)$IrCl_3$] (98 mg, 0.15 mmol), 4′-MeO-tppy (54 mg, 0.16 mmol), and $AgNO_3$ (125 mg, 0.74 mmol) was refluxed in degassed ethylene glycol (13 mL) in the dark and under argon for 22 h. After cooling, the mixture was filtered through Celite to remove AgCl. The Celite was washed with MeOH and subsequently evaporated. Water was added, and the aqueous layer was extracted with $CHCl_3$ (three times). The organic solutions were combined and evaporated to dryness. The crude product was purified by column chromatography on SiO_2 [CH_3CN/saturated aqueous KNO_3 (10/1)]. The first eluted orange band was recovered and the solvent evaporated. The resulting red solid was saponified in a mixture MeOH (30 mL)/1 M NaOH (20 mL), and the solution was heated to 80 °C for 3 h. After cooling, the solution was adjusted to pH = 7 with 2 M HCl and solvents were evaporated. The solid was purified by column chromatography on SiO_2 [CH_3CN/saturated aqueous KNO_3 (10/1)]. The red powder was washed with water and dried under vacuum to afford $[\mathbf{IrN_4C_2}]^+$ with 40% yield (63 mg). ^{1}H NMR (CD_3CN, 300 MHz): δ 9.00 (s, 2H, H_3' and H_5' of tpy-C_6H_4-COOH), 8.67 (d, 2H, H_3 and H_3'' of tpy-C_6H_4-COOH, J_{H3-H4} = 7.8 Hz), 8.36 (d, 2H, H_a of tpy-C_6H_4-COOH, J_{Ha-Hb} = 8.6 Hz), 8.29 (s, 2H, H_3' and H_5' of tppy-OMe), 8.28 (d, 2H, H_b of tpy-C_6H_4-COOH, J_{Hb-Ha} = 8.6 Hz), 8.13 (d, 2H, H_b of tppy-OMe, J_{Hb-Ha} = 8.4 Hz), 8.03−7.96 (m, 4H, H_4 and H_4'' of tpy-C_6H_4-COOH and H_3 and H_3'' of tppy-OMe), 7.89 (d, 2H, H_6 and H_6'' of tpy-C_6H_4-COOH, J_{H6-H5} = 5.1 Hz), 7.31−7.24 (m, 4H, H_5 and H_5'' of tpy-C_6H_4-COOH and H_a of tppy-OMe), 7.01 (td, 2H, H_4 and H_4'' of tppy-OMe, $J_{H4-H5\ (H3)}$ = 7.4 Hz, J_{H4-H6} = 1.1 Hz), 6.78 (td, 2H, H_5 and H_5'' of tppy-OMe, $J_{H5-H4\ (H6)}$ = 7.3 Hz, J_{H5-H3} = 1.0 Hz), 6.28 (dd, 2H, H_6 and H_6'' of tppy-OMe, J_{H6-H5} = 7.3 Hz, J_{H6-H4} = 0.9 Hz), 3.97 (s, 3H, OMe). HRMS (ESI). Calcd for $[C_{46}H_{32}N_4O_3{}^{193}Ir - NO_3]^+$: *m*/*z* 881.2098. Found: *m*/*z* 881.2088.

RESULTS

Synthesis. The synthesis of both complexes was achieved in two steps by heating iridium(III) chloride salts with the desired ligand in ethylene glycol according to methodologies previously described.[9,16] It is worth mentioning that the synthesis of $[\mathbf{IrN_4C_2}]^+$ requires harsher conditions than that of $[\mathbf{IrN_6}]^{3+}$, as expected from the greater inertness of the cyclometalated ligand. $[\mathbf{IrN_6}]^{3+}$ and $[\mathbf{IrN_4C_2}]^+$ display very similar structural features. Thanks to the derivatization on the 4′ position, they have several symmetry elements, hence circumventing the problem of the occurrence of geometrical isomers as encountered for tris-bidentate arrangements. Both complexes have thus been unambiguously characterized by ^{1}H NMR spectroscopy and HRMS (see the Experimental Section).

Electrochemistry. The redox potentials of both complexes were determined by cyclic voltammetry measurements. The data are gathered in Table 1. $[\mathbf{IrN_6}]^{3+}$ displays two irreversible

Table 1. Electrochemical Data Measured at Room Temperature in DMF for $[IrN_6]^{3+}$ and in CH_3CN for $[IrN_4C_2]^+$ with 0.1 M Bu_4NClO_4 as the Supporting Electrolyte[a]

	$[IrN_6]^{3+}$	$[IrN_4C_2]^+$
E_{ox} (V vs Ag/AgCl)	>2.2	1.14 (r, ΔE_p = 58 mV)
E_{red} (V vs Ag/AgCl)	−0.81 (ir), −1.22 (ir)	−1.24 (r, ΔE_p = 54 mV)
E_{ox}* (V vs Ag/AgCl)		−1.22
E_{red}* (V vs Ag/AgCl)	1.38	1.12

[a] r = reversible; ir = irreversible; ΔE_p (the peak-to-peak separation) is close to 59 mV.

one-electron-reduction waves at −0.81 and −1.22 V vs Ag/AgCl (Figure S1 in the SI). No oxidation process could be detected up to +2.2 V vs Ag/AgCl, suggesting that the oxidation is highly energetic and probably metal-centered. In contrast, $[IrN_4C_2]^+$ is characterized by one reversible reduction wave and one reversible oxidation wave, at −1.24 and +1.14 V vs Ag/AgCl, respectively (Figures S2 and S3 in the SI). The oxidation of $[IrN_4C_2]^+$ is probably due to the cyclometalated iridium fragment (Ir−C^N^C). The potentials in the excited state (namely, E_{ox}* and E_{red}*)[17] for both complexes have been estimated from the ground-state redox potentials and the energy of the excited state corresponding to the maximum of the emission spectrum at 298 K, i.e., $\lambda_{max\ Em}$ = 568 nm (2.19 eV) for $[IrN_6]^{3+}$ and $\lambda_{max\ Em}$ = 528 nm (2.36 eV) for $[IrN_4C_2]^+$. Not surprisingly, $[IrN_6]^{3+}$ is strongly oxidizing (E_{red}* = +1.38 V vs Ag/AgCl) in its excited state.

Absorption and Emission Spectroscopy. Absorption and emission spectra in CH_3CN under air at room temperature for both complexes are shown in Figure 2. Table 2 gathers the corresponding data. For both complexes, absorption (ε > 30000 M^{-1} cm^{-1}) bands in the UV region tailing into the visible are observed.

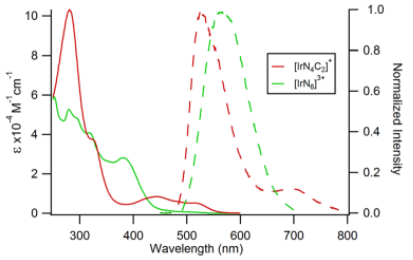

Figure 2. Absorption (solid lines) and emission (dashed lines; λ_{exc} = 350 nm) for $[IrN_6]^{3+}$ (green) and $[IrN_4C_2]^+$ (red) complexes in CH_3CN under air at room temperature.

$[IrN_6]^{3+}$ and $[IrN_4C_2]^+$ emit in CH_3CN under air ($\Phi \sim 10^{-3}$). A broad-band emission centered at around 568 nm ($\tau_{RT,air}$ = 470 ns) is observed for $[IrN_6]^{3+}$, whereas $[IrN_4C_2]^+$ exhibits a dual-band emission, centered at 528 nm ($\tau_{RT,air}$ = 1 μs) and 697 nm ($\tau_{RT,air}$ = 260 ns). Although there is almost no emission band shift between CH_3CN and water, the excited-state lifetimes are affected upon solvent change and increase by a factor of 2 or 3 in water for both complexes. It is worth mentioning that, in an air-equilibrated solvent, a decrease in the luminescence intensity with respect to degassed solutions is observed, showing a sensitization of $^1O_2$ by excited iridium(III) complexes. Because all of our experiments have been carried out under the same conditions, the influence of oxygen is kept constant and is therefore not further investigated in the present manuscript.

Table 2. Absorption and Luminescence Data for the Iridium(III) Complexes

		$[IrN_6]^{3+}$	$[IrN_4C_2]^+$	
$\lambda_{max\ Abs}$, nm (ε, ×10^{-3} M^{-1} cm^{-1})	CH_3CN	382 (28.1), 319 (40.8), 279 (52.7), 252 (59.0)	512 (5.2), 439 (8.4), 325 (37.4), 281 (102.8)	
$\lambda_{max\ Em}$[a] (nm) under air at 298 K	CH_3CN	568	528	697
	H_2O[b]	560	514	682
$\lambda_{max\ Em}$[a] (nm) at 77 K	EtOH/MeOH (4/1)	505	505	663
τ (μs) under air at 298 K	CH_3CN	0.47	1.00	0.26
	H_2O[b]	1.31	1.76	0.39
Φ[c]	CH_3CN	0.0010	0.0055	0.0006
	H_2O[b]	0.0019	0.0291	0.0227
k_r (×10^{-3} s^{-1})[d]	CH_3CN	2.2	5.5	2.3

[a] Excitation wavelength = 350 nm. [b] $[IrN_4C_2]^+$ was dissolved in a H_2O/CH_3CN (90/10) mixture because of its low solubility in water. [c] The quantum yield (±5%) was measured under air using $[Ru(bpy)_3]^{2+}$ as a reference; ϕ_{ref} = 0.028 in CH_3CN,[18] λ_{Exc} = 420 nm, and 293 K. [d] Radiative rate constant at 298 K ($k_r = \Phi/\tau$).

Luminescence Behavior of Iridium(III) Complexes in the Presence of Deoxynucleotides. With respect to the excited-state potentials of iridium(III) complexes and the ability of some DNA bases to act as an electron donor or acceptor, a photooxidative or photoreductive electron-transfer process could be thermodynamically possible between the excited complex and some DNA building blocks (deoxynucleotides). Thanks to the ability of iridium complexes to emit in aqueous solution, monitoring the luminescence in the presence of increased concentration of a given nucleotide can be performed. It is worth mentioning that all of the experiments presented here were carried out with nucleobase concentrations far below the aggregation and self-association limit.[19] In addition, because of the poor solubility of $[IrN_4C_2]^+$ in pure water, 10% CH_3CN (v/v) was added for each experiment with deoxynucleotides. Figure 3 shows the relative emission decrease of both $[IrN_6]^{3+}$ and $[IrN_4C_2]^+$ upon increased concentrations of deoxyguanosine-5′-monophosphate (dGMP). It is striking that solely the higher-energy emission band (λ_{em} = 514 nm) for $[IrN_4C_2]^+$ is quenched, whereas the other band (λ_{em} = 682 nm) is not affected by the presence of dGMP. A linear Stern−Volmer relationship in the luminescence intensity can be obtained from these data (Figure 3, inset), suggesting that pure dynamic quenching[20] of the excited state of both $[IrN_6]^{3+}$ and $[IrN_4C_2]^+$ is occurring in the presence of dGMP.

In the presence of deoxyadenosine-5′-monophosphate (dAMP), a luminescence quenching and a decrease of the excited-state lifetime ($\tau_0/\tau > 1$) are observed only for $[IrN_6]^{3+}$. However, in that case, a negative deviation from the Stern−Volmer linear relationship in intensity is observed (Figure 4). This presumably shows that the luminescence quenching of $[IrN_6]^{3+}$ in the presence of dAMP is more complicated than a

dx.doi.org/10.1021/ic402476b | Inorg. Chem. 2014, 53, 1507−1512

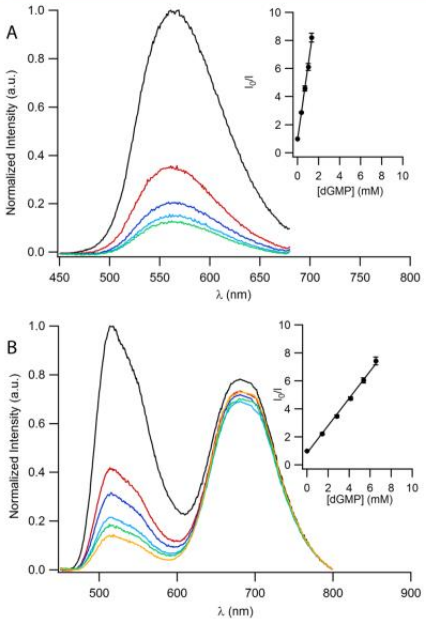

Figure 3. Luminescence spectra (λ_{exc} = 350 nm) of (a) $[\mathbf{IrN_6}]^{3+}$ and (b) $[\mathbf{IrN_4C_2}]^{+}$ in the presence of increased concentration of dGMP (50 mM Tris buffer, pH = 7.4, RT).[21] Inset: Stern–Volmer plots obtained upon the addition of dGMP for (a) $[\mathbf{IrN_6}]^{3+}$ and (b) $[\mathbf{IrN_4C_2}]^{+}$ measured at λ_{em} = 560 and 514 nm, respectively.

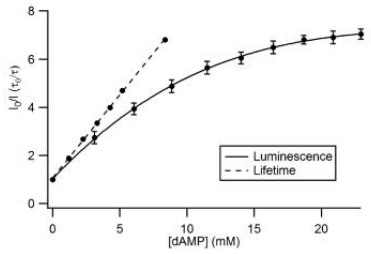

Figure 4. Stern–Volmer plots measured using the excited-state luminescence lifetime (dashed line) and luminescence intensity (solid line) of $[\mathbf{IrN_6}]^{3+}$ upon increased concentration of dAMP (50 mM Tris buffer, pH = 7.4, RT) at λ_{em} = 560 nm (λ_{exc} = 350 nm).

simple dynamic diffusion between the excited complex and dAMP monomers.[20] The addition of dCMP or dTMP to $[\mathbf{IrN_6}]^{3+}$ or $[\mathbf{IrN_4C_2}]^{+}$ did not affect their luminescence behavior, excluding thus any photoinduced process involving these nucleobases.

Luminescence Behavior of $[\mathbf{IrN_6}]^{3+}$ in the Presence of Polynucleotides. Because of the relatively low solubility of $[\mathbf{IrN_4C_2}]^{+}$ in aqueous buffer, we have decided to limit our study of the influence of polynucleotides on the spectroscopic properties of the complex to $[\mathbf{IrN_6}]^{3+}$.

Although no significant change in the absorption spectra of $[\mathbf{IrN_6}]^{3+}$ is observed when interacting with the polynucleotide, its luminescence is dramatically altered. Figure 5 shows the

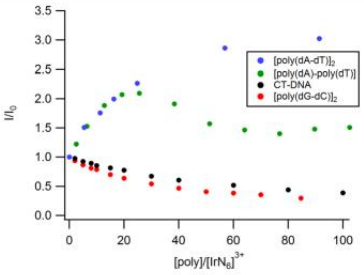

Figure 5. Relative luminescence intensity of $[\mathbf{IrN_6}]^{3+}$ measured at λ_{em} = 560 nm in the presence of increased concentrations of [poly(dA-dT)] $_2$ (blue circle), [poly(dA)-poly(dT)] (green circle), CT-DNA (black circle), and $[poly(dG\text{-}dC)]_2$ (red circles). All of the measurements were performed with a constant complex concentration of 32 μM in a 50 mM Tris-HCl buffer aqueous solution (pH = 7.4) with 50 mM NaCl (λ_{exc} = 350 nm).

relative luminescence intensity changes I/I_0 for $[\mathbf{IrN_6}]^{3+}$ upon the addition of selected polynucleotides. Two distinct behaviors are observed. In the presence of GC base pairs containing polynucleotides (i.e., $[poly(dG\text{-}dC)_2]$, 100% GC base pairs; CT-DNA, 42% GC base pairs[22]), a luminescence quenching is observed. In contrast, in the presence of AT base pairs containing polynucleotides (i.e., $[poly(dA\text{-}dT)_2]$ or [poly(dA)-poly(dT)], 100% AT base pairs), a somewhat more complex behavior is observed with a strong luminescence increase followed by a plateau value of $I/I_0 \approx 3$ for $[poly(dA\text{-}dT)_2]$ or followed by a decrease for [poly(dA)-poly(dT)].

■ DISCUSSION

Photophysics of the Complexes Alone in Solution. Iridium(III) complexes are well-known in the literature for their rich photophysics and photochemistry. Indeed, because of a strong spin–orbit coupling and an important influence of the ancillary ligands, a mixture of different excited states usually participates in the radiative deactivation of the complex. In the case of $[Ir(tpy)_2]^{3+}$ and parent compounds, it has been shown that the emission arises from a ligand-centered (^{3}LC) excited state, with a small but nonnegligible contribution of a metal-to-ligand charge-transfer (^{3}MLCT) excited state.[16]

For $[\mathbf{IrN_6}]^{3+}$, a change in the solvent polarity (i.e., from CH_3CN to water) does not influence the emission maximum, in agreement with a ^{3}LC excited state. However, the luminescence at room temperature in a polar fluid solvent is unstructured, decays in about 1 μs, and is blue-shifted at 77 K (Table 2), which is more in favor of a ^{3}MLCT excited state. In addition, the k_r value ($\approx 10^3$ s^{-1}) is relatively high, and usually such values are much smaller for pure ^{3}LC states.[23] Therefore, we propose that the lowest excited state in $[\mathbf{IrN_6}]^{3+}$ corresponds to a ^{3}LC centered on the electron-poorest ligand,

dx.doi.org/10.1021/ic402476b | Inorg. Chem. 2014, 53, 1507–1512

i.e., $^3[\pi \rightarrow \pi^*(4'\text{-COOH-Phtpy})]$, mixed with some ^{3}MLCT character, $^3[d\pi(\text{Ir}) \rightarrow \pi^*(4'\text{-COOH-Phtpy})]$.

In contrast, the cyclometalated compound $[\mathbf{IrN_4C_2}]^+$ displays a different photophysical behavior. Compared to $[\mathbf{IrN_6}]^{3+}$, the absorption is shifted to the red, in agreement with the greater donating ability of the cyclometalated ligand. In addition, a dual-band emission is observed. According to experimental[24] and theoretical[25] data, iridium(III) complexes made from terdentate cyclometalated ligands usually have an emitting state corresponding to a ligand-to-ligand charge transfer (LLCT), often combined with other ^{3}LC/^{3}MLCT excited states.

In the case of $[\mathbf{IrN_4C_2}]^+$, the emission at $\lambda_{em} \approx 520$ nm is similar to that of $[\mathbf{IrN_6}]^{3+}$ described above. Therefore, we ascribe this transition to a mixture ^{3}LC/^{3}MLCT, i.e., $^3[d\pi(\text{Ir}) \rightarrow \pi^*(4'\text{-COOH-Phtpy})$ and $\pi(4'\text{-COOH-Phtpy}) \rightarrow \pi^*(4'\text{-COOH-Phtpy})]$. The most bathochromic band ($\lambda_{em} = 697$ nm) is believed to correspond to a ^{3}LLCT, i.e., $^3[$cyclometalated iridium fragment (Ir−C^N^C) $\rightarrow \pi^*(4'\text{-COOH-Phtpy})]$. Indeed, the emission at 77 K is poorly resolved, in agreement with a CT process.[23] Moreover, the addition of protons (e.g., 2 M HNO_3; Figure S4 in the SI) in the solution leads to a complete disappearance of this ^{3}LLCT emission, probably arising from protonation of the −OMe group, hence inhibiting any CT processes involving the electron-donating Ir−C^N^C fragment.

Photochemical Behavior in the Presence of Mono- and Polynucleotides. Although the total emission of $[\mathbf{IrN_6}]^{3+}$ is quenched in the presence of a G unit, solely one emission band of $[\mathbf{IrN_4C_2}]^+$ undergoes a quenching process upon the addition of GMP (Figure 3b). On the basis of thermodynamic considerations, this luminescence quenching for both complexes could be ascribed to a photoinduced electron-transfer process from the G unit to the excited complexes (eqs 1 and 2).

$$[\text{IrN}_6]^{3+*} + \text{G} \rightarrow [\text{IrN}_6]^{2+} + \text{G}^{\bullet+} \quad (1)$$

$$[\text{IrN}_4\text{C}_2]^{+*} + \text{G} \rightarrow [\text{IrN}_4\text{C}_2] + \text{G}^{\bullet+} \quad (2)$$

Indeed, although the G oxidation potential has been debated for a long time in the literature, it is generally accepted that E_{ox} of isolated G is close to +1.10 V vs Ag/AgCl and even less positive when stacked to other G units (E_{ox}poly(dG-dC)$_2$] < +0.85 V vs Ag/AgCl).[26] Considering the oxidation power of the excited state of $[\mathbf{IrN_6}]^{3+}$ and using the empirical Rehm−Weller equation,[27] it is expected that process (1) will be exergonic by about 0.3 eV.[17] In the case of $[\mathbf{IrN_4C_2}]^+$, solely the most energetic emission band ($\lambda_{em} = 514$ nm) is quenched via a photoreductive electron transfer (eq 2), favored by less than 0.1 eV based on thermodynamic assumptions. The low oxidizing power of the less energetic excited state (LLCT) does not allow any G oxidation. Efficient quenching in the presence of G units is also in agreement with the high value of the quenching rate constant (k_q) obtained from the Stern−Volmer plot of $[\mathbf{IrN_6}]^{3+}$ and $[\mathbf{IrN_4C_2}]^+$ with dGMP (vide supra; Stern−Volmer plots, Figure 3, inset; $k_q = 3.9 \times 10^9$ M^{-1} s^{-1} for $[\mathbf{IrN_6}]^{3+}$ and 5.3×10^8 M^{-1} s^{-1} for $[\mathbf{IrN_4C_2}]^+$), both close to the diffusion limit.

The behavior of $[\mathbf{IrN_6}]^{3+}$ in the presence of A units is less common. The emission lifetimes dramatically decrease upon the addition of dAMP, evidencing an efficient quenching of the excited state with $k_q = 5.3 \times 10^8$ M^{-1} s^{-1} (Figure 4). However, a deviation from the linearity of the Stern−Volmer relationship for the emission intensity (I_0/I) is observed (Figure 4). This usually arises when static quenching is operative, but in that particular case, an upward curvature is observed. Instead, for $[\mathbf{IrN_6}]^{3+}$, a downward curvature indicates that other processes have to be taken into account. A similar behavior has been reported in the literature for the fluorescence quenching of doxorubicin in the presence of AMP.[28] Two conformers (i.e., with one or two intramolecular hydrogen-bonded hydrophenolic moieties) of doxorubicin in the ground state with different accessibility to the quencher were shown to be responsible for the emission quenching behavior. In the present case, (de)protonation of the carboxylic acid moiety could generate two ground states with a different quenching constant by dAMP. Experiments at different pH values in buffered aqueous solution showed that the proton concentration of the medium has only a small influence on the quenching behavior (Figure S5 in the SI). Moreover, converting the acid function into an ester has no effect (Figures S6 and S7 in the SI). Therefore, it is likely that the behavior of $[\mathbf{IrN_6}]^{3+}$ in the presence of dAMP originates from the complex mixture of excited states participating in the emission, with each state being successively reductively quenched by dAMP with different rate constants. In the presence of oligonucleotides, the change of luminescence of $[\mathbf{IrN_6}]^{3+}$ strongly depends on the nature of the nucleobase content. In agreement with the behavior observed in the presence of dGMP, quenching of excited $[\mathbf{IrN_6}]^{3+}$ with [poly(dG-dC)]$_2$ or CT-DNA would arise from the photoinduced electron-transfer process from a G unit of the polynucleotide to the excited complex, hence generating oxidative damage within the DNA double helix. The plateau value, reflecting the quenching efficiency, does not seem to depend on the percentage of GC of the polynucleotide, in contrast to G photooxidizing ruthenium(II) complexes.[22] This shows that the quenching of the excited state of $[\mathbf{IrN_6}]^{3+}$ is highly efficient, in agreement with its very high oxidation power when irradiated by light.

In contrast, in the presence of adenine-rich polynucleotides such as [poly(dA-dT)]$_2$ or [poly(dA)-poly(dT)], a luminescence increase is recorded, in spite of the sufficiently reducing power of A for quenching the excited state of $[\mathbf{IrN_6}]^{3+}$ (vide supra; Figure 4). The luminescence of the complex in the presence of these specific polynucleotides probably originates from two antagonist processes: (i) protection of the complex from the solvent molecules and from oxygen by the DNA hydrophobic environment (via intercalation or groove binding, for instance), resulting in a luminescence increase, and (ii) quenching by the A moieties, resulting in a luminescence decrease. In the case of the alternating copolymeric [poly(dA-dT)]$_2$, the luminescence enhancement is monotonic, reflecting a constant involvement of both processes at any [poly]/[IrN$_6$]$^{3+}$ ratio, with the protection effect being predominant. For the homopolymeric [poly(dA)-poly(dT)], a different behavior is observed; this could originate from a different type of interaction with the double helix, depending on the polynucleotide loading level by the complex (Figure 5). Thus, because of these structural changes, at [poly]/[IrN$_6$]$^{3+}$ > 40, the quenching by the A units would become predominant compared to their protection, which would account for the inflection observed in the titration curve.

■ CONCLUSION

We managed to synthesize two new bis-terdendate iridium(III) complexes. Both have been obtained thanks to successive addition of the ligands on the metal center. The spectroscopic

and electrochemical data revealed that several excited states contribute to the overall luminescence. Oxidative quenching of the $[IrN_6]^{3+}$ emission in the presence of dGMP or dAMP confirms the high oxidizing ability of the excited complex. The behavior of $[IrN_4C_2]^+$ is less common. Indeed, a selective quenching of the most energetic excited state is observed in the presence of dGMP. No quenching in the presence of dTMP or dCMP was evidenced for both complexes. This shows that these two iridium(III) complexes are not sufficiently reducing (or oxidizing) in their excited state to reduce (or oxidize) thymine or cytosine derivatives. Therefore, selective oxidative electron-transfer processes involving DNA purine bases can be triggered upon irradiation of these new iridium(III) complexes.

■ ASSOCIATED CONTENT

Supporting Information

Synthetic details and spectroscopic properties of esterified $[IrN_6]^{3+}$, luminescence experiments in the presence of dGMP for esterified $[IrN_6]^{3+}$, luminescence experiments in the presence of dAMP at different pH values for $[IrN_6]^{3+}$, ^{1}H NMR spectra and HRMS data for all complexes, disappearance of luminescence of $[IrN_4C_2]^+$ upon the addition of HNO_3, and cyclic voltammograms. This material is available free of charge via the Internet at http://pubs.acs.org.

■ AUTHOR INFORMATION

Corresponding Author

*E-mail: Benjamin.Elias@uclouvain.be.

Present Address

†A.K-D.: Service de Chimie Organique et Photochimie, Université libre de Bruxelles, CP160/08, 50 Av F. D. Roosevelt, B-1050 Brussels, Belgium.

Author Contributions

All authors have given approval to the final version of the manuscript.

Notes

The authors declare no competing financial interest.

■ ACKNOWLEDGMENTS

The authors gratefully acknowledge the Fonds National pour la Recherche Scientifique (F.R.S.-F.N.R.S.), the Fonds pour la Formation à la Recherche dans l'Industrie et dans l'Agriculture (F.R.I.A.), the Région Wallonne, the Université catholique de Louvain, and the Prix Pierre et Colette Bauchau for financial support. We are also grateful to L. Marcélis and L. Troian-Gautier for their scientific help.

■ REFERENCES

(1) (a) Du, P.; Knowles, K.; Eisenberg, R. *J. Am. Chem. Soc.* **2008**, *130*, 12576−12577. (b) DiSalle, B. F.; Bernhard, S. *J. Am. Chem. Soc.* **2011**, *133*, 11819−11821. (c) Ozawa, H.; Sakai, K. *Coord. Chem. Rev.* **2007**, *251*, 2753−2766.

(2) (a) Gasser, G.; Ott, I.; Metzler-Nolte, N. *J. Med. Chem.* **2011**, *54*, 3−25. (b) Le Gac, S.; Rickling, S.; Gerbaux, P.; Defrancq, E.; Moucheron, C.; Kirsch-De Mesmaeker, A. *Angew. Chem., Int. Ed.* **2009**, *48*, 1122−1125. (c) Gianferrara, T.; Bratsos, I.; Alessio, E. *Dalton Trans.* **2009**, *37*, 7588−7598.

(3) (a) Erkkila, K. E.; Odom, D. T.; Barton, J. K. *Chem. Rev.* **1999**, *99*, 2777−2796. (b) Elias, B.; Kirsch-De Mesmaeker, A. *Coord. Chem. Rev.* **2006**, *250*, 1627−1641. (c) McKinley, A. W.; Lincoln, P.; Tuite, E. M. *Coord. Chem. Rev.* **2011**, *255*, 2676−2692. (d) Moucheron, C. *New J. Chem.* **2009**, *33*, 235−245. (e) Smith, J. A.; George, M. W.; Kelly, J. M. *Coord. Chem. Rev.* **2011**, *255*, 2666−2675. (f) Lo, K. K-W.; Zhang, K. Y. *RSC Adv.* **2012**, *2*, 12069−12083.

(4) (a) Dixon, I. M.; Collin, J.-P.; Sauvage, J.-P.; Flamigni, L.; Encinas, S.; Barigelletti, F. *Chem. Soc. Rev.* **2000**, *29*, 385−391. (b) Flamigni, L.; Collin, J.-P.; Sauvage, J.-P. *Acc. Chem. Res.* **2008**, *41*, 857−871. (c) Baranoff, E.; Collin, J.-P.; Flamigni, L.; Sauvage, J.-P. *Chem. Soc. Rev.* **2004**, *33*, 147−155.

(5) (a) Zhao, Q.; Liu, S.; Shi, M.; Li, F.; Jing, H.; Yi, T.; Huang, C. *Organometallics* **2007**, *26*, 5922−5930. (b) Lo, K. K-W.; Louie, M.-W.; Zhang, K. Y. *Coord. Chem. Rev.* **2010**, *254*, 2603−2622.

(6) (a) Elias, B.; Genereux, J. C.; Barton, J. K. *Angew. Chem., Int. Ed.* **2008**, *47*, 9067−9070. (b) Shao, F.; Elias, B.; Barton, J. K. *Inorg. Chem.* **2007**, *46*, 10187−10199. (c) Shao, F.; Barton, J. K. *J. Am. Chem. Soc.* **2007**, *129*, 14733−14738.

(7) Campagna, S.; Cavazzini, M.; Cusumano, M.; Di Pietro, M. L.; Giannetto, A.; Puntoriero, F.; Quici, S. *Inorg. Chem.* **2011**, *50*, 10667−10672.

(8) Wang, J.; Hanan, G. S. *Synlett* **2005**, *8*, 1251−1254.

(9) Shinpuku, Y.; Inui, F.; Nakai, M.; Nakabayashi, Y. *J. Photochem. Photobiol. A* **2011**, *222*, 203−209.

(10) Goldstein, D. C.; Chen, Y. Y.; Schmidt, T. W.; Bhadbhade, M.; Thordarson, P. *Dalton Trans.* **2011**, *40*, 2053−2061.

(11) Adib, M.; Tahermansouri, H.; Koloogani, S. A.; Mohammadi, B.; Bijanzadehb, H. R. *Tetrahedron Lett.* **2006**, *47*, 5957−5960.

(12) Felsenfeld, G.; Hirschman, S. Z. *J. Mol. Biol.* **1965**, *13*, 407−427.

(13) Inman, R. B.; Baldwin, R. L. *J. Mol. Biol.* **1962**, 172−184.

(14) Cui, T.; Wei, S.; Brew, K.; Leng, F. *J. Mol. Biol.* **2005**, *352*, 629−645.

(15) Wells, R. D.; Larso, J. E.; Grant, R. C.; Shortle, B. E.; Cantor, C. R. *J. Mol. Biol.* **1970**, *54*, 465−497.

(16) Collin, J.-P.; Dixon, I. M.; Sauvage, J.-P.; Williams, G. A.; Barigelletti, F.; Flamigni, L. *J. Am. Chem. Soc.* **1999**, *121*, 5009−5016.

(17) $\Delta G_{ET} = E_{ox}(\text{deoxynucleobase}) - E_{red}^*$, where E_{ox}(deoxynucleobase) is the oxidation potential of a selected deoxynucleobase and E_{red}^* is the reduction potential of $[IrN_6]^{3+}$ and $[IrN_4C_2]^+$ in their excited states. Therefore, we have obtained $\Delta G_{ET} = 1.10 - 1.38 = -0.28$ eV and $\Delta G_{ET} = 1.10 - 1.12 = -0.02$ eV respectively for $[IrN_6]^{3+}$ and $[IrN_4C_2]^+$.

(18) Juris, A.; Balzani, V.; Barigelletti, F.; Campagna, S.; Belser, P.; Von Zelewsky, A. *Coord. Chem. Rev.* **1988**, *84*, 85−277.

(19) Wong, A.; Ida, R.; Spindler, L.; Wu, G. *J. Am. Chem. Soc.* **2005**, *127*, 6990−6998.

(20) Balzani, V.; Scandola, F. *Supramolecular Photochemistry*; Ellis Horwood: Chichester, U.K., 1991.

(21) The low solubility of $[IrN_4C_2]^+$ prevents its dissolution in a pure aqueous Tris buffer. Therefore, 10% of acetonitrile has been added to the buffer in order to have complete dissolution of the complex.

(22) Ortmans, I.; Elias, B.; Kelly, J. M.; Moucheron, C.; Kirsch-De Mesmaeker, A. *Dalton Trans.* **2004**, *4*, 668−676.

(23) Flamigni, L.; Barbieri, A.; Sabatini, C.; Ventura, B.; Barigelletti, F. *Top. Curr. Chem.* **2007**, *281*, 143−203.

(24) Polson, M.; Fracasso, S.; Bertolasi, V.; Ravaglia, M.; Scandola, F. *Inorg. Chem.* **2004**, *43*, 1950−1956.

(25) Polson, M.; Ravaglia, M.; Fracasso, S.; Garavelli, M.; Scandola, F. *Inorg. Chem.* **2005**, *44*, 1282−1289.

(26) Steenken, S.; Jovanovics, V. J. *Am. Chem. Soc.* **1997**, *119*, 617−618.

(27) Rehm, D.; Weller, A. *Ber. Bunsen Ges.* **1969**, *73*, 834−839.

(28) Htun, T. *J. Fluoresc.* **2004**, *14*, 217−222.

JOC The Journal of Organic Chemistry
Note
pubs.acs.org/joc

Access to Functionalized Luminescent Multi-2,2′:6′,2″-terpyridine Ligands

Alexandre Jacques, Simon Cerfontaine, and Benjamin Elias*

Université catholique de Louvain, Institut de la Matière Condensée et des Nanosciences (IMCN) − Molécules, Solides et Réactivité (MOST) Place Louis Pasteur 1, bte L4.01.02, B-1348 Louvain-la-Neuve, Belgium

Supporting Information

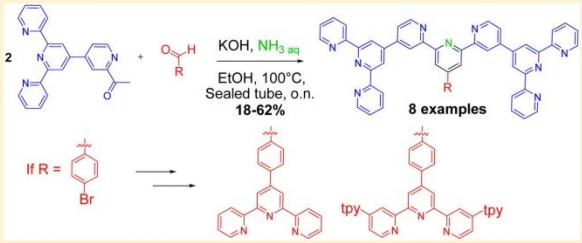

ABSTRACT: A one-pot synthesis of substituted multi-2,2′:6′,2″-terpyridines (multi-tpy) has been achieved using an acetylquaterpyridine precursor with various aryl aldehydes in basic media. This strategy enables ready access to functionalized terpyridines. Utilizing a Suzuki-type cross-coupling, larger structures such as tetra- or even hexa-tpy were obtained from our tri-tpy precursor. These macromolecular units are ideal building blocks for the construction of transition-metal-based supramolecular assemblies.

2,2′:6′,2″-Terpyridines (tpy) have become some of the most useful N/C-coordinating ligands for building transition-metal complexes. Indeed, interesting spectro-electrochemical, magnetic, and structural properties characterize the resulting assemblies, which can be useful in several fields of endeavor,[1] especially in supramolecular chemistry.[2] For example, supramolecular aggregates made up of metal−tpy subunits have been widely studied.[3−7] Tpy−polymer-based structures have also led to numerous applications ranging from polymer light-emitting diodes (PLED's)[8,9] to the development of advanced multiblock copolymers.[10,11] The increasing interest for tpy ligands originates from their reproducible syntheses and their ease of functionalization.[12] Numerous methods have been described and continuously improved, affording an increasing number of readily available derivatized tpy. More recently, multi-tpy-based ligands have been developed and used as luminescence sensors[13] and in self-assembled supramolecular systems (2D and 3D architectures).[13−17] Thus far, the multi-tpy systems have usually been obtained from thiol[13] or palladium cross-coupling strategies,[18−20] in which only a few functional groups were introduced.

Herein, we report an approach to overcome this issue based on a one-pot strategy using a common easily accessible precursor. Accordingly, novel tpy scaffolds bearing various substituents have been obtained and their spectroscopic properties studied. To demonstrate the strength and versatility of our synthetic approach, larger structures bearing four or six tpy units have been prepared with these new functionalized ligands. The structural and photophysical features of our new macromolecular units open doors to applications in different fields. For instance, they can be used as building blocks for the construction of transition metal-based supramolecular assemblies.

Usually, the tpy motif is obtained through a one-pot Kröhnke synthesis, in which key intermediates are required. In our case, a key precursor (**5**) for the synthesis of multi-tpy has been synthesized in five steps (Scheme 1), starting from methyl 2-acetylisonicotinate **1**. The acetal derivative **2** is then reduced by sodium borohydride in refluxing EtOH to yield the corresponding alcohol **3**. Aldehyde **4** was obtained upon treatment of **3** using a Swern oxidation. The synthesis of the key intermediate tpy **5** was adapted from a procedure developed by Schubert et al.[21] leading to the acetal−tpy **4′** followed by an aqueous acidic treatment. It is worth mentioning that this strategy was easily applied to multigram scales.

Our one-pot strategy toward functionalized luminescent multi-tpy is presented in Scheme 2. Acetylpyridine **5** reacts with aromatic aldehydes in the presence of potassium hydroxide through a Claisen-Schmidt aldol condensation and subsequent 1,4-Michael addition. The central pyridine ring is obtained from

Received: August 14, 2015
Published: October 16, 2015

DOI: 10.1021/acs.joc.5b01897
J. Org. Chem. 2015, 80, 11143−11148

Scheme 1. Synthetic Route Followed to Yield the Intermediate 5

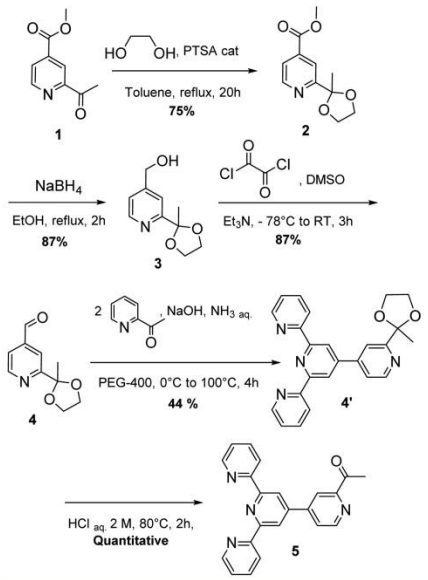

Scheme 2. One-Pot Synthesis of Tri-tpy

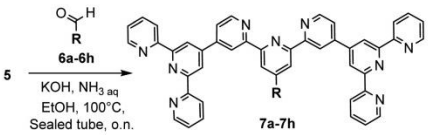

the reaction of the 1,5-dione intermediate with concentrated aqueous ammonia in a sealed tube at 100 °C in EtOH. Upon reflux at atmospheric pressure, only very low conversion was observed. The reaction also works in MeOH despite lower quantities of pure products being recovered. Typically, after 10 min of reaction, complete dissolution of tpy **5** was observed. The tri-tpy derivatives **7a−h** smoothly precipitated from the reaction mixture and were easily recovered by filtration. For purification, the crude product was suspended in large amount of EtOH, sonicated, and heated at reflux and then filtrated or purified by column chromatography depending on the nature of the substituent.

Thanks to the versatility of our synthetic approach, different substituted aromatic aldehydes (**6a−h**) can be used for the synthesis of multi-tpy (Table 1). The various pendant functional groups on the central pyridine core show the ease of structural modification and renders our method advantageous and competitive compared to multi-tpy-based strategies, which usually rely on metal-promoted cross-coupling or thiol chemistry.[18−20] It is worth mentioning that aldehydes bearing electron-rich groups (e.g., **6e**,**g**,**h**, Table 1) lead to better yields, although the reason for these results remains unclear with respect to the mechanism of the reaction. Interestingly, the solubility of the novel tri-tpy was strongly modulated by the nature of the functional groups, ranging from poorly soluble for **7a−c** (typically saturated in the 1 mmol L^{-1} range in CH_2Cl_2) to moderately soluble for **7d−i** (typically saturated in the 10 mmol L^{-1} range in CH_2Cl_2). Strikingly, a completely insoluble product was obtained when 4-carboxaldehyde pyridine was used as an aromatic aldehyde (**7j**, Table 1).

In order to gain insight into the spectroscopic behavior of our tri-tpy, their absorption and emission properties were examined. All of the compounds exhibit broad absorption bands below ca. 350 nm with a maximum close to 250 nm (ε between 50000 and 100000 M^{-1} cm^{-1}) (see Figure S1 and Table 1). These bands are attributed to $^1\pi-\pi^*$ transitions as observed for monotpy chromophores.[22] Moreover, each tri-tpy emits in CH_2Cl_2 at room temperature in air (Φ_{em} values between 0.05 and 0.27). The emission maximum is close to 370 nm except for **7d** which emits at a longer wavelength maximum ($\lambda_{max\ em}$ = 404 nm). Such a red-shifted emission has previously been reported in the literature for 4′-(4-(methylthio)phenyl)-2,2′;6′,2″-terpyridine[13] indicating that the methylthio group clearly induces a reduction in the HOMO−LUMO gap.

Based on these functionalized tri-tpy, a wide variety of multi-tpy structures become readily available. Initially, the use of terephthalaldehyde (dialdehyde) to reach a "hexa-tpy" was explored. However, a mixture of intermediates precipitated prior to completion of the reaction. As a result, another strategy relying on coupling reactions was investigated and turned out to be more successful. The Suzuki coupling was chosen due to the ease of preparation of organoboron derivatives, its usual relatively high stability, and the low toxicity of byproducts.[24] Homocoupling[17] of **7c** was achieved in good yield via a one-pot tandem Miyaura boronic ester formation and subsequent Suzuki coupling (Scheme 3). The resulting luminescent ($\lambda_{max\ em}$ = 484 nm, Φ_{em} = 0.07 in CH_2Cl_2 under air)[25] hexa-tpy product **8** possesses a unique structure. However, its poor solubility prevents its ease of use. To tackle this issue, the tetra-tpy **9** was also synthesized by a Suzuki coupling[26] between the brominated ligand **7c** and the readily available 4′-boronato-phenyl-2,2′:6′,2″-terpyridine[27] with good yield (Scheme 4). Alternatively, the boronate ester **7i** was prepared upon treatment of **7c** with the commercially available bis-(neopentylglycolato)diboron. Suzuki coupling of **7i** with 4′-(bromophenyl)-2,2′:6′,2″-terpyridine[28] also gave the product **9** ($\lambda_{max\ em}$ = 383 nm, Φ_{em} = 0.29 in CH_2Cl_2 under air) showing the versatility of our new synthetic protocol. As expected, this product exhibits relatively high solubility compared to the hexa-tpy **8**.

In conclusion, this paper demonstrates our efforts in expanding the classical terpyridine synthetic scheme in order to build novel multi-tpy ligands. The functionalization of these scaffolds was successfully achieved by selection of the desired aldehydes. We took advantage of this versatility to synthesize tetra- and hexa-tpy by utilizing the Suzuki−Miyaura coupling. As a result, the design and synthesis of supramolecular assemblies such as metallo-supramolecular polymers has become feasible using our synthetic methodology.

■ EXPERIMENTAL SECTION

Methyl 2-(2-Methyl-1,3-dioxolan-2-yl)isonicotinate (2). Ethylene glycol (0.56 mL, 10.08 mmol, 1.5 equiv) and PTSA (0.030 g,

DOI: 10.1021/acs.joc.5b01897
J. Org. Chem. 2015, 80, 11143−11148

Table 1. Functionalized Tri-tpy

Entry	R	Yield (%)	$\lambda_{max\ abs}$ (nm - ε*10^{-3} M^{-1} cm^{-1})[a]	$\lambda_{max\ em}$ (nm)[a,b]	Φ_{em}[b]
7a		36	248 (93.6), 273 (sh, 65.4), 311 (sh, 30.6)	366	0.20
7b		18	249 (59.5), 270 (sh, 48.6), 314 (sh, 18.4)	365	0.17
7c		31	247 (75.8), 275 (sh, 59.5), 313 (sh, 26.0)	366	0.23
7d		62	241 (97.1), 282 (63.0), 295 (sh, 59.5), 310 (sh, 55.7)	404	0.05
7e		40	245 (89.4), 283 (69.7), 294 (sh, 65.0)	368	0.12
7f		25	243 (88.3), 278 (sh, 47.0), 313 (sh, 24.6)	366	0.14
7g		51	242 (90.4), 283 (54.1), 295 (sh, 49.5), 313 (sh, 35.6)	368	0.21
7h		52	250 (103.3), 269 (sh, 85.2), 294 (sh, 60.9), 315 (sh, 38.8)	374	0.27
7i[c]		68	-[d]	-[d]	-[d]
7j[e]		-[e]	-[e]	-[e]	-[e]

[a]Measured in CH_2Cl_2 at rt. [b]Quantum yield was measured under air using quinine sulfate as reference Φ_{ref} = 0.546 in aqueous 0.5 M H_2SO_4,[23] λ_{Exc} = 250 nm, 293 K. [c]**7i** was obtained upon treatment of **7c** with bis(neopentylglycolato)diboron. [d]Spectroscopic properties were not measured due to difficulties in the purification of **7i**. [e]The compound **7j** was totally insoluble in the common organic solvent; hence, no spectroscopic data could be measured.

Scheme 3. Synthetic Scheme for the Hexa-tpy

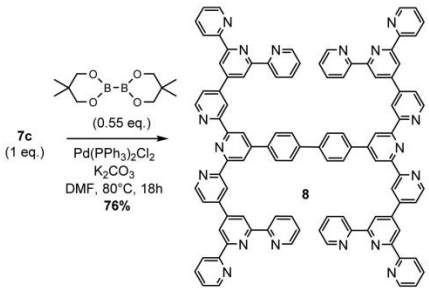

Scheme 4. Synthetic Scheme for the Tetra-tpy

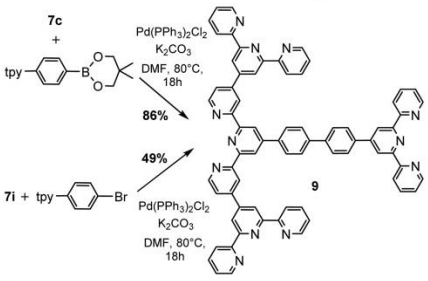

0.17 mmol, 0.03 equiv) were added to methyl 2-acetylisonicotinate (**1**) (1.200 g, 6.72 mmol, 1 equiv) in anhydrous toluene (25 mL). The mixture was refluxed for 20 h with a Dean−Stark trap. A 0.05 M NaOH solution (20 mL) was added, and the aqueous layer was extracted with AcOEt (3 × 25 mL). The organic layers were combined and dried over $MgSO_4$ and solvents removed. The brown residue was purified by column chromatography on SiO_2 (eluent: cyclohexane/ethyl acetate (2/1)) to give a white powder with 75% yield (1.120 g). The ^1H NMR spectrum agreed with that found in the literature.[29] Mp: 61−64 °C. ^1H NMR ($CDCl_3$, 300 MHz): δ (ppm), 8.80 (dd, 1H, J = 5.0 Hz, 0.7 Hz), 8.10 (dd, 1H, J = 1.5 Hz, 0.6 Hz), 7.78 (dd, 1H, J =

DOI: 10.1021/acs.joc.5b01897
J. Org. Chem. 2015, 80, 11143−11148

5.0 Hz, 1.6 Hz), 4.12 (m, 2H), 3.97 (s, 3H), 3.90 (m, 2H), 1.75 (s, 3H). MS (APCI) m/z: 224.2 $[M + H]^+$.

(2-(2-Methyl-1,3-dioxolan-2-yl)pyridin-4-yl)methanol (3). Ester **2** (1.120 g, 5.02 mmol, 1 equiv) was stirred in EtOH (50 mL) until the solid dissolved. $NaBH_4$ (570 mg, 15.05 mmol, 3 equiv) was added, and the mixture was refluxed for 2 h. The reaction was quenched with water (20 mL) and EtOH removed under vacuum. The aqueous layer was extracted with CH_2Cl_2 (4 × 25 mL). The organic layers were combined and dried over $MgSO_4$, and solvent was removed. A colorless oil was obtained with 87% yield (920 mg). The ^{1}H NMR spectrum agreed with that found in literature.[30] ^{1}H NMR ($CDCl_3$, 300 MHz): δ (ppm), 8.60 (d, 1H, J = 5.0 Hz), 7.56 (s, 1H), 7.25 (d, 1H, J = 4.9 Hz), 5.30 (s, 1H), 4.78 (s, 2H), 4.10 (m, 2H), 3.88 (m, 2H), 1.73 (s, 3H).

2-(2-Methyl-1,3-dioxolan-2-yl)isonicotinaldehyde (4). DMSO (0.87 mL, 12.20 mmol, 2.4 equiv) was added to oxalyl chloride (0.87 mL, 10.20 mmol, 2 equiv) in anhydrous CH_2Cl_2 (30 mL) at −78 °C. Alcohol **3** (1.0 g, 5.10 mmol, 1 equiv) dissolved in anhydrous CH_2Cl_2 (6 mL) was added, and the mixture was allowed to react for 45 min at −78 °C until a white salt was obtained. Et_3N (3.55 mL, 25.50 mmol, 5 equiv) was added and the reaction warmed to room temperature over 1 h 30 min. CH_2Cl_2 (50 mL) was added and the mixture washed with brine (50 mL) and water (2 × 50 mL). The organic phase was dried over $MgSO_4$ and the solvent removed under vacuum. The crude product was purified by flash chromatography on SiO_2 (cyclohexane/AcOEt (1/1)) to afford colorless oil with 87% yield (860 mg). ^{1}H NMR ($CDCl_3$, 500 MHz): δ (ppm), 10.10 (s, 1H, H_g), 8.90 (d, 1H, H_a, J_{Ha-Hb} = 4.8 Hz), 7.97 (dd, 1H, H_c, J_{Hc-Hb} = 1.4 Hz, J_{Hc-Ha} = 1.0 Hz), 7.65 (dd, 1H, H_b, J_{Hb-Hc} = 4.9 Hz, J_{Hb-Ha} = 1.5 Hz), 4.14 (m, 2H, H_e), 3.91 (m, 2H, H_f), 1.96 (s, 3H, H_d). ^{13}C NMR ($CDCl_3$, 125 MHz): δ (ppm), 191.7, 163.4, 151.1, 142.4, 121.5, 118.5, 108.4, 77.4, 65.3, 25.5. HRMS (APCI): m/z calcd for $[C_{10}H_{12}NO_3 + H]^+$ 194.0812, found 194.0813.

4′-(2-(2-Methyl-1,3-dioxolan-2-yl)pyridin-4-yl)-2′,2′:6′,2″-terpyridine (4′). Acetal-pytpy **4′** was prepared using an adapted literature procedure.[21] 2-Acetylpyridine (2.133 g, 1.975 mL, 17.6 mmol, 2 equiv) was added to a stirred suspension of NaOH (0.704 g, 17.6 mmol, 2 equiv) in PEG-400 (10 mL) at 0 °C. After 5 min, aldehyde **4** (1.700 g, 8.8 mmol, 1 equiv) was added, and the reaction mixture was kept at 0 °C for 2 h. Then a concentrated solution of NH_3 aq (10 mL) was added, and the suspension was heated at 100 °C for 15 min. During this period, product formed as an off-white precipitate. The product was filtrated, washed with H_2O (200 mL), and recrystallized from EtOH to yield pure product (1.533 g, 44%). Mp: 177−180 °C. ^{1}H NMR ($CDCl_3$, 300 MHz): δ (ppm), 8.79 (dd, 1H, H_a, J_{Ha-Hb} = 5.1 Hz, J_{Ha-Hc} = 0.7 Hz), 8.78 (s, 2H, $H_{3'}$ and $H_{5'}$), 8.75 (ddd, 2H, H_6, J_{H6-H5} = 4.8 Hz, J_{H6-H4} = 1.7 Hz, J_{H6-H3} = 0.7 Hz), 8.69 (dd, 2H, H_3, J_{H3-H4} = 8.0 Hz, J_{H3-H5} = 1.0 Hz), 8.04 (dd, 1H, H_c, J_{Hc-Hb} = 1.7 Hz, J_{Hc-Ha} = 0.7 Hz), 7.91 (td, 2H, H_4, $J_{H4-H3(H5)}$ = 7.8 Hz, J_{H4-H6} = 1.8 Hz), 7.73 (dd, 1H, H_b, J_{Hb-Ha} = 5.0 Hz, J_{Hb-Hc} = 1.8 Hz), 7.39 (ddd, 2H, H_5, J_{H5-H4} = 7.5 Hz, J_{H5-H6} = 4.8 Hz, J_{H5-H3} = 1.1 Hz), 4.15 (m, 2H, H_f), 3.95 (m, 2H, H_e), 1.81 (s, 3H, H_d). ^{13}C NMR ($CDCl_3$, 75 MHz): δ (ppm), 162.2, 156.5, 155.8, 150.4, 149.3, 148.0, 146.9, 137.2, 124.3, 121.6, 121.2, 119.0, 117.6, 108.8, 65.2, 25.8. HRMS (APCI): m/z calcd for $[C_{24}H_{20}N_4O_2 + H]^+$ 397.1659, found 397.1658.

1-(6′-(2-Pyridin-2-yl)[2,2′:6′,2″-terpyridin]-2″-yl]ethan-1-one (5). Acetal-pytpy **4′** (1.000 g, 2.55 mmol, 1 equiv) was dissolved in HCl_{aq} 2 M (5 mL), and the mixture was heated at 80 °C for 2 h. After the mixture was cooled, saturated $NaHCO_{3aq}$ was added to neutralize the reaction. The aqueous layer was extracted with CH_2Cl_2 (three times). The organic layers were combined and dried over $MgSO_4$, and solvent was removed to give a white powder with a quantitative yield (890 mg). Mp: 187−190 °C. ^{1}H NMR ($CDCl_3$, 300 MHz): δ (ppm), 8.82 (dd, 1H, H_a, J_{Ha-Hb} = 5.1 Hz, J_{Ha-Hc} = 0.7 Hz), 8.80 (s, 2H, $H_{3'}$ and $H_{5'}$), 8.73 (ddd, 2H, H_6, J_{H6-H5} = 4.8 Hz, J_{H6-H4} = 1.7 Hz, J_{H6-H3} = 0.8 Hz), 8.66 (dd, 2H, H_3, J_{H3-H4} = 8.0 Hz, J_{H3-H5} = 1.0 Hz), 8.55 (dd, 1H, H_c, J_{Hc-Hb} = 1.8 Hz, J_{Hc-Ha} = 0.7 Hz), 7.97 (dd, 1H, H_b, J_{Hb-Ha} = 5.1 Hz, J_{Hb-Hc} = 1.8 Hz), 7.89 (td, 2H, H_4, $J_{H4-H3(H5)}$ = 7.8 Hz, J_{H4-H6} = 1.8 Hz), 7.38 (ddd, 2H, H_5, J_{H5-H4} = 7.5 Hz, J_{H5-H6} = 4.8 Hz, J_{H5-H3} = 1.2 Hz), 2.80 (s, 3H, H_d). ^{13}C NMR ($CDCl_3$, 75 MHz): δ (ppm), 200.1, 156.7, 155.7, 154.5, 150.0, 149.3, 147.3, 146.9, 137.1, 125.1, 124.3, 121.5, 119.8, 118.8, 26.2. IR (thin film): ν_{max} = 3053, 3011, 1697, 1583, 1566, 1537, 1468, 1410, 1389, 1352, 1283, 1267, 1248, 1213, 1124, 1092, 1072, 1041, 989, 964, 891, 845, 789, 733, 671, 660 cm^{-1}. HRMS (APCI): m/z calcd for $[C_{22}H_{17}N_4O + H]^+$ 353.1397, found 353.1396.

General Procedure for tri-tpy's 7a−h. Acetyl-pytpy **5** (200 mg, 0.568 mmol, 2 equiv) was added to a solution of the corresponding benzaldehyde **6a−c** (0.284 mmol, 1 equiv), potassium hydroxide (31.9 mg, 0.568 mmol), and aqueous ammonia (28%, 2 mL, 92.3 mmol) in absolute EtOH (10 mL). The mixture was heated for 18 h at 100 °C into a sealed tube. The off-white precipitate was filtered and washed with warm EtOH.

7a−c. A suspension of crude product was sonicated for 15 min in EtOH (100 mL) and the mixture refluxed and then filtered. This procedure was repeated three times. The resulting white powder was dried to afford the pure tri-tpy.

7d−h. The crude product was purified by chromatography column on neutral alumina with a CH_2Cl_2/MeOH (95/5) mixture as the eluent.

Compound 7a. Yield: 36% (80 mg). White powder. Mp: >280 °C. ^{1}H NMR ($CDCl_3$, 500 MHz): δ (ppm), 9.18 (d, 2H, H_c, J_{Hc-Hb} = 1.0 Hz), 8.84 (s, 4H, $H_{3'}$ and $H_{5'}$), 8.81 (d, 2H, H_a, J_{Ha-Hb} = 5.0 Hz), 8.76 (s, 2H, H_d), 8.44 (d, 4H, H_3 and $H_{3''}$, J_{H3-H4} = 7.9 Hz), 8.37 (d, 4H, H_6 and $H_{6''}$, J_{H6-H5} = 4.7 Hz), 7.97 (dd, 2H, H_e, J_{He-Hf} = 8.5 Hz, J_{He-Hg} = 1.4 Hz), 7.80 (dd, 2H, H_b, J_{Hb-Ha} = 5.0 Hz,, J_{Hb-Hc} = 1.8 Hz), 7.74 (td, 4H, H_4 and $H_{4''}$, $J_{H4-H5(H3)}$ = 7.7 Hz, J_{H4-H6} = 1.8 Hz), 7.56 (t, 2H, H_f, $J_{Hf-He(Hg)}$ = 7.4 Hz), 7.50 (t, 1H, H_g, J_{Hg-Hf} = 7.3 Hz), 7.16 (ddd, 4H, H_5 and $H_{5''}$, J_{H5-H4} = 7.4 Hz, J_{H5-H6} = 4.7 Hz, J_{H5-H3} = 1.1 Hz). ^{13}C NMR ($CDCl_3$, 75 MHz): δ (ppm), 157.0, 156.1, 155.8, 155.7, 149.7, 149.0, 147.9, 147.0, 138.6, 137.6, 136.6, 129.1, 127.5, 123.8, 121.8, 121.0, 120.0, 119.4, 118.9. IR (thin film): ν_{max} = 1582, 1566, 1539, 1468, 1396, 1356, 1246, 1076, 1042, 988, 887, 839, 791, 735, 696 cm^{-1}. HRMS (APCI): m/z calcd for $[C_{51}H_{33}N_9 + H]^+$ 772.2932, found 772.2934.

Compound 7b. Yield: 18% (36 mg). White powder. Mp: >280 °C. ^{1}H NMR ($CDCl_3$, 500 MHz): δ (ppm), 9.16 (d, 2H, H_c, J_{Hc-Hb} = 1.1 Hz), 8.78 (s, 4H, $H_{3'}$ and $H_{5'}$), 8.76 (d, 2H, H_a, J_{Ha-Hb} = 5.0 Hz), 8.68 (s, 2H, H_d), 8.41 (d, 4H, H_3 and $H_{3''}$, J_{H3-H4} = 7.9 Hz), 8.34 (d, 4H, H_6 and $H_{6''}$, J_{H6-H5} = 4.7 Hz), 8.01 (d, 2H, H_f, J_{Hf-He} = 8.4 Hz), 7.84 (d, 2H, H_e, J_{He-Hf} = 8.4 Hz), 7.76 (dd, 2H, H_b, J_{Hb-Ha} = 5.0 Hz,, J_{Hb-Hc} = 1.7 Hz), 7.71 (td, 4H, H_4 and $H_{4''}$, $J_{H4-H5(H3)}$ = 7.7 Hz, J_{H4-H6} = 1.7 Hz), 7.13 (ddd, 4H, H_5 and $H_{5''}$, J_{H5-H4} = 7.3 Hz, J_{H5-H6} = 4.7 Hz, J_{H5-H3} = 1.0 Hz). IR (thin film): ν_{max} = 2924, 2851, 2228, 1584, 1566, 1541, 1466, 1356, 1259, 1076, 1051, 1018, 837, 791, 733 cm^{-1}. HRMS (APCI): m/z calcd for $[C_{52}H_{32}N_{10} + H]^+$ 797.2884, found 797.2885. Note: compound **7b** was found to be too insoluble to record a carbon NMR.

Compound 7c. Yield: 31% (72 mg). White powder. Mp: >280 °C. ^{1}H NMR ($CDCl_3$, 500 MHz): δ (ppm) 9.22 (d, 2H, H_c, J_{Hc-Hb} = 1.3 Hz), 8.87−8.84 (m, 6H, H_a, $H_{3'}$ and $H_{5'}$), 8.76 (s, 2H, H_d), 8.48 (d, 4H, H_3 and $H_{3''}$, J_{H3-H4} = 7.9 Hz), 8.38 (dd, 4H, H_6 and $H_{6''}$, J_{H6-H5} = 4.6 Hz, J_{H6-H4} = 0.7 Hz), 7.84 (d, 4H, H_b and H_e, J_{He-Hf} = 8.2 Hz), 7.76 (td, 4H and $H_{4''}$, H_4, $J_{H4-H5(H3)}$ = 7.7 Hz, J_{H4-H6} = 1.7 Hz), 7.69 (d, 2H, H_f, J_{Hf-He} = 8.5 Hz), 7.18 (ddd, 4H, H_5 and $H_{5''}$, J_{H5-H4} = 7.4 Hz, J_{H5-H6} = 4.7 Hz, J_{H5-H3} = 1.0 Hz). ^{13}C NMR ($CDCl_3$, 125 MHz): δ (ppm), 156.5, 156.0, 155.6, 155.5, 149.7, 148.9, 147.0, 145.7, 137.1, 136.5, 132.1, 128.9, 123.7, 121.9, 120.9, 119.9, 118.9, 118.8. IR (thin film): ν_{max} = 2928, 2843, 1582, 1566, 1541, 1466, 1394, 1354, 1259, 1074, 1038, 1018, 889, 791, 731 cm^{-1}. HRMS (APCI): m/z calcd for $[C_{51}H_{32}N_9{}^{79}Br + H]^+$ 850.2037, found 850.2034.

Compound 7d. Yield: 62% (142 mg). Clear yellow powder. Mp: >280 °C. ^{1}H NMR ($CDCl_3$, 500 MHz): δ (ppm) 8.96 (d, 2H, H_c, J_{Hc-Hb} = 0.8 Hz), 8.62 (s, 4H, $H_{3'}$ and $H_{5'}$), 8.58 (d, 2H, H_a, J_{Ha-Hb} = 4.9 Hz), 8.49 (s, 2H, H_d), 8.25 (d, 4H, H_6 and $H_{6''}$, J_{H6-H5} = 4.1 Hz), 8.22 (d, 4H, H_3 and $H_{3''}$, J_{H3-H4} = 7.9 Hz), 7.82 (d, 2H, H_e, J_{He-Hf} = 8.3 Hz), 7.58 (td, 4H and $H_{4''}$, H_4, $J_{H4-H5(H3)}$ = 7.8 Hz, J_{H4-H6} = 1.7 Hz), 7.57 (m, 2H, H_b), 7.39 (d, 2H, H_f, J_{Hf-He} = 8.3 Hz), 7.02 (ddd,

DOI: 10.1021/acs.joc.5b01897
J. Org. Chem. 2015, 80, 11143−11148

4H, H_5 and $H_{5''}$, J_{H5-H4} = 7.4 Hz, J_{H5-H6} = 4.9 Hz, J_{H5-H3} = 0.7 Hz), 2.61 (s, 3H, H_g). ^{13}C NMR ($CDCl_3$, 125 MHz): δ (ppm) 156.8, 155.8, 155.6, 155.5, 149.4, 148.8, 147.7, 146.9, 140.1, 136.4, 135.0, 127.7, 126.6, 123.6, 121.7, 120.9, 120.0, 118.8, 118.6, 15.7. IR (thin film): ν_{max} = 3053, 2920, 2851, 1582, 1566, 1537, 1499, 1468, 1394, 1356, 1246, 1124, 1095, 1076, 1040, 988, 887, 839, 820, 791, 735, 669 cm^{-1}. HRMS (APCI): m/z calcd for $[C_{52}H_{35}{}^{32}S_1N_9 + H]^+$ 818.28089, found 818.28088.

Compound 7e. Yield: 40% (90 mg). White powder. Mp: >280 °C. ^1H NMR ($CDCl_3$, 500 MHz): δ (ppm) 9.00 (s, 2H, H_c), 8.68 (s, 4H, $H_{3'}$ and $H_{5'}$), 8.63 (d, 2H, H_a, J_{Ha-Hb} = 4.9 Hz), 8.54 (s, 2H, H_d), 8.32−8.26 (m, 8H, H_3, $H_{3''}$, H_6 and $H_{6''}$), 7.88 (d, 2H, H_e, J_{He-Hf} = 8.6 Hz), 7.66−7.60 (m, 6H, H_b, H_4 and $H_{4''}$), 7.08−7.04 (m, 6H, H_f, H_5 and $H_{5''}$), 3.94 (s, 3H, H_g). ^{13}C NMR ($CDCl_3$, 125 MHz): δ (ppm) 160.6, 157.0, 155.9, 155.6, 155.5, 149.5, 149.3, 148.9, 147.8, 146.9, 136.5, 130.9, 128.7, 123.7, 121.7, 121.0, 120.0, 118.8, 118.6, 114.4, 55.6. IR (thin film): ν_{max} = 3053, 3013, 2955, 2922, 2853, 1609, 1582, 1566, 1539, 1516, 1468, 1396, 1356, 1292, 1263, 1252, 1180, 1116, 1076, 1040, 987, 887, 831, 791, 735, 704, 658 cm^{-1}. HRMS (APCI): m/z calcd for $[C_{52}H_{35}O_1N_9 + H]^+$ 802.30373, found 802.30366.

Compound 7f. Yield: 25% (60 mg). White powder. Mp: >280 °C. ^1H NMR ($CDCl_3$, 500 MHz): δ (ppm) 9.08 (d, 2H, H_c, J_{Hc-Hb} = 0.9 Hz), 8.82 (dd, 1H, H_b J_{Hf-He} = 5.0 Hz, J_{Hf-Hg} = 0.6 Hz), 8.74 (s, 4H, $H_{3'}$ and $H_{5'}$), 8.71 (d, 2H, H_a, J_{Ha-Hb} = 5.0 Hz), 8.65 (s, 2H, H_d), 8.35 (d, 4H, H_3 and $H_{3''}$, J_{H3-H4} = 7.9 Hz), 8.31 (dd, 4H, H_6 and $H_{6''}$, J_{H6-H5} = 4.5 Hz, J_{H6-H4} = 0.6 Hz), 8.08 (dd, 1H, H_g, J_{Hg-He} = 1.7 Hz, J_{Hg-Hf} = 0.6 Hz), 7.73−7.70 (m, 3H, H_e and H_b), 7.68 (td, 4H, H_4 and $H_{4''}$, $J_{H4-H5(H3)}$ = 7.7 Hz, J_{H4-H6} = 1.7 Hz), 7.11 (ddd, 4H, H_5 and $H_{5''}$, J_{H5-H4} = 7.4 Hz, J_{H5-H6} = 4.7 Hz, J_{H5-H3} = 1.0 Hz), 4.21 (m, 2H, H_i), 4.02 (m, 2H, H_i), 1.87 (s, 3H, H_h). ^{13}C NMR ($CDCl_3$, 125 MHz): δ (ppm) 162.6, 156.6, 156.4, 156.2, 155.8, 150.8, 149.9, 149.2, 147.9, 147.6, 147.3, 147.1, 136.8, 124.0, 122.3, 121.4, 121.2, 120.4, 119.4, 119.1, 117.8, 109.2, 65.6, 26.1. IR (thin film): ν_{max} = 3053, 2955, 2928, 1582, 1566, 1539, 1468, 1445, 1394, 1356, 1265, 1200, 1123, 1076, 1040, 988, 887, 839, 791, 735, 702, 669 cm^{-1}. HRMS (APCI): m/z calcd for $[C_{54}H_{38}O_2N_{10} + H]^+$ 859.32520, found 859.32518.

Compound 7g. Yield: 51% (104 mg). White powder. Mp: >280 °C. ^1H NMR ($CDCl_3$, 500 MHz): δ (ppm) 9.20 (d, 2H, H_c, J_{Hc-Hb} = 0.7 Hz), 8.87−8.84 (s, 4H, $H_{3'}$ and $H_{5'}$), 8.75 (s, 2H, H_a, $J_{Ha'-Hb}$ = 4.9 Hz), 8.66 (s, 2H, H_d), 8.48 (d, 4H, H_3 and $H_{3''}$, J_{H3-H4} = 7.9 Hz), 8.39 (dd, 4H, H_6 and $H_{6''}$, J_{H6-H5} = 4.5 Hz, J_{H6-H4} = 0.6 Hz), 8.09−8.06 (m, 1H, H_k), 7.99−7.95 (m, 2H, H_k and H_e), 7.80 (dd, 2H, H_b, J_{Hb-Ha} = 4.9 Hz, J_{Hb-Hc} = 1.7 Hz), 7.76 (td, 4H, H_4 and $H_{4''}$, $J_{H4-H5(H3)}$ = 7.7 Hz, J_{H4-H6} = 1.7 Hz), 7.67 (dd, 1H, H_g, J_{Hg-Hf} = 7.0 Hz, J_{Hg-He} = 1.2 Hz), 7.61 (dd, 1H, H_f, J_{Hf-He} = 7.1 Hz, J_{Hf-Hg} = 7.0 Hz), 7.63−7.58 (m, 2H, H_i and H_i), 7.17 (ddd, 4H, H_5 and $H_{5''}$, J_{H5-H4} = 7.4 Hz, J_{H5-H6} = 4.7 Hz, J_{H5-H3} = 1.0 Hz). ^{13}C NMR ($CDCl_3$, 125 MHz): δ (ppm) 157.1, 156.3, 155.8, 155.6, 150.0, 149.1, 148.0, 147.1, 136.8, 133.9, 133.6, 131.2, 128.9, 128.6, 127.7, 127.3, 126.8, 126.2, 125.8, 125.5, 123.9, 123.0, 122.0, 121.1, 120.0, 119.0. IR (thin film): ν_{max} = 3053, 3008, 2955, 2922, 2853, 1584, 1566, 1539, 1468, 1396, 1356, 1263, 1122, 1074, 1041, 988, 889, 839, 791, 777, 739 cm^{-1}. HRMS (APCI): m/z calcd for $[C_{55}H_{35}N_9 + H]^+$ 822.3088, found 822.3082.

Compound 7h. Yield: 52% (122 mg). Off-white powder. Mp: >280 °C. ^1H NMR ($CDCl_3$, 500 MHz): δ (ppm) 9.01 (s, 2H, H_c), 8.66 (s, 4H, $H_{3'}$ and $H_{5'}$), 8.63 (s, 2H, H_d), 8.61 (d, 2H, H_a, J_{Ha-Hb} = 4.9 Hz), 8.36 (d, 1H, H_k, J_{Hk-He} = 1.0 Hz), 8.27−8.23 (m, 8H, H_3, $H_{3''}$, H_6 and $H_{6''}$), 8.02−7.90 (m, 4H, H_e, H_f, H_g and H_i) 7.60−7.56 (m, 4H, H_b, H_k and H_i), 7.58 (td, 4H and $H_{4''}$, H_4, $J_{H4-H5(H3)}$ = 7.6 Hz, J_{H4-H6} = 1.5 Hz), 7.02 (dd, 4H, H_5 and $H_{5''}$, J_{H5-H4} = 7.1 Hz, J_{H5-H6} = 4.9 Hz). ^{13}C NMR ($CDCl_3$, 125 MHz): δ (ppm) 157.1, 156.1, 155.9, 155.7, 149.8, 149.0, 147.8, 147.1, 136.6, 135.8, 133.7, 133.7, 128.9, 128.8, 127.9, 126.9, 126.8, 126.7, 125.2, 123.8, 121.9, 121.0, 120.1, 119.5, 118.9. IR (thin film): ν_{max} = 3030, 1582, 1566, 1539, 1468, 1396, 1367, 1340, 1263, 1122, 1074, 1040, 988, 887, 856, 791, 746, 737, 704, 652 cm^{-1}. HRMS (APCI): m/z calcd for $[C_{55}H_{35}N_9 + H]^+$ 822.3088, found 822.3087.

4‴-(4-(5,5-Dimethyl-1,3,2-dioxaborinan-2-yl)phenyl)-6′,6‴′-di(pyridin2-yl)-2,2′:4′,4″:2‴,2⁗:6⁗,2‴′:4‴′,4⁗′:2‴′,2⁗′-sepipyridine (7i). A Schlenk tube was charged with $Pd(dppf)Cl_2$ (3.4 mg, 0.0042 mmol, 0.05 equiv), KOAc (24.6 mg, 0.251 mmol, 3 equiv), **7c** (74.0 mg, 0.084 mmol, 1 equiv), and bis(neopentylglycolato)diboron (28.4 mg, 0.126 mmol, 1.5 equiv) and flushed with argon. Anhydrous DMF (8 mL) was added, and the reaction mixture was degassed by five freeze−pump−thaw cycles. The mixture was heated for 6 h at 80 °C under argon. The DMF was evaporated. The crude mixture was dissolved with dichloromethane (250 mL) and filtered over Celite. The resulting solution was washed five times with deionized water (100 mL). The dichloromethane was removed by evaporation to give an off-white product with 68% yield (50 mg). Mp: >280 °C. ^1H NMR ($CDCl_3$, 500 MHz): δ (ppm), 9.17 (d, 2H, H_c, J_{Hc-Hb} = 1.4 Hz), 8.84−8.79 (m, 8H, H_a, H_b, $H_{3'}$and $H_{5'}$), 8.76 (s, 2H, H_d), 8.44 (d, 4H, H_3 and $H_{3''}$, J_{H3-H4} = 7.9 Hz), 8.36 (d, 4H, H_6 and $H_{6''}$, J_{H6-H5} = 4.9 Hz), 7.97 (d, 2H, H_e, J_{He-Hf} = 1.8 Hz), 7.79 (dd, 2H, H_b, J_{Hb-Ha} = 5.0 Hz, J_{Hb-Hc} = 1.4 Hz), 7.74 (td, 4H, H_4 and $H_{4''}$, $J_{H4-H3(HS)}$ = 7.7 Hz, J_{H4-H6} = 1.7 Hz), 7.16 (ddd, 4H, H_5 and $H_{5''}$, J_{H5-H4} = 7.7 Hz, J_{H5-H6} = 5.0 Hz, J_{H5-H3} = 1.1 Hz), 3.84 (s, 4H, H_g), 1.08 (s, 6H, H_f). ^{13}C NMR (125 MHz, CD_2Cl_2): δ (ppm), 156.0, 155.5, 155.3, 154.9, 148.9, 148.5, 147.8, 146.6, 136.2, 134.4, 126.1, 123.4, 121.4, 120.6, 119.8, 118.5, 72.6, 31.9, 21.7. IR (thin film): ν_{max} = 2964, 2928, 1584, 1566, 1541, 1468, 1420, 1394, 1356, 1315, 1308, 1261, 1132, 1076, 1040, 1020, 987, 908, 837, 791, 735 cm^{-1}. HRMS (ESI): m/z calcd for $[C_{56}H_{44}O_2N_9{}^{11}B + H]^+$ 884.3627, found 884.3634.

4,4′-Bis(6′,6‴′-di(pyridin-2-yl)-[2,2′:4′,4″:2‴,2⁗:6‴,2‴′:-4‴′,4⁗′:2⁗′,2‴′-sepipyridin]4‴-yl)-1,1′-biphenyl (8). A Schlenk tube was charged with $Pd(PPh_3)_2Cl_2$ (3.0 mg, 0.0042 mmol, 0.05 equiv), K_2CO_3 (35.2 mg, 0.254 mmol, 3 equiv), **7c** (75.0 mg, 0.085 mmol, 1 equiv), and bis(neopentylglycolato)diboron (10.5 mg, 0.046 mmol, 0.55 equiv) and flushed with argon. DMF (10 mL) was added, and the reaction mixture was degassed by five freeze−pump−thaw cycles. The mixture was heated for 18 h at 80 °C under argon. The reaction mixture was centrifuged, and the resulting solid was washed with water, ethanol, and chloroform. An off-white powder was obtained with 76% yield (32.6 mg). Mp: >280 °C. ^1H NMR ($CDCl_3$/$(CF_3)_2CHOH$:9/1, 500 MHz): δ (ppm), 8.83 (d, 4H, H_a, J_{Ha-Hb} = 5.4 Hz), 8.81 (s, 4H, H_c), 8.60 (d, 8H, H_6 and $H_{6''}$, J_{H6-H5} = 5.2 Hz), 8.53 (s, 8H, $H_{3'}$ and $H_{5'}$), 8.48 (s, 4H, H_d), 8.43 (d, 8H, H_3 an $H_{3''}$, J_{H3-H4} = 7.9 Hz), 8.07 (m, 16H, H_b, H_e or H_f, H_4 and $H_{4''}$), 7.90 (d, 4H, H_e or H_f, J_{He-Hf} = 8.3 Hz), 7.59 (dd, 4H, H_5 an $H_{5''}$, J_{H5-H6} = 5.2 Hz, J_{H5-H4} = 7.9 Hz). IR (thin film): ν_{max} = 2959, 2920, 2905, 2851, 1584, 1568, 1558, 1541, 1521, 1506, 1472, 1456, 1418, 1396, 1362, 1339, 1261, 1096, 1078, 1040, 1020, 791, 773, 669, 656 cm^{-1}. HRMS (ESI): m/z calcd for $[C_{102}H_{64}N_{18} + H]^+$ 1541.5634, found 1542.5617. Note: compound **8** was found to be too insoluble to record a carbon NMR.

4‴-(4′-([2,2′:6′,2″-Terpyridin]-4′-yl)[1,1′-biphenyl]-4-yl)-6′,6‴′-di(pyridin-2-yl)-2,2′:4′,4″:2‴,2⁗:6‴,2‴′:4‴′,4⁗′:-2⁗′,2‴′-sepipyridine (9). (A) A Schlenk tube was charged with $Pd(PPh_3)_2Cl_2$ (3.1 mg, 0.0043 mmol, 0.05 equiv), K_2CO_3 (36.1 mg, 0.261 mmol, 3 equiv), **7c** (77.0 mg, 0.087 mmol, 1 equiv), and 4′-(boronatophenyl)-2,2′:6′,2″-terpyridine (55.0 mg, 0.131 mmol, 1.5 equiv) and flushed with argon. DMF (10 mL) was added, and the reaction mixture was degassed by five freeze−pump−thaw cycles. The mixture was heated for 18 h at 80 °C under argon. The DMF was removed by rotary evaporation. The crude mixture was washed successively with water and ethanol and centrifuged. An off-white powder was obtained with 86% yield (78 mg). Mp: >280 °C. ^1H NMR ($CDCl_3$, 500 MHz): δ (ppm), 9.12 (s, 2H, $H_{c'}$), 8.80 (m, 10H, H_a, $H_{a'}$, $H_{e'}$, $H_{3'}$ and $H_{5'}$), 8.68 (d, 2H, $H_{d'}$), $J_{Hd'-Hc'}$ = 8.1 Hz), 8.36 (d, 4H, $H_{3'}$ and $H_{3''}$, J_{H3-H4} = 7.8 Hz), 8.33 (d, 4H, H_6 and $H_{6''}$, J_{H6-H5} = 4.7 Hz), 8.05 (dd, 4H, H_f and $H_{g'}$, J_{Hf-He} = 8.2 Hz, $J_{Hf-Hg'}$ = 1.8 Hz), 7.88 (td, 2H, $H_{c'}$, $J_{Hc'-Hb'\ (d')}$ = 7.7 Hz, $J_{Hc'-Ha'}$ = 1.6 Hz), 7.84 (d, 4H, H_e and H_F, J_{He-Hf} = 8.3 Hz), 7.72 (dd, 2H, H_b, J_{Hb-Ha} = 5.1 Hz, $J_{Hb-Hc'}$ = 1.8 Hz), 7.68 (td, 4H, H_4 and $H_{4''}$, $J_{H4-H3(S)}$ = 7.8 Hz, J_{H4-H6} = 1.8 Hz), 7.36 (ddd, 2H, $H_{b'}$, $J_{Hb'-Hc'}$ = 7.7 Hz, $J_{Hb'-Ha'}$ = 4.6 Hz, $J_{Hb'-Hd'}$ = 1.2 Hz), 7.36 (ddd, 2H, $H_{b'}$, $J_{Hb'-Hc'}$ = 7.7 Hz, $J_{Hb'-Ha'}$ = 4.6 Hz, $J_{Hb'-Hd'}$ = 1.2 Hz), 7.10 (ddd, 4H, H_5 and $H_{5''}$, J_{H5-H4} = 7.8 Hz, $J_{H5-H6'}$ = 4.6 Hz, J_{H5-H3} = 1.4 Hz). ^{13}C NMR (125 MHz, $CDCl_3$): δ (ppm), 157.3, 156.6, 156.4, 156.3, 156.1, 155.9, 150.0, 149.6, 149.2, 148.1, 147.3, 137.3, 136.8, 128.2, 128.0, 124.2, 124.0, 122.1, 121.8, 121.3, 120.3,

DOI: 10.1021/acs.joc.5b01897
J. Org. Chem. 2015, 80, 11143−11148

119.4, 119.2, 119.1. IR (thin film): ν_{max} = 3055, 3005, 2922, 1584, 1566, 1539, 1506, 1466, 1394, 1356, 1265, 1123, 1074, 988, 885, 837, 818, 789, 764, 745, 733 cm^{-1}. HRMS (ESI): m/z calcd for $[C_{72}H_{46}N_{12} + H]^+$ 1079.4041, found 1079.4030.

(B) A Schlenk tube was charged with $Pd(PPh_3)_2Cl_2$ (2.0 mg, 0.0028 mmol, 0.05 equiv), K_2CO_3 (23.6 mg, 0.171 mmol, 3 equiv), **7i** (50.4 mg, 0.057 mmol, 1 equiv), and 4′-(bromophenyl)-2,2′:6′,2″-terpyridine (3320 mg, 0.085 mmol, 1.5 equiv) and flushed with argon. DMF (10 mL) was added, and the reaction mixture was degassed by five freeze−pump−thaw cycles. The mixture was heated for 18 h at 80 °C under argon. The DMF was removed by rotary evaporation. The crude mixture was washed successively with water and ethanol and centrifuged. An off-white powder was obtained with 49% yield (30 mg).

■ ASSOCIATED CONTENT

Supporting Information

The Supporting Information is available free of charge on the ACS Publications website at DOI: 10.1021/acs.joc.5b01897.

^1H and ^{13}C NMR and $^1H-^1H$ COSY NMR spectra; absorption and emission spectra of tri-tpy, tetra-tpy and hexa-tpy (PDF)

■ AUTHOR INFORMATION

Corresponding Author

*E-mail: benjamin.elias@uclouvain.be.

Author Contributions

The manuscript was written through contributions of all authors.

Notes

The authors declare no competing financial interest.

■ ACKNOWLEDGMENTS

We gratefully acknowledge the Fonds National pour la Recherche Scientifique (F.R.S.-FNRS), the Fonds pour la Formation à la Recherche dans l'Industrie et dans l'Agriculture (F.R.I.A.), the Région Wallonne, the Université catholique de Louvain, and the Prix Pierre et Colette Bauchau for financial support.

■ REFERENCES

(1) Schubert, U. S.; Winter, A.; Newkome, G. R. *Terpyridine-Based Materials: For Catalytic, Optoelectronic and Life Science Applications*; Wiley, 2011.

(2) Wild, A.; Winter, A.; Schlutter, F.; Schubert, U. S. *Chem. Soc. Rev.* **2011**, *40*, 1459.

(3) Schofield, E. R.; Collin, J.-P.; Gruber, N.; Sauvage, J.-P. *Chem. Commun.* **2003**, 188.

(4) Barboiu, M.; Petit, E.; Vaughan, G. *Chem. - Eur. J.* **2004**, *10*, 2263.

(5) Schroeder, T.; Brodbeck, R.; Letzel, M. C.; Mix, A.; Schnatwinkel, B.; Tonigold, M.; Volkmer, D.; Mattay, J. *Tetrahedron Lett.* **2008**, *49*, 5939.

(6) Collin, J.-P.; Heitz, V.; Sauvage, J.-P. *Top. Curr. Chem.* **2005**, *262*, 29.

(7) Durola, F.; Sauvage, J.-P.; Wenger, O. S. *Coord. Chem. Rev.* **2010**, *254*, 1748.

(8) Ulbricht, C.; Beyer, B.; Friebe, C.; Winter, A.; Schubert, U. S. *Adv. Mater.* **2009**, *21*, 4418.

(9) Grimsdale, A. C.; Leok Chan, K.; Martin, R. E.; Jokisz, P. G.; Holmes, A. B. *Chem. Rev.* **2009**, *109*, 897.

(10) Gohy, J.-F.; Lohmeijer, B. G. G.; Schubert, U. S. *Chem. - Eur. J.* **2003**, *9*, 3472.

(11) Gohy, J.-F. *Coord. Chem. Rev.* **2009**, *253*, 2214.

(12) Tu, S.; Jia, R.; Jiang, B.; Zhang, J.; Zhang, Y.; Yao, C.; Ji, S. *Tetrahedron* **2007**, *63*, 381.

(13) Fermi, A.; Bergamini, G.; Roy, M.; Gingras, M.; Ceroni, P. *J. Am. Chem. Soc.* **2014**, *136*, 6395.

(14) Bauer, T.; Zheng, Z.; Renn, A.; Enning, R.; Stemmer, A.; Sakamoto, J.; Schlüter, A. D. *Angew. Chem., Int. Ed.* **2011**, *50*, 7879.

(15) Zheng, Z.; Ruiz-Vargas, C. S.; Bauer, T.; Rossi, A.; Payamyar, P.; Schütz, A.; Stemmer, A.; Sakamoto, J.; Schlüter, A. D. *Macromol. Rapid Commun.* **2013**, *34*, 1670.

(16) Zheng, Z.; Opilik, L.; Schiffmann, F.; Liu, W.; Bergamini, G.; Ceroni, P.; Lee, L.-T.; Schutz, A.; Sakamoto, J.; Zenobi, R.; VandeVondele, J.; Schluter, A. D. *J. Am. Chem. Soc.* **2014**, *136*, 6103.

(17) Wang, M.; Wang, C.; Hao, X.-Q.; Li, X.; Vaughn, T. J.; Zhang, Y.-Y.; Yu, Y.; Li, Z.-Y.; Song, M.-P.; Yang, H.-B.; Li, X. *J. Am. Chem. Soc.* **2014**, *136*, 10499.

(18) Schultz, A.; Li, X.; McCusker, C. E.; Moorefield, C. N.; Castellano, F. N.; Wesdemiotis, C.; Newkome, G. R. *Chem. - Eur. J.* **2012**, *18*, 11569.

(19) Han, F. S.; Higuchi, M.; Kurth, D. G. *Org. Lett.* **2007**, *9*, 559.

(20) Pabst, G. R.; Sauer, J. *Tetrahedron* **1999**, *55*, 5067.

(21) Winter, A.; van den Berg, A. M. J.; Hoogenboom, R.; Kickelbick, G.; Schubert, U. S. *Synthesis* **2006**, *2006*, 2873.

(22) Yoshikawa, N.; Yamabe, S.; Kanehisa, N.; Takashima, H.; Tsukahara, K. *J. Phys. Org. Chem.* **2009**, *22*, 410.

(23) Eaton, D. F. *Pure Appl. Chem.* **1988**, *60*, 1107.

(24) Li, C.-J. *Angew. Chem., Int. Ed.* **2003**, *42*, 4856.

(25) The low solubility of **8** prevents its dissolution in pure dichloromethane. Therefore, 10% of 1,1,1,3,3,3-hexafluoro-2-propanol was added to the CH_2Cl_2 solution in order to achieve complete dissolution of the compound.

(26) Miyaura, N.; Yanagi, T.; Suzuki, A. *Synth. Commun.* **1981**, *11*, 513.

(27) Aspley, C. J.; Williams, J. A. G. *New J. Chem.* **2001**, *25*, 1136.

(28) Spahni, W.; Calzagerri, G. *Helv. Chim. Acta* **1984**, *67*, 450.

(29) Ishihara, M.; Tsuneya, T.; Shiga, M.; Kawashima, S.; Yamagishi, K.; Yoshida, F.; Sato, H.; Uneyama, K. *J. Agric. Food Chem.* **1992**, *40*, 1647.

(30) Bur, D.; Corminboeuf, O.; Cren, S.; Fretz, H.; Grisostomi, C.; Leroy, X.; Pothier, J.; Richard-Bildstein Preparation of Aminotriazole Derivatives as ALX Receptor Agonists. Patent WO 2009/077990 A1, 2009.

DOI: 10.1021/acs.joc.5b01897
J. Org. Chem. 2015, 80, 11143−11148

Chapter 11 - References

(1) Schulz, M.; Karnahl, M.; Schwalbe, M.; Vos, J. G. *Coord. Chem. Rev.* **2012**, *256*, 1682.

(2) Wu, L.-Z.; Chen, B.; Li, Z.-J.; Tung, C.-H. *Acc. Chem. Res.* **2014**, *47*, 2177.

(3) Service, R. F. *Science* **2005**, *309*, 548.

(4) Blankenship, R. E.; Tiede, D. M.; Barber, J.; Brudvig, G. W.; Fleming, G.; Ghirardi, M.; Gunner, M. R.; Junge, W.; Kramer, D. M.; Melis, A.; Moore, T. A.; Moser, C. C.; Nocera, D. G.; Nozik, A. J.; Ort, D. R.; Parson, W. W.; Prince, R. C.; Sayre, R. T. *Science* **2011**, *332*, 805.

(5) Armaroli, N.; Balzani, V. *Angew. Chem., Int. Ed.* **2007**, *46*, 52.

(6) Zuttel, A.; Borgschulte, A.; Schlapbach, L.; Editors *Hydrogen as a future energy carrier*; Wiley-VCH Verlag GmbH & Co. KGaA, **2008**.

(7) Fujishima, A.; Honda, K. *Nature* **1972**, *238*, 37.

(8) Osterloh, F. E. *Chem. Mater.* **2008**, *20*, 35.

(9) Chen, X.; Shen, S.; Guo, L.; Mao, S. S. *Chem. Rev.* **2010**, *110*, 6503.

(10) Walter, M. G.; Warren, E. L.; McKone, J. R.; Boettcher, S. W.; Mi, Q.; Santori, E. A.; Lewis, N. S. *Chem. Rev.* **2010**, *110*, 6446.

(11) Kudo, A.; Miseki, Y. *Chem. Soc. Rev.* **2009**, *38*, 253.

(12) Brancho, J. J.; Bartlett, B. M. *Chemistry of Materials* **2015**.

(13) Ni, M.; Leung, M. K. H.; Leung, D. Y. C.; Sumathy, K. *Renewable Sustainable Energy Rev.* **2006**, *11*, 401.

(14) Maeda, K.; Saito, N.; Lu, D.; Inoue, Y.; Domen, K. *J. Phys. Chem. C* **2007**, *111*, 4749.

(15) Ikeda, S.; Hara, M.; Kondo, J. N.; Domen, K.; Takahashi, H.; Okubo, T.; Kakihana, M. *Chem. Mater.* **1998**, *10*, 72.

(16) Kim, H. G.; Hwang, D. W.; Bae, S. W.; Jung, J. H.; Lee, J. S. *Catal. Lett.* **2003**, *91*, 193.

(17) Kato, H.; Asakura, K.; Kudo, A. *J. Am. Chem. Soc.* **2003**, *125*, 3082.

(18) Rao, C. N. R.; Lingampalli, S. R. *Small* **2015**, Ahead of Print.

(19) Ran, J.; Zhang, J.; Yu, J.; Jaroniec, M.; Qiao, S. Z. *Chem. Soc. Rev.* **2014**, *43*, 7787.

(20) Etacheri, V.; Di Valentin, C.; Schneider, J.; Bahnemann, D.; Pillai, S. C. *J. Photochem. Photobiol., C* **2015**, *25*, 1.

(21) Rau, S.; Schaefer, B.; Gleich, D.; Anders, E.; Rudolph, M.; Friedrich, M.; Goerls, H.; Henry, W.; Vos, J. G. *Angew. Chem., Int. Ed.* **2006**, *45*, 6215.

(22) Wasylenko, D. J.; Palmer, R. D.; Berlinguette, C. P. *Chem. Commun.* **2013**, *49*, 218.

(23) Duan, L.; Bozoglian, F.; Mandal, S.; Stewart, B.; Privalov, T.; Llobet, A.; Sun, L. *Nat. Chem.* **2012**, *4*, 418.

(24) Kohler, L.; Kaveevivitchai, N.; Zong, R.; Thummel, R. P. *Inorg. Chem.* **2014**, *53*, 912.

(25) Han, Z.; McNamara, W. R.; Eum, M.-S.; Holland, P. L.; Eisenberg, R. *Angew. Chem., Int. Ed.* **2012**, *51*, 1667.

(26) Lehn, J. M.; Sauvage, J. P. *Nouv. J. Chim.* **1977**, *1*, 449.

(27) Brown, G. M.; Brunschwig, B. S.; Creutz, C.; Endicott, J. F.; Sutin, N. *J. Am. Chem. Soc.* **1979**, *101*, 1298.

(28) Artero, V.; Chavarot-Kerlidou, M.; Fontecave, M. *Angew. Chem., Int. Ed.* **2011**, *50*, 7238.

(29) Singh Bindra, G.; Schulz, M.; Paul, A.; Soman, S.; Groarke, R.; Inglis, J.; Pryce, M. T.; Browne, W. R.; Rau, S.; MacLean, B. J.; Vos, J. G. *Dalton Trans.* **2011**, *40*, 10812.

(30) Lei, P.; Hedlund, M.; Lomoth, R.; Rensmo, H.; Johansson, O.; Hammarstroem, L. *J. Am. Chem. Soc.* **2008**, *130*, 26.

(31) Li, C.; Wang, M.; Pan, J.; Zhang, P.; Zhang, R.; Sun, L. *J. Organomet. Chem.* **2009**, *694*, 2814.

(32) Ott, S.; Kritikos, M.; Akermark, B.; Sun, L. *Angew. Chem., Int. Ed.* **2003**, *42*, 3285.

(33) Masaoka, S.; Mukawa, Y.; Sakai, K. *Dalton Trans.* **2010**, *39*, 5868.

(34) Mulfort, K. L.; Tiede, D. M. *J. Phys. Chem. B* **2010**, *114*, 14572.

(35) Arachchige, S. M.; Brown, J. R.; Chang, E.; Jain, A.; Zigler, D. F.; Rangan, K.; Brewer, K. J. *Inorg. Chem.* **2009**, *48*, 1989.

(36) Fihri, A.; Artero, V.; Pereira, A.; Fontecave, M. *Dalton Trans.* **2008**, 5567.

(37) Probst, B.; Rodenberg, A.; Guttentag, M.; Hamm, P.; Alberto, R. *Inorg. Chem.* **2010**, *49*, 6453.

(38) Zhang, P.; Wang, M.; Li, C.; Li, X.; Dong, J.; Sun, L. *Chem. Commun.* **2010**, *46*, 8806.

(39) Peuntinger, K.; Lazarides, T.; Dafnomili, D.; Charalambidis, G.; Landrou, G.; Kahnt, A.; Sabatini, R. P.; McCamant, D. W.; Gryko, D. T.; Coutsolelos, A. G.; Guldi, D. M. *J. Phys. Chem. C* **2013**, *117*, 1647.

(40) Kobayashi, M.; Masaoka, S.; Sakai, K. *Angew. Chem., Int. Ed.* **2012**, *51*, 7431.

(41) Sakai, K.; Ozawa, H. *Coord. Chem. Rev.* **2007**, *251*, 2753.

(42) Ozawa, H.; Haga, M.; Sakai, K. *J. Am. Chem. Soc.* **2006**, *128*, 4926.

(43) You, Y.; Nam, W. *Chem. Soc. Rev.* **2012**, *41*, 7061.

(44) Valeur, B. In *Molecular Fluorescence*; Wiley-VCH Verlag GmbH: **2001**, 381.

(45) Kasha, M. *Discuss. Faraday Soc.* **1950**, *No. 9*, 14.

(46) Wilemski, G.; Fixman, M. *J. Chem. Phys.* **1973**, *58*, 4009.

(47) Collins, F. C. *J. Colloid Sci.* **1950**, *5*, 499.

(48) Collins, F. C.; Kimball, G. E. *J. Colloid Sci.* **1949**, *4*, 425.

(49) Stern, O.; Volmer, M. *Phys. Z.* **1919**, *20*, 183.

(50) Rehm, D.; Weller, A. *Ber. Bunsenges. Phys. Chem.* **1969**, *73*, 834.

(51) Ladouceur, S.; Zysman-Colman, E. *Eur. J. Inorg. Chem.* **2013**, *2013*, 2985.

(52) Yang, C.-H.; Cheng, Y.-M.; Chi, Y.; Hsu, C.-J.; Fang, F.-C.; Wong, K.-T.; Chou, P.-T.; Chang, C.-H.; Tsai, M.-H.; Wu, C.-C. *Angew. Chem., Int. Ed.* **2007**, *46*, 2418.

(53) You, Y.; Park, S. Y. *Dalton Trans.* **2009**, 1267.

(54) Tamayo, A. B.; Garon, S.; Sajoto, T.; Djurovich, P. I.; Tsyba, I. M.; Bau, R.; Thompson, M. E. *Inorg. Chem.* **2005**, *44*, 8723.

(55) Yu, M.; Zhao, Q.; Shi, L.; Li, F.; Zhou, Z.; Yang, H.; Yi, T.; Huang, C. *Chem. Commun.* **2008**, 2115.

(56) Lo, K. K.-W.; Louie, M.-W.; Zhang, K. Y. *Coord. Chem. Rev.* **2010**, *254*, 2603.

(57) Lo, K. K.-W.; Zhang, K. Y. *RSC Adv.* **2012**, *2*, 12069.

(58) Shiu, H.-Y.; Chong, H.-C.; Leung, Y.-C.; Zou, T.; Che, C.-M. *Chem. Commun.* **2014**, *50*, 4375.

(59) Bae, H. J.; Kim, H.; Lee, K. M.; Kim, T.; Eo, M.; Lee, Y. S.; Do, Y.; Lee, M. H. *Dalton Trans.* **2013**, *42*, 8549.

(60) Lu, F.; Yamamura, M.; Nabeshima, T. *Dalton Trans.* **2013**, *42*, 12093.

(61) Chirdon, D. N.; McCusker, C. E.; Castellano, F. N.; Bernhard, S. *Inorg Chem* **2013**, *52*, 8795.

(62) Omae, I. *Coord. Chem. Rev.* **2015**, Ahead of Print.

(63) Yoshihara, T.; Hosaka, M.; Terata, M.; Ichikawa, K.; Murayama, S.; Tanaka, A.; Mori, M.; Itabashi, H.; Takeuchi, T.; Tobita, S. *Anal. Chem.* **2015**, *87*, 2710.

(64) Yoshihara, T.; Yamaguchi, Y.; Hosaka, M.; Takeuchi, T.; Tobita, S. *Angew. Chem., Int. Ed.* **2012**, *51*, 4148.

(65) Lowry, M. S.; Bernhard, S. *Chem. - Eur. J.* **2006**, *12*, 7970.

(66) Flamigni, L.; Collin, J.-P.; Sauvage, J.-P. *Acc. Chem. Res.* **2008**, *41*, 857.

(67) Balzani, V.; Editor *NATO Advanced Science Institutes Series: Series C: Mathematical and Physical Sciences, Vol. 214: Supramolecular Photochemistry. [Proceedings of the NATO Advanced Workshop Held in Anacapri, Italy, April 5-10, 1987]*; D. Reidel Publ. Co., **1987**.

(68) Meyer, T. J. *Pure Appl. Chem.* **1986**, *58*, 1193.

(69) Flamigni, L.; Barbieri, A.; Sabatini, C.; Ventura, B.; Barigelletti, F. *Top. Curr. Chem.* **2007**, *281*, 143.

(70) Mamo, A.; Stefio, I.; Parisi, M. F.; Credi, A.; Venturi, M.; Di Pietro, C.; Campagna, S. *Inorg. Chem.* **1997**, *36*, 5947.

(71) Tamayo, A. B.; Alleyne, B. D.; Djurovich, P. I.; Lamansky, S.; Tsyba, I.; Ho, N. N.; Bau, R.; Thompson, M. E. *J. Am. Chem. Soc.* **2003**, *125*, 7377.

(72) Ayala, N. P.; Flynn, C. M., Jr.; Sacksteder, L.; Demas, J. N.; DeGraff, B. A. *J. Am. Chem. Soc.* **1990**, *112*, 3837.

(73) Collin, J.-P.; Dixon, I. M.; Sauvage, J.-P.; Williams, J. A. G.; Barigelletti, F.; Flamigni, L. *J. Am. Chem. Soc.* **1999**, *121*, 5009.

(74) Kahl, J. L.; Hanck, K. W.; DeArmond, K. *J. Phys. Chem.* **1978**, *82*, 540.

(75) Cerfontaine S., Mémoire, Université catholique de Louvain, **2014**.

(76) Wang, J.; Hanan, G. S. *Synlett* **2005**, 1251.

(77) Winter, A.; van den Berg, A. M. J.; Hoogenboom, R.; Kickelbick, G.; Schubert, U. S. *Synthesis* **2006**, 2873.

(78) Voisin, E.; Maris, T.; Wuest, J. D. *Cryst. Growth Des.* **2008**, *8*, 308.

(79) Kameta, N.; Hiratani, K. *Chem. Commun.* **2005**, 725.

(80) Abrahams, B. F.; Price, D. J.; Robson, R. *Angew. Chem., Int. Ed.* **2006**, *45*, 806.

(81) Katagiri, H.; Miyagawa, T.; Furusho, Y.; Yashima, E. *Angew. Chem., Int. Ed.* **2006**, *45*, 1741.

(82) Danjo, H.; Hirata, K.; Yoshigai, S.; Azumaya, I.; Yamaguchi, K. *J. Am. Chem. Soc.* **2009**, *131*, 1638.

(83) IUPAC. Compendium of Chemical Terminology, 2nd ed. (the "Gold Book"). Compiled by A.D. McNaught and A. Wilkinson, Blackwell Scientific Publications, Oxford, UK (1997). (b) XML on-line corrected version: http://goldbook.iupac.org (2006-) created by M. Nic, J. Jirat, and B. Kosata; updates compiled by A.D. Jenkins.

(84) Joseph, R.; Nkrumah, A.; Clark, R. J.; Masson, E. *J. Am. Chem. Soc.* **2014**, *136*, 6602.

(85) Mock, W. L.; Shih, N. Y. *J. Org. Chem.* **1986**, *51*, 4440.

(86) Biedermann, F.; Uzunova, V. D.; Scherman, O. A.; Nau, W. M.; De Simone, A. *J. Am. Chem. Soc.* **2012**, *134*, 15318.

(87) Florea, M.; Nau, W. M. *Angew. Chem., Int. Ed.* **2011**, *50*, 9338.

(88) Moghaddam, S.; Yang, C.; Rekharsky, M.; Ko, Y. H.; Kim, K.; Inoue, Y.; Gilson, M. K. *J. Am. Chem. Soc.* **2011**, *133*, 3570.

(89) Rekharsky, M. V.; Mori, T.; Yang, C.; Ko, Y. H.; Selvapalam, N.; Kim, H.; Sobransingh, D.; Kaifer, A. E.; Liu, S.; Isaacs, L.; Chen, W.; Moghaddam, S.; Gilson, M. K.; Kim, K.; Inoue, Y. *Proc. Natl. Acad. Sci. U. S. A.* **2007**, *104*, 20737.

(90) Niemeyer, C. M.; Editor *Bioconjugation Protocols: Strategies and Methods. [In: Methods Mol. Biol. (Totowa, NJ. U.S.); 283]*; Humana Press Inc., **2004**.

(91) Willner, I.; Katz, E.; Editors *Bioelectronics: From Theory to Applications*; Wiley-VCH Verlag GmbH & Co. KGaA, **2005**.

(92) Peterson, J. R.; Smith, T. A.; Thordarson, P. *Org. Biomol. Chem.* **2010**, *8*, 151.

(93) Hvasanov, D.; Mason, A. F.; Goldstein, D. C.; Bhadbhade, M.; Thordarson, P. *Org. Biomol. Chem.* **2013**, *11*, 4602.

(94) Peterson, J. R.; Smith, T. A.; Thordarson, P. *Chem. Commun.* **2007**, 1899.

(95) Leslie, W.; Batsanov, A. S.; Howard, J. A. K.; Williams, J. A. G. *Dalton Trans.* **2004**, 623.

(96) Dixon, I. M.; Collin, J.-P.; Sauvage, J.-P.; Barigelletti, F.; Flamigni, L. *Angew. Chem., Int. Ed.* **2000**, *39*, 1292.

(97) Dixon, I. M.; Collin, J.-P.; Sauvage, J.-P.; Flamigni, L. *Inorg. Chem.* **2001**, *40*, 5507.

(98) Shinpuku, Y.; Inui, F.; Nakai, M.; Nakabayashi, Y. *J. Photochem. Photobiol., A* **2011**, *222*, 203.

(99) Wilkinson, A. J.; Puschmann, H.; Howard, J. A. K.; Foster, C. E.; Williams, J. A. G. *Inorg. Chem.* **2006**, *45*, 8685.

(100) Polson, M.; Ravaglia, M.; Fracasso, S.; Garavelli, M.; Scandola, F. *Inorg. Chem.* **2005**, *44*, 1282.

(101) Polson, M.; Fracasso, S.; Bertolasi, V.; Ravaglia, M.; Scandola, F. *Inorg. Chem.* **2004**, *43*, 1950.

(102) Cave, G. W. V.; Raston, C. L. *J. Chem. Soc., Perkin Trans. 1* **2001**, 3258.

(103) Garces, F. O.; King, K. A.; Watts, R. J. *Inorg. Chem.* **1988**, *27*, 3464.

(104) Lamansky, S.; Djurovich, P.; Murphy, D.; Abdel-Razzaq, F.; Lee, H.-E.; Adachi, C.; Burrows, P. E.; Forrest, S. R.; Thompson, M. E. *J. Am. Chem. Soc.* **2001**, *123*, 4304.

(105) Nazeeruddin, M. K.; Kay, A.; Rodicio, I.; Humphry-Baker, R.; Mueller, E.; Liska, P.; Vlachopoulos, N.; Graetzel, M. *J. Am. Chem. Soc.* **1993**, *115*, 6382.

(106) Katoh, R.; Furube, A.; Barzykin, A. V.; Arakawa, H.; Tachiya, M. *Coord. Chem. Rev.* **2004**, *248*, 1195.

(107) Nazeeruddin, M. K.; Klein, C.; Liska, P.; Graetzel, M. *Coord. Chem. Rev.* **2005**, *249*, 1460.

(108) Gratzel, M. *Nature* **2001**, *414*, 338.

(109) Ning, Z.; Zhang, Q.; Wu, W.; Tian, H. *J. Organomet. Chem.* **2009**, *694*, 2705.

(110) Mayo, E. I.; Kilsa, K.; Tirrell, T.; Djurovich, P. I.; Tamayo, A.; Thompson, M. E.; Lewis, N. S.; Gray, H. B. *Photochem. Photobiol. Sci.* **2006**, *5*, 871.

(111) Balzani, V.; Bergamini, G.; Campagna, S.; Puntoriero, F. *Top. Curr. Chem.* **2007**, *280*, 1.

(112) Wilkinson, A. J.; Goeta, A. E.; Foster, C. E.; Williams, J. A. G. *Inorg. Chem.* **2004**, *43*, 6513.

(113) Freeman, G. R.; Williams, J. A. G. *Top. Organomet. Chem.* **2013**, *40*, 89.

(114) Collin, J. P.; Guillerez, S.; Sauvage, J. P.; Barigelletti, F.; De Cola, L.; Flamigni, L.; Balzani, V. *Inorg. Chem.* **1991**, *30*, 4230.

(115) Carell, T.; Behrens, C.; Gierlich, J. *Org. Biomol. Chem.* **2003**, *1*, 2221.

(116) O'Neill, M. A.; Barton, J. K. *Top. Curr. Chem.* **2004**, *236*, 67.

(117) Genereux, J. C.; Barton, J. K. *Chem. Rev.* **2010**, *110*, 1642.

(118) Indelli, M. T.; Bura, T.; Ziessel, R. *Inorg. Chem.* **2013**, *52*, 2918.

(119) Cavazzini, M.; Quici, S.; Scalera, C.; Puntoriero, F.; La Ganga, G.; Campagna, S. *Inorg. Chem.* **2009**, *48*, 8578.

(120) Hankache, J.; Niemi, M.; Lemmetyinen, H.; Wenger, O. S. *Inorg. Chem.* **2012**, *51*, 6333.

(121) Lambert, C.; Wagener, R.; Klein, J. H.; Grelaud, G.; Moos, M.; Schmiedel, A.; Holzapfel, M.; Bruhn, T. *Chem. Commun.* **2014**, *50*, 11350.

(122) Pal, A. K.; Nag, S.; Ferreira, J. G.; Brochery, V.; La Ganga, G.; Santoro, A.; Serroni, S.; Campagna, S.; Hanan, G. S. *Inorg. Chem.* **2014**, *53*, 1679.

(123) Nag, S.; Ferreira, J. G.; Chenneberg, L.; Ducharme, P. D.; Hanan, G. S.; La Ganga, G.; Serroni, S.; Campagna, S. *Inorg. Chem.* **2011**, *50*, 7.

(124) Pal, A. K.; Hanan, G. S. *Dalton Trans.* **2014**, *43*, 6567.

(125) Pal, A. K.; Serroni, S.; Zaccheroni, N.; Campagna, S.; Hanan, G. S. *Chem. Sci.* **2014**, *5*, 4800.

(126) Pal, A. K.; Zaccheroni, N.; Campagna, S.; Hanan, G. S. *Chem. Commun.* **2014**, *50*, 6846.

(127) Pal, A. K.; Ducharme, P. D.; Hanan, G. S. *Chem. Commun.* **2014**, *50*, 3303.

(128) Pal, A. K.; Hanan, G. S. *Dalton Trans.* **2014**, *43*, 11811.

(129) Hasan, K.; Pal, A. K.; Auvray. T. Zysman-Colman, E.; Hanan, G. S. *Chem. Commun*., **2015**, *submitted for publication*.

(130) Nguyen, J. D.; D'Amato, E. M.; Narayanam, J. M. R.; Stephenson, C. R. J. *Nat. Chem.* **2012**, *4*, 854.

(131) Terrett, J. A.; Clift, M. D.; MacMillan, D. W. C. *J. Am. Chem. Soc.* **2014**, *136*, 6858.

(132) Tinker, L. L.; Bernhard, S. *Inorg. Chem.* **2009**, *48*, 10507.

(133) Gennari, M.; Legalite, F.; Zhang, L.; Pellegrin, Y.; Blart, E.; Fortage, J.; Brown, A. M.; Deronzier, A.; Collomb, M.-N.; Boujtita, M.; Jacquemin, D.; Hammarstrom, L.; Odobel, F. *J. Phys. Chem. Lett.* **2014**, *5*, 2254.

(134) Lowry, M. S.; Hudson, W. R.; Pascal, R. A., Jr.; Bernhard, S. *J. Am. Chem. Soc.* **2004**, *126*, 14129.

(135) Elias, B.; Genereux, J. C.; Barton, J. K. *Angew. Chem., Int. Ed.* **2008**, *47*, 9067.

(136) Lo, K. K.-W.; Li, S. P.-Y.; Zhang, K. Y. *New J. Chem.* **2011**, *35*, 265.

(137) Auffrant, A.; Barbieri, A.; Barigelletti, F.; Collin, J.-P.; Flamigni, L.; Sabatini, C.; Sauvage, J.-P. *Inorg. Chem.* **2006**, *45*, 10990.

(138) Pal, A. K.; Hanan, G. S. *Chem. Soc. Rev.* **2014**, *43*, 6184.

(139) Kobayashi, M.; Masaoka, S.; Sakai, K. *Dalton Trans.* **2012**, *41*, 4903.

(140) Juris, A.; Balzani, V.; Barigelletti, F.; Campagna, S.; Belser, P.; Von Zelewsky, A. *Coord. Chem. Rev.* **1988**, *84*, 85.

(141) The oxygen effect on this excited state lifetime is usual for Ir cyclometalated complexes, as well as the rather high radiative rate constant calculated from the emission quantum yield and excited state lifetime under argon.

(142) Miehlich, B.; Savin, A.; Stoll, H.; Preuss, H. *Chem. Phys. Lett.* **1989**, *157*, 200.

(143) Lee, C.; Yang, W.; Parr, R. G. *Phys. Rev. B: Condens. Matter* **1988**, *37*, 785.

(144) Becke, A. D. *J. Chem. Phys.* **1993**, *98*, 5648.

(145) Rassolov, V. A.; Pople, J. A.; Ratner, M. A.; Windus, T. L. *J. Chem. Phys.* **1998**, *109*, 1223.

(146) Cundari, T. R.; Stevens, W. J. *J. Chem. Phys.* **1993**, *98*, 5555.

(147) Stevens, W. J.; Krauss, M.; Basch, H.; Jasien, P. G. *Can. J. Chem.* **1992**, *70*, 612.

(148) Binkley, J. S.; Pople, J. A.; Hehre, W. J. *J. Am. Chem. Soc.* **1980**, *102*, 939.

(149) Kuett, A.; Leito, I.; Kaljurand, I.; Soovaeli, L.; Vlasov, V. M.; Yagupolskii, L. M.; Koppel, I. A. *J. Org. Chem.* **2006**, *71*, 2829.

(150) Izutsu, K. *Acid-Base Dissociation Constants in Dipolar Aprotic Solvents*; Blackwell Scientific Publ., **1990**.

(151) It has been checked that no emission after protonation could be detected in a longer wavelength region of the spectrum, as observed with some Ru(II) complexes.

(152) Herman, L.; Elias, B.; Pierard, F.; Moucheron, C.; Kirsch-De Mesmaeker, A. *J. Phys. Chem. A* **2007**, *111*, 9756.

(153) Benesi, H. A.; Hildebrand, J. H. *J. Am. Chem. Soc.* **1949**, *71*, 2703.

(154) Whittle, V. L.; Williams, J. A. G. *Dalton Trans.* **2009**, 3929.

(155) Williams, J. A. G.; Wilkinson, A. J.; Whittle, V. L. *Dalton Trans.* **2008**, 2081.

(156) Weiss, M. *J. Am. Chem. Soc.* **1952**, *74*, 200.

(157) Adib, M.; Tahermansouri, H.; Koloogani, S. A.; Mohammadi, B.; Bijanzadeh, H. R. *Tet. Lett.* **2006**, *47*, 5957.

(158) Gaussian 09, Revision D.01, Frisch, M. J.; Trucks, G. W.; Schlegel, H. B.; Scuseria, . E.; Robb, M. A.; Cheeseman, J. R.; Scalmani, G.; Barone, V.; Mennucci, B.; Petersson, G. A.; Nakatsuji, H.; Caricato, M.; Li, X.; Hratchian, H. P.; Izmaylov, A. F.; Bloino, J.; Zheng, G.; Sonnenberg, J. L.; Hada, M.; Ehara, M.; Toyota, K.; Fukuda, R.; Hasegawa, J.; Ishida, M.; Nakajima, T.; Honda, Y.; Kitao, O.; Nakai, H.; Vreven, T.; Montgomery, J. A., Jr.; Peralta, J. E.; Ogliaro, F.; Bearpark, M.; Heyd, J. J.; Brothers, E.; Kudin, K. N.; Staroverov, V. N.; Kobayashi, R.; Normand, J.; Raghavachari, K.; Rendell, A.; Burant, J. C.; Iyengar, S. S.; Tomasi, J.; Cossi, M.; Rega, N.; Millam, J. M.; Klene, M.; Knox, J. E.; Cross, J. B.; Bakken, V.; Adamo, C.; Jaramillo, J.; Gomperts, R.; Stratmann, R. E.; Yazyev, O.; Austin, A. J.; Cammi, R.; Pomelli, C.; Ochterski, J. W.; Martin, R. L.; Morokuma, K.; Zakrzewski, V. G.; Voth, G. A.; Salvador, P.; Dannenberg, J. J.; Dapprich,

S.; Daniels, A. D.; Farkas, Ö.; Foresman, J. B.; Ortiz, J. V.; Cioslowski, J.; Fox, D. J. Gaussian, Inc., Wallingford CT, **2009**.

(159) Hohenberg P., Kohn W., Phys. Rev. B 1964, 136, 864.

(160) Parr, R. G.; Yang, W. *Density-functional Theory of Atoms and Molecules*; Clarendon Press, **1989**.

(161) Salahub, D. R.; Zerner, M. C.; Editors *ACS Symposium Series 394: The Challenge of d and f Electrons: Theory and Computation. Developed from a Symposium at the 3rd Chemical Congress of North America Toronto, Can., June 5-11, 1988*; American Chemical Society, **1989**.

(162) Casida, M. E.; Jamorski, C.; Casida, K. C.; Salahub, D. R. *J. Chem. Phys.* **1998**, *108*, 4439.

(163) Bauernschmitt, R.; Ahlrichs, R. *Chem. Phys. Lett.* **1996**, *256*, 454.

(164) Stratmann, R. E.; Scuseria, G. E.; Frisch, M. J. *J. Chem. Phys.* **1998**, *109*, 8218.

(165) Dennington R. D. K. II, Keith T., Millam J., Eppinnett K., Hovell W. L., Gilliland R., GaussView 3.09, Semichem, Inc., Shawnee Mission, KS, **2003**.

(166) O'Boyle, N. M.; Tenderholt, A. L.; Langner, K. M. *J. Comput. Chem.* **2008**, *29*, 839.

(167) Skripnikov L., Chemissian, V4.33, 2005–2014.

(168) Tomasi, J.; Mennucci, B.; Cammi, R. *Chem. Rev.* **2005**, *105*, 2999.

(169) Miertus, S.; Scrocco, E.; Tomasi, J. *Chem. Phys.* **1981**, *55*, 117.

(170) Du, P.; Knowles, K.; Eisenberg, R. *J. Am. Chem. Soc.* **2008**, *130*, 12576.

(171) Jarosz, P.; Du, P.; Schneider, J.; Lee, S.-H.; McCamant, D.; Eisenberg, R. *Inorg. Chem.* **2009**, *48*, 9653.

(172) Bronner, C.; Veiga, M.; Guenet, A.; De Cola, L.; Hosseini, M. W.; Strassert, C. A.; Baudron, S. A. *Chem. - Eur. J.* **2012**, *18*, 4041.

(173) Soliman, A. M.; Fortin, D.; Harvey, P. D.; Zysman-Colman, E. *Chem. Commun.* **2012**, *48*, 1120.

(174) Dempsey, J. L.; Brunschwig, B. S.; Winkler, J. R.; Gray, H. B. *Acc. Chem. Res.* **2009**, *42*, 1995.

(175) Khnayzer, R. S.; McCusker, C. E.; Olaiya, B. S.; Castellano, F. N. *J. Am. Chem. Soc.* **2013**, *135*, 14068.

(176) Eckenhoff, W. T.; McNamara, W. R.; Du, P.; Eisenberg, R. *Biochim. Biophys. Acta, Bioenerg.* **2013**, *1827*, 958.

(177) Hu, X. L.; Brunschwig, B. S.; Peters, J. C. *J. Am. Chem. Soc.* **2007**, *129*, 8988.

(178) Razavet, M.; Artero, V.; Fontecave, M. *Inorg. Chem.* **2005**, *44*, 4786.

(179) Schrauzer, G. N. *Accounts Chem. Res.* **1968**, *1*, 97.

(180) Fihri, A.; Artero, V.; Razavet, M.; Baffert, C.; Leibl, W.; Fontecave, M. *Angew. Chem., Int. Ed.* **2008**, *47*, 564.

(181) Kirch, M.; Lehn, J. M.; Sauvage, J. P. *Helv. Chim. Acta* **1979**, *62*, 1345.

(182) Chan, S. F.; Chou, M.; Creutz, C.; Matsubara, T.; Sutin, N. *J. Am. Chem. Soc.* **1981**, *103*, 369.

(183) Balzani, V.; Credi, A.; Venturi, M. *ChemSusChem* **2008**, *1*, 26.

(184) Kalyanasundaram, K. *Coord. Chem. Rev.* **1982**, *46*, 159.

(185) Graetzel, C. K.; Graetzel, M. *J. Am. Chem. Soc.* **1979**, *101*, 7741.

(186) Amouyal, E. *Sol. Energy Mater. Sol. Cells* **1995**, *38*, 249.

(187) Creutz, C.; Schwarz, H. A.; Sutin, N. *J. Am. Chem. Soc.* **1984**, *106*, 3036.

(188) Lehn, J. M.; Sauvage, J. P.; Simon, J.; Ziessel, R.; Piccinni-Leopardi, C.; Germain, G.; Declercq, J. P.; Van Meerssche, M. *Nouv. J. Chim.* **1983**, *7*, 413.

(189) Krishnan, C. V.; Brunschwig, B. S.; Creutz, C.; Sutin, N. *J. Am. Chem. Soc.* **1985**, *107*, 2005.

(190) Probst, B.; Kolano, C.; Hamm, P.; Alberto, R. *Inorg. Chem.* **2009**, *48*, 1836.

(191) Probst, B.; Guttentag, M.; Rodenberg, A.; Hamm, P.; Alberto, R. *Inorg. Chem.* **2011**, *50*, 3404.

(192) Guttentag, M.; Rodenberg, A.; Kopelent, R.; Probst, B.; Buchwalder, C.; Brandstaetter, M.; Hamm, P.; Alberto, R. *Eur. J. Inorg. Chem.* **2012**, *2012*, 59.

(193) Jasimuddin, S.; Yamada, T.; Fukuju, K.; Otsuki, J.; Sakai, K. *Chem. Commun.* **2010**, *46*, 8466.

(194) Wong, M. Y.; Xie, G.; Tourbillon, C.; Sandroni, M.; Cordes, D. B.; Slawin, A. M. Z.; Samuel, I. D. W.; Zysman-Colman, E. *Dalton Trans.* **2015**, *44*, 8419.

(195) Shavaleev, N. M.; Xie, G.; Varghese, S.; Cordes, D. B.; Slawin, A. M. Z.; Momblona, C.; Orti, E.; Bolink, H. J.; Samuel, I. D. W.; Zysman-Colman, E. *Inorg. Chem.* **2015**, *54*, 5907.

(196) Hasan, K.; Donato, L.; Shen, Y.; D. Slinker, J.; Zysman-Colman, E. *Dalton Trans.* **2014**, *43*, 13672.

(197) DiSalle, B. F.; Bernhard, S. *J. Am. Chem. Soc.* **2011**, *133*, 11819.

(198) Kagalwala, H. N.; Gottlieb, E.; Li, G.; Li, T.; Jin, R.; Bernhard, S. *Inorg. Chem.* **2013**, *52*, 9094.

(199) Mills, I. N.; Kagalwala, H. N.; Chirdon, D. N.; Brooks, A. C.; Bernhard, S. *Polyhedron* **2014**, *82*, 104.

(200) Chirdon, D. N.; Transue, W. J.; Kagalwala, H. N.; Kaur, A.; Maurer, A. B.; Pintauer, T.; Bernhard, S. *Inorg. Chem.* **2014**, *53*, 1487.

(201) Lalrempuia, R.; McDaniel, N. D.; Mueller-Bunz, H.; Bernhard, S.; Albrecht, M. *Angew. Chem., Int. Ed.* **2010**, *49*, 9765.

(202) Ladouceur, S.; Fortin, D.; Zysman-Colman, E. *Inorg. Chem.* **2011**, *50*, 11514.

(203) Swanick, K. N.; Ladouceur, S.; Zysman-Colman, E.; Ding, Z. *RSC Adv.* **2013**, *3*, 19961.

(204) A. Jacques, T. Auvray, M. Cibian, G. S. Hanan, A. Kirsch–De Mesmaeker, B. Elias, *Inorg. Chem.*, **2015**, submitted for publication.

(205) Geremia, S.; Dreos, R.; Randaccio, L.; Tauzher, G.; Antolini, L. *Inorg. Chim. Acta* **1994**, *216*, 125.

(206) Lopez, C.; Alvarez, S.; Solans, X.; Font-Altaba, M. *Inorg. Chem.* **1986**, *25*, 2962.

(207) Zhang, P.; Jacques, P.-A.; Chavarot-Kerlidou, M.; Wang, M.; Sun, L.; Fontecave, M.; Artero, V. *Inorg. Chem.* **2012**, *51*, 2115.

(208) Rousset, E.; Chartrand, D.; Ciofini, I.; Marvaud, V.; Hanan, G. S. *Chem. Commun.* **2015**, *51*, 9261.

(209) Trogler, W. C.; Stewart, R. C.; Epps, L. A.; Marzilli, L. G. *Inorg. Chem.* **1974**, *13*, 1564.

(210) Bakac, A.; Espenson, J. H. *J. Am. Chem. Soc.* **1984**, *106*, 5197.

(211) Porath, D.; Cuniberti, G.; di Felice, R. *Top. Curr. Chem.* **2004**, *237*, 183.

(212) Sontz, P. A.; Muren, N. B.; Barton, J. K. *Acc. Chem. Res.* **2012**, *45*, 1792.

(213) Merino, E. J.; Boal, A. K.; Barton, J. K. *Curr. Opin. Chem. Biol.* **2008**, *12*, 229.

(214) Kelley, S. O.; Jackson, N. M.; Hill, M. G.; Barton, J. K. *Angew. Chem., Int. Ed.* **1999**, *38*, 941.

(215) Slinker, J. D.; Muren, N. B.; Renfrew, S. E.; Barton, J. K. *Nat. Chem.* **2011**, *3*, 228.

(216) Clever, G. H.; Kaul, C.; Carell, T. *Angew. Chem., Int. Ed.* **2007**, *46*, 6226.

(217) Wang, X.; Ozkan, C. S. *Nano Lett.* **2008**, *8*, 398.

(218) Bandyopadhyay, A.; Ray, A. K.; Sharma, A. K.; Khondaker, S. I. *Nanotechnology* **2006**, *17*, 227.

(219) Erkkila, K. E.; Odom, D. T.; Barton, J. K. *Chem. Rev.* **1999**, *99*, 2777.

(220) Metcalfe, C.; Thomas, J. A. *Chem. Soc. Rev.* **2003**, *32*, 215.

(221) Wagner, C.; Wagenknecht, H.-A. *Chem. - Eur. J.* **2005**, *11*, 1871.

(222) Fazio, D.; Trindler, C.; Heil, K.; Chatgilialoglu, C.; Carell, T. *Chem. - Eur. J.* **2011**, *17*, 206.

(223) Ito, T.; Rokita, S. E. *Angew. Chem., Int. Ed.* **2004**, *43*, 1839.

(224) Lewis, F. D.; Liu, X.; Miller, S. E.; Hayes, R. T.; Wasielewski, M. R. *J. Am. Chem. Soc.* **2002**, *124*, 11280.

(225) Shao, F.; Elias, B.; Lu, W.; Barton, J. K. *Inorg. Chem.* **2007**, *46*, 10187.

(226) Gasser, G.; Ott, I.; Metzler-Nolte, N. *J. Med. Chem.* **2011**, *54*, 3.

(227) Le Gac, S.; Rickling, S.; Gerbaux, P.; Defrancq, E.; Moucheron, C.; Kirsch-De Mesmaeker, A. *Angew. Chem., Int. Ed.* **2009**, *48*, 1122.

(228) Gianferrara, T.; Bratsos, I.; Alessio, E. *Dalton Trans.* **2009**, 7588.

(229) McKinley, A. W.; Lincoln, P.; Tuite, E. M. *Coord. Chem. Rev.* **2011**, *255*, 2676.

(230) Elias, B.; Kirsch-De Mesmaeker, A. *Coord. Chem. Rev.* **2006**, *250*, 1627.

(231) Moucheron, C. *New J. Chem.* **2009**, *33*, 235.

(232) Smith, J. A.; George, M. W.; Kelly, J. M. *Coord. Chem. Rev.* **2011**, *255*, 2666.

(233) Dixon, I. M.; Collin, J.-P.; Sauvage, J.-P.; Flamigni, L.; Encinas, S.; Barigelletti, F. *Chem. Soc. Rev.* **2000**, *29*, 385.

(234) Baranoff, E.; Collin, J.-P.; Flamigni, L.; Sauvage, J.-P. *Chem. Soc. Rev.* **2004**, *33*, 147.

(235) Zhao, Q.; Liu, S.; Shi, M.; Li, F.; Jing, H.; Yi, T.; Huang, C. *Organometallics* **2007**, *26*, 5922.

(236) Shao, F.; Barton, J. K. *J. Am. Chem. Soc.* **2007**, *129*, 14733.

(237) Campagna, S.; Cavazzini, M.; Cusumano, M.; Di Pietro, M. L.; Giannetto, A.; Puntoriero, F.; Quici, S. *Inorg. Chem.* **2011**, *50*, 10667.

(238) ΔG_{ET} = E_{ox} deoxynucleobase - E_{red}* where E_{ox} deoxynucleobase is the oxidation potential of selected deoxynucleobase and E_{red}* is the reduction potential of $[IrN_6]^{3+}$ and $[IrN_4C_2]^{+}$ in their excited state. Therefore, we have obtained ΔG_{ET} = 1.10 - 1.38 = -0.28 eV and ΔG_{ET} = 1.10 - 1.12 = -0.02 eV respectively for $[IrN_6]^{3+}$ and $[IrN_4C_2]^{+}$.

(239) Wong, A.; Ida, R.; Spindler, L.; Wu, G. *J. Am. Chem. Soc.* **2005**, *127*, 6990.

(240) The low solubility of $[IrN_4C_2]^{+}$ prevents its dissolution it in pure aqueous TRIS buffer. Therefore, 10% of acetonitrile have been added to the buffer in order to have complete dissolution of the complex.

(241) Ortmans, I.; Elias, B.; Kelly, J. M.; Moucheron, C.; Kirsch-DeMesmaeker, A. *Dalton Trans.* **2004**, 668.

(242) Steenken, S.; Jovanovic, S. V. *J. Am. Chem. Soc.* **1997**, *119*, 617.

(243) Htun, T. *J. Fluoresc.* **2004**, *14*, 217.

(244) Goldstein, D. C.; Cheng, Y. Y.; Schmidt, T. W.; Bhadbhade, M.; Thordarson, P. *Dalton Trans.* **2011**, *40*, 2053.

(245) Felsenfeld, G.; Hirschman, S. Z. *J. Mol. Biol.* **1965**, *13*, 407.

(246) Inman, R. B.; Baldwin, R. L. *J. Mol. Biol.* **1962**, *5*, 185.

(247) Cui, T.; Wei, S.; Brew, K.; Leng, F. *J. Mol. Biol.* **2005**, *352*, 629.

(248) Wells, R. D.; Larson, J. E.; Grant, R. C.; Shortle, B. E.; Cantor, C. R. *J. Mol. Biol.* **1970**, *54*, 465.

(249) Jacques A., Mémoire, Université catholique de Louvain, **2011**.

(250) Esser, P.; Pohlmann, B.; Scharf, H.-D. *Angew. Chem.* **1994**, *106*, 2093.

(251) Bach, T.; Hehn, J. P. *Angew. Chem., Int. Ed.* **2011**, *50*, 1000.

(252) Hoffmann, N. *Chem. Rev.* **2008**, *108*, 1052.

(253) Schultz, D. M.; Yoon, T. P. *Science* **2014**, *343*, 985.

(254) Prier, C. K.; Rankic, D. A.; MacMillan, D. W. C. *Chem. Rev.* **2013**, *113*, 5322.

(255) Pirtsch, M.; Paria, S.; Matsuno, T.; Isobe, H.; Reiser, O. *Chem. - Eur. J.* **2012**, *18*, 7336.

(256) Revol, G.; McCallum, T.; Morin, M.; Gagosz, F.; Barriault, L. *Angew. Chem., Int. Ed.* **2013**, *52*, 13342.

(257) Huang, X.; Qi, X.; Boey, F.; Zhang, H. *Chem. Soc. Rev.* **2012**, *41*, 666.

(258) Georgakilas, V.; Otyepka, M.; Bourlinos, A. B.; Chandra, V.; Kim, N.; Kemp, K. C.; Hobza, P.; Zboril, R.; Kim, K. S. *Chem. Rev.* **2012**, *112*, 6156.

(259) Lee, C.; Wei, X.; Kysar, J. W.; Hone, J. *Science* **2008**, *321*, 385.

(260) Kumar, P.; Kumar, A.; Sreedhar, B.; Sain, B.; Ray, S. S.; Jain, S. L. *Chem. - Eur. J.* **2014**, *20*, 6154.

(261) Kumar, P.; Sain, B.; Jain, S. L. *J. Mater. Chem. A* **2014**, *2*, 11246.

(262) Barras, A.; Das, M. R.; Devarapalli, R. R.; Shelke, M. V.; Cordier, S.; Szunerits, S.; Boukherroub, R. *Appl. Catal., B* **2013**, *130-131*, 270.

(263) Barbante, G. J.; Ashton, T. D.; Doeven, E. H.; Pfeffer, F. M.; Wilson, D. J. D.; Henderson, L. C.; Francis, P. S. *ChemCatChem* **2015**, *7*, 1655.

(264) Tucker, J. W.; Nguyen, J. D.; Narayanam, J. M. R.; Krabbe, S. W.; Stephenson, C. R. J. *Chem. Commun.* **2010**, *46*, 4985.

(265) McMurtrie, J.; Dance, I. *CrystEngComm* **2005**, *7*, 216.

(266) Constable, E. C.; Dunphy, E. L.; Housecroft, C. E.; Neuburger, M.; Schaffner, S.; Schaper, F.; Batten, S. R. *Dalton Trans.* **2007**, 4323.

(267) Liu, Y.-L.; Chen, W.-H. *Macromolecules* **2007**, *40*, 8881.

(268) Xu, C.; Wang, X.; Wang, J.; Hu, H.; Wan, L. *Chem. Phys. Lett.* **2010**, *498*, 162.

(269) Vriamont, C.; Devillers, M.; Riant, O.; Hermans, S. *Chem. - Eur. J.* **2013**, *19*, 12009.

(270) Agilent Technologies, Xcalibur CCD system, CrysAlisPro Software system, Version 1.171.35.19.

(271) Sheldrick, G. M. *Acta Crystallogr., Sect. A: Found. Crystallogr.* **2008**, *64*, 112.

(272) Macrae, C. F.; Bruno, I. J.; Chisholm, J. A.; Edgington, P. R.; McCabe, P.; Pidcock, E.; Rodriguez-Monge, L.; Taylor, R.; van de Streek, J.; Wood, P. A. *J. Appl. Crystallogr.* **2008**, *41*, 466.

(273) Stubbert, B. D.; Peters, J. C.; Gray, H. B. *J. Am. Chem. Soc.* **2011**, *133*, 18070.

(274) Kroehnke, F. *Synthesis* **1976**, 1.

(275) Schubert, U. S.; Winter, A.; Newkome, G. R. *Terpyridine-based Materials: For Catalytic, Optoelectronic and Life Science Applications*; Wiley, **2011**.

(276) Wild, A.; Winter, A.; Schlutter, F.; Schubert, U. S. *Chem. Soc. Rev.* **2011**, *40*, 1459.

(277) Schofield, E. R.; Collin, J.-P.; Gruber, N.; Sauvage, J.-P. *Chem. Commun.* **2003**, 188.

(278) Barboiu, M.; Petit, E.; Vaughan, G. *Chem. - Eur. J.* **2004**, *10*, 2263.

(279) Schroeder, T.; Brodbeck, R.; Letzel, M. C.; Mix, A.; Schnatwinkel, B.; Tonigold, M.; Volkmer, D.; Mattay, J. *Tet. Lett.* **2008**, *49*, 5939.

(280) Collin, J.-P.; Heitz, V.; Sauvage, J.-P. *Top. Curr. Chem.* **2005**, *262*, 29.

(281) Durola, F.; Sauvage, J.-P.; Wenger, O. S. *Coord. Chem. Rev.* **2010**, *254*, 1748.

(282) Ulbricht, C.; Beyer, B.; Friebe, C.; Winter, A.; Schubert, U. S. *Adv. Mater.* **2009**, *21*, 4418.

(283) Grimsdale, A. C.; Leok Chan, K.; Martin, R. E.; Jokisz, P. G.; Holmes, A. B. *Chem. Rev.* **2009**, *109*, 897.

(284) Gohy, J.-F.; Lohmeijer, B. G. G.; Schubert, U. S. *Chem. - Eur. J.* **2003**, *9*, 3472.

(285) Gohy, J.-F. *Coord. Chem. Rev.* **2009**, *253*, 2214.

(286) Fermi, A.; Bergamini, G.; Roy, M.; Gingras, M.; Ceroni, P. *J. Am. Chem. Soc.* **2014**, *136*, 6395.

(287) Lu, X.; Li, X.; Cao, Y.; Schultz, A.; Wang, J.-L.; Moorefield, C. N.; Wesdemiotis, C.; Cheng, S. Z. D.; Newkome, G. R. *Angew. Chem., Int. Ed.* **2013**, *52*, 7728.

(288) Wang, M.; Wang, C.; Hao, X.-Q.; Li, X.; Vaughn, T. J.; Zhang, Y.-Y.; Yu, Y.; Li, Z.-Y.; Song, M.-P.; Yang, H.-B.; Li, X. *J. Am. Chem. Soc.* **2014**, *136*, 10499.

(289) Zheng, Z.; Opilik, L.; Schiffmann, F.; Liu, W.; Bergamini, G.; Ceroni, P.; Lee, L.-T.; Schutz, A.; Sakamoto, J.; Zenobi, R.; VandeVondele, J.; Schluter, A. D. *J. Am. Chem. Soc.* **2014**, *136*, 6103.

(290) Schultz, A.; Li, X.; McCusker, C. E.; Moorefield, C. N.; Castellano, F. N.; Wesdemiotis, C.; Newkome, G. R. *Chem. - Eur. J.* **2012**, *18*, 11569.

(291) Han, F. S.; Higuchi, M.; Kurth, D. G. *Org. Lett.* **2007**, *9*, 559.

(292) Pabst, G. R.; Sauer, J. *Tetrahedron* **1999**, *55*, 5067.

(293) Eaton, D. F. *Pure Appl. Chem.* **1988**, *60*, 1107.

(294) Yoshikawa, N.; Yamabe, S.; Kanehisa, N.; Takashima, H.; Tsukahara, K. *J. Phys. Org. Chem.* **2009**, *22*, 410.

(295) Li, C.-J. *Angew. Chem., Int. Ed.* **2003**, *42*, 4856.

(296) The low solubility of 10 prevents its dissolution in pure dichloromethane. Therefore, 10% of 1,1,1,3,3,3-hexafluoro-2-propanol has been added to the CH_2Cl_2 solution in order to have complete dissolution of the compound.

(297) Miyaura, N.; Yanagi, T.; Suzuki, A. *Synth. Commun.* **1981**, *11*, 513.

(298) Aspley, C. J.; Williams, J. A. G. *New J. Chem.* **2001**, *25*, 1136.

(299) Spahni, W.; Calzaferri, G. *Helv. Chim. Acta* **1984**, *67*, 450.

(300) Mikel, C.; Potvin, P. G. *Polyhedron* **2002**, *21*, 49.

(301) Ishihara, M.; Tsuneya, T.; Shiga, M.; Kawashima, S.; Yamagishi, K.; Yoshida, F.; Sato, H.; Uneyama, K. *J. Agric. Food Chem.* **1992**, *40*, 1647.

(302) Bur, D.; Corminboeuf, O.; Cren, S.; Fretz, H.; Grisostomi, C.; Leroy, X.; Pothier, J.; Richard-Bildstein, S. Preparation of Aminotriazole Derivatives as ALX Receptor Agonists. Patent WO 2009/077990 A1, **2009**.

(303) Collin, J.-P.; Durola, F.; Lux, J.; Sauvage, J.-P. *Angew. Chem., Int. Ed.* **2009**, *48*, 8532.

(304) Breuning, E.; Hanan, G. S.; Romero-Salguero, F. J.; Garcia, A. M.; Baxter, P. N. W.; Lehn, J.-M.; Wegelius, E.; Rissanen, K.; Nierengarten, H.; Van Dorsselaer, A. *Chem. - Eur. J.* **2002**, *8*, 3458.

(305) Jimenez-Molero, M. C.; Dietrich-Buchecker, C.; Sauvage, J.-P. *Chem. - Eur. J.* **2002**, *8*, 1456.

(306) Hwang, S.-H.; Wang, P.; Moorefield, C. N.; Godinez, L. A.; Manriquez, J.; Bustos, E.; Newkome, G. R. *Chem. Commun.* **2005**, 4672.

(307) Cho, T. J.; Moorefield, C. N.; Hwang, S.-H.; Wang, P.; Godinez, L. A.; Bustos, E.; Newkome, G. R. *Eur. J. Org. Chem.* **2006**, 4193.

(308) Barboiu, M.; Vaughan, G.; Graff, R.; Lehn, J.-M. *J. Am. Chem. Soc.* **2003**, *125*, 10257.

(309) Rapenne, G.; Dietrich-Buchecker, C.; Sauvage, J.-P. *J. Am. Chem. Soc.* **1999**, *121*, 994.

(310) Meier, M. A. R.; Wouters, D.; Ott, C.; Guillet, P.; Fustin, C.-A.; Gohy, J.-F.; Schubert, U. S. *Macromolecules* **2006**, *39*, 1569.

(311) Hasenknopf, B.; Lehn, J.-M.; Baum, G.; Fenske, D. *Proc. Natl. Acad. Sci. U. S. A.* **1996**, *93*, 1397.

(312) Chartrand D., PhD thesis, Université de Montréal, **2014**.

(313) Jameson, D. L.; Guise, L. E. *Tetrahedron Lett.* **1991**, *32*, 1999.

(314) Potts, K. T.; Usifer, D. A.; Guadalupe, A.; Abruna, H. D. *J. Am. Chem. Soc.* **1987**, *109*, 3961.

(315) Stublla, A.; Potvin, P. G. *Eur. J. Inorg. Chem.* **2010**, 3040.

(316) Mutai, T.; Cheon, J.-D.; Arita, S.; Araki, K. *J. Chem. Soc., Perkin Trans. 2* **2001**, 1045.

(317) Constable, E. C.; Handel, R. W.; Housecroft, C. E.; Morales, A. F.; Flamigni, L.; Barigelletti, F. *Dalton Trans.* **2003**, 1220.

(318) Tu, S.; Jia, R.; Jiang, B.; Zhang, J.; Zhang, Y.; Yao, C.; Ji, S. *Tetrahedron* **2007**, *63*, 381.

(319) Vander Jagt, D. L.; Deck, L. M.; Abcouwer, S. F.; Orlando, R. A.; Royer, R. E.; Weber, W. M.; Bobrovnikova-Marjon, E. V.; Hunsaker, L. A.; STC.UNM, USA . **2007**, 126.

(320) Heller, M.; Schubert, U. S. *Macromol. Rapid Commun.* **2002**, *23*, 411.

(321) Loim, N. M.; Kelbyscheva, E. S. *Russ. Chem. Bull.* **2004**, *53*, 2080.

(322) Persaud, L.; Barbiero, G. *Can. J. Chem.* **1991**, *69*, 315.